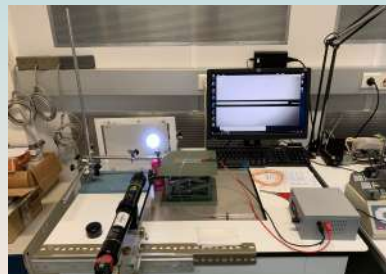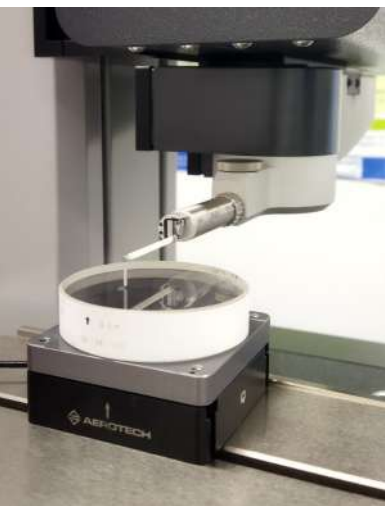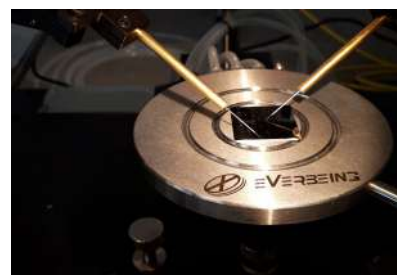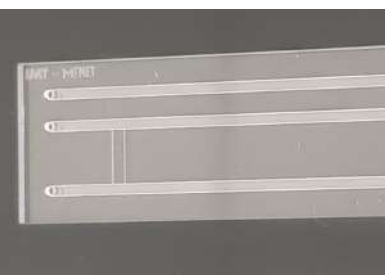Instituto Português da Qualidade

espaço Q

edição especial • maio 2025
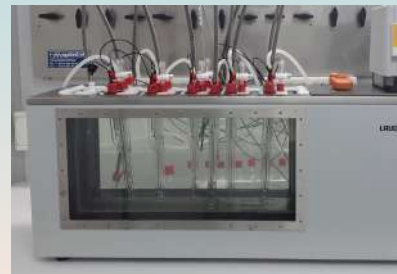
PUBLICAÇÕES
de METROLOGIA

ÍNDICE

Publicação *online*, que desde 2005, vem divulgando e partilhando com uma comunidade, cada vez mais alargada de subscritores e leitores, as iniciativas e os acontecimentos mais relevantes que têm ocorrido nos domínios da Metrologia, da Normalização e da Qualificação, cumprindo os objetivos que estão na sua génese.

Trata-se de um espaço informativo institucional que complementa a missão do Instituto Português da Qualidade de promover e divulgar os temas da qualidade, enquanto organismo nacional responsável pela coordenação da infraestrutura que constitui o enquadramento legal da Qualidade em Portugal: o Sistema Português da Qualidade (SPQ).

EDITORIAL

Caros(as) leitores(as)

É com grande satisfação que apresentamos a primeira edição especial da Espaço Q de 2025, dedicada a destacar algumas das publicações técnico-científicas mais relevantes desenvolvidas pelo Instituto Português da Qualidade (IPQ) ao longo de 2024. Como Instituição Nacional de Metrologia, o IPQ desempenha um papel fundamental no desenvolvimento da ciência da medição e das suas aplicações, e este número reflete a diversidade de temas e a abrangência e a profundidade das atividades realizadas no âmbito da Metrologia.

As publicações aqui apresentadas estão divididas em Revistas Internacionais, Revistas Nacionais, Artigos em Conferências e Posters. Nem todas as publicações estão em *Open Access*, pelo que nesse caso se apresenta apenas o respetivo *Abstract*.

Esta edição comtempla algumas das áreas de atuação do IPQ no âmbito da Metrologia, desde a investigação e o desenvolvimento metrológico até à aplicação de ferramentas de inteligência artificial e das tecnologias quânticas. Destacamos a importância da rastreabilidade das medições e das comparações interlaboratoriais na Metrologia aplicada, elementos essenciais para garantir a exatidão, a rastreabilidade e a comparabilidade dos resultados, nomeadamente em sistemas microfluídicos. São abordamos também os temas relacionados com as regras de escrita das unidades do Sistema Internacional de Unidades, um tema essencial para a uniformidade e o rigor na comunicação técnico-científica, bem como a utilização de ferramentas digitais em aplicações metrológicas, tal como os *digital twins*, e ainda uma fascinante aplicação da inteligência artificial à história da Metrologia, ilustrando como as tecnologias emergentes podem enriquecer a nossa compreensão do passado.

Este número especial inclui também publicações sobre temas associados ao desenvolvimento de materiais de referência certificados no âmbito das atividades desenvolvidas em projetos internacionais na área do ambiente e relacionados, e.g., com a captura e utilização de carbono, contribuindo para os esforços globais da descarbonização, com o desenvolvimento e a validação de métodos para a determinação da salinidade e com a influência da nova escala unificada de pH, a determinação das propriedades dos líquidos em dispositivos microfluídicos, a aplicação de memristores na Metrologia quântica, ou a importância da rastreabilidade na transferência de tempo e a sua aplicação em infraestruturas de comunicações quânticas ultra seguras.

As publicações incluídas nesta edição especial estão, direta ou indiretamente, relacionadas com os temas referidos acima, e foram desenvolvidas em colaboração com Institutos Nacionais de Metrologia congéneres e outras instituições nacionais e internacionais de reconhecido mérito científico.

Esperamos que esta edição especial da Espaço Q seja informativa e inspiradora, refletindo o compromisso contínuo do IPQ com a excelência e a inovação na Metrologia.

Boa leitura!

O Conselho Diretivo
João Pimentel
Maria João Graça

REVISTAS INTERNACIONAIS

Preparation of multicomponent mixtures to support carbon metrology

Florbela A. Dias [*], Cristina Palma, Carlos J. Costa

Instituto Português da Qualidade, Rua António Gião, 2, 2629-531 Caparica, Portugal

ARTICLE INFO

ABSTRACT

The Reference Gas Laboratory (LGR) of Portuguese Institute for Quality (IPQ) is participating in the project – Metrology Support for Carbon Capture Utilization and Storage (MetCCUS) under the new European Partnership on Metrology Program (EPM).

The goal of this project is to develop a metrological infrastructure that enables monitoring and detection of carbon dioxide leaks in energy and industrial processes, in transport networks and also allow the support of a better understanding of the life cycle of carbon dioxide.

The contribution of LGR involves the preparation of certified reference materials (CRM) to allow the measurement of impurities in CO_2 with the associated uncertainties and metrological traceability. The study is focused on the impurities: SO_2, H_2S, CO, O_2 and CH_4. This work also involves the study of interferents based on the analytical methods used. These CRM will provide support for the calibration and validation of instrumentation used in carbon capture processes.

1. Introduction

In recent years, the growing concern surrounding climate change has driven a substantial increase in environmental monitoring efforts. As a result, the demand for measurements with traceability has surged, aiming to ensure the reliability of data and minimize measurement uncertainties. It is important to note the relevance of gas mixtures in environmental monitoring and decarbonization research and how reliable gas mixtures are essential for calibrating instruments that measure atmospheric pollutants and greenhouse gases [1]. Decarbonization refers to the process of reducing carbon dioxide (CO_2) emissions resulting from human activities, with the goal of achieving a low-carbon or carbon–neutral economy. This is a critical strategy in addressing global climate change, driven by the need to reduce the amount fraction of greenhouse gases (GHGs) in the atmosphere. The accumulation of GHGs, particularly CO_2, in the atmosphere leads to global warming and climate change. High levels of CO_2 contribute to ocean acidification, extreme weather events, and loss of biodiversity. Carbon Capture Utilization and Storage (CCUS) is a set of technologies aimed at capturing CO_2 emissions from industrial and energy-related sources, utilizing the captured CO_2 in various applications, or storing it in geological formations to prevent its release into the atmosphere. Decarbonization and CCUS are integral components of global efforts to combat climate change. While there are significant challenges to overcome, advances in technology, supportive policies, and collaborative efforts provide a path forward for reducing carbon emissions and achieving a sustainable, low-carbon future [2,3].

The LGR at IPQ plays a pivotal role in this domain. It is responsible for producing, maintaining, and development of national primary standard gas mixtures in strict accordance with ISO 17034 [4]. These mixtures are meticulously prepared using a gravimetric approach, following an internal procedure aligned with the international standard ISO 6142-1 [5], thereby guaranteeing the utmost accuracy. The gravimetric method is a precise approach to creating standard gas mixtures and involves measuring the mass of each gas component accurately and combining them in specific ratios to achieve the desired amount fraction. It is also important the accuracy and precision in the preparation process and the need for meticulous calibration of equipment and careful handling of gases to minimize errors and ensure the reliability of the standards. With this method we can accomplish the metrological traceability, which ensures that measurements are consistent and comparable across different times and locations. This traceability is crucial for maintaining accuracy in various scientific and industrial applications [1,6,7,8]. The certification of these gas mixtures adheres to the international standard ISO 6143 [9,10], leveraging analytical techniques such as gas chromatography (GC), paramagnetic sensor, non-dispersive infrared spectroscopy (NDIR), and non-dispersive ultraviolet spectroscopy (NDUV).

* Corresponding author at: Instituto Português da Qualidade, Rua António Gião, 2, 2829-513 Caparica, Portugal.
E-mail address: florbelad@ipq.pt (F.A. Dias).

The quality control of these measurements is enhanced through active participation in projects and international comparisons [11,12,13,14,15,16]. Furthermore, recognition and inclusion in the *Bureau International des Poids et Mesures* (BIPM) database of Calibration and Measurement Capabilities (CMC) strengthens their commitment to quality [17].

The LGR's latest contribution focuses on preparing multicomponent gas mixtures [18] aimed at enhancing the accuracy, reliability, and traceability of carbon metrology measurements. Specifically, this paper outlines the work undertaken by LGR as part of the MetCCUS project.

The MetCCUS project is a collaborative European initiative aimed at developing advanced metrological techniques to support the accurate measurement and monitoring of carbon dioxide (CO_2) emissions and their capture, utilization, and storage processes. Started on October 1, 2022, with the participation of 21 partners and will lasts for 36 months. This project addresses the growing need for reliable and accurate data to ensure the effectiveness and safety of carbon management technologies, which are critical in mitigating climate change. The primary objectives of the MetCCUS project include development of accurate measurement techniques, improvement of standards and calibration, support for carbon capture and storage (CCS) technologies and utilization of CO_2 mainly in chemical manufacturing or enhanced oil recovery. The project encompasses several key activities namely research and development, field testing and validation, standardization and harmonization and stakeholder engagement and training. MetCCUS represents a critical effort in advancing the metrology of CO_2 measurement, with significant implications for the effectiveness of carbon capture, utilization, and storage technologies. By improving the accuracy and reliability of CO_2 measurements, MetCCUS supports the broader goal of reducing greenhouse gas emissions and combating climate change [19].

Under the MetCCUS project, the contribution of LGR involves the preparation of CRMs to allow the measurement of impurities in CO_2 with metrological traceability, providing support for methods validation and the calibration of instrumentation used in carbon capture processes. LGR had prepared the following bicomponent mixtures: SO_2 in CO_2 matrix and H_2S in CO_2 matrix; and two multicomponent mixtures SO_2+CO+O_2 in CO_2 and $H_2S+CO+CH_4+O_2$ in CO_2 matrix. This study successfully characterized four polluting gases and oxygen in CO_2 matrix within a cylinder under a pressure of approximately 40 bar, and it entailed an in-depth analysis of interferences and a stability study [20].

2. Gas mixtures preparation

As previously mentioned, reference gas mixtures are prepared according to an internal procedure based on the gravimetric method outlined in ISO 6142-1 [5]. The mixture was prepared by gravimetric addition of each component. The mole fractions of the components in the final mixtures were calculated using the following equation [5]:

$$x_i = \frac{\sum_{A=1}^{P}\left(\frac{x_{i,A} \cdot m_A}{\sum_{i=1}^{n} x_{i,A} \cdot M_i}\right)}{\sum_{A=1}^{P}\left(\frac{m_A}{\sum_{i=1}^{n} x_{i,A} \cdot M_i}\right)} \tag{1}$$

where: x_i is the mole fraction of the component i in the final mixture, $i = 1,….,n$; P is the total number of the parent gases; n is the total number of the components in the final mixture; m_A is the mass of parent gas A determined by weighing, $A=1,……, P$; M_i is the molar mass of the component i; $x_{i,A}$ is the mole fraction of the component i.

The method described on ISO 6142-1 section used applies specifically to gas mixtures or completely vaporized components, which can be introduced into the cylinder in either the gas or liquid state. The mixtures to be prepared can be either bicomponent or multicomponent.

The calculation of uncertainty associated with the amount fraction of each component requires the evaluation of contributions stemming from factors such weighing of source gases, purity of source gases and molar

masses. After these three categories of standard uncertainties have been determined, they are combined to obtain the final uncertainty corresponding to the amount fraction, through the expression:

$$u^2(x_i) = \sum_{i=1}^{n}\left(\frac{\partial x_i}{\partial M_i}\right)^2 \cdot u^2(M_i) + \sum_{A=1}^{p}\left(\frac{\partial x_i}{\partial m_A}\right)^2 \cdot u^2(m_A)$$
$$+ \sum_{A=1}^{p}\sum_{i=1}^{n}\left(\frac{\partial x_i}{\partial x_{iA}}\right)^2 \cdot u^2(x_{iA}) \tag{2}$$

where: $u(M_i)$ – uncertainty in molar mass; $U(m_A)$ – uncertainty in weighing; $u(x_{iA})$ – uncertainty in purity analysis

In order to obtain the expanded uncertainty, the combined uncertainty is multiplied by the coverage factor, k, which for a *t-distribution* with $v_{ef} = y$ effective degrees of freedom corresponds to an expanded probability of approximately 95 %.

During the preparation of gas mixtures, aluminium cylinders with a special coating are used to prevent the adsorption of mixture components on the inner walls.

Following the cylinder selection, a rigorous cleaning process is performed to ensure that any potential residues inside the cylinder do not impact the uncertainty of the composition of the final mixture. This step is particularly important when preparing mixtures with very low amount fractions.

Another critical step in the filling process is the transfer of gases from the parent cylinder, for each component, to the cylinder where the mixture is being prepared. The addition of each gas is carried out at a filling station equipped with electropolished tubes, valves, vacuum and pressure meters, and oil-free turbo molecular vacuum pumps (Fig. 1). The amount of gas added to the cylinder is carefully controlled using a mass comparator (Fig. 1).

The accurate mass of each gas component added to the cylinder is determined using a mass comparator, utilizing calibrated masses that are traceable to the national standard of mass. The traceability of gas measurements to the International System of Units (SI) is ensured using calibrated instrumentation.

By utilizing the results from the purity analysis certificates of the initial gases and the data obtained through the weighing process, the exact composition of the mixture and the associated uncertainties related to the various amount fractions obtained can be accurately calculated.

The gas mixtures were prepared with the following nominal amount fractions: SO_2 (20×10^{-6} mol/mol), H_2S (10×10^{-6} mol/mol) CO (750×10^{-6} mol/mol), CH_4 (2×10^{-2} mol/mol) and O_2 (1×10^{-2} mol/mol) that are the impurities in CO_2 matrix.

The defined limits are based on state-of-the-art knowledge from the latest research findings and available industry expertise. The project partners conducted a literature review and engaged in discussions with stakeholders, including CCS operators, CO_2 end-users, and industry representatives [19]. The CO_2 specification was developed by selecting relevant impurities and concentration levels to ensure material integrity, operability, and considerations for health, safety, and the environment for end-users.

The objective is to prepare standards of these multicomponent mixtures that are as close to reality as possible in order to simulate a real sample. We consider that these types of standards are an advantage for end users who want to carry out the calibration and validation of instrumentation used in carbon capture processes.

The cylinders containing the mixtures were placed in a rolling system for approximately an hour to ensure homogenization (Fig. 2).

3. Gas mixtures certification

The composition of the gas mixture is determined through an individual analysis of the amount fraction of each component. The procedure for determining the amount fraction is described in the international standard ISO 6143 [9]. The analytical method used is a comparative

Fig. 2. Rolling cylinder system.

each component in the prepared mixture is determined by comparing the equipment response to the standards used, and related with the gas under analysis, within appropriate measurement intervals.

The certification process takes place using an automated multi-channel sampling system, to which all the cylinders to be analysed are connected (Fig. 3).

During the analysis, cylinders are automatically selected, enabling individual circulation of gas through the analyser. This system employs the purpose-built *IPQAnaliseQui* software, which manages the sampling process and records all measurements taken by the analyser. Ultimately, all the collected data, including records of standard and sample analyses, are entered into a spreadsheet. The results are corrected with zero and pressure data.

The calibration function determination is carried out using the XGENLINE program developed by the NPL − National Physical Laboratory. This software calculates the most suitable low-degree polynomial calibration function (1, 2, 3 or 4) for a set of measurement data (X, Y), considering the uncertainties associated with the data. In our case XGENLINE program calculated the most suitable low-degree polynomial calibration function of first order for each calibration.

Hence, the determined calibration function is employed to derive estimates of the amount fraction values for the samples under analysis and their corresponding associated uncertainties.

The XGENLINE program, which meets the requirements of the ISO 6143 standard, handles uncertainty, and a standard uncertainty is obtained for each analytical test.

The expanded uncertainty presented is expressed by the combined uncertainty multiplied by the coverage factor k, which for a *t-distribution* with $v_{ef} =$ y effective degrees of freedom corresponds to an expanded probability of approximately 95 %.

4. Interferents study

The study of interferents was conducted using Primary Standard Material (PSM) and CRMs (Table 1). All these standard gas mixtures are prepared in nitrogen matrix. With these primary standards we can have traceability to the standards of these impurities in CO_2. In this case, the matrix will not influence the analysis because the analysers in question do not detect CO_2 just as they do not detect nitrogen. Each of them detects only the respective gas.

4.1. SO_2 analyser

Measurements of SO_2, H_2S, CO, CH_4, O_2, and CO_2 standards were conducted on the SO_2 analyser. The results obtained during the SO_2 analyser tests are presented in Table 2. *Zero* is the reading of the analyser

Fig. 1. Filling station and mass comparator.

method, as it employs primary reference standards to establish the calibration curve. The specific analytical methods used were GC, paramagnetic sensor, NDIR, and NDUV. The final results are presented together with their respective uncertainties in accordance with the Guide to the Expression of Uncertainty in Measurement [21].

The produced gas mixtures are certified using specific analysers for SO_2, H_2S, CO, CH_4 and O_2. In each certification, the amount fraction of

Fig. 3. Certification of Gas Mixtures Facility.

Table 1
PSM / CRM used for the study of interferents.

Interferent Gas	PSM /CRM (mol/mol)	Analytical method	Model of the analyser
H_2S	CRM412061 (9.2±0,5) x10^{-6}	NDUV	ABB Limas11 AO2020
SO_2	VSL4910 (25.00±0,37) x10^{-6}	NDIR	ABB URAS26 EL3040
CO	CRM034916 (823±4) x10^{-6}	NDIR	ABB URAS26 AO2040
O_2	VSL8612 (1.003±0,019) x10^{-2}	Paramagnetic	HB Magnos16
CH_4 / ar	CRM015377 (2.49±0,02) x10^{-2}	NDIR	ABB URAS26 AO2040
CO_2	CRM034907 (20.01±0,05) x10^{-2}	NDIR	ABB URAS26 AO2040
CH_4 / N_2	PSM202534 (2.501±0,012) x10^{-2}	NDIR	ABB URAS26 AO2040

A different analyser was used for each component.

Table 2
Results of interferents on the SO_2 analyser.

Cylinder	Amount Fraction mol/mol	Zero mV	Reading mV	S mV
CRM412061 (H_2S)	9.2×10^{-6}	−2560.95	−2556.61	0.67
VSL4910 (SO_2)	$\mathbf{25.00 \times 10^{-6}}$	**−2553.19**	**−2249.54**	**0.61**
CRM034916 (CO)	823×10^{-6}	−2547.53	−2546.61	0.53
VSL8612 (O_2)	1.003×10^{-2}	−2545.11	−2544.24	0.53
CRM015377 (CH_4 / ar)	2.49×10^{-2}	***−2543.55***	***7314.06***	0.69
CRM034907 (CO_2)	20.01×10^{-2}	−2531.41	−2540.10	0.81
PSM202534 (CH_4 / N_2)	2.501×10^{-2}	—	—	—

when the zero gas is passing, which is nitrogen. *Reading* is the value when the sample gas is passing. *S* is the standard deviation of the measurements.

According to ISO 6143, the content determination of a specified gas mixture component (analyte) is performed by measuring an instrumental response of the gas analyser. Thus, *Zero* value of the analyser does not have to be zero because the calculations are carried out with the zero correction.

We can observe that for the gases H_2S, CO, O_2 and CO_2, the zero in the Table 2 is similar to the reading. We consider that the values are similar when the difference between the reading and the zero is less than 10 mV. In this case we have a difference of 8.7 mV (Table 2), on CO_2

Table 3
Results of interferents on the H_2S analyser.

Cylinder	Amount Fraction mol/mol	Zero mV	Reading mV	S mV
CRM412061 (H_2S)	9.2×10^{-6}	-1054.93	-548.592	**4.893**
VSL4910 (SO_2)	25.00×10^{-6}	-1036.35	781.121	8.379
CRM034916 (CO)	823×10^{-6}	-1030.93	-1028.56	6.31
VSL8612 (O_2)	1.003×10^{-2}	-1027.85	-1025.05	7.16
CRM015377 (CH_4 / ar)	2.49×10^{-2}	—	—	—
CRM034907 (CO_2)	20.01×10^{-2}	-1024.66	-1022.14	4.89
PSM202534 (CH_4 / N_2)	2.501×10^{-2}	-2458.53	-2456.86	8.40

parameter, that is equivalent to 0.71×10^{-6} mol/mol which is within the measurement uncertainties of the used SO_2 primary standards (Table 12). This indicates that these gases do not interfere with the SO_2 gas reading on the SO_2 analyser. On the other hand, we have CH_4 gas interfering with the SO_2 sensor.

4.2. H_2S analyser

Measurements of SO_2, H_2S, CO, CH_4, O_2, and CO_2 standards were conducted on the H_2S analyser. The results obtained during the H_2S analyser tests are presented in Table 3.

We can observe that for the gases CO, O_2, CH_4 and CO_2, the zero in the table is similar to the reading. This indicates that these gases do not interfere with the H_2S gas reading on the H_2S analyser. On the other hand, we have SO_2 gas interfering with the H_2S sensor.

4.3. CO analyser

Measurements of SO_2, H_2S, CO, CH_4, O_2, and CO_2 standards were conducted on the CO analyser. The results obtained during the CO analyser tests are presented in Table 4.

We can observe that for the gases SO_2, H_2S, O_2 and CO_2, the zero in the table is similar to the reading. This indicates that these gases do not interfere with the CO gas reading on the CO analyser. In this case we have a difference of 7.9 mV (Table 4), on CO_2 parameter, that is equivalent to 1.1×10^{-6} mol/mol which is within the measurement uncertainties of the used CO primary standards (Table 12). Methane gas interferes with the CO analyser however the interference is negligible within the measurement uncertainty. This means that we have a difference of 31.3 mV (Table 4), on CH_4 parameter, that is equivalent to 4.6×10^{-6} mol/mol which is within the measurement uncertainties of the used CO primary standards (Table 12).

4.4. O_2 analyser

Measurements of SO_2, H_2S, CO, CH_4, O_2, and CO_2 standards were conducted on the O_2 analyser. The results obtained during the O_2 analyser tests are presented in Table 5.

Table 4
Results of interferents on the CO analyser.

Cylinder	Amount Fraction mol/mol	Zero mV	Reading mV	S mV
CRM412061 (H_2S)	9.2×10^{-6}	2180.90	2179.85	0.38
VSL4910 (SO_2)	25.00×10^{-6}	2179.17	2178.70	0.38
CRM034916 (CO)	**823×10^{-6}**	**2179.00**	**7819.40**	**0.67**
VSL8612 (O_2)	1.003×10^{-2}	2180.19	2178.71	0.42
CRM015377 (CH_4 / ar)	2.49×10^{-2}	2179.03	2147.72	0.46
CRM034907 (CO_2)	20.01×10^{-2}	2178.36	2170.43	0.36
PSM202534 (CH_4 / N_2)	2.501×10^{-2}	—	—	—

Table 5
Results of interferents on the O_2 analyser.

Cylinder	Amount Fraction mol/mol	Zero mV	Reading mV	S mV
CRM412061 (H_2S)	9.2×10^{-6}	3.7872	3.5922	0.1091
VSL4910 (SO_2)	25.00×10^{-6}	3.5856	3.4970	0.1089
CRM034916 (CO)	823×10^{-6}	3.4521	3.4017	0.1513
VSL8612 (O_2)	**1.003×10^{-2}**	**3.3812**	**13.502**	**0.111**
CRM015377 (CH_4 / ar)	2.49×10^{-2}	—	—	—
CRM034907 (CO_2)	20.01×10^{-2}	3.5417	2.4963	0.1468
PSM202534 (CH_4 / N_2)	2.501×10^{-2}	-5.5571	-6.7359	0.2068

Table 6
Results of interferents on the CH_4 analyser.

Cylinder	Amount Fraction mol/mol	Zero mV	Reading mV	S mV
CRM412061 (H_2S)	9.2×10^{-6}	2079.21	2078.47	0.19
VSL4910 (SO_2)	25.00×10^{-6}	2079.33	2080.43	0.20
CRM034916 (CO)	823×10^{-6}	2079.44	2079.35	0.20
VSL8612 (O_2)	1.003×10^{-2}	2079.87	2079.67	0.22
CRM015377 (CH_4 / ar)	**2.49×10^{-2}**	**2079.72**	**5944.30**	**0.29**
CRM034907 (CO_2)	20.01×10^{-2}	2081.01	2078.70	0.21
PSM202534 (CH_4 / N_2)	2.501×10^{-2}	—	—	—

We can observe that for the gases SO_2, H_2S, CO, O_2 and CO_2, the zero in the table is similar to the reading. The zero of methane standard is slightly different because was not carried out in the same day. This difference is not significant according to ISO 6143. This indicates that these gases do not interfere with the O_2 gas reading on the O_2 analyser.

4.5. CH_4 analyser

Measurements of SO_2, H_2S, CO, CH_4, O_2, and CO_2 standards were conducted on the CH_4 analyser. The results obtained during the CH_4 analyser tests are presented in Table 6.

We can observe that for the gases SO_2, H_2S, CO, O_2 and CO_2, the zero in the table is similar to the reading. This indicates that these gases do not interfere with the CH_4 gas reading on the CH_4 analyser.

Some of the type of the analysers described in this section can be also used for the analysis of impurities of CO_2 in the carbon capture processes in field.

As we can observe all analysers were tested with the amount fraction of 20 % of CO_2 and did not detect CO_2, which means that CO_2 does not interfere with these analysers regardless of the amount fraction of CO_2.

5. Results

Four gas mixtures, Primary Reference Material (PRM), were carefully prepared for analysis, including two binary combinations of SO_2 in a carbon dioxide matrix, designated as PRM408326 and PRM108593. Furthermore, two mixtures composed of H_2S in CO_2, labelled as PRM108595 and PRM108596, were also carefully assembled. This study facilitated the comprehensive characterization of these four mixtures,

Table 7
Standards used for SO_2 Component Certification.

Standards Used	X mol/mol	U mol/mol
VSL9159	2.554×10^{-5}	3.7×10^{-7}
VSL7897	2.992×10^{-4}	9.3×10^{-7}
VSL7886	1.0010×10^{-3}	3.2×10^{-6}

Table 8
Results of the analysis of the SO$_2$ component, in the prepared binary mixtures.

Results PRM408326 – SO$_2$ Date	X 10^{-6} mol/mol	U 10^{-6} mol/mol
2023-09-04	19.52	0.51

Results PRM108593 – SO$_2$ Date	X 10^{-6} mol/mol	U 10^{-6} mol/mol
202309-04	20.71	0.50

Table 9
Standards used for H$_2$S Component Certification.

Standards Used	X mol/mol	U mol/mol
NPL0274	4.610×10^{-6}	3.4×10^{-7}
VSL4408	5.000×10^{-6}	3.7×10^{-7}
VSL4982	1.001×10^{-5}	3.2×10^{-7}
VSL4427	5.000×10^{-5}	7.5×10^{-7}

Table 10
Results of the analysis of the H$_2$S component, in the prepared binary mixtures.

Results PRM108595 – H$_2$S Date	X 10^{-6} mol/mol	U 10^{-6} mol/mol
2023-09-11	9.97	0.48

Results PRM108596 – H$_2$S Date	$\times$ 10^{-6} mol/mol	U 10^{-6} mol/mol
2023-09-11	9.64	0.47

Table 11
Uncertainty budget for an analytical measurement, referring to the mixtures PRM108595 and PRM108596.

Cylinder PRM108595	X_i μmol/mol	Dist.	$u(X_i)$ μmol/mol	$u(y_i) = 1. u(X_i)$
run1	9.92×10^{-6}	normal	1.5×10^{-7}	1.5×10^{-7}
run2	10.02×10^{-6}	normal	1.7×10^{-7}	1.7×10^{-7}
Cylinder PRM108596	X_i μmol/mol	Dist.	$u(X_i)$ μmol/mol	$u(y_i) = 1. u(X_i)$
run1	9.63×10^{-6}	normal	$1{,}5 \times 10^{-7}$	$1{,}5 \times 10^{-7}$
run2	9.64×10^{-6}	normal	$1{,}6 \times 10^{-7}$	$1{,}6 \times 10^{-7}$

Table 12
Standards Used for Certification of the Components.

Standards Used	X mol/mol	U mol/mol
SO$_2$		
VSL9159	2.554×10^{-5}	3.7×10^{-7}
PSM502546	5.005×10^{-5}	4.0×10^{-7}
VSL7897	2.992×10^{-4}	9.3×10^{-7}
VSL7886	1.0010×10^{-3}	3.2×10^{-6}
H$_2$S		
NPL0274	4.610×10^{-6}	3.4×10^{-7}
VSL4408	5.000×10^{-6}	3.7×10^{-7}
VSL4982	1.001×10^{-5}	3.2×10^{-7}
VSL0536	2.000×10^{-4}	3.0×10^{-6}
CO		
PSM402577	5.002×10^{-4}	5.0×10^{-6}
NMI8601	5.501×10^{-4}	5.2×10^{-6}
NMI8622	7.005×10^{-4}	2.0×10^{-6}
NMI3707	8.003×10^{-4}	2.3×10^{-6}
NPL1720	9.994×10^{-4}	3.7×10^{-6}
CH$_4$		
NPL273	4.999×10^{-3}	1.9×10^{-5}
VSL6039	5.001×10^{-3}	1.8×10^{-5}
PSM202534	2.501×10^{-2}	1.2×10^{-4}
VSL6037	5.006×10^{-2}	1.0×10^{-4}
O$_2$		
VSL3704	5.00×10^{-3}	4.3×10^{-4}
VSL8612	1.003×10^{-2}	1.9×10^{-4}
VSL8554	1.0029×10^{-1}	2.6×10^{-4}

Table 13
Amount fractions of the multicomponent mixtures in CO$_2$.

PRM308978 2023-09-19		
Component in a Carbon Dioxide Matrix.	X mol/mol	U mol/mol
SO$_2$	14.26×10^{-6}	0.46×10^{-6}
CO	666.1×10^{-6}	2.7×10^{-6}
O$_2$	0.594×10^{-2}	0.027×10^{-2}

PRM202557 2023-09-20		
Component in a Carbon Dioxide Matrix.	X mol/mol	U mol/mol
H$_2$S	9.83×10^{-6}	0.48×10^{-6}
CO	669.5×10^{-6}	2.7×10^{-6}
CH$_4$	1.9685×10^{-2}	0.0060×10^{-2}
O$_2$	0.586×10^{-2}	0.027×10^{-2}

each contained within individual cylinders maintained at an approximate pressure of 40 bar.

Furthermore, two multicomponent mixtures were prepared in a CO$_2$ matrix, PRM308978 with the impurities SO$_2$, CO and O$_2$; and PRM202557, with the impurities H$_2$S, CO, O$_2$, and CH$_4$ at the previously mentioned amount fractions. These mixtures were contained within two cylinders at an approximate pressure of 40 bar each.

5.1. Results for the SO$_2$ mixtures

The binary mixtures PRM408326 and PRM108593 were certified using the SO$_2$ analyser with the standards presented in Table 7.

Table 8 shows the results of the analysis of the SO$_2$ component, in the two prepared binary mixtures, PRM408326 and PRM108593.

The values of the prepared mixtures for SO$_2$ are slightly outside the calibration range. However, the validity of the calibration is supported by the *Goodness of Fit* (*GoF*) results for the calibration curves, which are 1.85, 1.64, and 1.46. According to ISO 6143 must be *GoF*≤2 for a valid calibration curve.

5.2. Results for the H$_2$S mixtures

The binary mixtures PRM108595 and PRM108596 were certified using the H$_2$S analyser with the standards presented in Table 9.

Table 10 shows the results of the analysis of the H$_2$S component, in the two prepared binary mixtures, PRM108595 and PRM108596.

Below, as an example, we present the uncertainty budget Table 11 for an analytical measurement, referring to the mixtures PRM108595 and PRM108596, with the standard uncertainty ($u(x_i)$, $u(y_i)$), normal distribution and sensitivity coefficient 1.

The expanded uncertainty presented (Table 10) is expressed by the combined uncertainty (Eq. (2)) multiplied by the coverage factor $k = 2.04$, in this case, which for a *t-distribution* with $v_{ef} = 60$ effective degrees of freedom corresponds to an expanded probability of approximately 95 %.

5.3. Results for the multicomponent mixtures

The multicomponent mixtures PRM308978 and PRM202557 were certified using the SO_2, H_2S, CO, CH_4 and O_2 analysers with the standards presented in Table 12.

The number of standards used ranged from 3 to 5, for each component, according to the best calibration curve results based on the goodness of fit, in accordance with ISO 6143. The results of the amount fractions of the multicomponent mixtures PRM308978 (SO_2+CO+O_2 in CO_2) and PRM202557 (H_2S+CO+CH_4 + O_2 in CO_2) are presented in Table 13.

6. Summary

Under the MetCCUS project, the contribution of LGR involves the preparation of CRM to allow the measurement of impurities in CO_2 with metrological traceability, providing support for the calibration and validation of instrumentation used in carbon capture processes.

We can conclude that methane gas interferes with the SO_2 sensor when using the NDIR analytical method. Also, SO_2 gas interferes with the H_2S sensor when using the NDUV analytical method. Methane gas interferes with the CO analyser using NDIR, however the interference is negligible within the measurement uncertainty. Therefore, two multicomponent mixtures were prepared taking this information into account. One mixture does not contain SO_2 and the other does not contain CH_4 and H_2S.

Four bicomponent and two multi-component mixtures in CO_2 matrix were prepared, with uncertainties within expectations.

This work is being a joint study with project partners where some of the prepared multicomponent mixtures will be sent for analysis to some of the participating laboratories and then the results will be compared, and the conclusions will be published.

A stability study will be carried out in order to establish the shelf life of the different mixtures.

In the future, we intend to extend this study to mixtures with more components. To obtain more information regarding what is intended in the project. We intend to analyse these mixtures using other analytical methods to avoid the interferences.

These multicomponent gas mixtures standards can be used to calibrate analysers that measure the purity of carbon dioxide throughout the entire process, from capture to storage, including its industrial applications. The use of such standards is essential, as it promotes more accurate and traceable measurements.

CRediT authorship contribution statement

Florbela A. Dias: Writing – review & editing, Writing – original draft, Validation, Supervision, Project administration, Methodology, Investigation, Formal analysis, Conceptualization. **Cristina Palma:** Software, Methodology, Investigation, Formal analysis. **Carlos J. Costa:** Writing – review & editing, Software, Methodology, Formal analysis.

Declaration of competing interest

The authors declare the following financial interests/personal relationships which may be considered as potential competing interests: [Florbela Dias reports financial support was provided by EPM EURAMET. If there are other authors, they declare that they have no known competing financial interests or personal relationships that could have appeared to influence the work reported in this paper].

Data availability

Data will be made available on request.

References

[1] M. Sega, et al., Reference Materials: gas mixtures to support measurements for climate change studies, J. Phys.: Conf. Ser. 2192 (2022) 012016, https://doi.org/10.1088/1742-6596/2192/1/012016.

[2] https://www.iea.org/reports/ccus-in-clean-energy-transitions/ccus-in-the-transition-to-net-zero-emissions (accessed 20 June 2024).

[3] https://pubs.acs.org/doi/10.1021/acsengineeringau.3c00049 (accessed 20 June 2024).

[4] ISO/IEC 17034:2016 General requirements for the competence of reference material producers.

[5] ISO 6142-1:2015 – Gas analysis – Preparation of calibration gas mixtures – Part 1: Gravimetric method for Class I mixtures.

[6] E. Amico di Meane, M. Plassa, F. Rolle, M. Sega, Metrological traceability in gas analysis at I.N.Ri.M: gravimetric primary gas mixtures, Accred. Qual. Assur. 14 (2009) 607–611, https://doi.org/10.1007/s00769-009-0577-9.

[7] M.J.T. Milton, F. Guenther, W.R. Miller, A.S. Brown, Validation of the gravimetric values and uncertainties of independently prepared primary standard gas mixtures, Metrologia 43 (2006) 7.

[8] M.J.T. Milton, G.M. Vargha, A.S. Brown, Gravimetric methods for the preparation of standard gas mixtures, Metrologia 48 (2011) 5. https://iopscience.iop.org/volume/0026-1394/48.

[9] ISO 6143:2001 – Gas analysis – Comparison methods for determining and checking the composition of calibration gas mixtures.

[10] F.R. Guenther, A. Possolo, Calibration and uncertainty assessment for certified reference gas mixtures, Anal. Bioanal. Chem. 399 (2011) 489–500, https://doi.org/10.1007/s00216-010-4379-z.

[11] D. Kim, et al., International comparison CCQM-K41.2017, hydrogen sulphide in nitrogen, Metrologia 58 (2021) 08010, https://doi.org/10.1088/0026-1394/58/1A/08010.

[12] A. m. h., van der Veen et al, International comparison Euramet.QM-K111—propane in nitrogen, Metrologia 54 (2017) 08020, https://doi.org/10.1088/0026-1394/54/1A/08009.

[13] F.A. Dias, et al., Final report on international comparison EURO.QM-S5/1166: Carbon dioxide mixtures in nitrogen, Metrologia 50 (2013) 1A08017, https://doi.org/10.1088/0026-1394/50/1A/08017.

[14] F.R. Guenther, International comparison CCQM-K76: Sulphur dioxide in nitrogen, Metrologia, Tech. Suppl. 48 (2011) 08015, https://doi.org/10.1088/0026-1394/48/1A/08015.

[15] A. Botha, International comparison CCQM-K51: Carbon monoxide (CO) in nitrogen (5 μmol mol–1), Metrologia, Tech. Suppl. 47 (2010) 08008, https://doi.org/10.1088/0026-1394/47/1A/08008.

[16] G. Nieuwenkamp, Final report on international comparison CCQM-K71: Measurement of stack gas, Metrologia, Tech. Suppl. 47 (2010) 08021, https://doi.org/10.1088/0026-1394/47/1A/08021.

[17] KCDB https://www.bipm.org/kcdb/ (accessed 12 September 2023).

[18] F.A. Dias, C. Palma, C. Costa, Preparation of multicomponent gas mixtures, Revista Medições e Ensaios 17 (2023).

[19] https://metccus.eu/about-the-project/ (accessed 18 June 2024).

[20] ISO 13528:2022 – Statistical methods for use in proficiency testing by interlaboratory comparisons.

[21] Evaluation of measurement data – Guide to the expression of uncertainty in measurement JCGM 100:2008 (GUM 1995 with minor corrections).

Florbela A. Dias, PhD in Chemistry, is the Head of IPQ Reference Gas Laboratory and EURAMET/METCHEM Contact person and member of CCQM Gas Analysis WG. She is working in the gas analysis field since 2002. She participates in EPM MetCCUS project. She is contact person in national and international standardisation committees in the field of gas analysis.

Carlos J. Costa, degree in Physics and Chemistry, Senior scientist in the Amount of Substance and Electrochemistry Laboratory of the Portuguese Institute for Quality. He is currently developing activities in the Reference Gas Laboratory, namely gravimetric preparation and gas analysis.

Cristina Palma, degree in Chemical Engineering. She is a scientist doing research in the field of metrology in chemistry. She is currently developing activities in the Reference Gas Laboratory, namely gravimetric preparation and gas analysis.

Communication

The Importance of Dimensional Traceability in Microfluidic Systems

Elsa Batista, João Alves e Sousa, Fernanda Saraiva, André Lopes, Vania Silverio, Rui F. Martins and Luis Martins

Topic
Measurement Strategies and Standardization in Manufacturing

Edited by
Dr. Manuel Rodríguez-Martín, Dr. João Ribeiro and Dr. Roberto García Martín

Communication

The Importance of Dimensional Traceability in Microfluidic Systems

Elsa Batista [1,*], João Alves e Sousa [1], Fernanda Saraiva [1], André Lopes [2], Vania Silverio [3,4], Rui F. Martins [2] and Luis Martins [5]

[1] Metrology Department, Instituto Português da Qualidade, 2829-513 Caparica, Portugal; jasousa@ipq.pt (J.A.e.S.); fsaraiva@ipq.pt (F.S.)
[2] UNIDEMI, Department of Mechanical and Industrial Engineering, NOVA School of Science and Technology, Universidade NOVA de Lisboa, 2829-516 Caparica, Portugal; afcs.lopes@campus.fct.unl.pt (A.L.); rfspm@fct.unl.pt (R.F.M.)
[3] INESC Microsistemas e Nanotecnologias, INESC MN, 1000-029 Lisboa, Portugal; vania.silverio@tecnico.ulisboa.pt
[4] Department of Physics, Instituto Superior Técnico, Universidade de Lisboa, 1049-001 Lisboa, Portugal
[5] LNEC—Laboratório Nacional de Engenharia Civil, 1700-066 Lisboa, Portugal; lfmartins@lnec.pt
* Correspondence: ebatista@ipq.pt; Tel.: +351-212948167

Abstract: Dimensional measurements are fundamental in microfluidic device manufacturing and performance. The main focus of this study is the measurement of the connection port sizes in microfluidic devices and components and, accordingly, the possible existence of fluid leaks determined using the flow rate error. The sizes associated with three different microfluidic systems were determined using laser interferometry and through an optical measuring instrument, with metrological traceability to national length standards. It was possible to infer the method with the greatest accuracy and lowest measurement uncertainty for characterizing this kind of system. In conclusion, the results of this work directly address the current lack of dimensions measuring methods of microfluidic components by providing a comprehensive comparison of different protocols, ultimately suggesting a preferred option for immediate application within the microfluidic industry.

Keywords: dimensional traceability; microfluidic; leakage

1. Introduction

Microfluidics is the science that studies the behavior of fluids through paths with micrometric sizes (microchannels, microchambers, microvalves, etc.), and the technology for manufacturing them [1]. Microfluidic devices are small, simple, portable, and can be used in several emerging applications such as drug development, micro implantology, lab-on-a-chip (LOC), organs-on-chip (OoC), and organ-level physiology. LOCs are integrated systems used in various areas of biomedical and life science including diagnostics, therapeutics, drug delivery, biosensors, and tissue engineering [2,3]. OoCs are microfluidic cell culture devices used to mimic tissue [4,5]. Organ-level physiology consists of portable and cost-effective biomedical tools for pharmaceutical research [6] and personalized medicine [7], etc.

In several fields, including biomedical research and chemical analysis, microfluidic devices make it possible to accurately operate with and regulate small fluidic volumes and flow. The first microfluidic devices were developed in the 1990s [8] and had the main objective to miniaturizing analytical and chemical methods. Since then, manufacture techniques [9,10] and manipulation of the devices [11] have become more accessible. Microfluidic devices enabled the integration of different functional modules (or operational units) on a single platform and the building of a microsystem for total analysis [12,13], as it was envisioned in the early days of microfluidics [14]. However, it is essential to comprehend and take care of the key parameters that control the operation and performance of

microfluidic devices, such has connecting components, as they are crucial links between the microworld and the macroworld. To successfully integrate these parameters that affect the performance of the microfluidic systems, the following criteria should be considered: easy handling, overall compatibility of materials, adequate dimensions [1], no leakage, among others.

The EMPIR MFMET project—Establishing Metrology Standards in Microfluidic Devices, coordinated by the Portuguese Quality Institute (IPQ), has the following main objectives: (1) the development of transfer standards for miniaturized fluidic devices to be used in quality control of manufacturing processes, and (2) the development of protocols for measuring quantities, properties, dimensions, and positioning of interfaces between different materials [15].

In the scope of the EMPIR MFMET project, the present work consists of verifying the connectivity compatibility in three different microfluidic systems, which include chips of different materials, several components such as tubes, connectors, and reservoirs, etc. This components and chips were chosen due to their large applicability and current use in microfluidic systems. Also, both polydimethylsiloxane (PDMS) and polymer chips—Cyclic Olefin Copolymer (COC), tradename TOPAS©—are used as measuring substrates to identify the influence of material on the repeatability of the results. The flow rates of the systems and associated measurement errors were studied at the IPQ Volume and Flow Laboratory using the gravimetric method [16,17] and the front tracking method [18,19]. Its main focus was to measure the connection port sizes in the microfluidic devices and components, and, accordingly, the possible existence of fluid leaks in these systems. The dimensions associated with three microfluidic systems were determined using laser interferometry and an optical measuring instrument, with measurement results which were traced to national length standards. Indeed, the dimensions and tight fit between connectors and the chips are used to relate to the existence of fluid leaks in the microfluidic path.

As a collateral consequence, the comparison between the manufacturers' specifications of the three microfluidic systems and the measured dimensions of the latter enabled us to infer which method provides the greatest measurement accuracy and the lowest uncertainty for characterizing this kind of systems.

This work also highlighted the need for components manufacturing harmonization with metrological dimension quantity values traced to SI units. The knowledge gathered by this study will be included in a regulatory framework in order to improve the manufacturing process and quality control of this kind of microfluidic components.

2. Materials and Methods

2.1. Dimensional Measurement Methods

Optical metrology is the science and technology of making measurements with the use of light as standards or information carriers [20] and is being increasingly adopted in many applications where reliable data about the distance, displacement, dimensions, shape, roughness, surface properties, strain, and stress state of the object under test are required [21], mainly in manufacturing, fundamental research, and engineering applications, such as quality control, nondestructive testing, experimental mechanics, and biomedicine [22]. Interferometry is one of the most used optical techniques in fields like metrology, astronomy, fiber optics, engineering metrology, optical metrology, spectroscopy (and its applications to chemistry), quantum mechanics, surface profiling, and microfluidics [23].

Laser interferometry is used to measure the intensity of a wave resulting from the overlapping of two or more waves that have travelled over different distances and are superimposed on a single point [24]. On the broader sense, an interferometer is an optical arrangement in which two or more light waves are caused to interfere. This is often referred to as single-wavelength interferometry, and this phenomenon can be observed with a Michelson-type interferometer. In this case, the two vibrations (waves) that produce the interference signal have the same wavelength or the same frequency.

In this work, the laser measurement system, model 5528A, manufactured by Hewlett-Packard (HP), that follows the optical principle of interference at two wavelengths or heterodyne, was used. This HP system consists of the measurement display HP control unit, the laser head, the sensors for acquiring environmental conditions and measurement optics components. To carry out distance measurements, a linear interferometer is configured with a fixed polarizing beam splitter, a retroreflector, and a moveable retroreflector. The HP laser outputs two beams at 633 nm that changes whenever the measurement optics components move relative to each other. The processor weights the pulse difference and displays the indication. An integrated and automated computer with a LabVIEW-based IPQ-made application (Figure 1) was used to process the resulting indications.
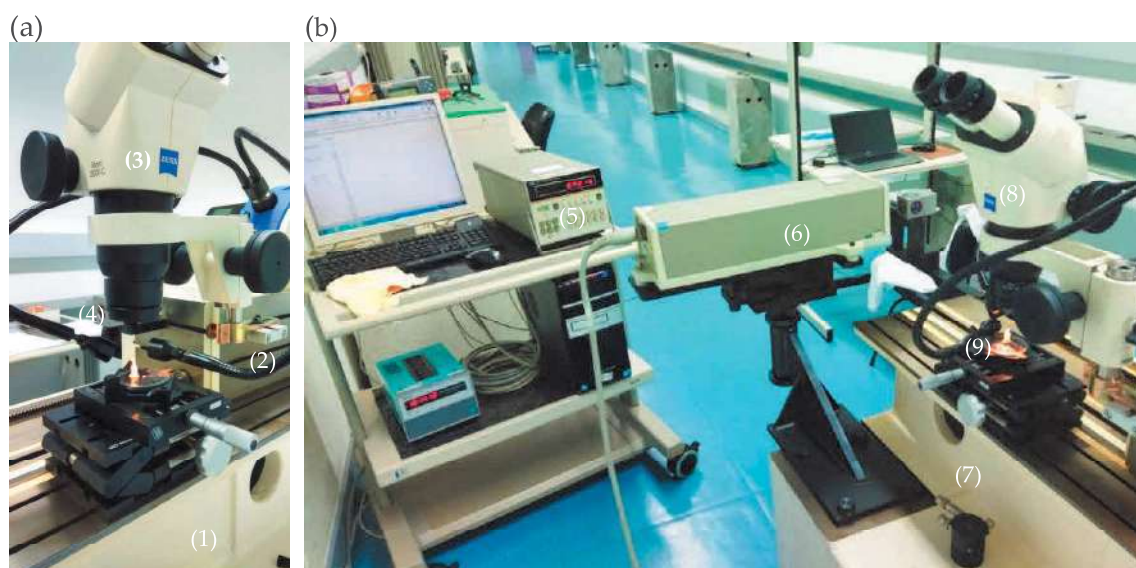
Figure 1. Measurement setup using the HP laser interferometry, the SIP 3 m bench, and the stereomicroscope. (**a**) SIP bench (1) and it's carriage (2) coupled with the stereomicroscope (3) and the HP mobile retroreflector (4). (**b**) HP control unit (5), the HP laser head (6) fixed to the SIP bench (7), the linear interferometer (8), and the stereomicroscope (without photographic camera) coupled to the carriage and the microfluidic component (9) to be measured in the top of an alignment system.

This HP laser interferometer was one of the optical technologies used in this work to measure the dimensions of connectors and tubes used in microfluidic systems. The setup includes a 3 m bench made by the Société Genevoise d'Instruments de Physique (SIP) that was used as support for fixing and align the HP laser head and a carriage. The HP mobile retroreflector was also fixed to the carriage, equipped with a stereomicroscope, namely the Zeiss Stemi 2000-C Stereo Microscope 10×–23× that has a vertical optical axis for focusing the plane of the artefact (in this case, the top of the chip). Inside the stereomicroscope display, a cross-shaped reticle is used to align the carriage movement with the distance to be measured in the microfluidic component and to define the points between which the distance is intended to be measured. Thanks to a camera attached to the top of the stereomicroscope, the planes of the viewed artifacts can be photographed. In this way, photos of the PDMS chips were made.

The measurement principle is based on the movement of the carriage fitted with the stereomicroscope and the HP mobile retroreflector (Figure 1), measured with the HP laser interferometer unit. With the help of the stereomicroscope reticle, the starting and ending points are defined on the plane of the microfluidic component. The internal (or external) diameter of the microfluidic component is determined based on the interferometer measurement of the carriage displacement, corresponding exactly to the distance between the internal (or external) diameter of the chip, visualized through the stereomicroscope.

The field of optical 3D metrology is gaining significant interest in recent years. Indeed, optical sensors can probe the geometry of workpieces and biological samples very fast, high accurately, and without any tactile physical contact to the surface object [25,26]. This 3D technology is the base of the other optical device used in this work, a three-dimensional optical measuring instrument, brand Mitutoyo Quick Vision, resolution 0.0001 mm (see Figure 2). This instrument includes a computational application, Mitutoyo Mitac Qvpack, version 7.401A, which ensures the virtual construction of geometric elements, such as lines and circles, among others, which are necessary to measure the dimensional and geometric quantities of interest. It is equipped with a digital camera installed in its instrumented vertical (Z) and transverse (Y) axes, oriented towards a reference glass plane, which is connected to the remaining instrumented longitudinal axis (X). It allows for the acquiring of images from an object, and determines the 3D coordinates of points of interest using a dedicated computer vision software, based on linear measurements related to the instrumented measurement axes (X, Y, Z). Although being able to perform 3D measurements, only 2D measurements were performed in this work. This 3D optical measuring instrument also has its own artificial lighting system, which can be adjusted to observe opaque and translucent objects with differentiated photometric characteristics. The raw data obtained are composed of 3D coordinates of points retrieved from the acquired 2D images. The diameter of the circular components was measured using the 3D coordinates of points regularly distributed in the circumference observed in the 2D image, followed by the use of a least square method in order to fit a circle to the measured points, therefore enabling the calculation of the corresponding diameter.

Figure 2. Three-dimensional optical measuring instrument and corresponding examples of use.

Both three-dimensional optical measuring instruments and laser interferometers are advanced tools used for length measurements. It should be noted that while both tools can provide extremely accurate dimensional measurements, the specific capabilities and resolutions might differ based on the particular model, design, or setup of the device.

2.2. Flow Measurement

Flow measurements were performed in each microfluidic chip assembly using the gravimetric method and the front track method in order to verify the best suitable method for leakage detection.

The gravimetric method [16] is used to determine a delivered mass of a liquid over a time interval. This method can be used for testing inline flow sensors and flow generators (Figure 3). In a gravimetric microfluidic setup, an electronic balance is used (Mettler AX26)

to determine the delivered mass of a fluid from/through the test object, which can be a flow generator, a microfluidic device, or a flow meter. The time interval in which the mass is delivered is determined by a timing module to derive the mass flow rate. The climatic conditions such as air temperature, relative humidity, and pressure are determined to correct for buoyancy effects on the balance. The liquid temperature is determined to convert the mass flow rate into a volumetric flow rate, considering the density of the liquid used [17]. In addition, this particular setup not only uses an evaporation trap to reduce evaporation, which is especially useful at low flow rates, but also a connecting tube was inserted below the water surface inside the weighing vessel of the balance to avoid the drop impact effect. The flow was generated with a programmable syringe pump Nexus 3000, from Chemyx, using a 1 mL ILS glass syringe connected to a polyethylene (PE) tube of 1.26 mm (0.05″) inner diameter.

Figure 3. Gravimetric flow measurement setup.

The front tracking method for flow measurements described in [18,19] is an optical method that consists of tracking the position of the meniscus of a liquid (liquid/air or liquid/liquid interface) inside a (typically) capillary tube over time. An optical image acquisition system and image processing software are used to achieve the position over time of the meniscus. Knowing the displacement of the meniscus over time and the cross-section area of the capillary, it is possible to calculate the flow rate. Alternatively, the front tracking method can be performed in a microfluidic channel if the inner dimensions of the channel are known along with their associated uncertainties. In this specific case, a high-resolution Alvium 1800 U-1240 camera with a resolution of 12 MP and a Qioptic Optem 7:1 telecentric zoom lens was used (Figure 4). The camera was connected to a computer and uses a Python-based program to identify the meniscus and calculate its position.
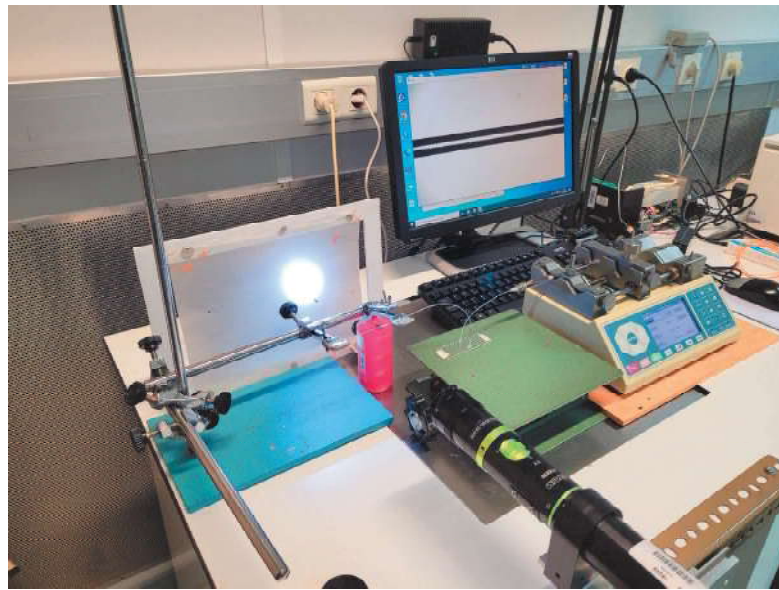
Figure 4. Front track flow measurement setup.

2.3. Microchips Used

Three different chips made of polydimethylsiloxane (PDMS) and of cyclic olefin copolymer (TOPAS) were used:

(i) PDMS chip with one channel of 100 μm width and 50 μm depth, with two 0.9 mm inlet holes; material: PDMS; dimensions: 40 mm × 10 mm; manufactured by INESC MN (Figure 5) and tested for assemblies with different components.

(ii) Chip A (see Figure 6): parallel channel array with fluid interface holes; material: TOPAS® (COC polymer for medical use); dimensions: 75.5 mm × 25.5 mm × 1.5 mm; with eight parallel channels of 100 μm width, 100 μm depth, 18 mm length; connectors are glued to the chip holes.

(iii) Chip C (see Figure 7): parallel channels with mini Luer fluidic interface; material: TOPAS® (COC polymer for medical use); dimensions: 75.5 mm × 25.5 mm × 4 mm; with eight parallel channels of 100 μm width, 100 μm depth, 18 mm length. Luer fluidic interface, similar to "female mini luer port" integrated directly on the chip.
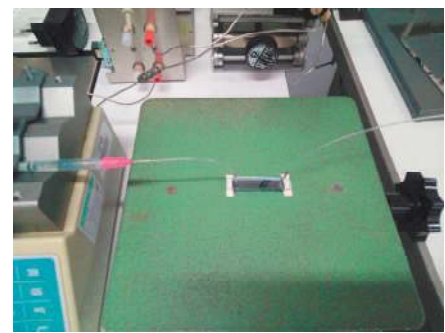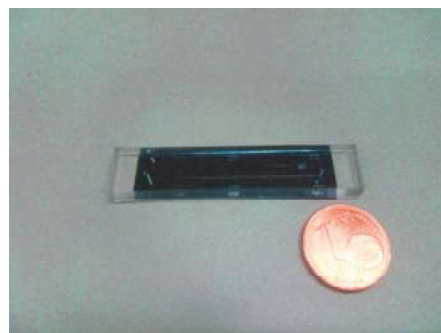
Figure 5. PDMS chip and correspondent assembly.
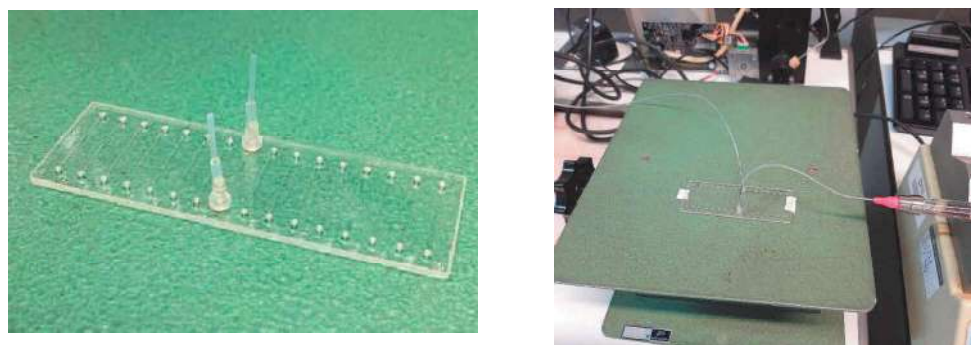
Figure 6. TOPAS® chip A and correspondent assembly.
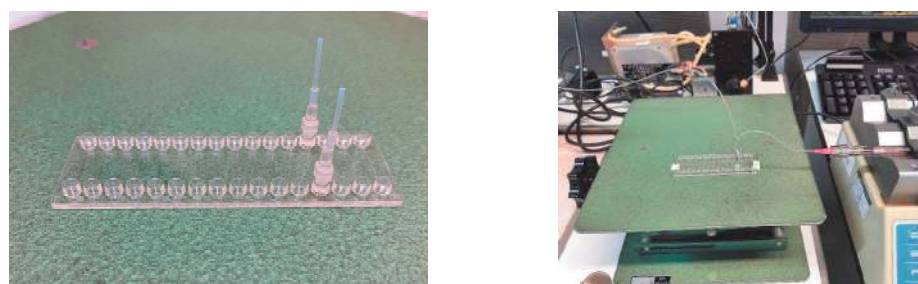
Figure 7. TOPAS® chip C and correspondent assembly.

3. Results

3.1. Dimensional Measurement Results

The dimensional measurement results for the three different assemblies using the laser interferometry and the 3D optical measuring instrument are shown in Figures 8–12. For all the assemblies, the inner diameter or external diameter of each microfluidic component was measured depending on the type of connection and accessory used.

In the case of accessories of translucent material when using laser interferometry, the image viewed on the stereomicroscope (even with the cross-shaped reticle in place), does not enable good repeatability in defining the starting and ending points of the diameter to be measured. This led to dimensional measurement results outside of laboratory acceptance criteria. When considered as unsatisfactory quality measurement results, only the measurement standard deviation was displayed, and the corresponding uncertainty was not estimated. For PE tube and stainless-steel catheter components, the measurement results were acceptable, and therefore the expanded uncertainty was presented with a coverage factor $k = 2$ which, for a normal distribution, corresponds to an approximately 95% coverage probability. These length measurement results are displayed in Figure 8.

	Measurand	Value	U /mm
PE Tube	Inner diameter	1.26 mm	0.04

	Measurand	Value	U /mm
Stainless steel catheter	External diameter	0.912 mm	0.010

Figure 8. "PE tube" and "stainless steel catheter" top planes photographed with the Zeiss stereomicroscope, and the respective the dimensions measured using the HP laser interferometer.

For the PE tube and the stainless steel components, the measurement uncertainties were determined using the interferometer. It was evidenced to be larger for the former than

for the latter due to the circularity measurement uncertainty component being greater for the plastic materials.

All the measurement results obtained from the 3D optical measuring instrument are presented with expanded uncertainty values, with a coverage factor k = 2, corresponding to an approximately 95% coverage probability.

The dimensional measurement uncertainty was calculated with the GUM methodology [27] using the following optical measuring instrument uncertainty components:

- calibration;
- instrumental drift;
- instrument resolution;
- geometrical shape deviation (circularity);
- linear thermal variation;
- measurement repeatability.

The values of the measurands in the Tables in Figures 9–13 were obtained with the HP laser interferometer, as described in Section 2.1.

	Measurand	Value	Standard Uncertainty
Hole in the chip	Inner diameter	0.710 mm	0.003 mm

Figure 9. Chip PDMS hole in the chip photographed with the Zeiss stereomicroscope, and dimensions measured using the HP laser interferometer; the assembly is shown in Figure 5.

	Measurand	Value	Standard Deviation
Rubber tube	Inner diameter	0.806 mm	0.005 mm

Figure 10. Topas chip A "rubber tube" top planes photographed with the Zeiss stereomicroscope, and the dimensions measured using the HP laser interferometer; the assembly is shown in Figure 6.

	Measurand	Value	Expanded Uncertainty
Rubber tube	Inner diameter	0.820 mm	0.039 mm
	Measurand	Value	Expanded Uncertainty
Connector	External diameter top	1.77 mm	0.44 mm
	Measurand	Value	Expanded Uncertainty
Hole in the Chip	Inner diameter	1.384 mm	0.038 mm

Figure 11. Topas chip A "rubber tube" top plane photographed with the Zeiss stereomicroscope, "Connector" and "Hole in the chip" photographed with the 3D measuring instrument, and the dimensions measured with the 3D optical measuring instrument; the assembly is shown in Figure 6.

3.1.1. Chip PDMS

The 3D optical measuring instrument was not used to determine the dimensions in the PDMS chip due to the problems in optical reading the connecting holes in this device.

For the hole of the chip, only standard deviation was displayed due to technical difficulties in measuring the rubber material sizes that do not enable obtaining acceptable measurement repeatability.

3.1.2. Chip A

For the rubber tube, only standard deviation was displayed because technical difficulties that do not enable acceptable measurement repeatability.

The uncertainty values for the connector measurements are higher than for the other components due to the form of the connector top. Nevertheless, as the values obtained for the rubber tuber using both optical methods are very similar, a coherence is provided for the measurement results.

3.1.3. Chip C

Chip C was studied with the laser interferometry and 3D optical measuring instrument methods. For both of them, it can be observed that the measurement results for the connector and hole in chip are very similar, with the measurement uncertainty or standard deviation being larger for the connector than for the hole in the chip. This difference is due to a corresponding larger circularity uncertainty component.

This dimension-measurement data analysis allows us to suggest that the measured length values and associated uncertainties/standard deviation are consistent. It is tempting to deduce that both methods may be used to determine the dimensions of the microfluidic components. However, the influence of the translucid components' variability on the uncertainty of the measurement determination requires further studies on the interferometer method to confirm the equivalent usability of the methods.

Shape deviations intrinsic to the components' characteristics such as roundness, cylindricity, and translucency of plastic material are identified as the main factors for the high standard deviations computed with the interferometric method. The order of magnitude of the latter is about 0.01 mm, when the interferometer has a resolution of 0.01 μm. This corresponds to dimensional measurement results of clearly unsatisfactory quality, for which the uncertainty estimate was not performed.

From the results with the 3D optical measuring instrument, in Figures 11 and 13, it can be concluded that uncertainty values obtained in the dimensional measurements are also dependent on the component material. The more rigid and less translucent the material, the smaller the uncertainty.

From the results of the Topas chip C connector outer diameter, in Figures 12 and 13, it can be concluded that the latter is smaller than the inner diameter of the hole in the chip. This insufficient match may be the origin of leaks.

Injection-molded COC/COP devices appear to have more uniform dimensions than PDMS. Indeed, the standard deviation obtained for the Topas chip C hole in the chip is almost half the value (0.24%) of the PDMS hole (0.42%).

	Measurand	Value	Standard Deviation
Connector	Small inner diameter	0.93 mm	0.11 mm
	Big external diameter	2.577 mm	0.012 mm
	Measurand	**Value**	**Standard Deviation**
Hole in the chip	Inner diameter	2.883 mm	0.007

Figure 12. Topas chip C connector and hole in the chip photographed with the 3D measuring instrument digital camara, and dimensions measured with the HP interferometer; the assembly is shown in Figure 7.

Figure 13. Topas chip C "connector" and "hole in the chip" photographed with the 3D measuring instrument digital camara, and dimensions measured with the 3D optical measuring instrument; the assembly is shown in Figure 7.

3.2. Flow Results

The flow measurement results, error, and uncertainty for the three different assemblies using the gravimetric method and the front track method are shown in Tables 1 and 2.

Table 1. Experimental flow results obtained with the gravimetric method.

	Gravimetric Method			
Chip	Nominal Flow, F_N/(mL/h)	Measured Out of Chip Flow, F_{meas}/(mL/h)	Error, E/%	U/%
PDMS	0.001	0.0011	11.94	25
	0.01	0.0107	4.84	4.1
	0.1	0.0907	8.17	2.5
	1	0.8875	0.55	2.4
A	0.01	0.0099	−1.0	5.0
	0.1	0.0983	−1.7	3.8
	1	0.9907	−0.93	0.19
C	0.01	0.0069	−31	5
	0.1	0.0970	−2.6	3.4
	1	1.0170	1.7	3.0

Table 2. Experimental flow results obtained with the front track method.

	Front Track Method			
Chip	Nominal Flow, F_N/(mL/h)	Measured Out of Chip Flow, F_{meas}/(mL/h)	Error, E/%	U/%
PDMS	0.001	−0.0014	241.3	14.0
	0.01	0.0113	−13.3	3.3
	0.1	0.0961	3.9	2.6
	1	1.0257	−2.6	4.0
A	0.01	0.0095	5.0	3.7
	0.1	0.0967	3.3	2.8
	1	0.9819	1.8	6.2
C	0.01	−0.0033	133.0	43
	0.1	0.0996	0.4	1.9
	1	1.0259	−2.6	4.0

Here, the measurement error is equal to the subtraction of the nominal or read flow value by the measured flow out of the chip value, which is the reference flow value.

The uncertainty calculation was performed according to the GUM procedure [27] and the relevant literature for each method [28,29]. The evaluation of the consistency of the gravimetric and flow track methods was analyzed according to the normalized error statistics (E_n) [30], and the results are presented in Table 3.

Table 3. Flow experimental consistency analysis of results obtained with the gravimetry and front track methods.

Chip	Nominal Flow, F_N/(mL/h)	E_n
PDMS	0.001	8.10
	0.01	−3.50
	0.1	−1.20
	1	0.67
A	0.01	−0.65
	0.1	−0.34
	1	−0.14
C	0.01	−2.34
	0.1	0.55
	1	0.18

From Tables 1–3, it can be observed that small deviations from nominal values were observed for the majority of the tested flow rates. The high error obtained for the smallest flow rates in Chip C (0.01 mL/h) can be explained by leakage occurring due to the incompatibility of dimensions between the connector outer diameter and the hole in the chip inner diameter, as mentioned in Section 3.1.3. In the case of the front track method, the observation of negative flow values corresponds to a situation with a null resulting flow going out of the chip, due to the meniscus moving in the opposite direction of the out-of-the-chip flow. The consistency of the methods was analyzed with the E_n value statistics. Since the majority of the results evidenced E_n lower than 1, it can be concluded that they are satisfactory.

4. Final Discussion and Conclusions

The objective of this work was to determine the sizes of the connection port of microfluidic devices and their components using two different methods, a laser interferometer and an optical 3D measuring instrument. One of the aftermaths was to evaluate the possible existence of fluid leaks in each system due to component dimensional incompatibility by determining the flow rate error of different microfluidic systems using the gravimetric and the front track methods.

The length-measured results obtained with the laser interferometer and optical 3D measuring instrument methods were found to be broadly metrologically compatible [31].

For the laser interferometry method, the definition of the measurement plane of the accessories in translucent material presented a technical difficulty due to the equipment available. As a consequence, it was only possible to compute a measurement standard deviation.

Shape deviations inherent to the plastic accessories, such as roundness, cylindricity and translucency, are known to be the main factors responsible for the evidenced standard deviation high values in this study. For instance, it was observed that for a 0.01 μm resolution interferometer, there was a 0.01 mm standard deviation order of magnitude. Indeed, the shape deviations and the constituents being plastic materials make the tubes and connector's dimensions very difficult to highly accurately measure with the interferometer.

Therefore, the measured values may only be associated with standard deviations and not uncertainties.

For the optical 3D measuring instrument, it was possible to calculate the associated uncertainties and images for all accessories, even the translucent ones. Therefore, it can be concluded that using 3D optical measuring instrument is the best measurement method for translucent material. It was also verified that uncertainty values in all dimensional measurements are completely dependent on the component material. The more rigid the material, the smaller the uncertainty.

From the dimensional measurements, Topas chip C, the connector's outer diameter, was evidenced to be smaller than the hole in the chip's inner diameter. Consequently, these components are not dimensionally compatible and tightly linked. This may have an influence for potential leakage in the system. This situation was validated by the flow tests.

Flow tests were performed in each chip assembly using the front track method and the gravimetric method in order to verify possible variabilities and advantages of the methods. The consistency of the methods was analyzed using the E_n value statistics, and it was verified that the majority of the results are satisfactory, i.e., evidencing E_n values lower than 1. Therefore, no significant difference was found in the performance of each method. As the uncertainty values of both methods are very similar, it can be concluded that both methods can be used for the flow determination of microfluid chips. The flow measurement results obtained also confirm the connection problem in the Topas chip C due to the size incompatibility between the connector and the microfluidic hole, where a leakage could be evidenced in both methods. Within the front track method, the connection problem is even more evident due to the negative values; this means that no flow came out of the chip, and the meniscus was moving in the opposite direction of the flow due to evaporation and negative pressure.

Injection-molded COC/COP devices appear to be more uniform than PDMS, mainly having the outer dimensions of a standard microscope slide or microtiter plate, 1.5 mm port size, and mini-Luers with a pitch of 4.5 mm. It is usually connected to flexible tubing, or a sleeve. These material components also provide better repeatability of measurements in both quantities: flow, and dimensions.

The results of this work directly address the current lack of measurement methods for dimensions of microfluidic structures, especially after assembly, by providing a comprehensive comparison of different protocols, ultimately suggesting a preferred option for immediate application within the microfluidic industry. Future work can be performed with glass chips and different microfluidic components.

Author Contributions: Conceptualization, E.B. Methodology, E.B. and F.S., A.L., V.S. and L.M.; formal analysis, E.B.; investigation, E.B., F.S., A.L. and L.M.; resources, E.B., F.S. and L.M.; data curation, E.B.; writing—E.B., F.S., L.M. and V.S. review and editing, R.F.M., J.A.e.S. and E.B.; visualization, R.F.M. and J.A.e.S.; supervision, E.B.; project administration, E.B.; funding acquisition, E.B. All authors have read and agreed to the published version of the manuscript.

Data Availability Statement: The data presented in this study are available on request from the corresponding author.

Conflicts of Interest: The authors declare no conflicts of interest.

References

1. *ISO 22916:2022*; Microfluidic Devices—Interoperability Requirements for Dimensions, Connections and Initial Device Classification. ISO: Geneva, Switzerland, 2022.
2. Azizipour, N.; Avazpour, R.; Rosenzweig, D.H.; Sawan, M.; Ajji, A. Evolution of Biochip Technology: A Review from Lab-on-a-Chip to Organ-on-a-Chip. *Micromachines* **2020**, *11*, 599. [CrossRef] [PubMed]
3. Grayson, A.C.R.; Shawgo, R.S.; Johnson, A.M.; Flynn, N.T.; Li, Y.; Cima, M.J.; Langer, R. A BioMEMS review: MEMS technology for physiologically integrated devices. *Proc. IEEE* **2004**, *92*, 6–21. [CrossRef]
4. Silverio, V.; Cardoso, S. Lab-on-a-chip: Systems integration at the microscale. In *Drug Delivery Devices and Therapeutic Systems*; Elsevier Science: Amsterdam, The Netherlands, 2021; Chapter E, ISBN 978-0-12-819838-4.
5. Leung, C.M.; de Haan, P.; Ronaldson-Bouchard, K.; Kim, G.-A.; Ko, J.; Rho, H.S.; Chen, Z.; Habibovic, P.; Jeon, N.L.; Takayama, S.; et al. A guide to the organ-on-a-chip. *Nat. Rev. Methods Prim.* **2022**, *2*, 33. [CrossRef]
6. Huh, D.; Leslie, D.C.; Matthews, B.D.; Fraser, J.P.; Jurek, S.; Hamilton, G.A.; Thorneloe, K.S.; McAlexander, M.A.; Ingber, D.E. A human disease model of drug toxicity–induced pulmonary edema in a lung-on-a-chip microdevice. *Sci. Transl. Med.* **2012**, *4*, ra147–ra159. [CrossRef] [PubMed]
7. Bhatia, S.N.; Ingber, D.E. Microfluidic organs-on-chips. *Nat. Biotechnol.* **2014**, *32*, 760–772. [CrossRef] [PubMed]
8. Berlanda, S.F.; Breitfeld, M.; Dietsche, C.L.; Dittrich, P.S. Recent Advances in Microfluidic Technology for Bioanalysis and Diagnostics. *Anal. Chem.* **2021**, *93*, 311–331. [CrossRef] [PubMed]
9. Paik, S.; Kim, G.; Chang, S.; Lee, S.; Jin, D.; Jeong, K.Y.; Lee, I.S.; Lee, J.; Moon, H.; Lee, J.; et al. Near-Field Sub-Diffraction Photolithography with an Elastomeric Photomask. *Nat. Commun.* **2020**, *11*, 805. [CrossRef] [PubMed]
10. Vanderpoorten, O.; Peter, Q.; Challa, P.K.; Keyser, U.F.; Baumberg, J.; Kaminski, C.F.; Knowles, T.P.J. Scalable Integration of Nano-, and Microfluidics with Hybrid Two-Photon Lithography. *Microsyst. Nanoeng.* **2019**, *5*, 4020. [CrossRef] [PubMed]
11. Li, W.; Yu, M.; Sun, J.; Mochizuki, K.; Chen, S.; Zheng, H.; Li, J.; Yao, S.; Wu, H.; Ong, B.S.; et al. Crack Engineering for the Construction of Arbitrary Hierarchical Architectures. *Proc. Natl. Acad. Sci. USA* **2019**, *116*, 23909–23914. [CrossRef] [PubMed]
12. Schmidt-Speicher, L.M.; Länge, K. Microfluidic integration for electrochemical biosensor applications. *Curr. Opin. Electrochem.* **2021**, *29*, 100755. [CrossRef]
13. Fernández-la-Villa, A.; Pozo-Ayuso, D.F.; Castaño-Álvarez, M. Microfluidics and electrochemistry: An emerging tandem for next-generation analytical microsystems. *Curr. Opin. Electrochem.* **2019**, *15*, 175–185. [CrossRef]
14. Manz, A.; Graber, N.; Widmer, H.M. Miniaturized Total Chemical Analysis Systems: A Novel Concept for Chemical Sensing. *Sens. Actuators B* **1990**, *1*, 244–248. [CrossRef]
15. Available online:. https://Mfmet.eu (accessed on 26 February 2024).
16. Batista, E.; Alves e Sousa, J.; Cardoso, S.; Silverio, V. Experimental testing for metrological traceability and accuracy of liquid microflows and microfluidics. *Flow Meas. Instrum.* **2021**, *71*, 101691. [CrossRef]
17. Bissig, H.; Petter, H.T.; Lucas, P.; Batista, E.; Filipe, E.; Almeida, N.; Ribeiro, L.F.; Gala, J.; Martins, R.; Savanier, B.; et al. Primary standards for measuring flow rates from 100 nL/min to 1 mL/min—Gravimetric principle. *Biomed. Eng.* **2015**, *60*, 301–316. [CrossRef] [PubMed]
18. Batista, E.; Sousa, J.A.; Alvares, M.; Afonso, J.; Martins, R. Development of an experimental setup for micro flow measurement using the front tracking method. *Meas. Sens.* **2021**, *18*, 100152. [CrossRef]
19. Boudaoud, A.W.; McGraw, J.D.; Lopez-Leon, T.; Ogheard, F. Traceability of the primary Nano-flow measurement System: Measuring the local inner diameter of a glass capillary. *Measurement* **2023**, *218*, 113141. [CrossRef]
20. Zuo, C.; Qian, J.; Feng, S.; Yin, W.; Li, Y.; Fan, P.; Han, J.; Qian, K.; Chen, Q. Deep learning in optical metrology: A review. *Light Sci. Appl.* **2022**, *11*, 39. [CrossRef] [PubMed]
21. Gåsvik, K.J. *Optical Metrology*, 3rd ed.; Wiley: Hoboken, NJ, USA, 2002.
22. Yoshizawa, T. *Handbook of Optical Metrology: Principles and Applications*, 2nd ed.; CRC Press: Boca Raton, FL, USA, 2017.
23. Hariharan, P. *Basics of Interferometry*; Elsevier Inc.: New York, NY, USA, 2007.
24. Donges, A.; Noll, R. *Laser Measurement Technology—Fundamentals and Applications*; Springer: Berlin, Germany, 2014; ISBN 978-3-662-43633-2.
25. Engel, T. 3D optical measurement techniques. *2023 Meas. Sci. Technol.* **2002**, *34*, 032002. [CrossRef]
26. Su, X.; Zhang, Q. Dynamic 3-D shape measurement method: A review. *Opt. Laser Eng.* **2010**, *48*, 191–204. [CrossRef]
27. *JCGM 100:2008*; BIPM, IEC, IFCC, ILAC, ISO, IUPAC, IUPAP, and OIML, Evaluation of Measurement Data—Guide to the Expression of Uncertainty in Measurement. BIPM: Paris, France, 2008.
28. Batista, E. Innovative Contributions on Calibration Methodologies towards Reliable Microflow Measurements. Ph.D. Thesis, Mechanical Engineering, FCT/UNL, Caparica, Portugal, 2022.
29. Ahrens, M.; Klein, S.; Nestler, B.; Damiani, C. Design, uncertainty assessment of a setup for calibration of microfluidic devices down to 5 nL min^{-1}. *Meas. Sci. Technol.* **2014**, *25*, 015301. [CrossRef]

30. *ISO 13528:2022*; Statistical Methods Used in Proficiency Testing by Interlaboratory Comparisons. ISO: Geneva, Switzerland, 2022.
31. *JCGM 200:2012*; BIPM, IEC, IFCC, ILAC, ISO, IUPAC, IUPAP, and OIML, International Vocabulary of Metrology | BASIC and General Concepts and Associated Terms (VIM). Joint Committee for Guides in Metrology: Paris, France, 2012.

Article

Digital Twin for a Frequency Mixer Used as a Phase Sensor

Carlos Pires, Manuel Abreu, Isabel Godinho, Rui Agostinho and João A. Sousa

Special Issue

Article

Digital Twin for a Frequency Mixer Used as a Phase Sensor

Carlos Pires [1] ![ID], **Manuel Abreu** [2,*] ![ID], **Isabel Godinho** [1] ![ID], **Rui Agostinho** [2] ![ID] and **João A. Sousa** [1] ![ID]

[1] Instituto Português da Qualidade, Rua António Gião, 2, 2829-513 Caparica, Portugal; carlosp@ipq.pt (C.P.); igodinho@ipq.pt (I.G.); jasousa@ipq.pt (J.A.S.)

[2] Physics Department, Faculdade de Ciências da Universidade de Lisboa, 1749-016 Lisboa, Portugal; rjagostinho@ciencias.ulisboa.pt

* Correspondence: maabreu@ciencias.ulisboa.pt

Abstract: The Portuguese Institute for Quality is responsible for the realization and dissemination of the frequency standard in Portugal. There are several techniques for frequency transfer, but we use a frequency mixer to detect phase variations between two light signals with different wavelengths, traveling along an optical fibre. In this paper, we present the development of a digital twin (DT) that replicates the use of a frequency mixer to improve the frequency transfer problem. A setup was built to train and validate the technique: a frequency mixer was used to determine the phase difference between the two signals, which are caused by temperature gradients in the fibre, together with real-time temperature data from sensors placed along the fibre and on the mixer itself. The DT was trained with two machine learning algorithms, in particular, ARIMA and LSTM networks. To estimate the accuracy of the frequency mixer working as a phasemeter, several sources of uncertainty were considered and included in the DT model, with the goal of obtaining a phase value measurement and its uncertainty in real time. The JCGM 100:2008 and JCGM 101:2008 approaches were used for the estimation of the uncertainty budget. With this work, we merge DT technology with a frequency mixer used for phase detection to provide its value and uncertainty in real time.

Keywords: digital twin; phase measurements; metrology; traceability; frequency mixer

1. Introduction

Metrology day is celebrated annually on May 20th, and in 2022 the theme was "Metrology in the Digital Era". This theme highlights the importance of digital technology, such as Digital-SI, Big Data, Artificial Intelligence, and machine learning (ML), which are revolutionizing metrology as some of the most exciting societal trends of today. In 2020, the European Commission published the strategy 'Shaping Europe's digital future', alongside its European Industry Strategy, Data Strategy, and the White Paper on Artificial Intelligence. As stated in a joint message by the directors of the Bureau International des Poids et Measures (BIPM) and International Bureau of Legal Metrology (BIML): "The digital transformation of metrology can bring many benefits to our community. It can expedite time to market for measurement products and services and reduce delays associated with approval processes. In turn, this contributes to innovation, product agility and sustainability" [1].

In this context, all National Metrology Institutes (NMIs) were encouraged to apply these "new" digital tools to metrology. As the Portuguese National Metrology Institute, the Portuguese Institute for Quality, IPQ, is responsible for the realization and dissemination of the national reference time scale, UTC(IPQ). Thus, digital transformation has begun in the Laboratory of Time and Frequency (LTF), where we are implementing a digital twin (DT) to measure phases using a frequency mixer. Transferring the standard frequency allows users to syntonize their local oscillators to the reference time scale. Of the existing techniques for frequency transfer, one uses a frequency mixer for relative phase-difference detections [2], which allows corrections in the process of frequency transfer with the objective of increasing

the frequency stability at the end-user level. Applying these new digital tools to frequency transfer is one way to give traceability to the synchronization of oscillators.

In many research projects, simulations serve as a tool to replicate various system processes, enabling analysis and optimization at lower costs. However, traditional simulations often rely on theoretical models and lack real data. The concept of the digital twin, developed in recent years, addresses these limitations. While it utilizes the same mathematical models as simulations, a digital twin integrates real-world data, employs machine learning methods for prediction, and incorporates a user-friendly interface. This creates a significantly richer and more dynamic environment for studying and optimizing systems.

In communication systems, phase detection is essential for synchronizing signals. A frequency mixer is a key component in phase detection, especially in systems like Phase-Locked Loops (PLLs), radio communications, and signal processing. Although some nonideal characteristics exist, theoretically, any frequency mixer could be used as a phase detector. In this mode, a mixer compares the phases of two input signals by multiplying them and producing an output that reflects their phase difference.

The primary objective of implementing a DT for phase detection is to enhance the prediction performance of an optical channel transmission, including all terminal equipment, when sending a frequency standard signal over fibre optics. Furthermore, the DT of a frequency transmission setup enables the evaluation of all devices' stability by detecting phase fluctuations induced by thermal perturbations over the entire medium, with a level of accuracy compatible with the standards required in some applications. By accurately measuring the signal's phase, temperature-induced fluctuations can be compensated for, thereby improving stability and reliability in the frequency transfer.

In general, the frequency stability of an oscillator in free mode and in small integration times is better than the frequency stability of a secondary oscillator at the end of a transport medium, the reason being that the medium becomes the biggest source of uncertainty to the secondary oscillator, regardless of its inherent stability or accuracy.

The experimental setup of this work is represented in Figure 1 and the physical part of it is a 1000 m optical fibre link between two laboratories. In one laboratory, a 10 MHz reference frequency is generated by three caesium (Cs) clocks with a stability value of the order of 5×10^{-14} for one day, traceable to the Coordinated Universal Time (UTC) designated as UTC(IPQ). The temperature and relative humidity conditions were measured and recorded at a rate of one measurement per minute.

Figure 1. Representation of the physical system for phase measurement, which includes two lasers to transform the signal from UTC(IPQ) into light, two wavelength multiplexers (MUX and DMUX), two photodetectors to detect light, a frequency mixer, and a multimeter to measure voltage.

The experimental setup includes the following equipment: two lasers with different wavelengths, namely 1310 nm and 1550 nm, two Bias-T instruments for amplitude modulation with the reference frequency, and a wavelength division multiplexer (WDM) to send both signals through the optical fibre. The 1000 m long optical fibre linking the two laboratories is standard in telecommunications (SMF-28, ETC, Portugal, 2021). The fibre runs on the rooftop of the building and is folded over, backward and forward, several times on the same path. In this way, more than 90% of the fibre is affected by the outside temperature.

In the second laboratory, we have a WDM for separating the light according to the wavelength, one photodetector for each of the wavelengths, a frequency mixer, and a multimeter to measure voltage at the output terminal of the mixer.

With the setup, we can correlate the mixer's output voltage with temperature gradients in the optical fibre.

The development of the DT followed these key concepts:

- Final goal—predict a phase value with respective uncertainty.
- Collect data—gather data from all sensors along the system.
- Create a virtual model of the transit time of the light signals and the frequency mixer.
- Connect physical and digital model—obtain temperature values from the sensors every few minutes and predict phase values. This is a real-time interaction.
- Validate and test—several algorithms were used and validated.

The DT facilitates monitoring the parameters impacting frequency transfer delays and predicts corrective measures by adjusting these same parameters. All uncertainty contributions are assessed, with the DT calculating a phase value and its associated standard uncertainty as outputs.

2. Frequency Mixer for Phase Measurement: Principles

A frequency mixer is a nonlinear electrical circuit that generates new frequencies from two input signals. In its simplest form, it takes two applied signals and produces new signals equal to the sum and difference of the original frequencies. Additionally, other frequency components can be generated in a standard frequency mixer. The primary use of frequency mixers is for heterodyning signals, but they can also serve as phase detectors [3].

The basic concept upon which phase detection rests is that applying two identical frequencies with constant amplitude signals to a mixer generates a DC output proportional to the phase difference between the two signals.

There are different types of frequency mixers, but they all have the same basic connections. These frequency mixers have three ports, two inputs and one output, as follows:

- RF: This input is used for the signal whose frequency is to be changed. It is typically the incoming signal and normally of a relatively low level compared to the other input.
- LO: This is for the local oscillator signal. The input level here is generally much larger than the RF input.
- IF: This is the output port with the "mixed" signal.

For this work, we used a double-balanced mixer. Basic traditional double-balanced mixers typically use four Schottky diodes in a quad-ring configuration. The baluns or hybrids are placed at both the RF and LO ports, while the IF signal is tapped off from the RF balun [4]. When a double-balanced mixer is used as a phase detector and when we apply two in phase (frequency-matched) voltage signals to the LO and RF ports, the current will flow into the IF balun, creating a positive DC voltage at the IF port. When applying out-of-phase signals, the current is always pulled out of the IF balun, thus creating a negative DC voltage at the IF port. For quadrature signals, equal current flows both into and out of the IF balun; no DC current is created and no voltage is apparent.

For phase detection, we can assume that the output voltage (IF port) can be described as $V_{IF} = V\cos(\Delta\varphi + \pi)$, where V is the amplitude of the maximum voltage observed at $\Delta\varphi = 0, \pi$. Assuming that the frequency mixer is in its linear response region, with some mathematical manipulation we can obtain the following Equation [3]:

$$V_{out} = V\left(\Delta\varphi - \frac{\pi}{2}\right) \tag{1}$$

From Equation (1) we obtain

$$\Delta\varphi = \frac{V_{out}}{V} + \frac{\pi}{2} \tag{2}$$

Which relates phase, in radians, with the output voltage of the mixer.

3. Transit Time

The technique used for time transfer characterization is based on the group delay difference (transit time) between two different wavelength signals propagating in a single-mode fibre. They have different propagation speeds in the fibre. An important parameter to consider is the fibre's temperature T, as the variation in transfer time is a function of it.

In this work, a single-mode optical fibre was used.

The two main effects degrading the signal, both critical to its performance, are attenuation and dispersion.

The time of flight (*tof*) through an optical fibre of length L for a wavelength λ is given by

$$\tau_p = \frac{L\, n(\lambda)}{c} = tof \tag{3}$$

where c is the speed of light in vacuum and n the optical fibre's refractive index.

The system is composed of two lasers with different wavelengths: 1310 nm and 1550 nm.

The difference between the propagation times for two different wavelengths is given by

$$d\tau_p = \tau_{p1} - \tau_{p2} = \frac{L}{c}(n_1 - n_2) \tag{4}$$

From a physical point of view, the group delay time, τ_g, i.e., the wave group *tof* along the fibre, is proportional to the derivative of the refractive index $n(\lambda)$. This is the propagation time of a signal in a fibre, or the group delay time for a single-mode fibre [2]:

$$\tau_g = \frac{L}{c}\left(n - \lambda\frac{dn}{d\lambda}\right) \tag{5}$$

From Equation (5), one concludes that different wavelengths will propagate at different velocities in the same fibre. The difference in the propagation time of two signals with different λ's produces a phase difference between them.

The effect of temperature on an optical fibre is determined by changes in the variation in both of its length and refractive index. By measuring the temperature of the fibre, we can correlate and determine these phase variations.

Assuming that polarization mode dispersion is small compared to chromatic dispersion for the wavelengths of interest, we can dismiss this effect on the transit time. Deriving Equation (5) with respect to temperature and combining it for different wavelengths, we obtain the phase-difference temperature variation for two signals traveling throughout the fibre [2]:

$$\left.\frac{d\tau}{dT}\right|_{\lambda_1 - \lambda_2} = \frac{1}{c}\left(\frac{dL}{dT}\left((n_{\lambda_1} - n_{\lambda_2}) + \lambda_2\frac{dn_{\lambda_2}}{d\lambda_2} - \lambda_1\frac{dn_{\lambda_1}}{d\lambda_1}\right) + L\frac{d}{dT}\left((n_{\lambda_1} - n_{\lambda_2}) + \lambda_2\frac{dn_{\lambda_2}}{d\lambda_2} - \lambda_1\frac{dn_{\lambda_1}}{d\lambda_1}\right)\right) \tag{6}$$

Equation (6) is included in the DT to calculate the theoretical phase. This will be discussed later in this paper.

4. Digital Twin

We consider a digital twin as a computerized version of a physical (or real) system that can be programmed to behave like the real system, enabling one to run scenarios and obtain a response to these scenarios. A DT is a technology that is more than just the digital representation of the real object; it also enables bi-directional data exchange and real-time management.

To create a digital twin, we need physical data, simulated data, and the interaction data between the two to map them together to produce a digital replica of the system, i.e., a digital representation of a physical object, process, or system as a numerical model. Real-time data, algorithms (simulation), and machine learning are used to create this virtual representation. This means that changes in the physical twin will be reflected in the virtual

twin. The data collected by the digital part are strictly dependent on the physical part, which makes the digital twin very accurate.

In most cases, digital twins are built from five fundamental capabilities: sensors, data, integration, modelling/analysis, and actuation.

For this experiment, we intend to use this concept in the following way:

1. Transform the equipment that generates and sends the 10 MHz signal to the optical fibre into a digital twin. Copy into digital format (numerical models) the characteristics of the lasers plus their uncertainties, the 10 MHz signal plus its uncertainty, the signal modelling and temperature sensors associated with the lasers, and any other equipment.
2. Add the optical fibre to the DT, e.g., the refractive index of the optical fibre and the two multiplexers at the beginning and end of the fibre, and also the temperature sensor data that measure the fibre.
3. Likewise, on the reception part, include detectors, temperature sensors, the frequency mixer, and the equipment that measures the phase between the two signals that pass through the optical fibre.
4. Data from the temperature sensor and multimeter are measured simultaneously, stored in files, and retrieved by the DT.
5. Train and validate an algorithm to predict a phase value.
6. Data from every sensor or piece of measurement equipment have an associated uncertainty, which allows the knowledge of a phase value with its associated uncertainty.
7. The exchange data between the virtual part of the DT and the physical part consist of the simultaneous measurement, temperature, and voltage values.

This allows us to obtain a detailed simulation of the entire system, complemented with real data, and predictions for phase values.

The use of ML in digital twins is normally only considered when there are many input variables and there is no linear relationship between the system's inputs and outputs. In our case, data are acquired from several temperature sensors and the relation between the temperature values and phase values is not linear, according to Equation (6), which justifies the use of ML in the digital twin.

Neural networks are one way to build a digital twin model by using data, especially when a physics-based model is not accurate or even not available [5,6]. In this way, a neural network will be used as a first approach for the implementation of the digital twin. As data from the system accumulates, there is another approach that we will try: the use of Deep Neural Networks to detect patterns that are not visible to the user.

5. Implementing the Digital Twin

An accurate knowledge of a system's behaviour is crucial to ensure the reliability and trustworthiness of the phase measurement system to be implemented. To help achieve these goals, we "replicated" the physical system into a digital counterpart. The schematics of the physical system up to the measure phase are represented in Figure 1.

The strategy to build the DT consists of modelling the transit time, obtaining a theoretical phase value that represents the passage of the modulated light in the fibre, and comparing this value with the phase measured by the multimeter.

Several factors that can influence the phase value will not be considered, e.g., the light modulation, the effect caused by the passage in the WDM, and the effects caused by fibre connections. The DT will focus solely on the propagation of light in the optical fibre and the phase variations caused by the temperature influence on the fibre path, on the lasers, on the photodetectors, and on the frequency mixer.

Before this work, several experiments were performed to calculate the effect of the temperature of the lasers and the detectors on the phase value, as well as the temperature influence of the mixer on the output voltage. These experiments are not included in this paper but will be presented in a later work. The values obtained for the temperature coefficients for the three pieces of equipment are presented in Table 1.

Table 1. Temperature coefficients measured for the lasers, detectors, and mixer.

	Lasers	Detectors	Mixer
Temperature Coefficient	-0.00235×10^{-9} s/°C	-0.00153×10^{-9} s/°C	3.9×10^{-4} V/°C

To transform the physical part of the system into its digital counterpart, we needed to convert the output of the mixer into time values, i.e., phase, and to compare this to the theoretical phase calculated from Equation (6). For this purpose, the schema from Figure 2 was used.
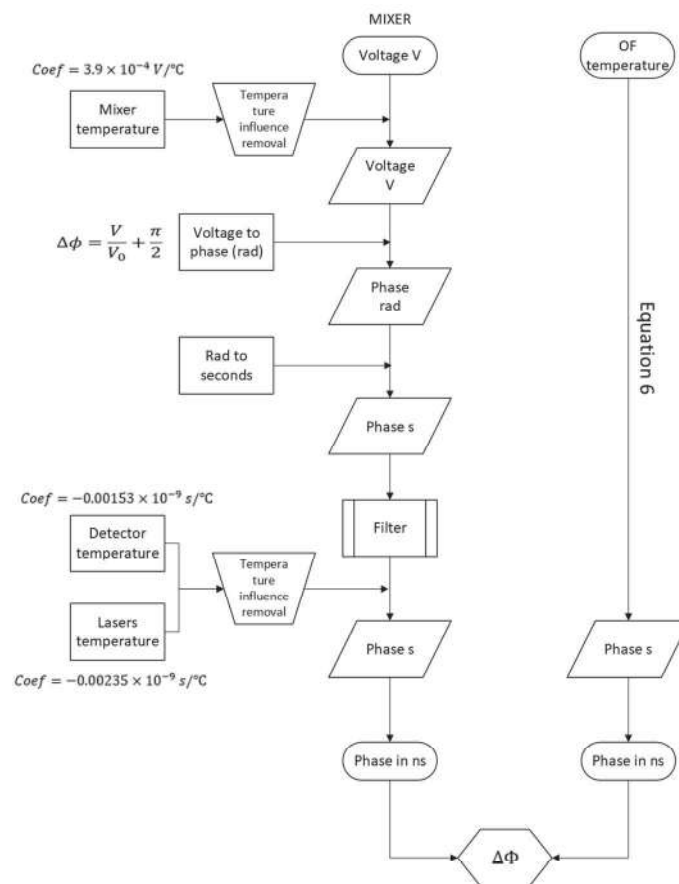
Figure 2. Schema for the calculation of the theoretical phase and experimental phase.

This modelling was divided in two parts: 1—computing a phase value from the mixer output; and 2—obtaining a phase value at the end of the optical fibre.

5.1. Phase from the Mixer Output

From the output voltage of the mixer, the effect of temperature on the mixer was added to the model; then, with Equation (1), the phase value was calculated in radians. This value was converted to seconds and filtered to eliminate higher-frequency noise. The temperature influence of the lasers and detectors was also added to the model, obtaining phase values in ns.

This transformation can be observed in Figure 3, with the application of all steps mentioned above. In red, the temperature of the lasers is represented; in green, the temperature of the mixer and the detectors is represented; in blue, in chart (a), the temperature of the optical fibre is represented; in yellow, in chart (a), the voltage measured in the mixer is represented; and also in yellow, in chart (b), the processed phase obtained by the schema from Figure 2 is represented. A good agreement can be observed between the calculated values for phase and the temperature of the optical fibre.
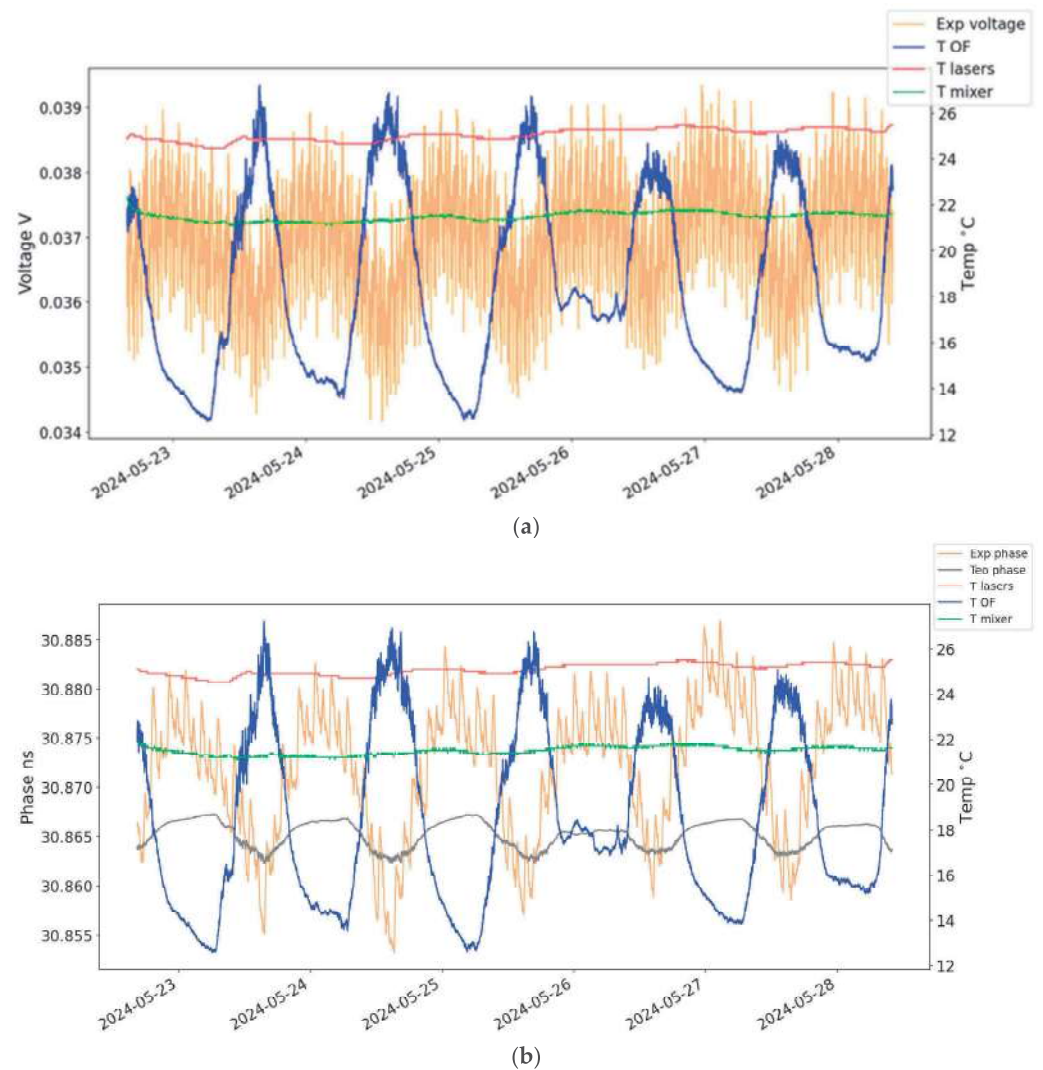
(a)

(b)

Figure 3. (**a**) Voltage values on the left axis and temperature values on the right axis. (**b**) Experimental and theoretical phase values on the left axis and temperature of the lasers, optical fibre, detectors, and mixer on the right axis.

5.2. Phase from the Optical Fibre

To calculate the theoretical differential phase delay, the procedure was the following: start with the measured temperature of the optical fibre (in blue, Figure 3a); apply it to Equation (6) to obtain the phase difference between the two signals traveling the optical fibre (in grey, Figure 3b).

The phase difference between the two values was calculated to be $\Delta\Phi = 3.4$ ns. For a better visualization, this gap was removed in Figure 3b. This discrepancy may be due to the different lengths of the "non-common" transmission paths. Specifically, these include the paths between the splitter, which divides the 10 MHz reference signal, and the WDM in the emission part, as well as the WDM and the phase meter inputs in the photodetector section. Additionally, the path difference between the photodetectors and the mixer, along with the copper connection cables from the detectors to the phase meter, may also contribute. These factors are not accounted for in the current digital twin model.

6. Estimation of the Measurement Uncertainty

One of the objectives of this work was to provide, as an output of the DT, a phase value with the associated uncertainty. All uncertainty components were identified and

combined using the traditional approach of the Guide to the Expression of Uncertainty in Measurement, GUM [7], and the Monte Carlo method [8].

To estimate the uncertainty, several factors that contributed to the overall uncertainty were considered. The uncertainty associated with the measurement instruments was evaluated. For some equipment, calibration certificates were available, while for others, the uncertainty was estimated based on the literature and experiments conducted to assess the equipment's performance, as was the case with the mixer. The mathematical model used for both approaches was based on Equation (6).

For convenience, and to simplify the determination of the uncertainty budget considering the use of the mathematical model, the Ishikawa diagram was used, as shown in Figure 4.
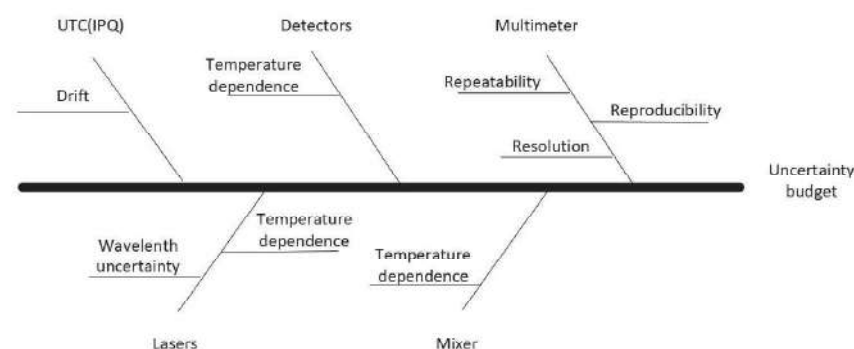

Figure 4. Determination of uncertainty budget using Ishikawa diagram.

As mentioned above, the uncertainty was obtained by the GUM and by supplement 1 of the GUM. Both methods were used to validate the uncertainty, and the results obtained are represented in Figure 5 and Table 2. The Monte Carlo method is shown in blue and the GUM approach in red. The vertical lines represent the 95% confidence interval.
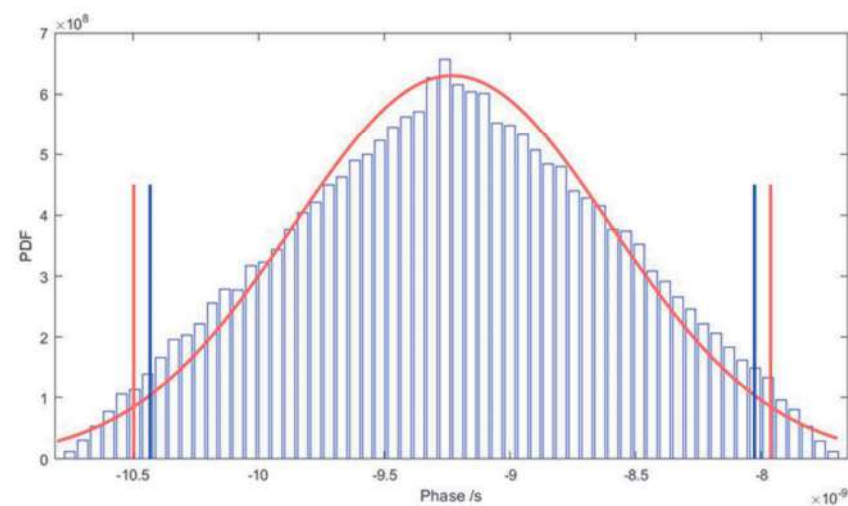

Figure 5. Chart of the comparison of uncertainty distribution. In blue is the Monte Carlo approach and in red is the GUM approach.

As recommended by the GUM, the uncertainty values shown in Table 2 have two significant digits, representing a difference of 10% between methods. Using more significant digits (1.201×10^{-9}, 1.265×10^{-9}) for the Monte Carlo and GUM, respectively, the difference falls to 5.3%, which represents a good agreement between the methods. Also, in the GUM approach, the Central Limit Theorem says that the combined uncertainty distribution converges to a normal distribution, which sometimes is not the case. In the Monte Carlo approach, the distribution of the combined uncertainty is determined by propagating the actual distributions of the input quantities and not merely their mean

and standard deviation. In this case, since the distribution of the uncertainty is normal, according to Monte Carlo, and the obtained value, by the same method, is lower than that of the GUM approach, which overestimates the uncertainty in this case, we can conclude that the uncertainty calculation is validated.

Table 2. Values obtained for combined uncertainty.

Method	Combined Uncertainty
GUM	1.3×10^{-9}
Monte Carlo	1.2×10^{-9}

7. DT Assembly and Test

The experimental data used as input for the digital twin were acquired over 6 days, using five temperature sensors and a multimeter. The multimeter used was a 34401A model from Agilent (Santa Clara, CA, USA) [9]. The temperature sensors were distributed along the external fibre path. A fourth temperature sensor was placed close to the laser source and a fifth one in the detector and mixer assembly. For the digital twin, temperature data were averaged from the three temperature sensors located outside. Figure 3a shows the acquired voltage values from the multimeter and the measured temperature values. At the instant of every voltage measurement, a temperature value from each sensor is also acquired.

To implement the digital twin, we used Python software Version 3.12, with several libraries and packages, e.g., Tensorflow Version 2.16.1, Keras Version 3, Numpy Version 1.26.1, and Pandas Version 3.1.3, just to mention a few [10].

The acquired data were transformed into a Pandas data frame, and the same pre-processing (data exploration) was performed on the raw data to search for missing data, outliers, and misclassifications.

After this process, the theoretical phase was calculated from the experimental values of the temperatures and added to the data frame as a new variable. The difference between this last variable and the experimental phase was also added as another variable. In this way, a data frame was built where some ML algorithms could be used. To train and validate the algorithm, the traditional hold-out sample method was used [5]. The data were divided into two parts to train the model and then validate and test it.

As mentioned previously, a neural network was used. In the process of building a neural network, one of the choices to make is what activation function should be used. The activation function decides whether a neuron should be activated or not by calculating the weighted sum and further adding bias to it. The purpose of the activation function is to introduce non-linearity into the output of a neuron, a process known as back-propagation [6,11]. Some tests were performed to evaluate the model's accuracy with different activation functions, and the one chosen was a Sigmoid activation function $= \frac{1}{1+e^{-x}}$.

The training and validation process is an essential part of the process of creating machine learning models and is followed by the evaluation of the model's accuracy. We used the Mean Absolute value of Error (MAE), which represents the difference between the original and predicted values, extracted by averaging the absolute difference over the data frame. The Mean Squared Error (MSE) is the square of the difference between the original and predicted values and represents the average difference over the data frame. These metrics were used to summarize and assess the quality of the machine learning model.

8. Results

With the experimental data represented in Figure 3, we trained two algorithms: a simple feedforward NN, also known as a Multilayer Perceptron with 64 neurons and a Sigmoid activation function, and a Long Short-Term Memory network (LSTM) with four memory cells and the Adam optimizer to adjust the model weights during training based on the computed gradients.

The LSTM network was chosen because these architectures are designed to work with sequences, making them ideal for tasks involving time or sequential data (e.g., time-series prediction or natural language processing) [12].

For the DT, the training focus was on the experimental phase, and the target was the difference between the theoretical phase and the experimental phase. After training, the training phase was added to the theoretical phase, being the output of the digital twin.

The digital twin training with the first NN can be observed in Figure 6, and we can see that the estimated phase follows the experimental data, which was the objective.
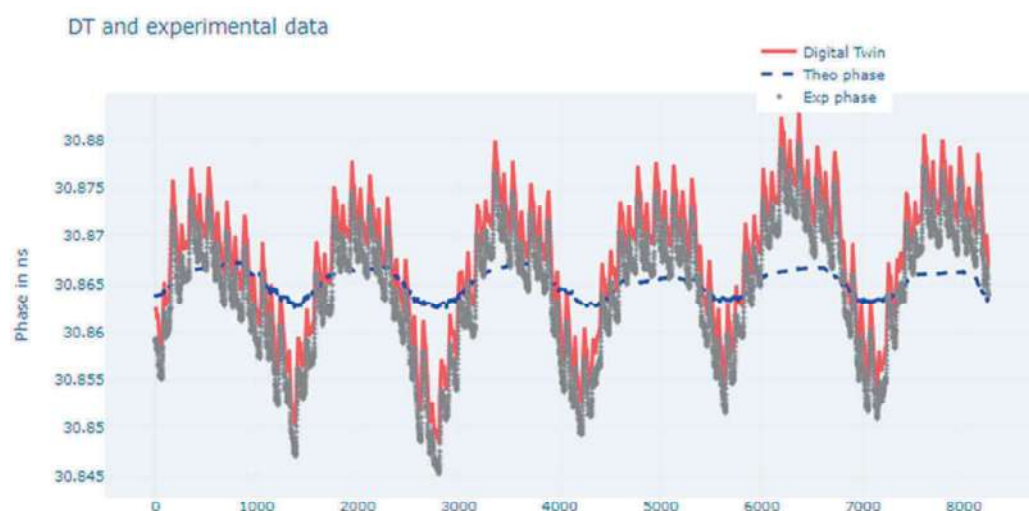

Figure 6. Chart of measured phase values, modelled values, and estimated values (digital twin) using a NN.

The metrics used to evaluate the performance of the algorithm were the Mean Absolute Error (MAE), which represents the average of the absolute difference between the actual and predicted values, i.e., measures the average of the residuals, and the Mean Squared Error (MSE), which represents the average of the squared difference between the original and predicted values, i.e., measures the variance of the residuals [6].

The values obtained were MAE = 0.006 and MSE = 5.1×10^{-5}.

Training with the LSTM network gave the results presented in Figure 7.
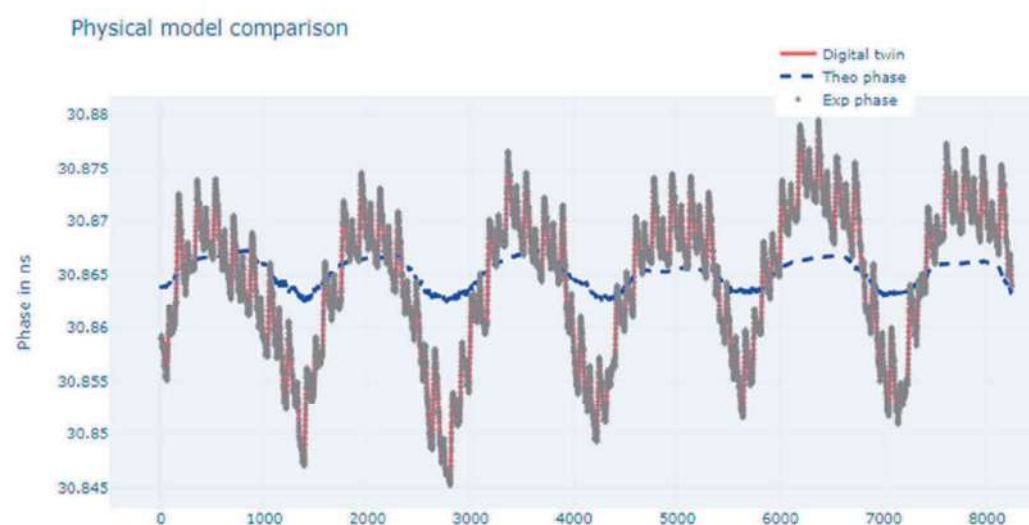

Figure 7. Chart for measured phase values, modelled values, and estimated values (digital twin) using LSTM network.

The MAE and the MSE metrics obtained were 5.0×10^{-3} ns and 3.5×10^{-5} ns, respectively.

There is very good matching between the experimental data and the output of the DT for both the trained networks, but since the metrics are better in the case of the LSTM network, this one was chosen to train the DT model.

For the implementation of the DT, the schema in Figure 8 was assumed, and to test the trained algorithm, a new set of data was acquired over 5 days.
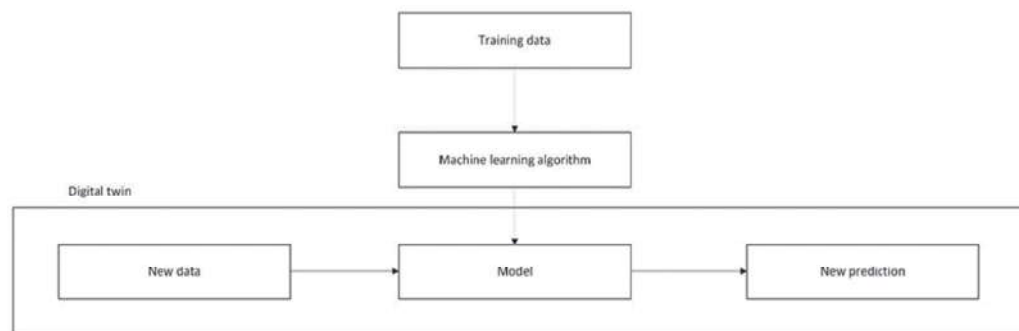

Figure 8. Schema for the digital twin.

These 5 days of data acquisition are shown in Figure 9 and were treated in accordance with the schema in Figure 2.
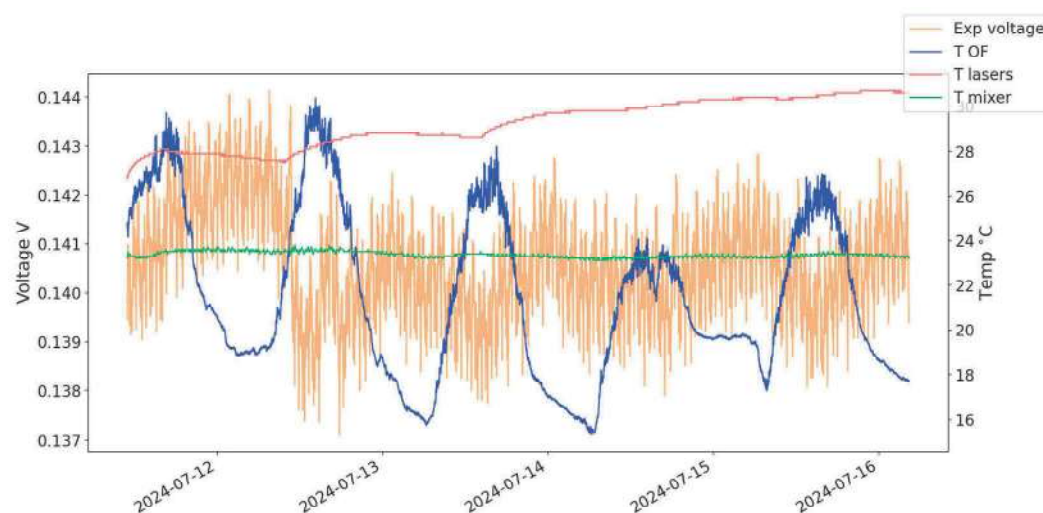

Figure 9. Five-day sequence of measurement data.

The results of applying the model to this new set of data can be seen in Figure 10. The metrics obtained were 1.7×10^{-2} ns for the MAE and 3.6×10^{-4} ns for the MSE. The model was applied to the theoretical data and trained with the experimental data, which could explain the gap between the theoretical values and the predicted ones. This was not the case when we applied the model to the experimental data (Figure 11), where a good match was found, with a slight improvement in the metrics MAE and MSE of 1.7×10^{-2} ns and 3.5×10^{-4} ns. The implementation revealed that the digital twin will follow the experimental data more closely than the theoretical data. This could be an interesting argument in favour as experimental data integrate all influence factors, while theoretical data are reduced to a small set of variables.
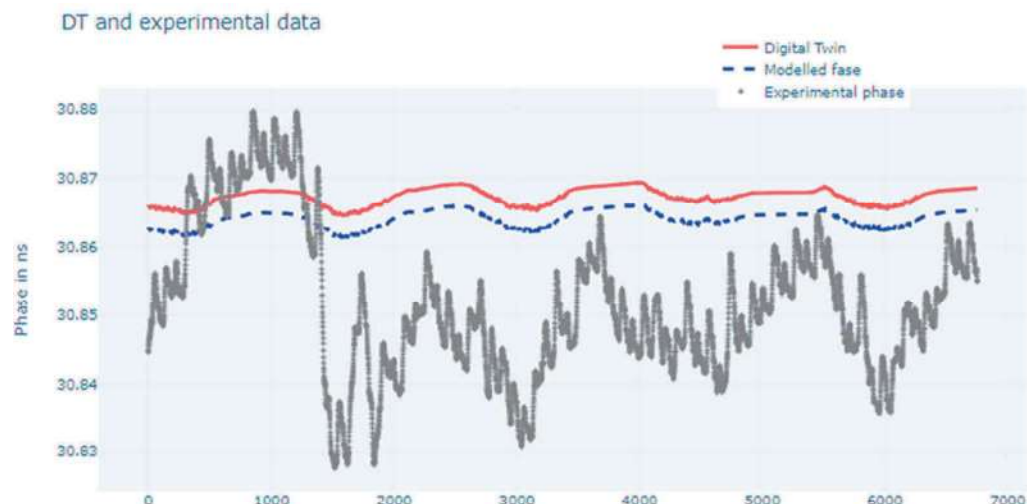
Figure 10. Trained model applied to theoretical data.
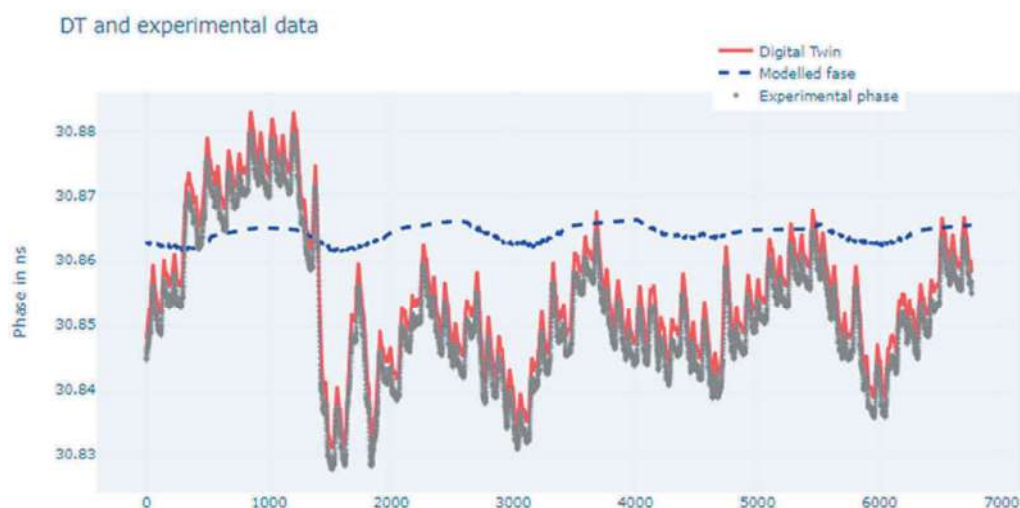
Figure 11. Trained model applied to experimental data.

9. Discussion/Conclusions

The digital twin, developed for use with a frequency mixer to detect phases, requires a combination of models and data to incorporate all the components of the physical model, as well as their respective uncertainty contributions.

This work presents a first attempt to train an algorithm focused on the use of a mixer to measure variations in the phases of two signals traveling over an optical fibre, allowing useful information to be obtained, leading to the correction factors that mitigate temperature effects. One of the benefits of the digital twin is that it will learn over time, with more data and with the introduction of other parameters of influence.

The implementation revealed that the digital twin aligns more closely with experimental data than theoretical data. This could be an interesting argument in favour as experimental data integrate all influence factors, while theoretical data are reduced to a small set of variables.

This digital twin includes all uncertainty contributions retrieved from the real data used for DT training and was estimated according to the GUM approach and validated with the Monte Carlo approach. The combined uncertainty of both methods with a difference of 5% shows a good agreement for both approaches.

However, the obtained uncertainty values are larger than the theoretical phase differences, as the combined uncertainty is in the order of ns, while the retrieved phase variations are in tens of ps. The main reason for this is that the main source of phase variation arises

from the terminal equipment (lasers, detectors, mixer), and with lesser significance, from the light propagation in the fibre medium.

Nevertheless, for longer optical fibre paths, this difference will tend to be smaller as the terminal equipment influence is constant, while the propagation factor increases with fibre length.

The use of virtual experiments will allow the study of the overall effect of minor changes in some parts of the system that in "real life" could not be considered. As an example, we can see at some time points the effect of frequency transfer due to the long-term drift of some equipment.

The implementation of the digital twin, despite not covering a complete physical model (only the transmission process and phase detection with the mixer), nevertheless represents a good approach to digital twins that includes the totality of the physical model, as well as the lasers and photodetectors, as represented in Figure 1. The major influence during measurements is temperature variation, but other aspects need to be considered, such as laser stability, frequency modulation, photodetector accuracy, and other parameters of influence. The lasers used are diode lasers, and as temperature increases, the bandgap energy decreases, which shifts the emitted wavelengths to longer wavelengths; since the speed of light in the fibre is wavelength-dependent, changes in the temperature can influence the transit time of the light and the phase value at the input of the mixer. The accuracy of the photodetectors can change with temperature; dark current increases exponentially with temperature because thermal energy increases the rate of carrier generation. This creates a higher noise floor, reducing the signal-to-noise ratio and making it harder to detect low-amplitude signals, consequently reducing accuracy.

The evaluation of the model's implementation and its application to new data was conducted by investigating the values obtained for MAE and MSE, which were close to zero, indicating the high accuracy of the model. The application of the model to new data revealed that the model should be applied to the experimental data, giving good concordance in values. We can assume that the LSTM network is a good choice for the algorithm.

We can conclude that using a frequency mixer as a phase detector, as represented in the DT, could be a viable solution for frequency transfer. It may be suitable for applications where the high level of accuracy typical of NMIs is not required. Although it can measure values in the range of tens of picoseconds, the resulting uncertainty is higher, in the order of nanoseconds. In future work, we want to compare, for small distances, this system to satellite-based systems used for frequency transfer, especially for small integration times.

As a concluding remark, we can add that this first implementation of a digital twin reveals its potential to be used as a low-budget system for phase detection using a mixer. A mixer less dependent on ambient temperature and more isolated to electric and magnetic effects would provide an output voltage with less noise, and in this way improve the accuracy of the measurements.

The data-based aspect, which is a major part of the DT, allows unknown parameters (not yet studied or discovered) to be compensated for in predictions.

We believe that the transformation of the physical part into the digital counterpart will allow the construction of a more robust digital twin that could eventually be adopted by NMIs (National Metrology Institutes) as a cost-effective solution for phase detection and frequency transfer.

Informed Consent Statement: Not applicable.

Data Availability Statement: The data presented in this study are available on request from the corresponding author.

Conflicts of Interest: The authors declare no conflict of interest.

References

1. Available online: https://www.iso.org/contents/news/2022/05/metrology-in-digital-era-1.html (accessed on 5 July 2024).
2. Sven-Christian Ebenhag, P.O. Fiber based one-way time transfer with enhanced accuracy. In Proceedings of the EFTF-2010 24th European Frequency and Time Forum, Noordwijk, The Netherlands, 13–16 April 2010; Space Research and Technology Centre of the European Space Agency: Noordwijk, The Netherlands, 2010.
3. Kurtz, S.R. *Mixers as Phase Detectors*; WJ Communications, Inc.: San Jose, CA, USA, 2001; pp. 23–25.
4. Poole, I. RF Mixing/Multiplication: Frequency Mixers. Available online: https://www.electronics-notes.com/articles/radio/rf-mixer/rf-mixing-basics.php (accessed on 5 September 2024).
5. Sun, C.; Shi, V.Z. A Combination of Physics-based Model and Neural Network Model for Digital Twins. PhysiNet. *arXiv* **2021**, arXiv:2106.14790. [CrossRef]
6. Larose, D.T. *Data Mining and Predictive Analytics*, 2nd ed.; Wiley: Hoboken, NJ, USA, 2015; ISBN 978-1-118-11619-7.
7. *JCGM 100:2008*; Evaluation of Measurement Data—Guide to the Expression of Uncertainty in Measurement. BIPM: Saint-Cloud, France, 2008.
8. *JCGM 101:2008*; Evaluation of Measurement Data—Supplement 1 to the "Guide to the Expression of Uncertainty in Measurement"—Propagation of Distributions Using a Monte Carlo Method. BIPM: Saint-Cloud, France, 2008.
9. Technologies, A. *34401A Digital Multimeter User's Guide*, 7th ed.; Keysight Technologies: Santa Rosa, CA, USA, 2015; pp. 34401–90004.
10. Géron, A. *Hands-On Machine Learning with Scikit-Learn, Keras, and TensorFlow*, 2nd ed.; O'Reilly Media: Sebastopol, CA, USA, 2019; ISBN 9781492032649.
11. Mitchell, T.M. *Machine Learning*; McGraw-Hill Education: New York, NY, USA, 1997; ISBN 0070428077.
12. Goodfellow, I.; Bengio, Y.; Courville, A. *Deep Learning*; MIT Press: Cambridge, MA, USA, 2016; Available online: www.deeplearningbook.org (accessed on 15 October 2024).

Evaluation of repeatability measurement procedures in gravimetric volume calibrations of glassware

- E. Batista and J. Alves e Sousa
Instituto Portugues da Qualidade,
Caparica, 2829-513, Portugal
E-mail: ebatista@ipq.pt
www.ipq.pt

Andrea Malendo and Davide Torchio
INRIM
Torino, 10135, Italy

Olaf Schnelle-Werner
ZMK & Analytik GmbH
Bitteerfeld-Wolfen, D 06766, Germany

Urška Turnšek
MIRS
Celje, 3000, Slovenia

Georgia Harris
NIST-OWM
Gaithersburg, 2600, USA

The EURAMET collaboration project 1525 on evaluation of repeatability measurement procedures in gravimetric volume calibrations of glassware was undertaken by six National Metrology Laboratories and Accredited laboratories, with the purpose of investigating the different approaches regarding repeatability measurements of glassware calibration using the procedures described in two volume standards (ISO 4787 and ASTM E542), and its influence on the determined volume and uncertainty. Six flasks of different volume capacity were calibrated. The consistency of the data was determined using several statistical methods and all results are presented in this paper, along with reproducibility analysis and uncertainty calculation.
Keywords: volume measurements, repeatability, uncertainty, glassware.

1. Introduction

Following the cooperation between EURAMET Technical Committee for Flow and ASTM Committee E41 it was decided to investigate the different approaches regarding repeatability measurements of glassware calibration performed by different National Metrology Laboratories, Accredited laboratories and

manufactures around the world and its influence on the determined volume and uncertainty.

Suitable repeatability estimates are needed for evaluating measurement results and for determining the measurement uncertainties. Lack of repeatability agreement within a set of measurement results can lead to significant problems with the operating characteristics of the volumetric instrument. The number of repeats affects the impact of the repeatability to the overall uncertainty and can be decided with respect to the scope of the specific volume determination (batch, verification, calibration). This paper describes the different approaches in repeatability measurements from each participant and its influence on the final uncertainty calculation and volume determination of three sets of flasks of 100 mL, 500 mL and 1000 mL. Two common approaches for obtaining repeatability statistics were investigated: The first approach uses standard deviation control charts to monitor the measurement process at the time of calibration by ensuring that observed and accepted standard deviations agree. This method requires maintaining standard deviation control charts to monitor the measurement process and to determine a pooled standard deviation. It enables a smaller number of repeated measurements for each calibration. The second approach uses a larger number of repeated measurements for each calibration (5 or 10 replicates).

2. Calibration method

Calibration of the flasks consists of the determination of the amount of water contained in the flask at reference temperature of 20 ℃, using the gravimetric method. The following Eq. (1) equation described in ISO standard 4787:2021 [1] and in ASTM E 542 –01: 2022 [2] was used to determine the volume (V_{20}) of each flask.

$$V_{20} = (I_L - I_E) \times \frac{1}{\rho_W - \rho_A} \times (1 - \frac{\rho_A}{\rho_B}) \times [1 - \gamma(t - 20)] \tag{1}$$

The value of the density of mass pieces (ρ_B) and expansion of the material of the flask (γ) must be known in advanced.

The participating laboratories used their own test procedure of calibration. The simplified calibration procedure is:
- Measure ambient conditions in order to determine the density of air (ρ_A).
- Weigh the empty dry flask and record the mass, I_E.
-Fill the flask up to the reference line and measure the liquid temperature (t) in order to determine the density of the water (ρ_W).

- Adjust the meniscus and wipe out (drying) any water drops above the reference line. The meniscus of the flasks shall be set so that the plane of the upper edge of the graduation line is horizontally tangential to the lowest point of the meniscus. The shape of the meniscus is set such that the surface of the liquid forms a curve that meets the glass tangentially.
-Weigh the filled flask and record the mass, I_L.

3. Measurement results

3.1. *Evaluation of the results*

To determine the reference value the formula of the weighted mean is used, by means of the inverses of the squares of the associated standard uncertainty are the weighing factors [3].

$$y = \frac{x_1/u^2(x_1)+\ldots+x_n/u^2(x_n)}{1/u^2(x_1)+\ldots+1/u^2(x_n)} \tag{2}$$

To determine the standard uncertainty $u(y)$ associated with y is used the following expression: (3)

$$u(y) = \sqrt{\frac{1}{1/u^2(x_1)+\ldots+1/u^2(x_n)}}$$

To identify an overall consistency of the results the E_n value also calculated [4].

$$E_n = \frac{V_{Lab}-V_{Re f}}{\sqrt{U_{Lab}^2-U_{Re f}^2}} \tag{4}$$

3.2. *Stability of the artifacts*

In order to identify the stability of the artifacts IPQ performed measurements in the beginning of the comparison (IPQ-1) and in the end of the comparison (IPQ-2). The results are presented in the following table. For two of the flasks this stability could not be assessed because they were broken during transportation.

Table 1. Volume variation measurement results

		Nominal volume	Volume (µl)	U_{exp} (µl)	ΔV (µl)
Flask 9572	IPQ – 1	100	99,955	0,013	0,002
	IPQ - 2	100	99,953	0,012	
Flask 9573	IPQ – 1	100	99,962	0,015	0,002
	IPQ - 2	100	99,960	0,012	
Flask 9577	IPQ – 1	500	499,863	0,053	0,025
	IPQ - 2	500	499,838	0,050	

Flask 9578	IPQ – 1	1000	999,71	0,10	0,05
	IPQ - 2	1000	999,66	0,10	

From the obtained results its can be verify that all the flasks were stable, the volume variation is smaller than the uncertainty for all cases. For the determination of the reference value only the first results from IPQ were used.

3.3. *Volume results*

The obtained volume results and uncertainty for the two 100 mL flasks are the following:

Table 2. Volume results of 100 mL flasks

	Flask 9572		Flask 9573	
Participant	Volume (mL)	U (mL)	Volume (mL)	U (mL)
IPQ	99,955	0,013	99,962	0,015
INRIM	99,942	0,013	99,963	0,013
MIRS	99,955	0,031	99,987	0,023
ZMK	99,928	0,050	99,964	0,050
Artel	99,937	0,031	99,969	0,031
NIST OWM	99,911	0,046	99,920	0,046
Reference value	99,946	0,008	99,965	0,008

The normalized error was determined for both flasks. The results are described in figure 1.
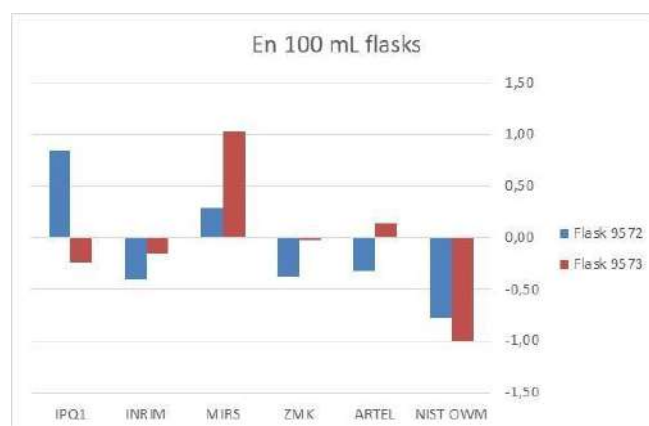

Fig. 1. En values for the 100 mL flask

From this figure it can be observed that all the volume results are consistent but two of them very close to 1. The obtained volume results and uncertainty for the three 500 mL flasks are the following:

Table 3. Volume results of 500 mL flaks

	Flask 9577		Flask 9576		Flask 1926	
Participant	Volume (mL)	U (mL)	Volume (mL)	U (mL)	Volume (mL)	U (mL)
IPQ	499,863	0,053	499,818	0,057	499,951	0,050
INRIM	499,879	0,024	499,847	0,024	-	-
MIRS	499,918	0,052	499,897	0,051	500,032	0,042
ZMK	499,85	0,23			499,95	0,23
Artel	499,990	0,077			499,95	0,08
NIST OWM	499,814	0,070			499,77	0,07
Reference value	499,851	0,020	499,877	0,019	49,990	0,029

The normalized error was determined for the three flasks. The results are described in figure 2.

Fig. 2. En values for the 500 mL flask

It can be observed from the previous figure that there were three inconsistent values, one from MIRS, another from Artel and other from NIST OWM. The obtained volume results and uncertainty for the three 1000 mL flasks are the following:

Table 4. Volume results of 1000 mL flaks

	Flask 9578		Flask 9579		Flask 1	
Participant	Volume (mL)	U (mL)	Volume (mL)	U (mL)	Volume (mL)	U (mL)
IPQ	999,71	0,10	1000,12	0,11	1000,16	0,10
INRIM	999,77	0,04	1000,165	0,036	-	-

MIRS	999,71	0,12	1000,14	0,14	-	-
ZMK	999,78	0,45	999,91	0,45	-	-
NIST OWM	999,52	0,17	-	-	999,92	0,17
Reference value	999,763	0,033	1000,158	0,033	1000,93	0,085

The normalized error was determined for the three flasks. The results are described in figure 3.
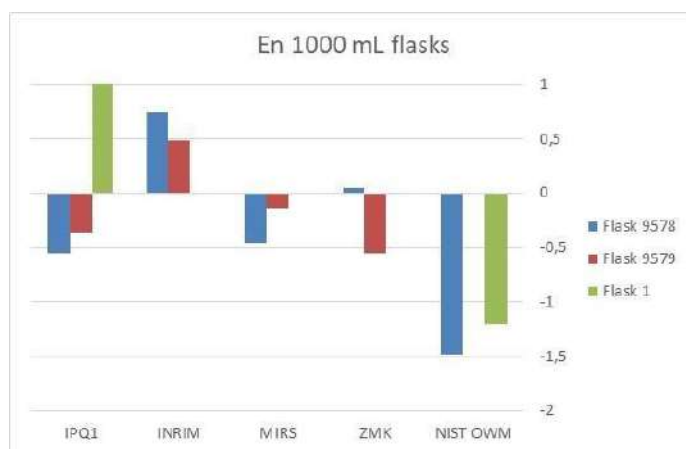
Fig. 3. En values for the 1000 mL flasks

For the 3 flasks measured it can be observed that there were two inconsistent values from NIST OWM.

4. Consistency results determination based on the NIST Consensus Builder tool

The NIST Consensus Builder web tool [5] was used to combine measurement results obtained by different laboratories, into a consensus estimate of the value of a scalar measurand and for the determination of consistency. Three different methods for data analysis were used:

- DerSimonian-Laird;
- Hierarchical Bayes;
- Linear Pool.

The results obtained for the DerSimonian-Laird method [6] can be found in figure 4 for the 500 mL flask number 9577.

Fig. 4. Consistency check using DerSimonian-Laird method

The mean value determined using the DerSimonian-Laird method was of 500,00 mL with and uncertainty of 0,018 mL. The results obtained by the Weighed mean method [3] are found in figure 5 for the same flask.

Fig. 5. Consistency check using the weighted mean
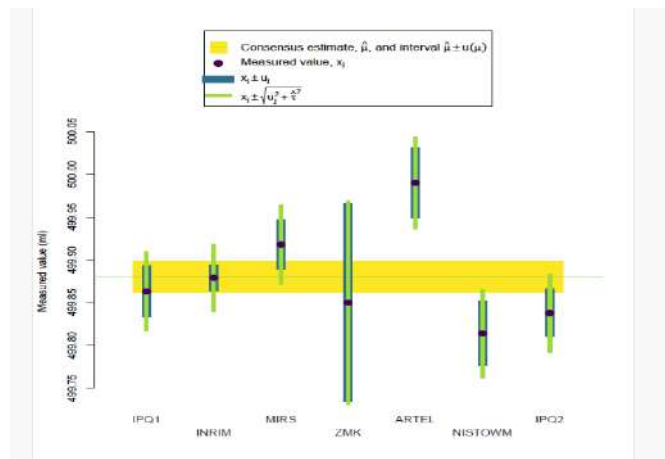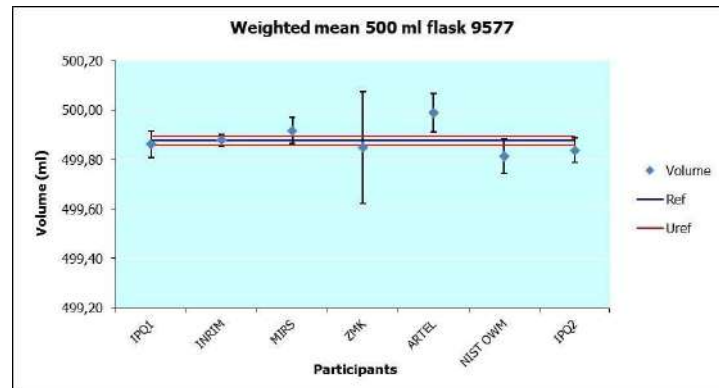
The mean value determined using the weighted mean was of 499,88 mL with and uncertainty of 0,019 mL.

The results were obtained by the NIST Consensus Builder tool [5] are consistent with the ones obtained from the weighing mean analysis [3] but a dark uncertainty, or laboratory random effect (τ) [7] of 0,01% value was found for the 500 mL flask 9577 and this value is in same order of magnitude as the participants expanded uncertainty. For the 100 mL flasks and 1000 mL flask no significant difference was found regarding the weighing mean analysis and also, no dark uncertainty was found.

5. Reproducibility of results

Two sets of each flask that were circulated by the participants, this allowed to verify if there was any variation within the laboratories.

In relative terms, the errors of the measurement's Di/V obtained by the laboratories are shown in figure 6, where the error bars correspond to the relative expanded uncertainties.
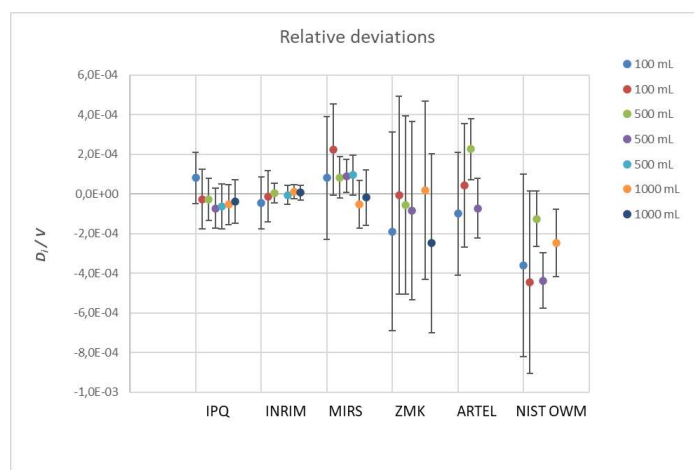
Fig. 6 Relative deviations of the volume flasks

From the figure above it can be seen that the results of each laboratory have similar relative uncertainty values and same relative error value when compared with the reference, with a strong correlation. It can also be verified that the majority of NIST OWM results are always lower values than the other laboratories due to the aforementioned meniscus reading differences but also consistent within each other. Assessing the standard deviation of the relative errors, the reproducibility of the measurements for each laboratory was evaluated, which, as expected, is proportional to the declared uncertainties, always remaining

below about 0.8 times the expanded uncertainty. The analysis is shown in figure 7, where the relative standard deviation is plotted against the mean value of the expanded relative uncertainties. This shows that the stated uncertainties are adequately evaluated, it is noted that the ZMK laboratory overestimated their uncertainty, and this was due to the CMC claim values.
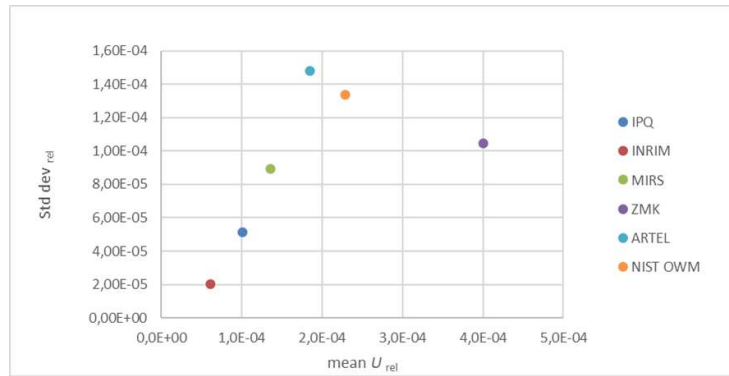
Fig. 7. Uncertainty analysis of the volume variation

6. Uncertainty calculations

Each laboratory described the uncertainty components. Both values, i.e. standard uncertainty and expanded uncertainty were stated, along with the relevant coverage factor k. The repeatability measurement procedure was described in detail; documented procedures were referenced (EURAMET cg-19 and NIST SOP 14 provide details).

For the evaluation of the measurement uncertainty, reference was made to the Guide to the Expression of Uncertainty in Measurement at approximately 95 % confidence interval [8]. In general, the laboratories that used EURAMET cg 19 [9] had lower uncertainty than the one using the NIST SOP 14 (NIST OWM). The largest source of uncertainty was the repeatability and meniscus for the European countries and the meniscus reading and control limits for the Artel and NIST OWM laboratories., respectively. For the repeatability measurements all laboratories used 10 replicated except for NIST OWM that used 5 repetitions.

7. Discussion

This project had the purpose to investigate the different approaches regarding repeatability measurements of glassware calibration performed by different NMIs, Accredited laboratories and manufactures around the world and its

influence on the determined volume and uncertainty. Two sets of flasks of the following 3 nominal volumes were calibrated:100 mL, 500 mL, 1000 mL.

NIST OWM has used the procedure described in NIST GMP 3 (Option A: setting bottom of the meniscus between upper and lower portion of graduation line ellipse), this led to lower volume values than the laboratories that use the ISO 4787 meniscus adjustment procedure resulting in inconsistent (biased) results. The consistency of results was also assessed using the NIST consensus builder tool and the results were different from the weighted mean analysis. A dark uncertainty of 0,01% was found for the 500 mL flask 9577 being this value in same order of magnitude as the participants expanded uncertainty. NIST OWM used the repeatability five runs and compared to historical process standard deviations with control charts to assess repeatability for each flask compared to an accepted value. In general, this approach led to a higher uncertainty value than the ones based on the EURAMET cg 19 and ISO 4787 Annex E, a) repeatability procedure determination, probably due to a larger dark uncertainty component.

8. Conclusions

This work performed the evaluation of repeatability measurement procedures of six laboratories (NMIs and accredited laboratories) around the world. Some inconsistency was verified within volume measurements results obtained along with different repeatability determination techniques that influenced the measurement uncertainty.

References

1. ASTM E 542:2022 - Standard practice for calibration of laboratory volumetric apparatus.
2. ISO 4787:2021; Laboratory glassware – Volumetric glassware – Methods for use and testing of capacity.
3. M.G. Cox, The evaluation of key comparison data, *Metrologia*, 39:589-595, 2002.
4. ISO 13528 - Statistical methods used in proficiency testing by interlaboratory comparisons.
5. https://consensus.nist.gov/app/nicob.
6. A. Koepke, T. Lafarge, A. Possolo and B. Toman 2016 NIST Consensus Builder user's manual (Gaithersburg, MD: National Institute of Standards; Technology)
7. M. Thompson, S.L.R. Ellison, Dark uncertainty. *Accred Qual Assur* 16: 483–487, 2011.

8. BIPM, IEC, IFCC, ISO, IUPAC, IUPAP, OIML; Guide to the expression of uncertainty in measurement (GUM), Geneva, 1995.

9. EURAMET calibration guide-19 Version 3.0, Guidelines on the determination of uncertainty in gravimetric volume calibration

Development of measurement procedures for volume and flow related quantities in microfluidic devices

ARTICLE INFO

ABSTRACT

The precise control of fluids within channels is the common feature of the microfluidic systems, which endows them with innovative applications and makes them widely applied in multidisciplinary areas. This work carried out under the EMPIR project 20NRM02 MFMET has the focus on the development of procedures regarding volume and flow related quantity measurements using liquids such as water, simulated body fluid (SBF), and phosphate buffer saline (PBS), used for microfluidic and medical applications. The results and uncertainties obtained in the tested microfluidic devices made of glass, Cyclic Olefin Copolymer (TOPAS®) and Poly-dimethylsiloxane (PDMS) demonstrate the importance of traceable and comparable measurements to the characterization of microfluidic systems and their subsequent validation.

1. Introduction

Microfluidics, concerned with fluid-handling in the millilitre to nanolitre scale, has major applications in biomedical and chemical analysis, and recently specific applications of microfluidics, such as organ-on-chip, have had exponential growth. The development of microfluidics, and nanofluidics benefits from the advancements of engineering techniques, especially in the aspect of high resolution, low cost, easy processing, flexible design, and high throughput. Inspired by microelectromechanical systems, essential components, including channel, filter, valve, mixer, and pump, could be standardized and incorporated in a single chip to design highly portable innovative fluidic devices [1,2]. Therefore, the integrated fluidic devices are able to provide a versatile platform for the manipulation of flows at different length scales, and the advancements of microfluidics, and nanofluidics have stimulated the discoveries of novel materials and new sciences but so far, quality control of microfluidic devices has mainly derived from manufacturer and/or academia expertise, without reliance on well-established calibration procedures or standards that could potentially streamline and accelerate production [3,4]. Despite the expected impact of microfluidics (societal, health, well-being, environment, etc.), commercial success stories are rare in comparison with the number of laboratorial developments. The main reason for this is the gap between microfluidics advancements made with custom-made devices and the lack of reliable and reproducible products in the market. This is because chips and connections are often developed and fabricated in-house, the test protocols are customized, the materials are not compatible with high volume production, etc. Therefore, it is fundamental to develop guidelines as future standards in the areas of design, materials, and tests, which are of direct relevance to industrial players and end-users in this area.

This work, carried out under the EMPIR project 20NRM02 MFMET – Establishing Metrology Standards in Microfluidic Devices [4], had the purpose of testing different microfluidic devices concerning flow and volume quantities and develop the corresponding technical procedures. The methodologies developed are expected to be used in regulatory documents and standards and thus highly benefit the characterization of microfluidic devices, the accuracy of their physical and chemical functionality, and all metrological operations involved in their lifetime, from manufacturing to its application by the end-user.

2. Methods and procedures

The determination of volume and flow in a microfluidic device can be done using several measurements techniques. These will be explained in the following sections.

2.1. Flow measurements

Flow describes the unit quantity delivered over a unit time. Fluid flow related to the gravimetric method consists of mass flow rate [kg/s] and volume flow rate [m^3/s].

There are various methods for determining the flow rate, e.g. gravimetric method, front tracking, displacement methods (piston prover as flow generator, interferometry), μPIV and others [5]. In addition, there are also secondary methods (e.g. flow meters) which are not included in this report.

2.1.1. Gravimetric method

The gravimetric method is used to determine a delivered mass of a liquid over a time interval. The method can be used for measurements of both inline flow sensors and flow generators. To achieve the measurements a weighing vessel, placed on a balance, collects the liquid to determine the mass delivered. While the delivery time interval for the collection of the mass is determined as well.

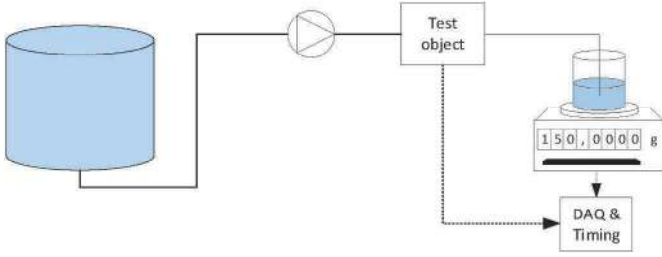The mass flow rate relates the delivered mass and the delivery time

Fig. 1. Scheme of a gravimetric setup.

Fig. 2. IPQ gravimetric setup with glass chip.

and the volume flow rate relates to the mass flow rate and the liquid density as presented in Eq. (1) and Eq. (2) respectively:

$$q_m = \frac{m}{t} = \frac{I_L - I_E}{t} \left(\frac{1 - \frac{\rho_0}{\rho_B}}{1 - \frac{\rho_A}{\rho_L}} \right) .$$

(1)

$$q_v = \frac{Q_m}{\rho_L t} = \frac{I_L - I_E}{\rho_L t} \left(\frac{1 - \frac{\rho_0}{\rho_B}}{1 - \frac{\rho_A}{\rho_L}} \right) .$$

(2)

Where:

q_m Mass flow rate
q_v Volume flow rate
m Mass
I_L Balance indication of the weighing vessel with final amount of liquid
I_E Balance indication of the weighing vessel with initial amount of liquid
t Time
ρ_L Density of liquid
ρ_A Density of air
ρ_0 Density at reference conditions for weighing (1.2 kg/m^3)
ρ_B Density of the mass pieces (8000 kg/m^3)

In microfluidic applications flow measurements other corrections should be applied, namely the needle/tube buoyancy effect over the weighing vessel (since the needed is immersed in the water), evaporation, and surface tension between the needle and the liquid. The calculation of these effects is described in detail in the work of Bissig et al. [6] and in TIR 101 [7].

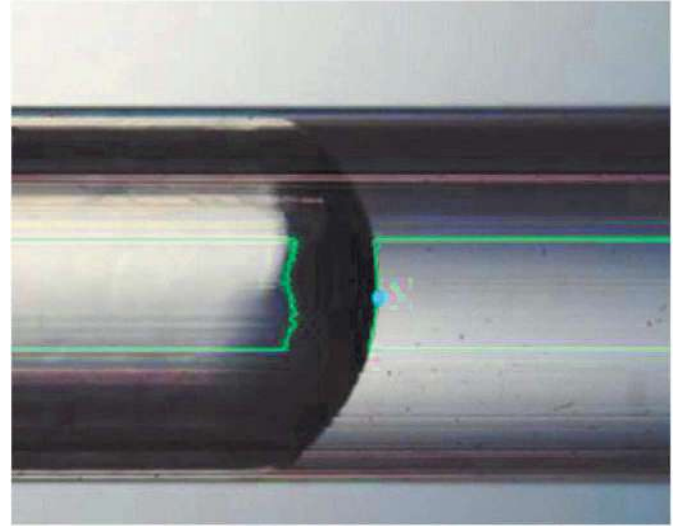In a gravimetric microfluidic setup (Fig. 1), an electronic balance is

Fig. 3. Example of a meniscus reading inside a capillary.

used in most cases to determine the delivered mass of a fluid from/through a test object (can be a flow generator, a microfluidic device, or a flow meter). The time interval in which the mass is delivered is determined by a timing module to derive the mass flow rate. The climatic conditions such as air temperature, relative humidity and pressure are determined to correct for buoyancy effects on the balance in AAMI TIR 101 [7]. The liquid temperature is determined to convert the mass flow rate into a volumetric flow rate, considering the density of the liquid used. Often a layer of oil is applied on top of the water surface in the weighing tank (beaker) to reduce evaporation, especially at low flow rates and the needle is immersed in the liquid of the weighing vessel to avoid the drop count effect.

In this work the flow will be measured gravimetrically with and without the microfluidic chips in order to access the influence of the microfluidic channels is the accuracy and stability of the imposed flow.

The gravimetric used setup at IPQ with a glass chip is presented in Fig. 2.

2.1.2. Front track method

The front tracking method [8,9] for flow measurements is an optical method that consists of tracking the position of the meniscus of a liquid (liquid/air or liquid/liquid interface) inside a (typically) capillary tube over time. An optical image acquisition system and image processing software is used to achieve the position over time of the meniscus. Knowing the displacement of the meniscus over time and the cross-section area of the capillary, it is possible to calculate the flow rate. Alternatively, the front tracking method can be applied directly in a microfluidic channel if the inner dimensions of the channel are known along with their associated uncertainties.

The fluid flowrate related to the front tracking method relates the optically acquired velocity of the fluid $\left(\frac{x_2 - x_1}{\Delta t} \right)$ to the dimensions of the capillary tube (πr^2). If the flow is measured inside a channel, replace (πr^2) by the channel's cross-section (Eq. (3)).

$$q_v = \frac{x_2 - x_1}{\Delta t} \pi r^2 .$$

(3)

Where:

x_1 Initial position of the meniscus
x_2 Final position of the meniscus
Δt Time interval between the positions
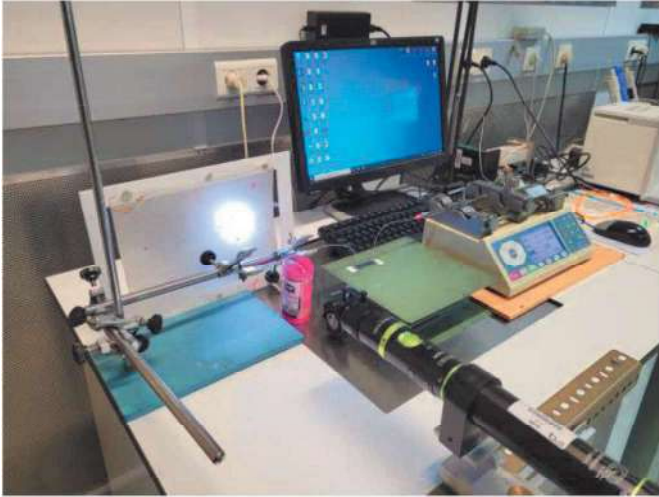r Capillary section radius.

Fig. 4. IPQ front track setup with PDMS chip.

Fig. 5. PDMS chip.

The test method includes calibration of the camera (determining the pixel size), image processing, and determination of position of the meniscus (Fig. 3).

- The calibration of the camera determines the relationship between dimensions of a known and calibrated object (for example the outer diameter of the capillary) and pixels of an image. Usually, the output of the camera's calibration is the pixel size in microns (μm).

The front track method used setup at IPQ with the PDMS chip is presented in Fig. 4.

2.2. Volume measurements

The volume of a microfluidic channel can be determined gravimetrically according to the formula described in ISO 4787 [10]:

$$V_{20} = (I_L - I_E) \times \frac{1}{\rho_L - \rho_A} \times \left(1 - \frac{\rho_0}{\rho_B}\right) \times [1 - \gamma(t - 20)] . \qquad (4)$$

Where:

V_{20} vol at a reference temperature of 20 °C
I_L Balance indication of the vessel with the contained liquid
I_E Balance indication of the vessel with empty vessel
ρ_L Density of liquid
ρ_A Density of air
ρ_0 Density at reference conditions for weighing (1,2 kg/m^3)
ρ_B Density of the mass pieces (8000 kg/m^3)
t Temperature
γ is the coefficient of cubical thermal expansion of the material of which the chip tested is made

Each microfluidic channel is tested separately. The difference obtained in the weighing measurements gives the mass of the liquid contained in a particular channel, converted to volume using equation (4).

For the residual volume determination, the chips are weighted with the contained liquid and afterword the liquid is removed by aspiration. The difference between the two masses gives the residual volume, converted to volume using equation (4).

3. Microfluidic CHIPS

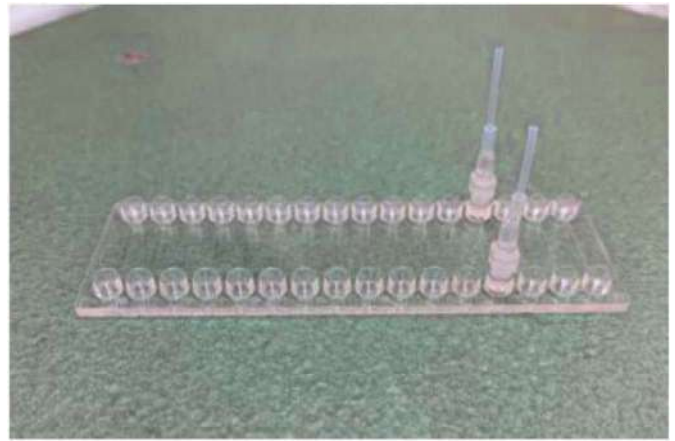Three specific examples of microfluidic chips were used for the experiments:
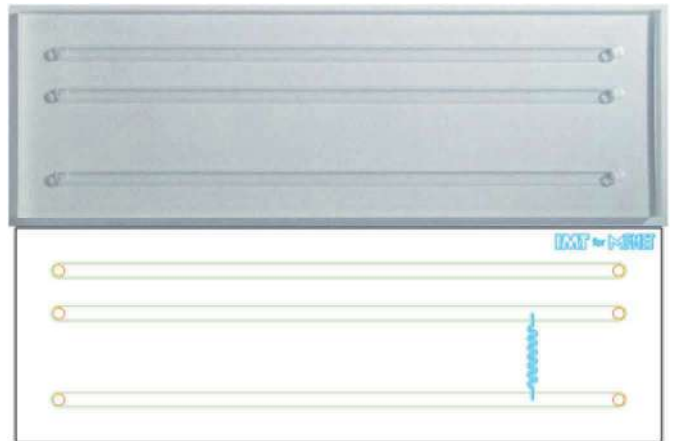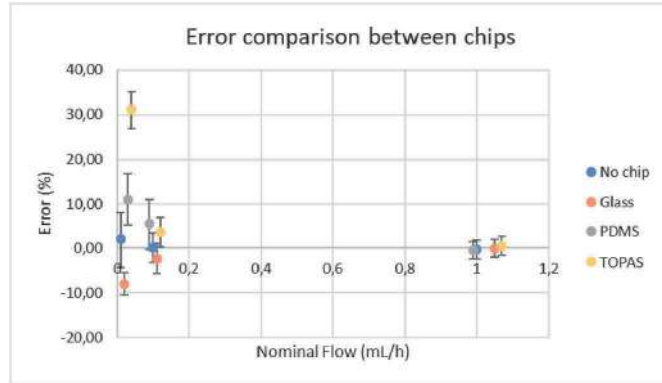

Fig. 6. TOPAS chip.

Fig. 7. Glass chip.

(i) Polydimethylsiloxane (PDMS) chip with one channel of 100 μm width and 50 μm depth, with two 0,9 mm inlet holes; material: PDMS; dimensions: 40 × 10 mm; manufactured by INESC MN (Fig. 5).

Table 1
Dimensions of the glass chip.

Dimensions	Width (mm)	Depth (mm)	Length (mm)
Main channels (green)	1.000	0.100	≈40
Leakage channels (blue)	0.150	0.002	≈10
Inlets and outlets	0.800		

Fig. 8. Gravimetric flow results using different chips.

(ii) Topas Chip (see Fig. 6): parallel channels with mini Luer fluidic interface; material: TOPAS® (Cyclic Olefin Copolymer for medical use); dimensions: 75,5 mm x 25,5 mm × 4 mm; with eight parallel channels of 100 μm width, 100 μm depth, 18 mm length. Luer fluidic interface, similar to "female mini luer port" integrated directly on the chip, manufactured by microfluidic chip shop.

(iii) Glass chip (see Fig. 7): dimensions 45 × 15 × 2 mm (Table 1) material: glass; manufactured by IMTAG (Fig. 7).

4. Measurement results

4.1. Flow

Measurements of flow rate were performed in the 3 microfluid chips using the gravimetric method and the front track method. Three liquids were used, water, simulated body fluid (SBF), and phosphate buffer saline (PBS). Tests were performed at three different flow rates. The results are presented below:

4.1.1. Influence of the chip

In this test 3 different chips were tested at 0,01 mL/h, 0,1 mL/h and 1 mL/h. The results of the flow without the chip and with the different chips are presented in Fig. 8:

The error obtained is the difference between the flow set in the pump and the value determined in the balance.

From the results it can be observed the results and uncertainties at the large flow rate for all chips are very similar. At lower flow rate the error of the measurement with the chips are larger than the value of flow without the chip, meaning that there is an influence of the artifact in the results of flow rate (Fig. 8).

4.1.2. Influence of the liquid

Two different chips, PDMS and TOPAS were tested with 3 different liquids, water, PBS and SBF at 0,01 mL/h, 0,1 mL/h and 1 mL/h using the gravimetric method and a Nexus flow generator. The determined errors are obtained by the difference between the flow results obtained with and without the chip. The results are presented in Figs. 9 and 10:

It can be verified that the SBF and PBS liquid have larger errors than
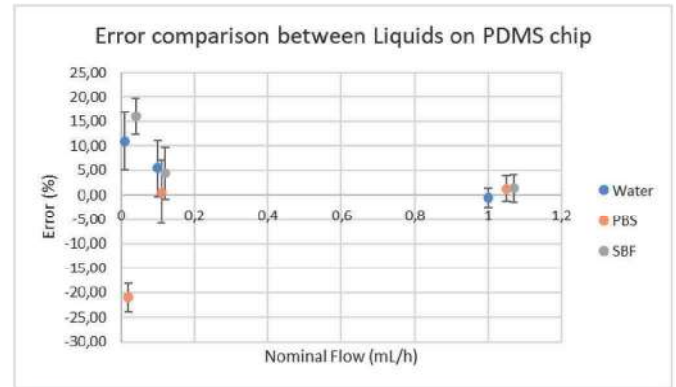
Fig. 9. PDMS chips flow results.
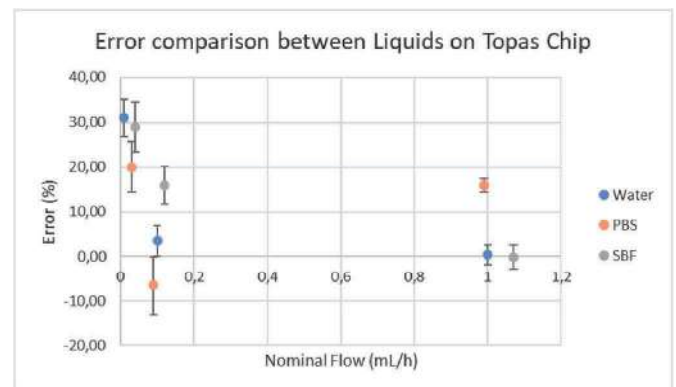
Fig. 10. TOPAS chips flow results.

Table 2
Method comparison results.

Method	Generated Flow (ml/h)	Tested Flow (ml/h)	Error (%)	U (%)
Gravimetric	0,1	0,097	2,6	3,4
	1	1,017	−1,7	3,0
Front track	0,1	0,0996	0,5	1,9
	1	1,0259	−2,5	4,0

the water. The uncertainties are very similar for all liquids and flow rates.

The liquid variation effect in the flow rate is smaller in the PDMS chip compared with the TOPAS chip.

4.1.3. Different methods

The TOPAS chip was used in the method comparison. Two flow rates were tested with water as refence liquid. The results are presented in Table 2.

It can be seen from the results that the error and uncertainty obtained for each method is quite similar, with a En value of 0,55 for the 0,1 mL/h and 0,18 for 1 mL/h, therefore the two methods are consistent.

4.2. Hydrodynamic resistance

In a microchannel, it is possible to drive a flow by applying a pressure difference, for example using a pump. Here, the hydrodynamic resistance R_{hyd} is defined as the ratio of the pressure difference to the flow rate. For a given microchannel, R_{hyd} is a constant parameter that quantitatively describes the flow characteristics of the microchannel.

Using a Sensirion SLI-1000 flowmeter and Fluigent pressure unit S,

Table 3
Results from paired measurements of flow rate and pressure difference for chip 4-1.

Setup	Flow	Flow unc. ($k=1$)	Pressure	Pressure unc. ($k=1$)
	(µL/min)	(µL/min)	(mbar)	(mbar)
System	50.7	1.5	12.1	1.7
	209.7	5.5	21.4	1.6
	420.	11.	32.3	1.6
	625.	16.	42.4	1.8
	828.	21.	54.6	2.4
	1027.	26.	68.2	2.
System	1028.	27.	70.5	2.8
	828.	21.	56.8	2.1
	628.	17.	41.3	2.5
	417.	11.	31.4	2.2
	210.2	5.9	20.7	1.8
	51.5	1.5	12.6	1.8
Main	50.7	1.5	15.5	1.8
	209.8	5.5	44.8	1.5
	421.	11.	72.7	1.5
	624.	16.	103.2	1.6
	827.	21.	128.7	1.6
	1026.	26.	157.2	1.6
Main	1029.	26.	155.8	1.7
	827.	22.	128.9	1.8
	624.	16.	100.3	1.7
	420.	11.	69.	1.9
	209.7	5.6	45.2	2.8
	50.7	1.4	13.3	1.5
Leakage	0.04711	0.00034	1989.	21.
	0.0856	0.00057	3900.	38.
	0.1181	0.0014	4128.	72.
	0.1457	0.0021	4173.	68.
Leakage	0.12927	0.00089	3750.	20.
	0.0985	0.0017	2937.	22.
	0.07	0.0011	2275.	20.
	0.04256	0.00031	1632.	32.
	0.0248	0.00041	1118.	22 (see Fig. 10).

Fig. 12. Plot of flow rate and pressure data of the microfluidics test system plus the leakage channel of chip 4-1. Also shown are associated linear fits.

Table 4
Chi-square goodness of fit tests (Gof-test) for linear fits to the results in Table 3. Interpreted values of R_{hyd} are presented for fits where the Gof-test passed.

Setup	Statistics	Gof-test	R_{hyd}	R_{hyd} unc. ($k=1$)
	(χ^2, dof, p-value)	(p-value>0.05)	(mbar/µL/min)	(mbar/µL/min)
System	1.3, 4, **0.86**	Pass	0.0556	0.0025
System	3.0, 4, **0.55**	Pass	0.0574	0.0028
Main	7.4, 4, **0.12**	Pass	0.1449	0.0034
Main	7.4, 4, **0.12**	Pass	0.1471	0.0033
Leakage	335, 2, **0,0**	Fail	N/A	N/A
Leakage	3.8, 3, **0.29**	Pass	24972.	345.

Fig. 7. The results are presented in Table 3.

Linear fits were attempted for the results in Table 3. If the fits passed a chi-square goodness of fit test (Gof-test), the slope of the fit was interpreted as the hydrodynamic resistance R_{hyd}. The data and fits are illustrated in Figs. 11 and 12. The resulting Gof-tests and possible hydraulic resistances are presented in Table 4.

In Table 4, the hydrodynamic resistance was well reproduced for the system and for the main channel. It was not possible to reproduce the hydrodynamic resistance for the leakage channel, and thus the reliability of the determined value for the leakage channel is more uncertain. Notice that the hydrodynamic resistance of the main channel and the leakage channel alone could be inferred by subtracting hydrodynamic resistance from elements to be excluded, i.e. the system or the system and the main channel.
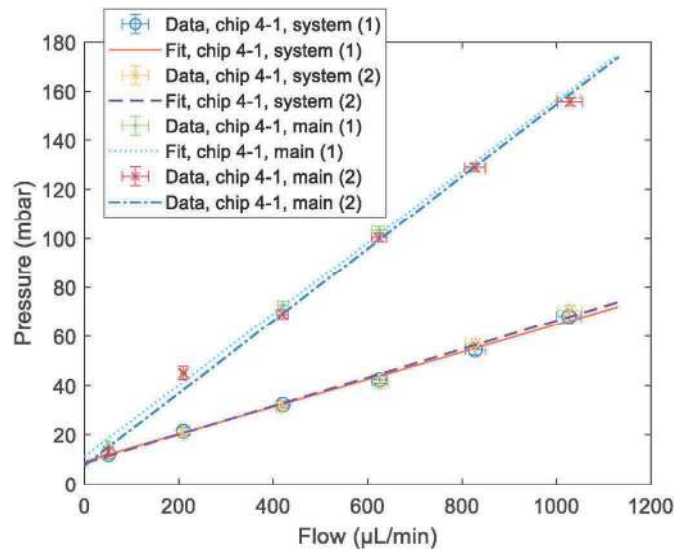

Fig. 11. Plot of flow rate and pressure data of the microfluidics test system and the system plus the main channel of chip 4-1. Also shown are associated linear fits.

measurements of flow rate and pressure were performed for larger flows through a main channel of chip 4-1, see Fig. 7. These sensors were also used to measure flow and pressure for the system, i.e. the microfluidic test system without the chip. Using the gravimetric method and a Fluigent pressure unit XL, measurements of flow rate and pressure were performed for smaller flows through the leakage channel of chip 4-1, see

Table 5
Results of the contained volume in different chips.

Chip	Liquid	Volume (mL)	U (mL)
PDMS	Water	0,00241	0,00013
	SBF	0,002329	0,000046
	PBS	0,002332	0,000066
TOPAS	Water	0,00368	0,00010
	SBF	0,003624	0,00011
	PBS	0,003531	0,000073
GLASS	Water	0,00423	0,00011
	SBF	0,004167	0,000072
	PBS	0,004157	0,000067

Table 6
Results of the residual volume in different chips.

Chip	Liquid	Volume (mL)	U (mL)
PDMS	Water	0,00023	0,00017
	SBF	0,000135	0,000034
	PBS	0,00039	0,00027
TOPAS	Water	0,000040	0,000048
	SBF	0,000191	0,000051
	PBS	0,000080	0,000030
GLASS	Water	0,000174	0,000036
	SBF	0,000201	0,000072
	PBS	0,000161	0,000072

4.3. Volume

Measurements of contained and residual volume in one microfluidic channel were performed in the 3 microfluidic chips using the gravimetric method.

4.3.1. Contained volume
The results of the contained volume can be observed in Table 5:

It can be verified that the contained volume and uncertainty with water is larger than for SBF and PBS liquid for all chips and this is probably due to evaporation effect of the water being larger than for the other liquids.

4.3.2. Residual volume
The results of the contained volume can be observed in Table 6:

It can be verified that the residual volume for glass is very similar for the 3 liquids. For PDMS there is a big variability in the residual volume depending on the liquid use, maybe due to the elasticity of the chip material.

5. Conclusions

In order to assess the accuracy of flow measurements and volume (contained and residual) in different types of microfluidic chips tests were performed using various liquids and calibrations methods.

It was observed a clear influence of the chips in the flow rate probably due to the channel flow resistance. Also, different liquids influence the flow rate depending on the type of material used for the chip. This also happens for volume determination.

From the two methods used, the gravimetric and the front track there were no significant variation found and the uncertainty were very similar.

The results and uncertainties obtained in the tested microfluidic devices made of glass, TOPAS and PDMS demonstrate the importance of traceable and comparable measurements to the characterization of microfluidic systems and their subsequent validation.

Acknowledgments

References

[1] P. Johan, K. Mattias, C. Daniel, Microfluidic technologies in drug discovery, Drug Discov. Today 10 (20) (2005).

[2] V. Silverio, S. Cardoso, Lab-on-a-chip: systems integration at the microscale, Chapter E, in: Drug Delivery Devices and Therapeutic Systems, Elsevier Science, 2021. ISBN: 978-0-12-819838-4.

[3] D.R. Reyes, H. van Heeren, J. Res. Natl. Inst. Stand Technol. 124 (2019) 1–22, https://doi.org/10.6028/jres.124.001, 2019.

[4] https://MFMET.eu.

[5] EURAMET cg 27, Guidelines for the Calibration of Drug Delivery Devices and Infusion Device Analysers, 2024.

[6] H. Bissig, E. Batista, et al., Primary standards for measuring flow rates from 100 nl/min to 1 ml/min – gravimetric principle, Biomed. Eng. 60 (4) (2015) 301–316.

[7] AAMI TIR 101, Fluid Delivery Performance Testing for Infusion Pumps, 2021.

[8] E. Batista, J. Sousa, M. Álvares, J. Afonso, R. Martins, Application of the front tracking method in micro flow measuring devices, Meas. Sens. 23 (2022) 100397, https://doi.org/10.1016/j.measen.2022.100397.

[9] E. Batista, J. Sousa, M. Álvares, J. Afonso, R. Martins, Development of an experimental setup for micro flow measurement using the front tracking method, Meas. Sens. 18 (2021) 100152, https://doi.org/10.1016/j.measen.2021.100152.

[10] ISO 4787, Laboratory Glass and Plastic Ware - Volumetric Instruments - Methods for Testing of Capacity and for Use, 2021.

Elsa Batista[a,*], Vania Silverio[b,c], Kevin Romieu[d], João Alves e Sousa[a], Thomas Schrøder Daugbjerg[e]

[a] *IPQ, Caparica, Portugal*
[b] *INESC MN, Lisboa, Portugal*
[c] *IST-UL, Lisboa, Portugal*
[d] *CETIAT, Villeurbanne, France*
[e] *DTI, Aahrus, Denmark*

[*] Corresponding author.
E-mail addresses: ebatista@ipq.pt (E. Batista), vania.silverio@tecnico.ulisboa.pt (V. Silverio), kevin.romieu@cetiat.fr (K. Romieu), jas@ipq.pt (J. Alves e Sousa), tsda@teknologisk.dk (T.S. Daugbjerg).

Gaussian processes and sensor network calibration

ABSTRACT

Sensor networks provide a new measurement modality addressing the measurement requirements of societal challenges relating to climate change and environment, for example. In this paper, we first discuss issues with applying the GUM uncertainty framework to uncertainty quantification for sensor network measurements. We then discuss the calibration of the sensors *in situ* by exploiting the spatio-temporal correlation in the signal being measured. In particular, we look at collocation experiments in which a number of reference and test sensors are located in proximity so that the test sensors can be calibrated against the reference sensors.

1. Introduction

The metrology community is investing resources to address the measurement requirements of societal challenges relating to climate change and environment, for example. To date, the main methodologies developed in metrology have been focused on measurements of a single quantity, in laboratory conditions using instruments whose responses are well-understood and characterised. By contrast, environmental monitoring is necessarily made outside laboratory conditions and subject to influence factors that are only partially characterised. Furthermore, the measurands involved are often spatial and/or temporal averages over a continuous domain whereas the measurements are usually taken by multiple sensors [1] at discrete locations in space/time. In such cases, the concepts of measurement models, uncertainty quantification, traceability and calibration need to be extended so that they can also apply in these more complex conditions.

Gaussian processes (GPs) have proved effective in modelling spatio-temporal systems [2,3] and provide a flexible approach to modelling response variables over a domain. GP models are usually specified in terms of a modest number of statistical hyper-parameters that describe the variance associated with the modelled effects and the strength of their correlation as a function of spatial and/or temporal distance.

In this paper, we first discuss issues with applying the GUM uncertainty framework to uncertainty quantification for sensor network measurements, section 2. We then look at issues associated with the co-calibration of the sensors *in situ* by exploiting the spatio-temporal correlation in the signal being measured. In particular, we look at collocation experiments in which a number of reference and test sensors are located in proximity so that the test sensors can be calibrated against the reference sensors, sections 3 and 4. Our concluding remarks are given in section 5.

2. GUM uncertainty framework and sensor network measurements

The GUM uncertainty framework [4,5] is designed largely for experiments measuring a single quantity or a finite number of quantities in laboratory conditions, using well-characterised measurement systems. Uncertainty quantification is based on propagating uncertainties associated with influence factors through a known measurement model. Sensor network measurements [6] generally have the following characteristics that make it difficult to apply the GUM framework directly.

2.1. Multiple instruments measuring the same quantities

The GUM does deal in depth on how to aggregate measurements of the same quantity from different measurement systems, even for the case on interlaboratory comparison (ILCs) studies. However, it can be argued that the GUM is based on the law of propagation of uncertainty (LPU) and that LPU can be used to assign uncertainties associated with least squares parameter estimation in ILCs [7] and in more general metrology applications [8], and for other estimation methodologies such as maximum likelihood estimation.

2.2. Partially-characterised sensor responses

The measurement challenges in many emergent areas related to climate and environment, or energy, among others, involve measurements outside laboratory conditions. While the sensor responses may have been characterised by well-established methods in laboratory conditions, the measurement models need to be modified so that concepts of traceability, uncertainty evaluation and calibration can also apply in those more complex conditions.

The GUM (and LPU) assumes a known, fixed model and cannot easily accommodate a number of plausible models or other aspects of model uncertainty. Model selection techniques, and Bayesian model averaging [9,10] can be applied in a metrology setting to account for some aspects of model uncertainty. The uncertainty evaluation methodology must also cope with the fact that sensors may fail or give unreliable measurements.

2.3. Measurands defined over a spatio-temporal domain

In many environmental applications the underlying measurand, such as pollution levels, is defined over a spatio-temporal domain, varying with location and time, and for which summary quantities, such as the average amount of pollution over an area or time period, are sought. The measurements available are at only a finite number of locations and finite time steps and averages have to be inferred from these measurements. Gaussian process (GP) models are important because they give a way of evaluating such quantities and provide a way of accounting for the finite sampling effect in the associated uncertainties.

GP models are a flexible way of modelling data that is not limited by a functional form. They do so by regarding the values of the variable at different spatial locations as being correlated and describing the strength of the correlation in a flexible way as a function of spatial and/or temporal separation. The idea of GP regression is to learn the correlation behaviour from measured data collected at known, fixed locations and then use this knowledge for prediction/interpolation within an area of interest [11]. In effect, the estimated value of the variable at a given location is evaluated as a weighted average of the measured data from the sensors where the weights depend on the spatial correlation behaviour and hence in the distances (spatial, temporal) of the sensors from the given point.

2.4. Experimental design

Experimental design associated with sensor measurements is much more complex than for standard metrological experiments and involve questions on a) how many and what type of sensors (high cost well-characterised reference sensors versus low cost sensors of variable performance), b) where to place the sensors and c) how often to measure. The answers to these questions depend on the nature of the signal, particularly the strength of the underlying spatio-temporal correlation, which determines the effective number of freedom associated with the signal [12]. Some experimental design issues associated with GP models and sensor networks are considered in Ref. [13], for example.

3. Collocation experiments

3.1. Micro- and macro-calibration of a sensor network

The fact that sensor behaviour is likely to be only partially characterised and that there may be many sensors, perhaps thousands, means that calibrating a sensor network can be challenging [14]. Micro-calibration refers to the strategy of calibrating each sensor *in situ*, a process that is likely to be time consuming and costly to the point of being impractical. Macro-calibration refers to the calibration of the sensor network as a whole and often relies on the fact that subsets of the sensors at times measure the same or approximately the same signal, allowing the sensors to be compared with each other and possibly calibrated against each other. This section is concerned with a type of macro-calibration strategy using collocation experiments.

3.2. Exact collocation experiments

Collocation studies, see e.g. Refs. [15–17], are used to assess the performance of air quality sensors, for example, NO2 diffusion samplers [18]. In a collocation study, a number of test sensors to be assessed are placed along side a calibrated reference sensor. Measurements are gathered at regular time intervals from all the sensors and these are then used to calibrate the test sensors relative to the calibrated sensor. Standard approaches to calibrate the test sensors usually involve a series of independent analyses involving the data from the reference sensor and each of the test sensors, an approach used in many fields; see, e.g., Ref. [19]. However, there are advantages in analysing the data for the complete ensemble of sensors since all the sensors are nominally measuring the same signal. In this section, we discuss an ensemble model of a collocation study of the form:

$$y_i = a_k + b_k z_j + \epsilon_i, \epsilon_i \in N\left(0, \phi_k^{-1}\sigma_{i,0}^2\right) \tag{1}$$

where y_i is the observation recorded by sensor $k = k(i)$ at time $j = j(i)$, z_j is the underlying signal at time j, a_k and b_k are calibration parameters associated with the kth sensor $\sigma_{i,0}$, is an estimate of the standard deviation of the random effects associated with the ith measurement, and ϕ_k is a precision parameter associated with the kth instrument that can be used to provide a scale adjustment of the $\sigma_{i,0}$ associated the observations recorded by the kth instrument. Prior information about ϕ_k is available in the form

$$\phi_k \sim G\left(\frac{m_{k,0}}{2}, \frac{m_{k,0}}{2}\right) \tag{2}$$

where $m_{k,0}$ encodes the degree of belief in the prior estimates $\sigma_{i,0}$. The reference sensor enters into the model in the same way as the other sensors but has an informative Gaussian prior associated with its calibration parameters while the calibration parameters for the uncalibrated sensors have non-informative or vague priors.

We use the term "exact collocation experiment" to indicate that all sensors are assumed to be measuring the same signal z_j at each time step. This requirement is weakened when considering "approximate collocation" experiments below in section 4.

3.3. Model: σ_i known

At time t_j the kth sensor measures the quantity z_j to produce an observation modelled as

$$y_i = a_k + b_k z_j + \epsilon_i, \epsilon_i \in N\left(0, \sigma_i^2\right). \tag{3}$$

From the data $\mathbf{y} = (y_1, ..., y_m)^{\mathrm{T}}$, we wish to estimate the signal parameters $\mathbf{z} = (z_1, ..., z_n)^{\mathrm{T}}$ and the $n_0 = 2n_K$ calibration parameters $\mathbf{a} = (a_1, b_1, a_2, ..., b_{n_K})^{\mathrm{T}}$. It is assumed that at least one of the sensors (the reference sensor(s)) has been calibrated, so there is calibration information that can be modelled as $B\mathbf{a} = \mathbf{b}_0 + \boldsymbol{\delta}$, with $\boldsymbol{\delta} \in N(0, I)$. Assuming that σ_i are known, estimates of the model parameters $\boldsymbol{\alpha}^{\mathrm{T}} = (\mathbf{z}^{\mathrm{T}}, \mathbf{a}^{\mathrm{T}})$ are found by solving

$$\min_{\alpha} F_Y(\boldsymbol{\alpha}) + F_A(\boldsymbol{\alpha}) \tag{4}$$

where

$$F_Y(\boldsymbol{\alpha}) = \sum_{i=1}^{m} f_i^2(\boldsymbol{\alpha}) = \mathbf{f}_Y^{\mathrm{T}}\mathbf{f}_Y,$$

$$f_i(\boldsymbol{\alpha}) = w\_i(y_i - a_k - b_k z_j), \ w_i = 1 / \sigma_i, \text{and}$$

$$F_A(\boldsymbol{\alpha}) = (\mathbf{b}_0 - B\mathbf{a})^{\mathrm{T}}(\mathbf{b}_0 - B\mathbf{a}) = \mathbf{f}_A^{\mathrm{T}}\mathbf{f}_A.$$

If $\boldsymbol{\alpha}_q$ is an estimate of the solution of (4), then an updated estimate is given by $\boldsymbol{\alpha}_q = \boldsymbol{\alpha}_q + \mathbf{p}_q$, where

$$p_q = -\left(J_q^T J_q\right)^{-1} J_q^T \mathbf{f}_q, \mathbf{f}_q = \begin{bmatrix} \mathbf{f}_Y(\boldsymbol{\alpha}_q) \\ \mathbf{f}_A(\boldsymbol{\alpha}_q) \end{bmatrix}$$

and J_q is the $(m + p) \times (n + n_0)$ Jacobian matrix of partial derivatives of the $m + p$ summand functions $\mathbf{f}_q$ in (4) with respect to evaluated at $\boldsymbol{\alpha}_q$. For better numerical stability, $\mathbf{p}_q$ is usually evaluated using an orthogonal factorisation of J [20]. The fact that each summand function in (4) involves at most one z_j gives the Jacobian matrix a block-angular structure that can be exploited to derive computationally efficient algorithms [8,21,22].

Table 1

Values of the statistical hyper-parameters associated with the numerical simulations: values used in the data generation (Truth), prior estimates (Prior), estimates for experiments A and B using (6), (A1, B1) and the posterior weighting scheme (A2, B2). These estimates are generated solving (4) and ignoring the spatial correlation present in the experiment B.

	Truth	Prior	A1	A2	B1	B2
$\sigma_R/\ \mu\text{gm}^{-3}$	3.00	3.00	1.71	2.98	2.26	3.51
$\sigma_S/\ \mu\text{gm}^{-3}$	5.00	10.00	5.69	5.06	7.52	6.23
$u_{R,a}/\ \mu\text{gm}^{-3}$	5.00	5.00	2.84	5.02	3.76	5.02
$u_{R,b}/1$	0.05	0.05	0.03	0.05	0.04	0.05
$u_{S,a}/\ \mu\text{gm}^{-3}$	10.00	50.00	28.43	21.37	37.59	20.04
$u_{S,b}/1$	0.20	0.40	0.23	0.17	0.30	0.16

3.4. Missing data

If at all time steps at least one reference sensor makes a measurement, then all parameters of the model can usually be determined. However, even if the reference sensors provide no data at some time steps, the system may still be solvable. If a reference sensor and a second sensor both measure at least two distinct signal values, then the calibration parameters associated with the second sensor can be estimated, along with all the quantities z_j measured by the second sensor. A bootstrapping scheme can cycle through the data and, at each cycle, increase, if possible, the number of sensors that can be calibrated and the number of z_js that can be estimated. The scheme terminates when no new information is gathered during a cycle, with some or all the parameters identified.

3.5. Uncertainty evaluation

If f and J are the residuals and Jacobian matrix at convergence of the Gauss-Newton algorithm, the variance matrix associated with the fitted parameters based on the input uncertainty estimates is given by

$$V_\alpha = \left(J^{\mathrm{T}}J\right)^{-1}. \tag{5}$$

If there are more observations than parameters, $m + p > n + n_0$, then a posterior adjusted estimate of the variance matrix [8] is given by

$$V_\alpha = \widehat{\sigma}^2\left(J^{\mathrm{T}}J\right)^{-1}, \qquad \widehat{\sigma}^2 = \frac{f^{\mathrm{T}}f}{m + p - n - n_0}. \tag{6}$$

3.6. Model: partial information about σ_i

For the case of partial information about σ_i, we replace the model (3) by the more general model given by (1) and (2).

The prior estimate of ϕ_k is 1. Posterior estimates of ϕ_k can be determined by the general scheme described in Ref. [23].

3.7. Numerical example A: exact collocation experiment

We first report on numerical simulations involving synthesized data derived from measurements of NO2 in the London Air Quality Network [24]. The simulations involve $n_S = 8$ "standard" instruments to be calibrated against $n_R = 2$ "reference" instruments in an exact collocation experiment. The simulations involve the following statistical hyper-parameters: σ_R and σ_S, the standard deviation for the random effects associated with the reference (R) instruments and standard (S) instruments, $u_{R,a}$, $u_{R,b}$, $u_{S,a}$ and $u_{S,b}$, the standard uncertainties associated with prior values $a_{k,0}$ and $b_{k,0}$ for the reference and standard instruments.
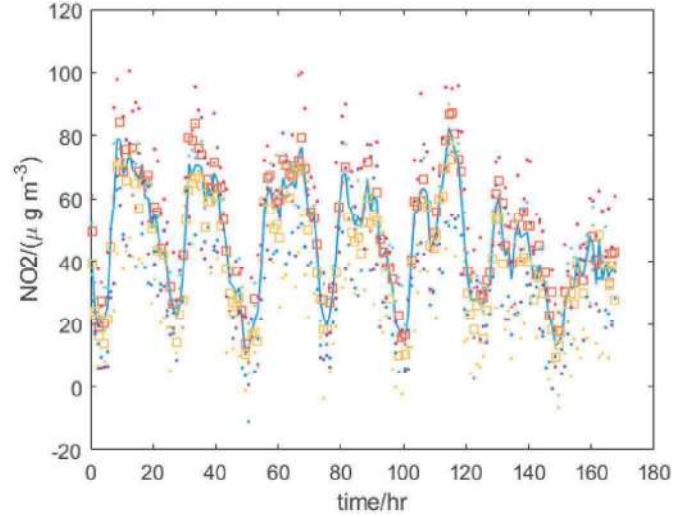

Fig. 1. Synthesized data involving two calibrated reference instruments and eight instruments to be calibrated measuring a "ground truth" signal, graphed as a solid curve, at 24 hourly time steps over a week, giving a total of $n = 168$ time steps. The reference instrument measurements are marked by a square while those of the standard instruments are marked by a dot. The data are generated according to the model (3) using the statistical hyper-parameter values given in Table 1.

The data is generated according to the model given in (3) where z_j represents the "ground truth" signal of NO2 levels derived from air quality measurement data. The "ground truth" values of a_k and b_k for the reference instruments drawn at random according to $a_k \in N\left(0, u_{R,a}^2\right)$ and $b_k \in N\left(1, u_{R,b}^2\right)$ while those for the standard instruments drawn at random according to $a_k \in N\left(0, u_{S,a}^2\right)$ and $b_k \in N\left(1, u_{S,b}^2\right)$.

Table 1 shows, in the first two numerical columns, the "ground truth" values of the statistical hyper-parameters used in generating the data along with the prior estimates of these hyper-parameters. For the reference instruments, the prior information is informative in that the values of a_k and b_k are consistent with the prior information. For the standard instruments, the prior information is more vague in that the ground truth values of a_k and b_k are closer to their nominal values than expected according to the prior information.

The data simulates measurements by the $n_R + n_S = 10$ instruments at hourly intervals over one week so that $n = 7 \times 24 = 168$. The "design" of the experiment is almost completely random except for the requirement that the signal is measured by least one instrument (not necessarily a reference instrument) at each time step. Of a possible 1680 measurements a random subset of $m = 1008$ measurements has been selected, a 60 % fraction of the possible total.

Fig. 1 graphs the synthesized data for the experiment involving two calibrated reference instruments and eight instruments to be calibrated. The "ground truth" signal, graphed as a solid curve, reflects the diurnal pattern of NO2 pollution associated with traffic burning fossil fuels in an urban environment. There are low levels at night-time ($t = 0$ corresponds to midnight), building up during the morning rush hour with a second peak associated with the evening rush hour, particularly on Friday, day five. The NO2 levels are noticeably smaller on Saturday and Sunday, days six and seven. Estimates of the model parameters are given by three calculations, the first, A0, solving (4) using the ground truth values of the statistical hyper-parameters and then computing the uncertainties according to (5), the second algorithm solving (4) using the prior estimates of the statistical hyper-parameters and then computing the uncertainties according to (6). The third algorithm, A2, uses a posterior weighting scheme, section 3.6, using four further hyper-parameters ϕ_k such that $\sigma_R^2 = \phi_1^{-1}\sigma_{R,0}^2$, $\sigma_R^2 = \phi_2^{-1}\sigma_{S,0}^2$, $u_{R,a} = \phi_3^{-1}u_{R,a,0}^2$,
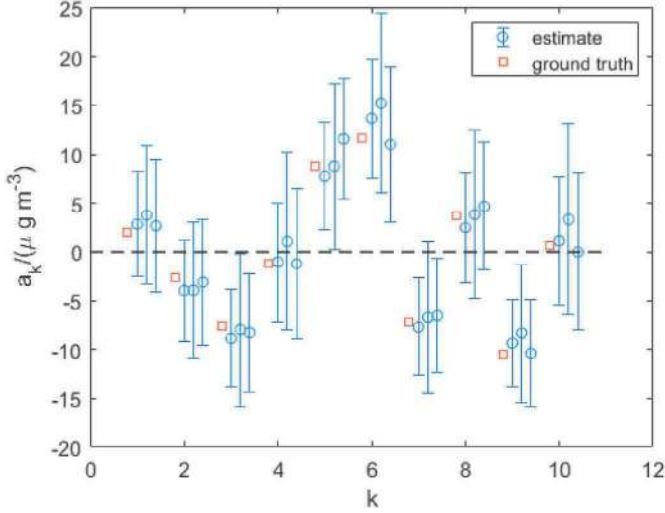
Fig. 2. Estimates $\widehat{a}_k$ of the intercept parameters and uncertainty bars $\pm 2u(\widehat{a}_k)$ derived from synthesized collocation data involving two calibrated reference instruments, k = 1,2 and eight standard instruments, k = 3, …,10. The three sets of estimates, left to right, are given by calculations A0, A1 and A2, respectively; see main text.

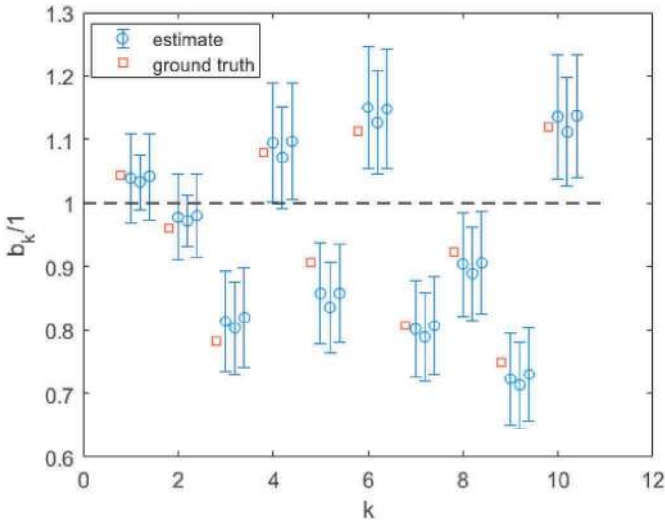**Fig. 3.** As Fig. 2 but for estimates $\widehat{b}_k$ of the slope parameters.

$u_{R,b}^2 = \phi_3^{-1} u_{R,b,0}^2$, $u_{S,a}^2 = \phi_4^{-1} u_{S,a,0}^2$, and $u_{S,b}^2 = \phi_4^{-1} u_{S,b,0}^2$, where the 0 subscript denotes the prior estimate of the hyper-parameter. The degree of belief in the prior estimates is parametrized by $m_{k,0}$, k = 1,2,3,4, with prior estimates associated with the well-characterised reference algorithms given a higher degree of belief, $m_{1,0} = m_{3,0} = 300$, while those associated with the standard instruments given a low degree of belief, $m_{2,0} = 5$ and $m_{4,0} = 1$. Calculation A0 represents the calculations that could be performed if the ground truth was available and provides a benchmark for the other calculations.

Fig. 2 shows the estimates of the intercept parameters a_k for the three calculations while Fig. 3 gives the same information but for the slope parameters b_k. The figures show that the uncertainties associated with the standard instrument parameters are of the same order as that for the reference instruments, confirming that they have been calibrated. The uncertainties associated with the reference instruments are also smaller than their prior estimates due to the fact that each reference instrument is benefiting from the information supplied by the other instruments, particularly the other reference instrument. Posterior estimates of the

statistical hyper-parameters for calculations A1 and A2 are given in able 2. The posterior weighting approach, calculation A2, is seen to give an estimate much closer to the ground truth value of σ_S than calculation A1.

4. Approximate collocation experiments

The collocation experiment considered in section 3 assumes that collocated instruments are sensing the same signal z_j by virtue of the fact that all the instruments are collocated, i.e., in the same place. In an approximate collocation experiment, we assume that the instruments are near each other but not necessarily sensing the same signal. Instead we have a model of the form in which if z is sensed by instrument k and z' is sensed by instrument k', the covariance between z and z' is specified by a correlation kernel $\text{cov}(z,z') = K(k,k')$. For example, K could reflect the spatial separation of the different instruments in some suitable metric. We are sometimes able to specify K on the basis of spatial separation but we may wish to learn or adjust K on the basis of the observed data [11].

4.1. Approximate collocation experiment taking into account spatial correlation

We consider a model of the form

$$y_i = a_k + b_k z_{j,k} + \epsilon_i, \epsilon_i \in N\left(0, \sigma_i^2\right). \tag{7}$$

where y_i is the measured response corresponding to signal $z_{j,k}$ at time t_j and at the kth location. We assume that the signals $\mathbf{z}_j = \left(z_{j,1} \ldots, z_{j,n_k}\right)^\mathrm{T}$ are such that

$$\mathbf{z}_j \in N\left(E z_{j,0}, V_j\right), E = (1, \ldots, 1)^\mathrm{T}, \tag{8}$$

where V_j is an $n_K \times n_K$ variance matrix encoding the correlation in the signals $z_{j,k}$ at time t_j. The term $z_{j,0}$ represents the spatial mean at time t_j. The variance matrix V_j controls the degree of smoothness of the departure from the spatial mean as a function of spatial separation. If V_j has Cholesky factorisation $V_j = L_j L_j^\mathrm{T}$ [20], we can write

$$z_{j,k} = z_{j,0} + \mathbf{l}_{j,k} \mathbf{e}_j, \mathbf{e}_j \in N(\mathbf{0}, I), \tag{9}$$

where $\mathbf{l}_{j,k}$ is the kth row of L_j.

4.2. Approximate collocation experiments as noisy collocation experiments

We can use algorithms for an exact collocation experiment to analyse data in an approximate collocation experiment by replacing the model in (7) by

$$y_i = a_k + b_k z_{j,0} + b_{k,0} \mathbf{l}_{j,k} \mathbf{e}_j + \epsilon_i \tag{10}$$

Where $b_{k,0}$ is a prior, fixed estimate of b_k, e.g., $b_{k,0} = 1$. The above model looks similar to the model (3) except that the random effects contribution to the measured response y_i involves a measurement component ϵ_i as before but also the term $\mathbf{l}_{j,k} \mathbf{e}_j$ representing a correlated effect modelling the departure of the signal at the kth location from the mean $z_{j,0}$. If we let $\mathbf{y}_j$ be the $m_j \times 1$ vector of responses at time t_j, and rename $z_{j,0}$ by z_j, then the model (10) can be presented as

$$\mathbf{y}_j = C_j \mathbf{a} + z_j D_j \mathbf{a} + \boldsymbol{\epsilon}_j, \boldsymbol{\epsilon}_j \in N\left(\mathbf{0}, V_{\mathbf{y}_j}\right), \tag{11}$$

where C_j and D_j are $m_j \times 2 n_K$ matrices expressing the modelled dependence of the response on z_j and $\mathbf{a}$, and $V_{\mathbf{y}_j}$ is the associated variance matrix constructed to account for the (scaled) spatially correlated and random effects.

Estimates of the model parameters can be made using the same approach as for the exact collocation case, solving the equivalent of (4), but taking into account the correlation between measurements taken at
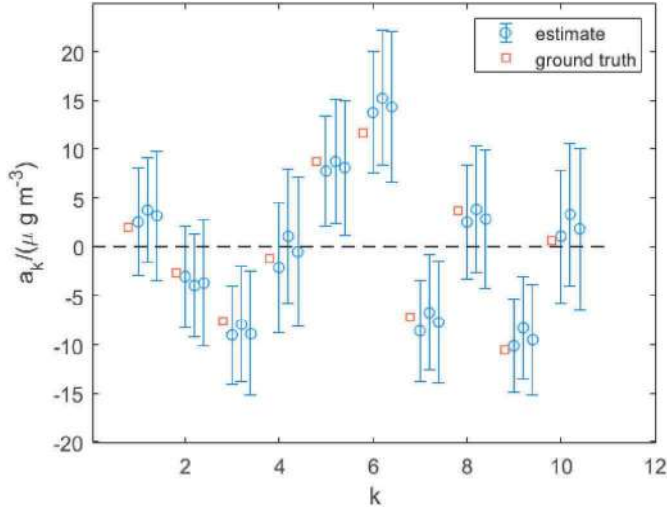
Fig. 4. Estimates $\widehat{a}_k$ of the intercept parameters and uncertainty bars $\pm 2u(\widehat{a}_k)$ derived from synthesized approximate collocation data. The three sets of estimates, left to right, are given by calculations B0, B1 and B2, respectively; see main text.
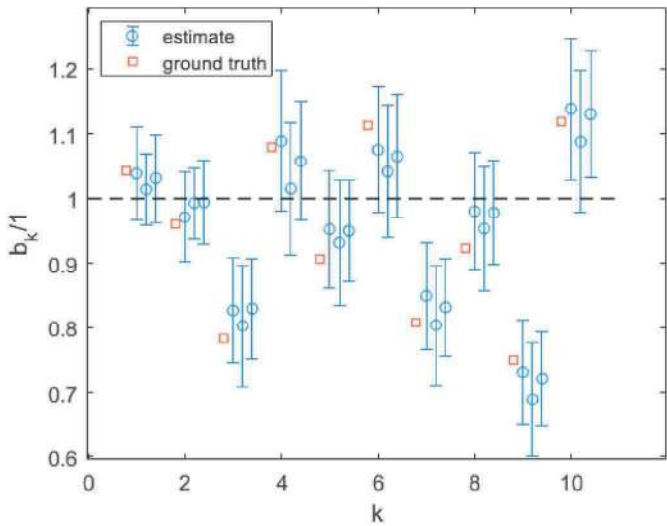

Fig. 5. As Fig. 3 but for estimates $\widehat{b}_k$ of the slope parameters.

the same time step. Again each summand function depends on at most one z_j so that the simple block-angular structure of the associated Jacobian matrix enables a computationally efficient solution algorithm.

4.3. Numerical example B: approximate collocation experiment

The second numerical example follows the same scheme as in section 3.7 except that the data is generated according to the model (7) and (8) with V_j derived from a spatial correlation matrix with diagonal values σ_E^2 with $\sigma_E = 5.00\ \mu\mathrm{gm}^{-3}$. (The data looks very similar to that in Fig. 1). We apply three calculations to the data. Calculations B1 and B2 correspond to calculations A1 and A2 in section 3.7 which treats the data as arising from an (exact) collocation experiment, treating the spatially correlated effects as additional, uncorrelated, random effects. The benchmark calculation B0 uses ground truth values of the statistical parameters to solve for the parameters based on model (10), taking into account spatial correlation, with estimates of $b_{k,0} = \widehat{b}_k$, where $\widehat{b}_k$ is the estimate provided by calculation B1.

Fig. 4 shows the estimates of the intercept parameters a_k for the three

calculations while Fig. 5 gives the same information but for the slope parameters b_k. Posterior estimates of the statistical hyper-parameters for calculations B1 and B2 are given in Table 1. The posterior weighting approach, calculation B2, gives estimates of σ_R and σ_S that are higher than the ground truth values to account for the additional random effects associated with the Gaussian process model. A posterior weighting scheme that directly takes into account the correlated effects is being developed.

5. Concluding remarks

Measurement problems involving sensor networks have requirements and features that make the application of conventional methods of calibration and uncertainty evaluation, and the use of established guidelines for uncertainty evaluation, challenging. A further challenge is that the behaviour and performance of the sensors in a network can be different from that under laboratory conditions where they may be calibrated and/or tested. The adoption of sensor networks in a metrological framework requires new modelling and uncertainty quantification methodologies beyond those found in the GUM. In this paper we have summarised these challenges and how some of them can be addressed through macro-calibration methodologies such as collocation studies.

References

[1] S. Tabandeh, A.P. Vedurmudi, H. Soderblom, S. Pourjamal, P. Harris, Sensor network metrology: current state and future directions, 17 others, in: XXIV IMEKO World Congress, August 2024, Hamburg, Germany, 2024.

[2] N. Cressie, C.K. Wikle, Statistics for Spatio-Temporal Data, Wiley, Hoboken, New Jersey, 2011.

[3] C.E. Rasmussen, C.K.I. Williams, Gaussian Processes for Machine Learning, MIT Press, Cambridge, Mass, 2006.

[4] JCGM, Evaluation of measurement data — guide to the expression of uncertainty in measurement. Joint Committee for Guides in Metrology, JCGM 100 (2008) 2008.

[5] JCGM, Evaluation of measurement data — Supplement 2 to the "Guide to the expression of uncertainty in measurement" — extension to any number of output quantities. Joint Committee for Guides in Metrology, JCGM 102 (2011) 2011.

[6] S. Eichstadt, A. Vedurmudi, M. Gruber, D. Hutzschen- reuter, Fundamental aspects in sensor network metrology, Acta IMEKO 12 (1) (2023) 1–6.

[7] M.G. Cox, The evaluation of key comparison data, Metrologia 39 (2002) 589–595.

[8] A.B. Forbes, Parameter estimation based on least squares methods, in: F. Pavese, A. B. Forbes (Eds.), Data Modeling for Metrology and Testing in Measurement Science, Birkhauser-Boston;, New York, 2009, pp. 147–176.

[9] X.-S. Yang, A.B. Forbes, Model and feature selection in metrology data approximation, in: E.H. Georgoulis, A. Iske, J. Levesley (Eds.), Approximation Algorithms for Complex Systems, SpringerVerlag, Heidelberg, 2010, pp. 293–307.

[10] A.E. Raftery, D. Madigan, J.A. Hoeting, Bayesian model averaging for linear regression, J. Am. Stat. Assoc. 92 (1997) 179–191.

[11] G. Kok, M. van Dijk, P.M. Harris, A. Vedurmudi, Modelling and determining correlations in sensor networks, in: XXIV IMEKO World Congress, August 2024. Hamburg, Germany.

[12] A.B. Forbes, Effective number of degrees of freedom associated with models, in: F. Pavese, A.B. Forbes, N.-F. Yang, A. Chunovkina (Eds.), Advanced Mathematical and Computational Tools for Metrology XII, World Scientific, Singapore, 2022, pp. 23–44.

[13] A. B Forbes, K. Jagan, J. Dunlevy, J.A. Sousa, Optimization of sensor distribution using Gaussian processes, Measurement: Sensors 18 (2021) 100128.

[14] S. Diez, S.E. Lacy, T.J. Bannan, M. Flynn, T. Gardiner, et al., Air pollution measurement errors: is your data fit for purpose? Atmos. Meas. Tech. 15 (13) (2022) 4091–4105.

[15] D.R. Peters, O.A.M. Popoola, R.L. Jones, N.A. Martin, J. Mills, et al., Evaluating uncertainty in sensor networks for urban air pollution insights, Atmos. Meas. Tech. 15 (2) (2022) 321–334.

[16] M.M. Twigg, A.J.C. Berkhout, N. Cowan, S. Crunaire, E. Dammers, et al., Intercomparison of in situ measurements of ambient NH_3: instrument performance and application under field conditions, Atmos. Meas. Tech. 15 (22) (2022) 6755–6787.

[17] A.R. Whitehill, M. Lunden, S. Kaushik, P. Solomon, Uncertainty in collocated mobile measurements of air quality, Atmos. Environ. X 7 (2020) 100080.

[18] J.N. Cape, The use of passive diffusion tubes for measuring concentrations of nitrogen dioxide in air, Crit. Rev. Anal. Chem. 39 (4) (2009) 289–310.

[19] D.G. Altman, J.M. Bland, Measurement in medicine: the analysis of method comparison studies, Journal of the Royal Statistical Society. Series D (The Statistician) 32 (3) (1983) 307–317.

[20] G.H. Golub, C.F. Van Loan, Matrix Computations, fourth ed., Johns Hopkins University Press, Baltimore, 2013.

[21] A. Bjorck, Numerical Methods for Least Squares Problems, SIAM, Philadelphia, 1996.

[22] M.G. Cox, The least-squares solution of linear equations with block-angular observation matrix, in: M.G. Cox, S. Hammarling (Eds.), Advances in Reliable Numerical Computation, Oxford University Press, 1989, pp. 227–240.

[23] A.B. Forbes, Weighting observations from multi-sensor coordinate measuring systems, Meas. Sci. Technol. 23 (2012) (online:025004).

[24] L. Mittal, G. Fuller, London Air Quality Network: Summary Report 2016, Technical report, King's College, London, June 2017.

João A. Sousa[a], Alistair B. Forbes[b],[*]

[a] *Laboratório Central de Metrologia, IPQ, Caparica, Portugal*
[b] *Data Science Department, National Physical Laboratory, Teddington, UK*

[*] Corresponding author.
E-mail address: alistair.forbes@npl.co.uk (A.B. Forbes).

Investigations on the performance of a newly developed pressure-driven flow controller used in microfluidic applications

ARTICLE INFO

ABSTRACT

This paper gives an overview of investigations with a newly developed pressure-driven flow controller, which has no mechanical components and can therefore provide pulsation-free flows. The performance of the pressure-driven flow controller is compared with high-precision syringe pumps used as reference systems in most laboratories and National Metrology Institutes.

The results show an astonishing performance of the pressure-driven flow controller, but also a strong dependence on the associated flow sensor. In contrast to a high-precision syringe pump, the system with a flow sensor is much more dependent on fluid properties, pressure and temperature.

However, the strength of the pressure-driven flow controller lies in rapid flow changes and flow stability. Here the system gives excellent results.

Another advantage of the system is that direct access to pressure values makes it easy to measure hydrodynamic resistances, which are important for lab-on-a-chip and organ-on-a-chip applications.

1. Introduction

Microfluidics is the technology of designing and manufacturing miniaturised devices consisting of chambers and channels. It is the science of manipulating and controlling fluids within them. The ability to control small flow rates very precisely is used in a wide range of applications, particularly in many areas of biology, medicine and engineering [1,2]. These include diagnostics, cell culture, drug discovery, rapid testing, organ-on-a-chip systems, single cell processing and sequencing, and other technical applications, particularly in the sensor, process and food industries [3]. In microfluidics, the effects of viscosity and capillarity are very important, and inertia and gravity are negligible. This condition affects the behaviour of the fluid and the way its flow is controlled. Flow in a microfluidic system is typically generated by peristaltic or syringe pumps, which are mechanical systems. Consequently, they cannot provide a completely pulsation-free flow and are limited in terms of response time and flow stability.

An alternative method of generating flow is the relatively new pressure-driven flow system, in which the liquid from a sealed container is forced into a more uniform motion by a gas supplied from an external pressure source, resulting in a pulsation-free flow that allows better flow control. Pressure-driven flow controllers only provide direct access to pressure by setting a setpoint pressure. To access flow values, a flow sensor must be added to the setup so that the inlet pressure is automatically adjusted to achieve the desired flow rate. The generated flow rate is proportional to the pressure difference with the microfluidic resistance as the proportional coefficient, which is a characteristic of the fluidic system and depends on the device geometry and liquid properties. This study investigated a novel pressure-driven flow controller and a fast-responding in-line flow sensor capable of measuring liquid flows down to 0.4 μL/min. In contrast to conventional pressure-driven flow

controllers, this prototype has a slightly lower response but very low gas consumption. The investigations included pressure control with flow monitoring and flow control with pressure monitoring measurements and simultaneous calibration of the entire microfluidic system, i.e. in this case the flow sensor was calibrated with a balance using the dynamic weighing method. In this context, different microfluidic resistance configurations were investigated using a thermoplastic polymer microfluidic chip (TOPAS chip) containing 8 different channel configurations accommodated on the same chip. To compare the results, the same microfluidic resistance measurements were also performed using high-precision syringe pumps and calibrated glass syringes, which are used as reference systems in most microflow laboratories. All these measurements were carried out using water as the test fluid, but also Simulated Body Fluid (SBF) and Phosphate Buffer Saline (PBS) at two different National Metrology Institutes under the scope of EMPIR project MFMET [4].

There are a variety of microfluidic applications that require fast dynamic response and precise flow rate control. The performance of the pressure-driven flow controller was investigated in terms of its dynamic behaviour by applying various predefined flow profiles (ramp, sine, square and triangular) and comparing them with the response behaviour of the fast-responding flow sensor.

2. Methods and procedures

The gravimetric method [5] is used to determine a delivered mass of a liquid over a time interval. This method can be used for testing inline flow sensors and flow generators. In a gravimetric microfluidic setup, an electronic balance is used to determine the delivered mass of a liquid from or through the test object, which can be a flow generator, a microfluidic device or a flow meter. In general, the desired flow rate is
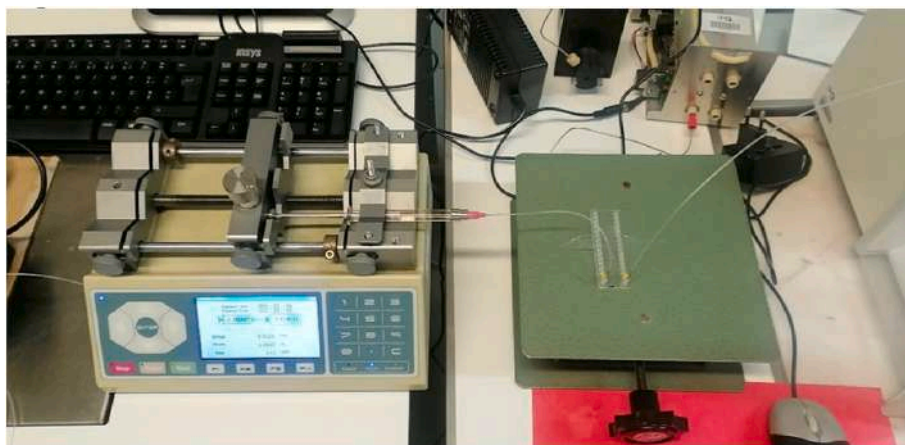
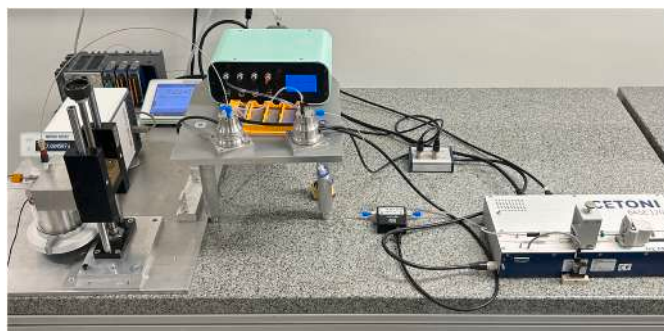Fig. 1. NEXUS pump system measurement setup at IPQ.

Fig. 2. Cetoni pump system measurement setup at RISE. In the configuration shown, the pressure drop over a channel of the microfluidic chip is measured.

generated using a high-precision syringe pump with a calibrated syringe of known size, material and volume and compared against the weighing scale. The calibrated system can then be used as a reference even without a weighing scale.

2.1. High-precision syringe pump

High-precision syringe pumps are dedicated syringe pumps that are often used in laboratories, medical research centres and other areas where extremely accurate fluid delivery is required due to the need of very reliable and reproducible results. These types of pumps have a very high accuracy and allow extremely accurate delivery of liquids with precise control over the flow rate, especially at low flow rates and volumes. These devices are suitable for a wide range of fluids and applications and often have programmable functions and recording capabilities.

2.1.1. NEXUS pump system at IPQ

At the Portuguese Quality Institute (IPQ) [6] flow is generated with a Nexus 3000 syringe pump (Fig. 1), from Chemyx, using a 1 mL ILS glass syringe connected to polyethylene (PE) tube of 1.26 mm (0.05") inner diameter which is immersed in the water in the weighing vessel on the balance (Mettler AX26, resolution 1 μg). In addition, this particular setup uses an evaporation trap to reduce evaporation, especially useful at low flow rates, and the connecting tube was inserted below the water surface inside the weighing vessel of the balance to avoid the drop impact effect. Thus, the mass flow rate is determined, and the volume flow rate can be calculated with the appropriate density of the liquid.

The time interval in which the mass is delivered is determined by a timing module to derive the mass flow rate. The data are collected from the balance every 250 ms during 60 min using a LabVIEW application. The flow rate is determined every 30 seconds.

The climatic conditions such as air temperature, relative humidity and pressure are determined to correct for buoyancy effects on the balance. The liquid temperature is measured in the beginning and at the end of the tests and used to convert the mass flow rate into a volumetric flow rate, considering the density of the liquid used.

At start of each measurement, it is required to put the system on charge, and after that let it run for 10 minutes to stabilise.

2.1.2. Cetoni pump system at RISE

For the measurements, the Nanoflow Test Facility at the Research Institutes of Sweden (RISE) was used, Fig. 2. A very detailed description and operating principle of the facility can be found in Ref. [7]. The main part of the test facility is a Mettler Toledo XPR10 microbalance (weighing scale) with a capacity of 10.1 g and a readability of 1 μg. The measuring principle of the test facility is based on the dynamic weighing method and has a flow rate range of 0.25 μL/h to 1 mL/h, which is adapted to the specifications of the weighing scale.

The weighing scale can be operated and read out using a Personal Computer (PC) and a self-written LabVIEW programme. For all measurements, the weighing scale was read out at 1 Hz.

The AAMI Technical Information Report (TIR) TIR101:2021 [8] gives recommendations for minimising evaporation. As described in Ref. [7], for all measurements the weighing vessel (beaker) was first filled with about 10 mm of water and then with about 5 mm of paraffin oil to minimise the effects of evaporation. The paraffin oil is denser than water and prevents evaporation on the surface. In addition, an evaporation trap was used.

A 27G needle with a nominal outer diameter (OD) of 0.413 mm, a nominal inner diameter (ID) of 0.210 mm and a length of 90 mm was used for all measurements as the focus is on very low flow rates. This is a Whitacre spinal needle (pencil point) which, unlike a standard Quincke spinal needle (cutting), has the opening on the side (at the end of the needle) and not directly at the end of the needle. The advantage is that this needle does not exert any direct forces when filling the weighing scale.

For all measurements, the tubing in the measuring range is 1/16″ OD Polyether Ether Ketone (PEEK) mostly with an ID of 0.13 mm but also some with an ID of 0.50 mm.

All tests were carried out at an ambient and water temperature of (23.0 ± 0.5) °C. The temperature of the test liquid was measured indirectly at various spots using type K thermocouples (TC) connected to a National Instruments compactRIO Data Acquisition (DAQ) system. The air pressure, room temperature and humidity in the laboratory were measured separately and recorded by a Vaisala PTU300.

O. Büker et al.

Table 1

Manufacturer specifications of the Elveflow Microfluidic Flow rate Sensor (MFS) MFS2.

Specifications MFS2	
Flow rate range	0 to $\pm$ 7 μL/min
Accuracy (bi-directional)	5 % m.v. between (0.42–7 μL/min)
Repeatability (bi-directional)	0.5 % m.v. between (0.70–7 μL/min)
Pressure drop at full scale flow rate, 23 °C	3 mbar
Total internal volume	1.5 μL
Sensor inner diameter	150 μm
Operating pressure	200 bar
Fitting type	UNF 1/4″-28

Fig. 3. MIC system measurement setup at IPQ.

2.2. Pressure-driven flow generator

A pressure-driven flow controller is a method to generate flow in microfluidics. The pressure driven flow controller is connected to an external pressure source. The device applies a precise gas pressure to a sealed reservoir filled with liquid. The pressure difference between the outside pressure (atmospheric pressure in an open system) and the pressure inside the reservoir forces the liquid to flow through the microfluidic device. The flow rate generated is therefore directly proportional to the difference in pressure between the inlet and outlet, known as the differential pressure.

The pressure-driven flow controller is operated by the software supplied, which allows to regulate the pressure by setting a target pressure. The higher the pressure difference, the higher the flow rate. The pressure-driven flow controller only provides direct access to pressure. To access flow values, a flow sensor (flow meter) must be added to the setup. The combination of a pressure-driven flow controller and a flow sensor offers the advantage of either working in pressure control with flow monitoring, or in flow control where the inlet pressure is automatically adjusted to achieve the target flow. In this case, a feedback loop is established between the flow sensor and the pressure controller via the control software.

The system provided by the Microfluidics Innovation Center (MIC) consists of the prototype pressure-driven flow controller and a commercially available Elveflow Microfluidic Flow Sensor (MFS). The MFS2 used is a thermal mass flow (TMF) time-of-flight (ToF) conductivity flow sensor with the specifications given in Table 1. The operating principle of the flow sensor is based on local heating of the liquid passing through a capillary inside the sensor and measuring the temperature upstream and downstream of the heater. The difference in temperature between the two spots allows the MFS to determine the flow rate. The relationship between the temperature difference and the flow rate depends on the properties of the liquid. Therefore, the sensor must be calibrated according to the liquid. The MFS2 comes with two different
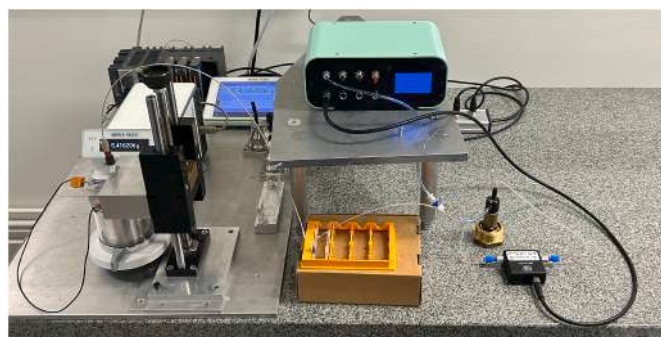
Fig. 4. MIC measurement setup at RISE.

preset calibrations available: water (H_2O) and isopropyl alcohol (IPA) at 23 °C.

The supplied MFS2 has a flow rate specification of 0.42 μL/min to 7 μL/min (0.0252 mL/h to 0.42 mL/h). In order to cover as wide a flow rate range as possible, three flow rates of 0.025 mL/h, 0.1 mL/h and 0.4 mL/h (a factor of 4 in between each) were selected for the measurement campaign.

In principle it is possible to calibrate the flow sensor for other liquids. However, all measurements shown in the following have been made using the factory calibration for water.

2.2.1. MIC system at IPQ

The measurement setup is shown in Fig. 3. First, the pump is connected to a pressure source (50 L, 200 bar nitrogen cylinder) and then positioned higher than the reservoir to prevent backflow. The reservoir is filled with the test fluid which flows through the tube and past the Elveflow MFS. The MFS is positioned slightly above the microchip, which is at the same level as the outlet. The Elveflow software can be used to select the desired flow rate, display it graphically in the software and store the results for further analysis.

It is recommended that the system is primed before starting measurements, then the pump is allowed to run for 10 minutes to stabilise before starting the measurement. After completing the first measurement, set the new flow rate, allow the pump to run for approximately 5 minutes to stabilise and then start the measurement; this step is recommended for each measurement.

2.2.2. MIC system at RISE

In order to obtain consistent results, a similar measurement setup to IPQ, as shown in Fig. 4, was realized. The pressure-driven flow controller allows the control of the output pressure value of 4 independent channels from 0 to 2000 mbar. The pressure source was provided by an Air Liquide ALPHAGAZ™ 1 nitrogen cylinder (50 L, 200 bar) connected by 6mm OD pneumatic tubing with push-in fittings. For the 2000 mbar pressure channel, the pressure source was set at a constant 5 bar using a pressure regulator. The pressure-driven flow controller was connected to the pressure reservoir with 4 mm OD, 2.7 mm ID clear tubing. The flow sensor was placed flat on the granite table as recommended by the supplier.

One difference to the IPQ setup was the measuring time. In this case, the measuring time was selected so that about 1 mL (one full syringe) was delivered in each measurement, regardless of the flow rate.

2.3. Microfluidic chip

Microfluidic chips are used for the precise manipulation and analysis of small amounts of liquid. These include analytical chips, micromixer chips, cell culture chips, lab-on-chip and organ-on-chip. Microfluidic chips contain microscopic channels through which fluids can flow in a very precise and controlled way. The three most common materials used to make these chips are silicon, glass and polymer. The fabrication of the

Fig. 5. Microfluidic polymer chip with 8 different channels, chip dimensions 75.5 × 25.5 mm, mini-luer access holes.

channels requires a high degree of precision and control to ensure that fluids can flow properly through the channels.

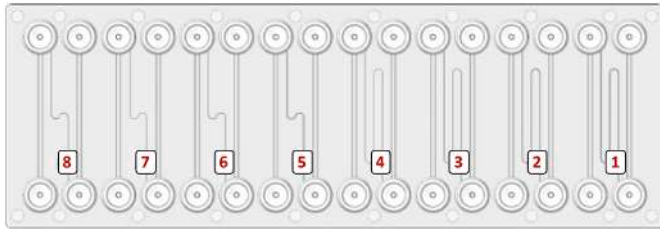In this study, measurements were made using the TOPAS microfluidic chip shown in Fig. 5. This chip has 8 different channels. TOPAS (Thermoplastic Olefin Polymer with Amorphous Structure) is a special thermoplastic polymer used in the manufacture of microfluidic chips due to its unique properties such as high transparency, chemical resistance and biocompatibility.

Due to the maximum pressure of the pump of 2000 mbar, only channel numbers 1, 2 and 5 could be considered for the envisaged flow range (Table 2). As channel no. 1 has the lowest pressure drop, this channel was deselected.

Measurements were performed with two configurations of channel no. 5 at IPQ and channel no. 2 at RISE. Herby the direct connection of the inlet and outlet with a height and weight of around 500 μm has the designation "large" and the configuration with the given height and width and length in Table 2 has the has the designation "small". The pressure drop over the "large" configuration is negligible for the given flow rates due to the dimensions.

3. Results and discussion

In the first step, measurements with a high-precision syringe pump are carried out and then compared with measurements with the pressure-driven flow controller.

3.1. High-precision syringe pump

For the measurements with the Nexus pump at IPQ and the Cetoni pump at RISE, with and without the chip, care was taken to ensure that the measurement set-up, test time, start position and syringe remained the same for tests.

The measurements were carried out in two stages:

- In the first stage (section 3.1.1), the test was carried out directly against the balance, without the microfluidic chip. In this stage, the test was performed at 0.025 mL/h, 0.1 mL/h and 0.4 mL/h. At RISE these tests were performed with water only but at IPQ with three test fluids: water, Simulated Body Fluid (SBF) and Phosphate Buffered Saline (PBS).
- In the second stage (section 3.1.2), the same test was carried out but with the microfluidic chip.

3.1.1. Calibration of the high-precision syringe pump against the weighing scale

The later calibrated system consisting of syringe pump and then calibrated syringe can then itself be used as a reference for flow generation (see e.g. section 3.3).

3.1.1.1. Measurements with the Nexus system at IPQ. As can be seen in Table 3, the error decreased as the flow rate increased and the uncertainty varied between 1.4 and 2.0 %. These values are consistent with the claimed Calibration and Measurement Capabilities (CMCs) of IPQ.

3.1.1.2. Measurements with the Cetoni system at RISE. The measurements were carried out using the manufacturer's specifications regarding the dimensions of the syringe. As can be seen in Table 4, the measured values correspond very well with these specifications. The measurements at all three flow points provide consistent results.

Table 3

Measurements with the Nexus system (1 mL ILS syringe) against the weighing scale using water as test liquid.

Calibration results at IPQ (Nexus system)		
1	Set flow rate: 0.025 mL/h	
	Measurement time:	2h 00 min
	Measured flow rate:	0.0257 mL/h
	Measurement error:	−2.80 %
	Uncertainty $U(k = 2)$	1.40 %
2	**Set flow rate: 0.100 mL/h**	
	Measurement time:	2h 00 min
	Measured flow rate:	0.0994 mL/h
	Measurement error:	+0.60 %
	Uncertainty $U(k = 2)$	2.00 %
3	**Set flow rate: 0.400 mL/h**	
	Measurement time:	2h 00 min
	Measured flow rate:	0.3985 mL/h
	Measurement error:	+0.38 %
	Uncertainty $U(k = 2)$	1.70 %

Table 4

Measurement results ($U(k = 2) \leq 0.5$ %) with the CETONI system (1 mL syringe) against the weighing scale.

Syringe calibration results at RISE		
1	0.025 mL/h	
	Measurement time:	39h 45 min
	Weighing scale (Ref.):	0.992708 mL
	Cetoni logfile (syringe):	0.993802 mL
	Measurement error:	+0.11 %
2	**0.100 mL/h**	
	Measurement time:	9h 45 min
	Weighing scale (Ref.):	0.974543 mL
	Cetoni logfile (syringe):	0.975058 mL
	Measurement error:	+0.05 %
3	**0.400 mL/h**	
	Measurement time:	2h 25 min
	Weighing scale (Ref.):	0.966534 mL
	Cetoni logfile (syringe):	0.966722 mL
	Measurement error:	+0.02 %

Table 2

Dimensions of the eight channels available on the microfluidic chip.

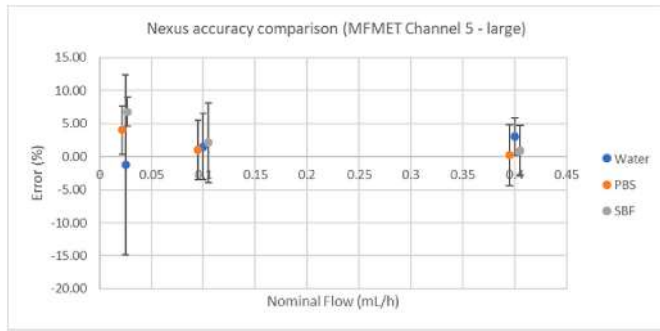| Channel no.	1	2	3	4	5	6	7	8
Height (μm)	100	50	20	10	50	20	10	5
Width (μm)	100	50	20	10	50	20	10	5
Length (mm)	40	40	40	40	20	20	20	20
Pressure drop (mbar) at 0.025 mL/h	0.79	12.6	493	7890	6.3	246	3940	6310
Pressure drop (mbar) at 0.400 mL/h	12.6	202	7890	126000	101	3940	63100	1010000

O. Büker et al.

Fig. 6. Error difference in the large configuration of channel 5 with and without the chip with the Nexus system at IPQ.

3.1.2. Measurements with the high-precision syringe pump and the microfluidic chip against the weighing scale

3.1.2.1. Measurements with the Nexus system at IPQ.
The differences between the results with and without the chip ("large" configuration of channel 5) for water, SBF and PBS using the Nexus pump as flow generator are shown in Fig. 6.

It can be verified that in general the uncertainty and the error values obtained with the different liquids are similar.

Unfortunately, due to the high pressure the Nexus system had to generate, IPQ was unable to measure the flow in the "small" configuration of channel 5.

3.1.2.2. Measurements with the Cetoni system at RISE.
Table 5 below shows the measurement results with the Cetoni system for the measurements with the "small" and "large" configuration of Chip 5 at RISE.

In comparison to Table 4, the results show a slight shift in the calibration curve of all flow points in a positive direction. The measurement deviation is higher at low flow rates (longer measurement times) and slightly higher in the "small" configuration of channel 5 (higher pressure). This could speculatively indicate evaporation or leakage, e.g. at the mini-luer connections on the microfluidic chip. From a fluidic point of view, these connections are not ideal. However, the results are still very good, especially for microflow.

Table 5
Measurement results ($U(k = 2) \leq 0.5$ %) of the "small" and the "large" configuration of channel 2 on the microfluidic chip with the Cetoni system at RISE.

Channel 2: "large" and "small" configuration			
		"large"	"small"
1	**0.025 mL/h**		
	Measurement time:	39h 30 min	39h 30 min
	Weighing scale (Ref.):	0.977142 mL	0.972392 mL
	Cetoni logfile (syringe):	0.987557 mL	0.987564 mL
	Measurement error:	+1.07 %	+1.56 %
2	**0.100 mL/h**		
	Measurement time:	9h 45 min	9h 45 min
	Weighing scale (Ref.):	0.973220 mL	0.968468 mL
	Cetoni logfile (syringe):	0.975064 mL	0.975036 mL
	Measurement error:	+0.19 %	+0.68 %
3	**0.400 mL/h**		
	Measurement time:	2h 20 min	2h 25 min
	Weighing scale (Ref.):	0.931187 mL	0.963585 mL
	Cetoni logfile (syringe):	0.933389 mL	0.966734 mL
	Measurement error:	+0.24 %	+0.33 %
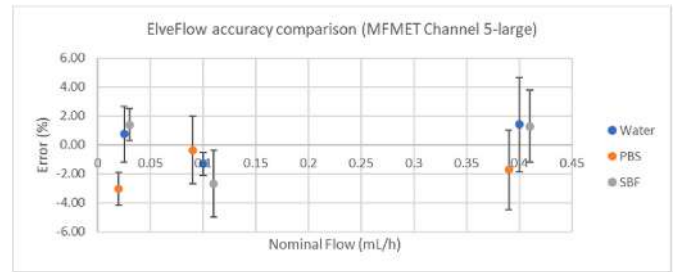
Fig. 7. Error difference in the large configuration of channel 5 with and without the microfluidic chip with the MIC system at IPQ.
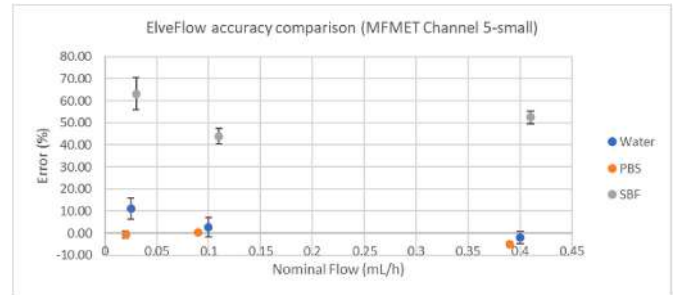
Fig. 8. Error difference in the small configuration of channel 5 with and without the microfluidic chip with the MIC system at IPQ.

3.2. Pressure-driven flow generator

For the measurements with the MIC system with and without chip, it was again taken into account that the setup and test time remained the same for all measurements.

The measurements were carried out in two stages:

- In the first stage (section 3.2.1), tests were performed against the weighing scale with the microfluidic chip. Measurements were made at 0.025 mL/h, 0.1 mL/h and 0.4 mL/h with three test fluids (water, SBF and PBS) at IPQ and with water at RISE.
- In the second stage (section 3.2.2), dynamic measurements were performed at RISE with the MIC system.

3.2.1. Measurements with the MIC system and the microfluidic chip against the weighing scale

3.2.1.1. Measurements with the MIC system at IPQ.
The differences between the results with and without the chip ("large" configuration of channel 5) for water, SBF and PBS using the MIC as flow generator are described in Fig. 7.

In this case there are some variations in the results using different liquids. TMFs are strongly dependent on the thermal properties of the liquid, such as specific heat capacity and thermal conductivity. It should be noted that all the results were obtained with the preset calibration for water at 23 °C.

In general, the uncertainty values of the MIC system are smaller than for the Nexus pump. The differences between the results with and without the chip of the channel 5, "small" configuration, for water, SBF and PBS using the MIC as flow generator are described in Fig. 8.

In this situation the uncertainty is larger than for the larger configuration, but the error values are similar, except for the SBF were some anomalies occurred during the tests.

What can be recognised, however, is that in general the uncertainties obtained at IPQ from the MIC system are smaller than for the Nexus pump. The error variation between the values with and without the chip

Table 6
Measurement results of the "small" and the "large" configuration of channel 2 on the microfluidic chip with the MIC system at RISE.

Channel 2: "large" and "small" configuration			
		"large"	"small"
1	**0.025 mL/h**		
	Measurement time:	39h 30 min	39h 30 min
	Weighing scale (Ref.):	0.945410 mL	0.958790 mL
	MFS logfile:	0.024992 mL/h	0.024988 mL/h
	Pressure	39.64 mbar	58.74 mbar
	Measurement error:	+4.42 %	+2.94 %
2	**0.100 mL/h**		
	Measurement time:	10h 00 min	10h 00 min
	Weighing scale (Ref.):	1.005302 mL	1.010770 mL
	MFS logfile:	0.099994 mL/h	0.099986 mL/h
	Pressure	70.28 mbar	123.33 mbar
	Measurement error:	−0.53 %	−1.08 %
3	**0.400 mL/h**		
	Measurement time:	2h 30 min	2h 30 min
	Weighing scale (Ref.):	1.115796 mL	1.129715 mL
	MFS logfile:	0.400063 mL/h	0.399951 mL/h
	Pressure	198.92 mbar	426.20 mbar
	Measurement error:	−10.36 %	−11.49 %

is similar for both pumps for the large configuration.

3.2.1.2. Measurements with the MIC system at RISE. As can be seen in Table 6, at the lowest flow rate the Elveflow MFS2 delivers a lower flow than is displayed. In contrast, the flow sensor delivers more than it indicates at the maximum flow rate. In the medium flow rate, the two values match more closely.

The flow values with the "small" chip configuration are similar values to those with the "large" ship configuration, possibly with a small shift of the entire calibration curve.

It should be mentioned that there are other influencing factors that can affect the measurement in the MIC system. For example, the inlet pressure changes depending on the filling volume of the reservoir. In the Eppendorf lid used with a filling volume of 2 mL, the first millilitre (from 2 ml to 1 ml filling volume) makes a difference of 1.6 mm and the second millilitre (from 1 mL to 0 mL filling volume due to the conical shape) makes a difference of 1.8 mm. Assuming that a water column of 100 cm represents a pressure of 100 mbar, this already means a pressure difference of 1.6 mbar for a measurement in which a volume of 1 mL is delivered, respectively a necessary increase in inlet pressure. At the same time, the weighing scale is filled and the back pressure increases. In the case of measurements at RISE (about 5.35 mm/ml), this means an additional 5.35 mbar per millilitre.

In order to maintain a constant pressure, the difference at the beginning of the measurement (2 mL in the reservoir) to the end of the measurement (1 mL in the reservoir) is about 7 mbar.

These considerations probably do not make much difference for large flow rates and the associated higher pressures. However, the situation is different with low flow rates and lower pressures.

3.2.2. Dynamic measurements with the MIC system at RISE

Flow control is achieved by a Proportional-Integral-Derivative (PID) controller feedback loop in the MIC system. The software supplied allows the PI parameters to be changed to achieve the desired response. The change of the PI values is usually sufficient for most applications. As a rule of thumb, if the system is slow to react or overshoots, P should be changed and if there is oscillation or the system slows as it approaches the target, I should be changed. The default parameters for P and I are 0.001, which means a quite sluggish system.

The most common test signal for characterising the transmission behaviour of a system is the step function. For this reason, it was examined to what extent the system can follow desired rapid flow changes. For this purpose, the pump (P:0.012, I:0.012) was subjected to
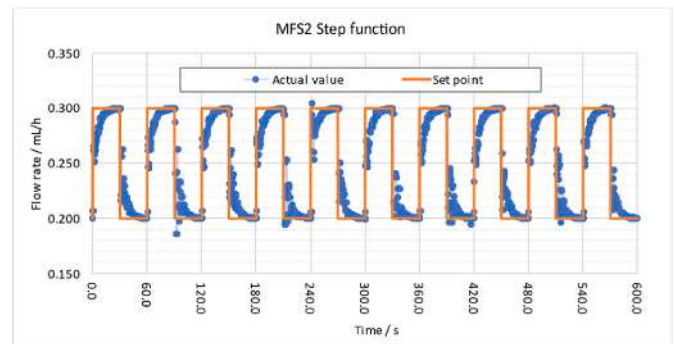
Fig. 9. Result of the step response tests with adjusted amplification factor.
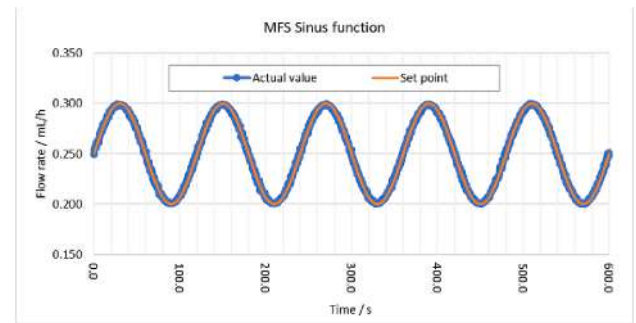
Fig. 10. Result of the sine excitation test with adjusted amplitude and phase.

a rectangular function between 0.2 mL/h and 0.3 mL/h with a period length of 60 s (step up, hold for 30 s, step down, hold for 30 s), Fig. 9.

In addition to the step function and pulse function, periodic input functions are also used as test signals to determine the transfer behaviour of dynamic systems. The frequency response is the relationship between the input and output signal of a linear time-invariant system with sinusoidal excitation in terms of amplitude and phase. Due to the linear behaviour of the system, the output signal has the same frequency as the input signal. However, the two signals differ in amplitude and phase. The ratio of the amplitudes of the input signal and the output signal as a function of the frequency is the amplitude response. The difference in phase between the input signal and the output signal as a function of frequency is the phase response. This means after a transient phase, the system also responds to a sinusoidal signal with a sinusoidal signal of the same frequency, but with a different amplitude and phase depending on the frequency.

As can be seen in Figs. 9 and 10, the MIC system is able to follow rapid changes. The period duration of the rectangular functions is already at the limit, at least for the setup at RISE. The response during excitation with the sine function is on the other hand extremely smooth.

3.3. Flow resistivity/Hydraulic resistance measurements

Microfluidic flows are characterised by their laminar nature and therefore viscous effects dominate over inertia. This leads to a simplification of the Navier-Stokes equations to the Poiseuille equation, which describes the pressure drop due to the viscosity of an incompressible fluid. The flow rate is then proportional to the pressure drop:

$$\Delta p = R_h \cdot Q \tag{1}$$

The flow resistance R_h, also called hydraulic resistance or hydrodynamic resistance, is a crucial parameter in microfluidic experiments. The flow resistance can be defined as the resistance that all microfluidic components in a measurement setup (tubing, valves, flow sensor, etc.) and the microfluidic chip present to the flow. When a fluid is

Table 7
Measurement results of the large configuration of channel 2 on the microfluid chip with the Cetoni system at RISE.

Cetoni system – Channel 2: "large" configuration			
Target flow (mbar)	Cetoni set flow (mL/h)	MFS log (mL/h)	Δp (mbar)
0.000	0.000	0.000474	0.00
0.025	0.024	0.025865	0.38
0.100	0.100	0.099685	0.48
0.200	0.200	0.197413	1.63
0.300	0.312	0.293645	2.22
0.400	0.450	0.403838	2.24

Table 8
Measurement results of the small configuration of channel 2 on the microfluid chip with the Cetoni system at RISE.

Cetoni system – Channel 2: "small" configuration			
Target flow (mbar)	Cetoni set flow (mL/h)	MFS log (mL/h)	Δp (mbar)
0.000	0.000	0.000606	0.00
0.025	0.024	0.025325	18.02
0.100	0.100	0.095104	57.72
0.200	0.200	0.202950	111.27
0.300	0.312	0.294966	161.33
0.400	0.445*	0.397255	225.61

Table 9
Measurement results of the large configuration of channel 2 on the microfluid chip with the MIC system at RISE.

MIC system – Channel 2: "large" configuration			
	MFS flow	Ref. flow	Pressure
	mL/h	mL/h	mbar
0.400	0.400063	0.446319	198.96
0.100	0.099994	0.100530	70.28
0.025	0.024992	0.023934	39.64
0.000	−0.000930	0	27.96

Table 10
Measurement results of the small configuration of channel 2 on the microfluid chip with the MIC system at RISE.

MIC System – Channel 2: "small" configuration			
	MFS flow	Ref. flow	Pressure
	mL/h	mL/h	mbar
0.400	0.399951	0.451886	426.20
0.100	0.099986	0.101077	123.33
0.025	0.024988	0.024273	58.74
0.000	0.000856	0	27.75

3.3.1. Measurements with the Cetoni system at RISE

The flow was generated using the high-precision syringe pump (Cetoni) and the 1 mL syringe which was calibrated for this purpose in section 3.1 (section 3.1.1). For the pressure drop measurement over the chip, two external pressure sensors (Cetoni) with a flat ceramic membrane and a nominal pressure of 500 kPa (5.0 bar) were used to measure the pressure before and after the microfluidic chip. The pressure sensors were connected directly to the Cetoni syringe pump via a Cetoni input/output (I/O) port splitter and the pressure values were recorded by the Cetoni software.

The measurement set-up was designed that the syringe pump was connected to the MFS, then the MFS to the upstream pressure sensor. After the downstream pressure sensor, the measuring line ends at an infusion needle that protrudes into the beaker.

For this application, the MFS was used as a flow sensor and not as a regulator as in the MFS system. As can be seen in Tables 7 and 8, the flow rate of the Cetoni pump was set in such a way that the MFS display shows the desired flow rate value in the software. This procedure enables better comparability with the MIC system, as the value of the MFS there is used as the flow reference. As can be seen in Table 7, for example, the flow rate value of the Cetoni pump need to be set to 0.450 mL/h so that the MFS displays a flow rate of 0.400 mL/h. According to the measurements and the evaluation of the MFS log file, the average value in this case was actually 0.403838 mL/h. Incidentally, this finding also corresponds very well with the measurements of the MFS against the weighing scale (Tables 6 and 9).

The pressure sensors have a resolution of 1.25 mbar and are therefore completely unsuitable for measuring such small pressure differences. However, the results shown in Table 7 confirmed that the pressure drop over the "large" configuration of channel 2 is negligible, as already mentioned in section 2.3.

Table 8 and Fig. 11 summarise the results of the pressure drop measurements with the Cetoni pump over the small configuration of channel 2 ($R_h = 518.0$ mbar h/mL). The results correspond well with the theoretical values ($R_h = 505.8$ mbar h/mL) which can be calculated using the channel width, channel height and channel length. The measured value is slightly larger, which could indicate that the actual

pressurised, the flow resistance determines the corresponding flow rate. The range and precision of the flow rate can be controlled by adjusting the flow resistance of the system.

In lab-on-a-chip experiments, for example, it is important to calculate the microfluidic flow resistance of a chip to understand the system and define the flow parameters (e.g. shear stress). This is determined by the design of the microchip. As a side note, by adjusting the material, length and diameter of the tubing, the flow resistance can be influenced to adapt or improve the performance of the flow control system.
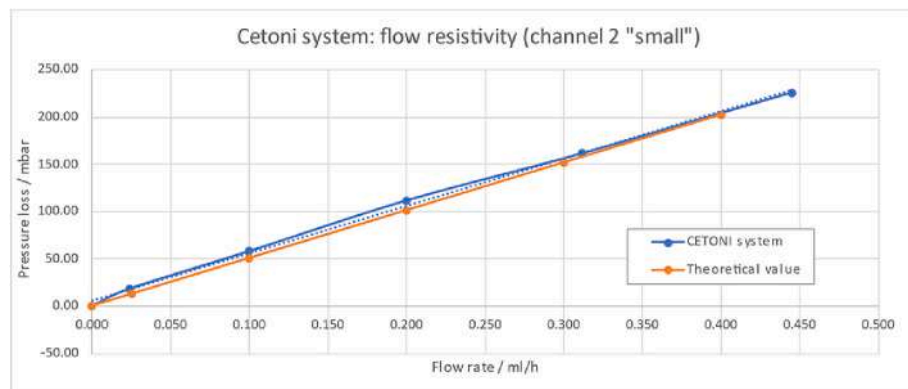

Fig. 11. Comparison of the results of the measurements with the Cetoni system with the theoretical value.
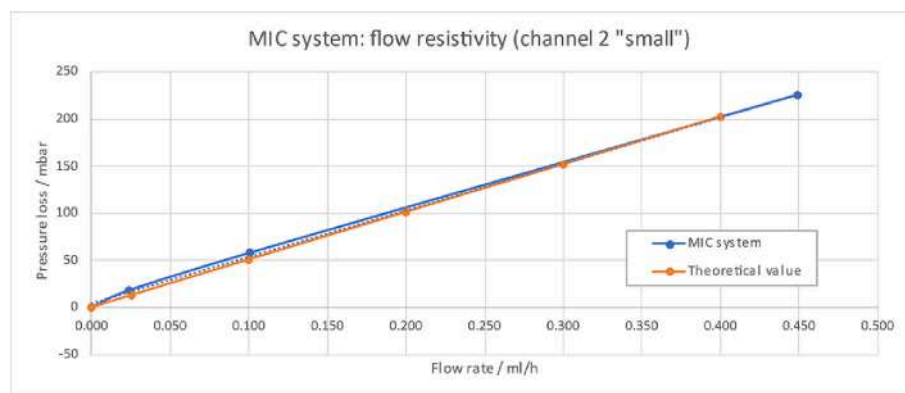
Fig. 12. Comparison of the results of the measurements with the MIC system with the theoretical value.

channel length and/or the channel width is slightly smaller, or the channel is slightly longer.

3.3.2. Measurements with the MIC system at RISE

The same measurements were made using the MIC system. The advantage of the MIC system is that, due to the nature of the operating principle, the pressure is directly available as a value provided by the system.

As the pressure drop over the large configuration of channel 2 is negligible, the pressure drop over the small configuration of channel 2 can be determined. If the measurement setup is identical in both configurations, the only difference is that the pressure drop over the chip plays a role in one case (small configuration of channel 2) and not in the other (large configuration of channel 2). This means that a much higher inlet pressure is required in one case than in the other. The back pressure is also the same in both cases. The difference between these two measurements should therefore only represent the pressure drop over the small configuration of channel 2.

The pressure drop measurements for both configurations are shown in Table 9 (large configuration of channel 2) and Table 10 (small configuration of channel 2).

It is noted that the pressure drop measurements were not taken at exactly the same flow rates. The results are presented by differentiating the pressure values and averaging the respective reference flow values obtained from the measurement against the weighing scale. As can be seen in Fig. 12, the measured value ($R_h = 506.4$ mbar h/mL) agrees very well with the theoretical value ($R_h = 505.8$ mbar h/mL). Again, the measured R_h value is slightly larger than the theoretical R_h value.

4. Conclusions

This study compares the performance of a pressure-driven flow system, comprising a novel pressure-driven flow controller and a commercial thermal mass flow meter, with that of established high-precision syringe pumps, which are typically employed as the reference for flow generation in most medical research and National Metrology Institutes.

The set pressure in a pressure-driven flow controller is proportional to the flow rate, with the microfluidic resistance serving as the proportionality factor. This factor depends on the measurement setup and the properties of the test fluid used. In microfluidic applications, such as lab-on-a-chip experiments, the microfluidic resistance of the microchip is essential because it defines the parameters for the experiment. For this reason, these measurements were realized with a microfluidic chip that can create different pressure conditions at the same flow rate by simply changing the channels or access holes on this chip. It should be noted that the flow sensor was not calibrated for the other test liquids under investigation, and the factory calibration for water was used. This offers

potential for further investigation. Finally, pressure-driven flow systems are regarded as fast-responding systems that produce pulsation-free flow. Due to fast pressure changes, it is theoretically possible to generate fast flow changes. For this reason, the dynamic behaviour was also investigated. The system showed a favourable performance.

With water as the test liquid, it was demonstrated that a pressure-driven flow system with a calibrated flow sensor can achieve excellent results. In particular, in the context of lab-on-a-chip experiments, such systems offer significant advantages, as they provide immediate feedback in the event of modifications to the chip design or other changes to the measurement setup. This is of paramount importance for medical research and development.

References

[1] N. Azizipour, R. Avazpour, D.H. Rosenzweig, M. Sawan, A. Ajji, Evolution of biochip technology, A review from lab-on-a-chip to organ-on-a-chip, Micromachines (Basel) 11 (6) (2020 Jun 18) 599.

[2] V. Silverio, S. Cardoso, Lab-on-a-chip: systems integration at the microscale, in: E. Chapter (Ed.), Drug Delivery Devices and Therapeutic Systems, Elsevier Science, 2021. ISBN: 978-0-12-819838-4.

[3] M. Engin, A. Demirel, E. Engin, M. Fedakar, Recent developments and trends in biomedical sensors, Measurement 37 (2) (2005) 173–188.

[4] Project website MFMET project: https://mfmet.eu/.

[5] H. Bissig, E. Batista, et al., Primary standards for measuring flow rates from 100 nl/min to 1 ml/min – gravimetric principle, Biomed. Eng. 60 (4) (2015) 301–316.

[6] E. Batista, J. Alves e Sousa, S. Cardoso, V. Silverio, Experimental testing for metrological traceability and accuracy of liquid microflows and microfluidics, Flow Meas. Instrum. 71 (2021).

[7] O. Büker, K. Stolt, RISE test facilities for the measurement of ultra-low flow rates and volumes with a focus on medical applications, Appl. Sci. 12 (16) (2022) 8332, https://doi.org/10.3390/app12168332.

[8] AAMI TIR101:2021, Fluid Delivery Performance Testing for Infusion Pumps, American National Standards Institute (ANSI), Washington, DC, USA, 2021.

Oliver Büker[a],[*], Krister Stolt[a], Elsa Batista[b], Julia Sepulveda[c], Camila Betterelli Giuliano[c], Alan Morin[c], Diogo Nobre[d], Helena Navas[d]

[a] *RISE – Research Institutes of Sweden, Brinellgatan 4, 504 62, Borås, Sweden*

[b] *IPQ – Portuguese Quality Institute, R. António Gião 2, 2825-002, Caparica, Portugal*

[c] *Microfluidics Innovation Center, 172 rue de Charonne, 75011, Paris, France*

[d] *NOVA University Lisbon, Largo da Torre, 2829-516, Caparica, Portugal*

[*] Corresponding author.

E-mail address: oliver.buker@ri.se (O. Büker).

REVISTAS NACIONAIS

MEMÓRIAS
DA
ACADEMIA DAS CIÊNCIAS
DE
LISBOA

CLASSE DE LETRAS

Escrita das unidades de medida e grandezas de medição

Olivier Pellegrino

ACADEMIA DAS CIÊNCIAS
DE LISBOA

LISBOA • 2024

Escrita das unidades de medida e grandezas de medição

Olivier Pellegrino

Já foi! Já foi adotada a revisão do Sistema Internacional de unidades (SI)! De agora para a frente, todas as unidades de base do SI estão definidas por constantes fundamentais e já não a partir de artefactos. Este "agora" foi a conclusão da 26.ª reunião da Conferência Geral dos Pesos e Medidas (CGPM) ocorrida a 16 de novembro de 2018, em Versailles, nos arredores de Paris, França[1]. Essa reunião, que acontece em média de quatro em quatro anos, toma todas as decisões por votação de cada Estado-Membro referentes ao Bureau Internacional dos Pesos e Medidas (BIPM) e à organização da metrologia à escala internacional, nomeadamente sobre o SI. Antes da votação, transmitida em direto e em sessão pública, foram proferidas comunicações orais, entre as quais pelos laureados do prémio Nobel de Física Klaus von Klitzing (Nobel de 1985) e William D. Phillips (Nobel de 1997) que afirmaram que essa adoção da revisão do SI é a maior revolução na ciência da medição desde a revolução francesa!

Todavia, convém notar que essa revisão, que entrou em vigor a 20 de maio de 2019, no Dia Mundial da Metrologia (dia escolhido para celebrar a assinatura da Convenção do Metro, ocorrida a 20 de maio de 1875, que criou o BIPM, a CGPM e o Comité Internacional dos Pesos e Medidas – CIPM) desse ano, é o resultado de vários anos de investigação científica internacional com sistemas experimentais para alcançar valores consensuais das constantes fundamentais: a constante de Planck, h, a carga elementar, e, a constante de Boltzmann, k, e a constante de Avogadro, N_A[2]. Simultaneamente, o Grupo operacional sobre as constantes fundamentais (*Task Group on Fundamental Constants* – TGFC) do Comité sobre os dados em ciência e tecnologia (*Committee on Data for Science and Technology* – CODATA), que ajusta periodicamente os valores recomendados das constantes fundamentais e os fatores de conversão da Física e da Química, tinha sido convidado pela CGPM para determinar os valores consensuais das

constantes fundamentais a partir das realizações experimentais, na condição de ser consistentes com os valores adotadas antes da revisão do SI.

Em 1983, a redefinição da unidade de base do comprimento, o metro, teve por consequência de fixar para um valor exato a velocidade da luz no vazio, c, segundo várias determinações experimentais de grande exatidão. De mesmo modo, a revisão das definições das unidades de base da massa, o kilograma, da corrente elétrica, o ampere, da temperatura termodinâmica, o kelvin, e da quantidade de matéria, a mole, teve por consequência de fixar para valores exatos as constantes h, e, k e N_A, como estabelecidos pelo CODATA, baseados nas realizações experimentais por diferentes laboratórios entre 1988 e 2017, e resumidos no Quadro 1.

Quadro 1: Valores das constantes h, e, k e N_A para a revisão do SI[2].

Constante	Valor
h	6,626 070 15 × 10^{-34} J s
e	1,602 176 634 × 10^{-19} C
k	1,380 649 × 10^{-23} J K^{-1}
N_A	6,022 140 76 × 10^{23} mol^{-1}

A revisão do SI reformula as definições das unidades de base através da estipulação de valores fixados exatamente, i.e., sem incerteza, de constantes fundamentais (também designadas por "constantes definidoras"). Em consequência, foi necessário alterar a diretiva europeia relativa à aproximação das legislações dos Estados-Membros respeitantes às unidades de medida[3], o que obrigou à respetiva transposição na legislação nacional. Ora, desde o texto do primeiro Decreto-Lei, nomeadamente o Decreto-Lei n.º 427/83 de 7 de dezembro[4] que foi o primeiro, a adotar, por Portugal, o SI como sistema de unidades de medida legal, estão incluídas as recomendações para escrita e emprego dos símbolos e designações dos múltiplos e submúltiplos. Assim, o texto do Decreto-Lei n.º 128/2010 de 3 de dezembro[5], o mais recente em vigor antes da transposição da diretiva europeia de 2019, continha regras de escrita e utilização dos símbolos das unidades do SI, pelo que o Decreto-Lei n.º 76/2020 de 25 de setembro[6] adota a revisão do SI para o território nacional também inclui regras de escrita. Tais regras devem corresponder a um compromisso entre convenções adotadas pela

comunidade científica internacional, publicadas em normas e documentos internacionalmente reconhecidos[7,8,9] pelas especificidades nacionais, desde que haja um mínimo de coerência entre e no seio desses dois domínios. Todavia, respeitante à escrita em língua portuguesa, o Acordo Ortográfico da Língua Portuguesa de 1990 (AO90) permite novamente o uso das letras k, w e y, letras frequentemente utilizadas na escrita dos nomes das unidades de medida. Ora, observamos na base Ido AO90, "Do alfabeto e dos nomes próprios estrangeiros e seus derivados", do respetivo Anexo I, esse extrato 2.º) "As letras k, w e y usam-se nos seguintes casos especiais: (…) c) Em siglas, símbolos e mesmo em palavras adotadas como unidades de medida de curso internacional: … kg-kilograma, km-kilometro, kW-kilowatt, yd-jarda (yard); Watt." apresenta uma incoerência interna e com as regras de escrita internacionais da ciência da medição, incoerência que o Decreto-Lei n.º 76/2020 de 25 de setembro entre outros propósitos emenda, como propomos apresentar nesta intervenção.

Unidades de medida – Grandezas de medição

Até ao fim do século XVIII, tornou-se cada vez mais indispensável o uso de padrões de medição, para o progresso do conhecimento científico, com confiança. Com efeito, como garantir a reprodução quantitativa de uma experiência, para o estudo e desenvolvimento sem um valor de referência aceite pelos diferentes intervenientes? Antes do fim do século XVIII, utilizava-se padrões de medição que permitiam efetuar essa reprodução dos fenómenos físicos, cujo ato de quantificação foi traduzida pela famosa expressão de Galileo Galilei, em 1623, segunda a qual "… o universo... está escrito em língua matemática".

Também a existência de padrões de medição, cujo valor variava segundo a região ou até segundo a época do ano, limitava muito a troca de mercadorias e a expansão do comércio. Por exemplo, se no Império romano, existiam 11 unidades de medida de comprimento, os fatores múltiplos e submúltiplos entre eles tinham base binária, terceira ou decimal, sem coerência numérica[10]. É admitido que o Império de Carlos Magno, no século IX, corresponde ao último Estado com uma uniformização dos pesos e medidas na totalidade do território, i.e., desde o poder central e o utilizador final. Durante quase 1000 anos, nenhum Estado conseguiu uma uniformização dos pesos e medidas cujos padrões estavam impostos por senhores locais para pagamento de taxas (independentemente de e em oposição

ao poder central) cujos valores eram sujeitos a variação arbitrária através do tamanho dos padrões locais[11]. "Dois pesos, duas medidas" foi assim a expressão mais frequente nas reclamações nos Estados Gerais em França, convocados em maio de 1789 pelo rei Luís XVI. A 27 de junho de 1789, é criada uma comissão de membros da *Académie des Sciences*, que incluía o físico Charles-Augustin Coulomb, o matemático Pierre-Simon Laplace e o químico Antoine Lavoisier, para refletir e propor a uniformização dos pesos e medidas. A 4 de agosto de 1789, são abolidos os privilégios feudais e proclamada a Declaração dos direitos do homem e do cidadão, a 26 de agosto de 1789 (escrita a 14 de setembro de 1791, por Olympe de Gouges; a Declaração dos Direitos da Mulher e da Cidadã nunca foi aprovada pela Assembleia, tendo as mulheres, na pátria da Declaração dos Direitos do Homem e do Cidadão, o direito de voto apenas 154 anos mais tarde). A 15 de março de 1790, são abolidas as taxas de calibração e de pesagem. A 30 de março de 1791, é apresentado à Assembleia o relatório elaborado, a pedido da *Académie des Sciences*, por Borda, Lagrange, Laplace, Monge e Condorcet sobre a escolha de uma unidade de medida, que define o quarto do meridiano como base do novo sistema de medida, assim como a escala decimal, como única escala de divisão. O nascimento do metro é oficializado pelo Decreto de 1 de agosto de 1793: tem por comprimento a décima-milionésima parte do quarto do meridiano.

Estava a realizar-se a passagem do uso milenário dos pesos e medidas, como milhares de nomes de unidades e fatores de conversão, para unidades de medida universais, em número comparavelmente muito reduzido. A escolha dos Académicos, aceite pela Assembleia, foi então de abandonar o sistema em vigor e substituí-lo por um sistema novo, com nomes novos e segundo uma designação metódica, como tinha sido aplicado pouco antes na elaboração da nomenclatura em Química, em França, por Lavoisier, Guyton de Morveau, Fourcroy e Hassenfratz[12], com os princípios da nomenclatura binomial dos botânicos[13] e sobretudo do filósofo Étienne Bonnot de Condillac[14]. Estes últimos princípios são retomados por Lavoisier no Discurso Preliminar do Tratado Elementar de Química[15] quando afirma que "As palavras devem fazer nascer a ideia e a ideia deve invocar o facto, sendo, deste modo, três etapas de um mesmo processo. E, como são as palavras que conservam as ideias e as transmitem, não se pode aperfeiçoar a linguagem sem aperfeiçoar a ciência, nem a ciência sem aperfeiçoar a linguagem. É que, por mais certos que sejam os factos e mais exatas as ideias que os

fizeram nascer, eles transmitirão apenas impressões falsas se não tivermos expressões exatas para os designar."

Como para a nomenclatura em Química, os novos nomes foram escolhidos com origem nas línguas antigas: seguindo uma nomenclatura binária, os prefixos indicando submúltiplos são de raiz latina (deci-, centi-, mili-, etc.) e os múltiplos são de raizes gregas (deca-, hecto-, kilo-, etc.). Os radicais correspondem às diferentes grandezas: metro (do grego *métron*, por "medida"), para medições lineares, litro (do grego *litra*, por "medida líquida"), para medições de capacidades, e grama (do grego *gramma*, por "unidade de peso" nos Romanos) para medições de massas. São assim obtidas novas designações sistemáticas, universais e únicas em muito menos número para únicas realidades. Isso facilita imenso as trocas comerciais, técnicas e científicas. No entanto, podemos lamentar a perda do significado de centenas de palavras.

O Decreto de 7 de abril de 1795 estabelece o sistema métrico decimal. A partir da unidade de medida de base, o metro, podem ser deduzidas todas as outras unidades e todas as outras unidades de medida são proibidas. A Lei de 10 de dezembro de 1799 consagra os padrões definitivos do metro, construídos em platina, determinado a partir das medições do meridiano por Méchain e Delambre, entre Dunquerque e Barcelona, e do metro cúbico, determinado a partir de um cubo de dez centímetros de água destilada ao valor máxima da sua densidade, i.e., a 4 °C. Estão depositados nos Arquivos nacionais. O Decreto de 2 de novembro de 1801 torna obrigatório o sistema métrico em França… até ao Decreto imperial de 12 de fevereiro de 1812 que autoriza a não utilização! Perante a confusão criada nas transações comerciais, o Parlamento, pela Lei de 4 de julho de 1837, volta a tornar obrigatório em França o uso do sistema métrico decimal… a partir de 1 de janeiro de 1840. Como se vê, mesmo para o país que o criou, a adoção do sistema métrico decimal não foi fácil! Na mesma altura, a adoção é efetuada, em 1803, pela República Helvética, em 1816 pelos Países Baixos e, em 1836, pela Grécia.

Em Portugal, existia uma pletora de nomes de unidades de medida e fatores de conversão, como no resto da Península Ibérica, tendo sido ainda introduzidas unidades de medida árabes, complicando as transações comerciais, apesar dos sucessivos esforços acompanhando a consolidação do Estado português, como acontecia nos congéneres europeus. Por exemplo, na reforma manuelina[10], as 6

unidades de medida para o "peso" (presente no Museu da Metrologia, no Instituto Português da Qualidade – IPQ, o marco-padrão de D. Manuel I contém 16 peças desde 1 escrúpulo até 2 arrobas e tem uma massa de 1 quintal, ou seja 58,754 kg, igual a 4 arrobas, iguais a 100 arráteis, iguais a 200 marcos) passaram a 8 unidades de medida com fatores multiplicativos de 2, 64 e 256, e submúltiplos iguais a 1/8, 1/64, 1/192, e 1/4608, tendo os nomes das unidades mudado de significado na nova nomenclatura. Para um conhecimento sério da história da Metrologia em Portugal, recomendamos a leitura da obra detalhada e ricamente ilustrada, baseada em parte no acervo do Museu da Metrologia do IPQ por António Cruz, primeiro diretor do Departamento de Metrologia do IPQ, "Pesos e Medidas em Portugal"[10].

Passada a primeira metade do século XIX, politicamente agitada, foi possível a adoção do sistema métrico decimal pela rainha Dona Maria II através da Lei de 13 de dezembro de 1852, sendo o uso obrigatório a partir de 20 de junho de 1859. É notável observar, na obra de disseminação dessa Lei, "Novo Systema legal de medidas decretado em 12 de dezembro de 1852", extraído do "Compendio do Novo Systema Métrico Decimal", de Joaquim Henriques Fradesso da Silveira, Inspetor-Geral dos Pesos e Medidas do Reino, publicado pela Imprensa Nacional, em 1858[16], a ortografia utilizada para os nomes dos prefixos submúltiplos e múltiplos, na Figura 1, nomeadamente o kilometro.

NOMES SYSTEMATICOS	VALORES
Myriametro..	10000 metros
Kilometro...	1000 metros
Hectometro..	100 metros
Decametro...	10 metros
Metro......	1 metro, unidade fundamental
Decimetro...	0,1
Centimetro..	0,01
Millimetro...	0,001

Figura 1: Extrato do Novo Systema legal de medidas decretado em 12 de dezembro de 1852[16], apresentando os nomes sistemáticos das unidades de medida de comprimento.

É notável que essa ortografia se manteve durante 80 anos, até a reforma ortográfica de 1910, que eliminou as letras k, w e y do alfabeto da língua

portuguesa, deixando a correspondência entre símbolo e grafia dos nomes das unidades de medida.

Na evolução do sistema métrico decimal, tal como da física, da astronomia e da matemática, destaca-se a contribuição do Carl Friedrich Gauss, que promoveu ativamente a aplicação do sistema métrico, associado ao segundo. O primeiro a efetuar medições absolutas do campo magnético terrestre, utilizando um sistema decimal baseado nas unidades mecânicas do milímetro, do grama e do segundo, associadas às grandezas do comprimento, da massa e do tempo. Com a colaboração do físico Wilhelm Eduard Weber, foram continuadas essas medições, incluindo outros fenómenos elétricos. No seio da *British Association for the Advancement of Science* (BAAS), os matemáticos e físicos James Clerk Maxwell e William Thomson, mais tarde conhecido como 1.º Barão, ou Lorde, Kelvin, aperfeiçoaram essas medições nos domínios da eletricidade e do magnetismo. Em 1874, a BAAS criou o sistema CGS, baseado nas unidades mecânicas do centímetro, do grama e do segundo. Em 1881, são inseridos o ohm, o volt, o coulomb, o farad e respetivos múltiplos e submúltiplos decimais, e, em 1889, o joule, o watt e o antepassado do henry, o quadrante.

No meio do século XIX, manifestou-se a necessidade de um sistema decimal de pesos e medidas quando, na primeira Exposição Universal, em Londres, em 1851, e nas sucessivas, Paris, em 1855, Londres, em 1862 e Paris, em 1867, as quantidades de produtos apresentados eram referenciadas a padrões sem relação mútua. Simultaneamente, um sistema único de pesos e medidas foi recomendado pela Academia das Ciências de Paris, a Academia das Ciências de São Petersburgo, o *Bureau* das Longitudes de Paris e a Comissão Inglesa dos Padrões e a segunda conferência geral da Associação internacional de geodesia recomendava a adoção do sistema métrico. Em 1867, foi então constituído o "Comité dos Pesos e Medidas e das Moedas" e, em 1870, é criada uma Comissão do Metro.

Finalmente, a 20 de maio de 1875, é assinada a Convenção do Metro entre os representantes dos 17 países seguintes: Alemanha, Argentina, Áustria-Hungria, Bélgica, Brasil, Dinamarca, Espanha, Estados Unidos da América, França, Itália, Perú, Portugal, Rússia, Suécia e Noruega, Suíça, Turquia e Venezuela. Para facilitar as trocas e comparações de medições entre Estados e realizar um metro internacional, é criado o BIPM, sob a autoridade da CGPM e sob a supervisão do Comité Internacional dos Pesos e Medidas (CIPM), constituindo uma estrutura

permanente que permite aos Estados-Membros terem uma ação comum sobre todas os assuntos respeitantes às unidades de medida.

Na primeira reunião da CGPM, ocorrida em setembro de 1889, foi decidida a elaboração e conservação de novos protótipos internacionais do metro e do kilograma e comparar aos padrões nacionais distribuídos aos Estados-Membros. Em Portugal, foi necessário atualizar a legislação nacional no sentido de, através da Lei de 19 de abril de 1911, adotar os protótipos com número 10, que lhe tinham sido sorteados. O sistema de unidades de medida consagrado pela 1.ª CGPM é então o sistema MKS, por metro, kilograma e segundo (dos astrónomos). Em Portugal, os termos kilometro e os prefixos múltiplos e submúltiplos encontram-se institucionalizados através da publicação no Diário do Governo a 25 de abril de 1876.

Em 1901, o físico italiano Giovanni Giorgi demonstra a possibilidade de juntar as unidades mecânicas do sistema MKS às unidades elétricas. Após pareceres da União internacional de Física Pura e Aplicada (IUPAP) e da Comissão Eletrotécnica Internacional (IEC), o sistema baseado no sistema MKS e unidade da corrente elétrica, o ampere, o sistema MKSA é adotado, em 1946, pelo CIPM.

Em 1927, a 7.ª reunião da CGPM aprova a escala internacional de temperatura, tendo como unidade o grau centígrado, que é substituído pelo grau Celsius pela 9.ª CGPM que define a unidade de intensidade luminosa, a Candela, reunida em 1948. Em 1954, a 10.ª CGPM aprova as unidades de base da corrente elétrica, da temperatura termodinâmica e da intensidade luminosa: o ampere, o grau Kelvin (substituído pelo kelvin, na 13.ª CGPM, em 1968) e a candela, respetivamente.

A 11.ª CGPM, reunida em 1960, muda o nome do sistema MKSA para Sistema Internacional de Unidades, de símbolo SI. Uma sétima unidade de medida de base do SI foi aprovada pela 14.ª CGPM, em 1971, a mole, unidade da quantidade de matéria.

A 24.ª CGPM adota, em 2011, os princípios de uma nova definição do SI baseada em sete constantes da natureza e, como já referido, a 26.ª CGPM adota a nova definição do SI baseada nas sete constantes "definidoras", em 2018.

Devido à sua importância para as transações comerciais envolvidas, para as atividades económicas, para as atividades de saúdes e todas de carácter técnico-científica, os Estados-Membros dos diferentes espaços económicos em cada continente adotaram as evoluções efetuadas no BIPM sobre as definições e utilizações

das unidades de medida. De destacar a importância das convenções decididas para a escrita e símbolos associados que, para facilitar as comunicações intra- e internacionais tendem a ser aproximadas o mais possível às escalas nacionais. Na realidade, como pode ser constatado dos parágrafos anteriores, desde a criação e a oficialização de um sistema internacional de unidades de medida, poucas mudanças foram efetuadas nas definições e documentos publicados pelo BIPM, o que não provocou muitas mudanças nos textos legislativos europeus, o que, por sua vez, originou poucas mudanças na legislação nacional.

No seguimento da criação do espaço económico europeu e da existência do SI com 7 unidades de base, foi publicada a Directiva n.º 71/354/CEE, do Conselho, de 18 de outubro de 1971 (sem versão em língua portuguesa) destinada a efetuar a aproximação das legislações dos Estados-Membros respeitante às unidades de medida. Foi revogada e substituída pela Diretivas 80/181/CEE, do Conselho, de 20 de dezembro de 1979, por sua vez, alterada pelas diretivas 85/1/CEE, do Conselho, de 18 de dezembro de 1984, 89/617/CEE, do Conselho, de 27 de novembro de 1989 e 1999/103/CE, do Parlamento Europeu e do Conselho, de 24 de janeiro de 2000. O anexo técnico da Diretiva 80/181/CEE do Conselho foi alterado devido às sucessivas atualizações do SI publicadas pelo BIPM, nomeadamente através das edições correspondentes da *Brochure sur le SI* de 1998[17] e de 2006[18], levando às publicações da Diretiva 2009/3/CE do Parlamento Europeu e do Conselho, de 11 de março de 2009 e da Diretiva (UE) 2019/1258 da Comissão de 23 de julho, que é a mais recente diretiva europeia aprovada sobre as unidades de medida.

A aproximação das legislações dos Estados-Membros respeitantes às unidades de medida concretiza-se pela transposição na legislação nacional das diretivas europeias: as apresentadas no parágrafo anterior foram transpostas na legislação portuguesa pelo Decreto-lei n.º 238/94, de 19 de setembro, mais especificamente as sucessivas alterações à Diretiva 80/181/CEE de 20 de dezembro de 1979 desde a Diretiva 89/617/CEE, do Conselho, de 27 de novembro de 1989, uma vez que Portugal tinha entrado na Comunidade Económica Europeia (CEE), a 1 de janeiro de 1986. O Decreto-Lei n.º 427/83 de 7 de dezembro que corresponde, como já referido, à adoção por Portugal do SI como sistema de unidades de medida legal, alterado pelo Decreto-Lei n.º 320/84, de 1 de outubro, deve provavelmente ter facilitado a entrada de Portugal na CEE. Finalmente, a Diretiva

2009/3/CE do Parlamento Europeu e do Conselho de 11 de março de 2009 foi transposta na legislação portuguesa pelo Decreto-lei n.º 128/2010 de 3 de dezembro e o Decreto-Lei n.º 76/2020 de 25 de setembro corresponde à transposição da Diretiva (UE) 2019/1258 da Comissão de 23 de julho de 2019.

Fechamos essa parte com duas notas. Em primeiro lugar, no seguimento do artigo de referência de Jan de Boer "On the history of quantity calculus and the international system"[19], lembramos que a introdução do conceito de grandeza física é devida ao Maxwell no "Treatise on Electricity and Magnetism" escrito em 1873[20], em que insistiu sobre a distinção entre valor numérico e grandeza física. Em 1887, baseado neste conceito, Hermann von Helmholtz iniciou a axiomatização da teoria da medição[21], que continua, nos dias de hoje, com interessantes desenvolvimentos e generalizações, como evidenciaam os trabalhos de Luca Mari[22], por exemplo. Todavia, apesar do trabalho do matemático inglês Alfred Lodge em 1888[23], foram necessários cinquenta anos para que a álgebra das grandezas formalize a ideia do Maxwell através da expressão $Q = \{Q\} . [Q]$, em que Q é o símbolo de grandeza, $\{Q\}$, o símbolo do valor numérico e $[Q]$ o símbolo da unidade de medida, pela publicação do Julius Wallot, em 1926[24], começando a sua sistemática utilização em ciência.

Figura 2: Vista do Laboratório Nacional de Metrologia do Instituto Português da Qualidade

Uma segunda nota é dedicada à organização da metrologia mundial, na continuidade da assinatura da Convenção do Metro, hoje com 63 Estados-Membros e 37 Estados e entidades económicas associadas. Lembremos que a Convenção do Metro é uma organização intergovernamental cujos governos atuam em comum nos assuntos ligados à ciência das medições e aos padrões de medição. Trata de demonstrar a equivalência internacional dos padrões de medição nacionais e dos certificados de calibração emitidos pelas instituições nacionais de metrologia ou pelos instituições designados para criar, manter e desenvolver os padrões de medição nacionais. Trata de efetuar a troca de conhecimentos, informações e experiências à escala internacional. Finalmente, contribui à tomada de decisão, à escala internacional, sobre os avanços em metrologia. À escala de um continente, as instituições nacionais de metrologia associam-se em organizações regionais de metrologia (*Regional Metrology Organization* – MRO) que participam em ou efetuam comparações entre instituições nacionais de metrologia dentro ou entre MRO. Na Europa, o RMO é a Associação Europeia dos Laboratórios Nacionais de Metrologia (EURAMET) e, em Portugal, o IPQ tem a função de Instituição Nacional de Metrologia.

O IPQ detém os padrões nacionais da aceleração e vibrações, cumprimento, tempo e frequência, grandezas elétricas e magnéticas, fotometria e radiometria, massa, quantidade de pH, viscosidade e massa volúmica de líquidos, pressão, força, temperatura e volume[25]. Três institutos designados, o Laboratório de Química e Poluição do Meio Marinho do Instituto Hidrográfico, para padrões de Química Inorgânica e para os parâmetros Água do mar (sílica) e Sedimentos (mercúrio), o Laboratório de Metrologia das Radiações Ionizantes do Instituto Superior Técnico, para padrões das Radiações Ionizantes e a Unidade de Hidráulica Metrológica do Laboratório Nacional de Energia Civil, para padrões de Grande Caudal de Líquidos, completam a organização dos padrões nacionais em Portugal[26].

Finalmente, entre outros documentos científicos, monografias, ou ainda, como já foi referido, uma *Brochure sur le SI*, que reúne as resoluções e recomendações das CGPM e das CIPM[27], o BIPM edita Guias em Metrologia: o *Guide to the Expression of Uncertainty in Measurement* (conhecido como o "GUM") e o Vocabulário Internacional de Metrologia (conhecido como o VIM). Estes Guias são produzidos por dois Grupos de Trabalhos do *Joint Committee for Guides in*

Metrology (JCGM), compostos de representantes de organizações internacionais ligadas à metrologia. Trata-se do BIPM, da IEC, da Federação Internacional de Química Clínica e Medicina Laboratorial (IFCC), da ISO, da União Internacional de Química Pura e Aplicada (IUPAC), da IUPAP, da Organização Internacional de Metrologia Legal (OIML) e da Cooperação Internacional de Acreditação de Laboratórios (ILAC). A primeira edição do VIM foi publicada em 1984, resultado do trabalho do BIPM, a OIML, a IEC e a ISO. Foi traduzido, em 1985, para a língua portuguesa. Em 1993, uma 2.ª edição resultou da colaboração também da IFCC, da IUPAC e da IUPAP. Foi traduzido, em 1994, para a língua portuguesa. Para uma terceira edição do VIM, juntou-se a ILAC, mas a versão de 2007 necessitou que uma versão corrigida seja publicada em 2012, ano da publicação da versão luso-brasileira[28], fruto da colaboração entre o IPQ e a Instituição Nacional de Metrologia do Brasil, o Inmetro, ao abrigo do Acordo Ortográfico de 1990. Está atualmente em estudo o resultado da consulta para a 4.ª edição do VIM para uma nova consulta. A adoção pela 26.ª CGPM da revisão do SI teve como consequência a publicação da 9.ª edição da *Brochure sur le SI*[8], já traduzida em conjunto pelo IPQ e pelo Inmetro[29]. As edições em língua portuguesa produzidas pelos metrologistas do VIM e da Brochura sobre o SI foram baseadas nos paradigmas e regras da língua portuguesa para ser percebidas e utilizadas pelos falantes lusófonos e serviram de base às elaborações dos textos legais. Por ser documentos de especialidade metrologia, essas edições deviam e devem também seguir regras e paradigmas definidos e convencionadas internacionalmente. Tal é a abordagem que nos propomos apresentar e explicar a seguir.

Escrita do SI na língua portuguesa

Apresentemos então o paradigma e as regras que devem ser seguidos para a escrita da língua portuguesa e das unidades e grandezas de medição, em particular. Se bem nos lembramos[16], a Lei de 13 de dezembro de 1852 introduziu o sistema métrico decimal em Portugal através do "kilogramma" como "medida de peso", do "kilometro", igual a 1000 metros e do "kilo" como prefixo do múltiplo 1000. Ora, em 1911, acontece uma Reforma Ortográfica que faz sair do alfabeto as letras k, w, e y, como publicado no Diário do Governo de 12 de setembro de 1911. Todavia, essa reforma mantém a grafia "kilo" como prefixo multiplicativo, conservando a grafia "liquolgrama", mas admite "quilograma". E, após

80 anos das grafias "kilo", "kilometro" e "kilograma", no seguimento de um acordo entre a Academia das Ciências de Lisboa (ACL) e a Academia Brasileira das Letras, a letra "k" apenas é autorizada como símbolo de prefixo multiplicativo de unidade! Em 1945, um novo acordo ortográfico é ratificado entre Portugal e o Brasil que, através do Decreto n.º 35 228 de 8 de dezembro de 1945, mantém as opções da Reforma de 1911, sem ter em conta a evolução das organizações da Ciência, Economia e Comércio internacionais.

Figura 3: Capa da tradução luso-brasileira da 9.ª edição da Brochura sobre o SI[29].

A 16 de dezembro de 1990, é assinado o AO90 entre Angola, o Brasil, Cabo Verde, Guiné-Bissau, Moçambique, Portugal e São Tomé e Príncipe[30]. Segundo este acordo, as letras k, w e y estão reintroduzidas no alfabeto da língua portuguesa. Todavia, as grafias "kilograma" e "kilometro" mantém-se… apesar da grafia "kilowatt"… como já mencionado acima, com a alínea 2.ª da Base I do Anexo I. Aliás, a 1.ª edição do Dicionário da Língua Portuguesa Contemporânea,

da autoria da ACL[31] contém não somente as grafias kiloampere, kilobit, kilobyte, kilocoulomb, kilohertz, kilojoule, kiloparsec, kilovolt, kilovolt-ampere, kilowatt e kilowatt-hora… mas também quilocaloria, kilograma, quilojoule, quilojoule, quilolitro, kilometro, quilotonelada, quilowatt e quilowatt-hora!

Do lado do paradigma da escrita científica expressa no VIM luso-brasileiro de 2012[28], mas também da Brochura sobre o SI, na versão luso-brasileira[29], os nomes tendem seguir as opções adotadas às escalas internacionais, pelo menos das línguas oficiais utilizadas nos textos do BIPM e das normas da série ISO/IEC 80000, i.e., a língua francesa e a língua inglesa. Tal paradigma foi também aplicado na mais recente transposição6 na legislação nacional da diretiva europeia[3] que aprovou a revisão do SI. Vemos então algumas situações básicas. Para as pessoas interessadas em mais regras de escrita de apresentação dos resultados de medição, recomendamos a consulta de "Uma introdução às Regras de escrita das Unidades de medida e Grandezas segundo o SI"[32].

Os símbolos das unidades são sempre escritos em fonte romana (i.e., não itálica) e, por serem considerados entidades matemáticas, não levam a marca do plural. Os símbolos dos produtos são expressos com um espaço entre os símbolos das unidades ou separados com um ponto a meia-altura entre dois espaços.

Assim, por exemplo, o produto de um joule (de símbolo: 1 J) por dois segundos (símbolo: 2 s), que é o valor da grandeza física ação tem como valor dois joules segundos (também aceite a grafia: dois joules-segundos) e como símbolo: 2 J s ou 2 J . s.

Deste exemplo simples, poderá deduzir-se que:

– existe sempre um espaço entre o valor numérico e o símbolo da unidade;

– os nomes das unidades são nomes comuns, portanto variam em número (levam a marca do plural) e não começam por uma maiúscula;

– os nomes das unidades constituídas do produto de duas unidades são separados por um espaço (ou por um hífen) e levam cada um a marca do plural.

Os múltiplos e submúltiplos de unidades também são unidades, pelo que se aplicam as mesmas convenções que acima. Para o produto de duas unidades múltiplos ou submúltiplos da mesma unidade, apresenta-se um único fator multiplicativo.

Assim, $1 \text{ cm}^3 = (10^{-2} \text{ m})^3 = 10^{-6} \text{ m}^3$; $1 \text{ V/cm} = (1 \text{ V})/(10^{-2} \text{ m}) = 10^2 \text{ V/m} = 1 \text{ hV/m}$ e escreve-se: 10 mm e não 1 c mm

A junção do símbolo de um prefixo ao símbolo de uma unidade forma uma nova unidade com um novo símbolo, sem separação entre os símbolos do prefixo

e o da unidade.

Assim, a centésima parte de um metro escreve-se 1 cm e não 1 c m.

O nome dessa unidade escreve-se "centímetro" e não "centi metro" ou "centi-metro".

Aliás, de acordo com o que foi escrito acima, dois símbolos separados por um espaço têm por significado o símbolo de duas unidades. O símbolo de uma única unidade é composto de apenas um prefixo não separado da unidade principal.

Assim, a unidade um miligrama, constituída do prefixo m, para o submúltiplo milésima parte e da unidade principal de símbolo g, por grama, tem por símbolo mg. É diferente da unidade que é o produto da unidade metro, de símbolo m, e da unidade grama, de símbolo g, que tem por símbolo m g.

No Quadro 2, apresentamos os nomes e símbolos dos prefixos múltiplos e submúltiplos publicados no Decreto-Lei 76/2020 de 25 de setembro, ou seja, agora legalmente em vigor.

Quadro 2: Nomes e símbolos dos prefixos de fatores múltiplos e submúltiplos decimais das unidades SI[6]:

Fator	Nome	Símbolo	Fator	Nome	Símbolo
10^1	deca	da	10^{-1}	deci	d
10^2	hecto	h	10^{-2}	centi	c
10^3	kilo	k	10^{-3}	mili	m
10^6	mega	M	10^{-6}	micro	m
10^9	giga	G	10^{-9}	nano	n
10^{12}	tera	T	10^{-12}	pico	p
10^{15}	peta	P	10^{-15}	femto	f
10^{18}	exa	E	10^{-18}	atto	a
10^{21}	zetta	Z	10^{-21}	zepto	z
10^{24}	yotta	Y	10^{-24}	yocto	y

Podemos constatar que, por aplicação sistemática do AO90, que reintroduz as letras k e y no alfabeto da língua portuguesa, as grafias dos fatores 10^3, 10^{24} e 10^{-24} é agora kilo, yotta e yocto. Para o primeiro, trata-se da reposição de uma situação parada durante 110 anos. Agora, qualquer seja a unidade, utiliza-se a mesma grafia. Por outro lado, facilita-se a utilização por ser a mesma primeira letra que a que serve de símbolo, como para os outros prefixos.

Todavia, lembremos que os prefixos múltiplos e submúltiplos decimais das unidades SI também podem ser utilizados com unidades não SI mas aceites na utilização com o SI, desde que decimais. Por exemplo, não podem ser utilizados nem com as unidades de tempo (dia, hora e minuto), nem com as unidades de ângulo plano e de fase (segundo, minuto e grau).

Para expressar potências de 2, em vez dos prefixos decimais, devem ser utilizados os prefixos constando do Quadro 3.

Quadro 3: Nomes e símbolos dos prefixos múltiplos binários[6].

Fator	Nome	Símbolo
2^{10}	kibi	Ki
2^{20}	mebi	Mi
2^{30}	gibi	Gi
2^{40}	tebi	Ti
2^{50}	pebi	Pi
2^{60}	exbi	Ei
2^{70}	zebi	Zi
2^{80}	yobi	Yi

Assim, uma capacidade de 1024 bits é igual a 1 kibibit (símbolo: 1 Kibit) e não 1 kilobit (símbolo: 1 kbit), que é igual a 1000 bits.

No paradigma de escrita científica dos nomes das unidades de medida por extenso, como aplicado no Decreto-Lei n.º 76/2020 de 25 de setembro e traduções luso-brasileiras do VIM 2012[28] e da Brochura sobre o SI[29], seguindo a lógica de formação dos símbolos das unidades a partir dos símbolos das componentes (prefixo e unidade principal), efetua-se a junção sem espaço, nem hífen, sem duplicação de letra das grafias, ou colocação de acento. Assim:

– 10 ms escreve-se dez milisegundos e não dez milissegundos;

–10 mm escreve-se dez micrometros e não dez micrómetros, para diferenciar a unidade de medida do instrumento de medição.

Finalmente, para as escritas respeitantes às grandezas, os símbolos das grandezas são sempre escritos em fonte itálica e, por ser considerados entidades matemáticas, não levam a marca do plural.

Como vimos acima, o valor de uma grandeza, de símbolo Q, é o produto de um valor numérico, de símbolo $\{Q\}$, por uma unidade de medida, de símbolo $[Q]$ segundo a expressão:

$$Q = \{Q\} \cdot [Q].$$

Por exemplo, o valor do volume, V, de dez metros de comprimento, c, numa secção de um metro quadrado, s é igual a:

$$V = c \times s = 10 \text{ m} \times 1 \text{ m}^2 = (10 \text{ m})(1 \text{ m}^2) = 10 \text{ m}^3$$

Como para os nomes das unidades de medida, os nomes das grandezas são palavras comuns, começam por uma minúscula e variam em números.

Conclusão

Perante a existência de dois paradigmas ou convenções para a escrita dos resultados de medição em língua portuguesa, um linguístico, produzido e disseminado pelo Instituto de Lexicologia e Lexicografia da Língua Portuguesa, da ACL, pelo Instituto de Linguística Teórica e Computacional, pelo Instituto Internacional de Língua Portuguesa, e por Centros de investigação em Linguística e Terminologia Universitários e um outro baseado em convenções internacionais de comunicação científica, produzido e disseminado por normas internacionais, um compromisso tem de ser encontrado. Os textos regulamentares legais, a formação dos cidadãos e futuros cidadãos através do ensino precisam de coerência e clareza dos meios para comunicações e partilhas de informação inequívocas.

Com a implementação do sistema métrico decimal, perderam-se muitos termos e expressões linguísticas em todos os países. No entanto, novos termos e uma nova lógica sistemática permitiram aumentar a eficácia e melhorar um progresso da sociedade, nomeadamente através do seu conhecimento quantitativo. Essa terminologia, com mais de duzentos anos, mas ainda nova na escala da idade da humanidade, tem também enriquecido as culturas nacionais e, tal como o próprio SI, está em constante evolução, na via do progresso e na melhoria contínua.

Referências

[1] https://www.bipm.org/fr/committees/cg/cgpm/26-2018, consultado a 2022-06-11.

[2] Newell D B, Cabiati F, Fischer J, Fujii K, Karshenboim S G, Margolis H S, de Mirandés E, Mohr P J, Nez F, Pachucki K, Quinn T J, Taylor B N, Wang M, Wood B M and Zhang Z, Metrologia 55, L13, 2018.

[3] Diretiva (UE) 2019/1258 da Comissão de 23 de julho.

[4] Decreto-Lei n.o 427/83 de 7 de dezembro.

[5] Decreto-Lei n.o 128/2010 de 3 de dezembro.

[6] Decreto-Lei n.° 76/2020 de 25 de setembro.

[7] ISO 80000-1:2009 Quantities and units - Part 1: General.

[8] Le système international d'unités (SI), 9e édition, Bureau international des poids et mesures, 2019, https://www.bipm.org/en/publications/si-brochure/, consultado a 2022-06-11.

[9] Thompson, A., Taylor, B., N., *Guide for the Use of the International System of Units (SI)*, Natl. Inst. Stand. Technol. Spec. Publ. 811, 2008 Ed., (March 2008; 2nd printing November 2008).

[10] Cruz, A, *Pesos e medidas em Portugal.*, Instituto Português da Qualidade, Caparica, 2007.

[11] Guedj, D., *Le mètre du monde*, Le Seuil, Paris, 2000.

[12] Laszlo, P., *A palavra das coisas ou a linguagem da química*, trad. Gonçalves, R. e Simões, A., Gradiva, Lisboa, 1995.

[13] Bensaude-Vincent ,B., *Lavoisier*, Flammarion, Paris, 1993.

[14] Carneiro, A., *Química 102*, 25, 2006.

[15] Lavoisier, A., L., Discurso Preliminar do Tratado Elementar de Química em Fontes da Costa P, *Manifesto para uma Nova Química*, Palavrão, Caldas da Rainha, 2011.

[16] Novo Systema legal de medidas decretado em 12 de dezembro de 1852, Lisboa, Imprensa Nacional, 1858, extraído de Joaquim Henriques Fradesso da Silveira *Compendio do Novo Systema Métrico Decimal*, Lisboa, Imprensa Nacional, Inspetor-Geral dos Pesos e Medidas do Reino, 1856.

[17] *Le système international d'unités (SI)*, 7e édition, Bureau international des poids et mesures, 1998, https://www.bipm.org/en/publications/si-brochure/, consultado a 2022-06-11.

[18] *Le système international d'unités (SI)*, 8e édition, Bureau international des poids et mesures, 2006, https://www.bipm.org/en/publications/si-brochure/, consultado a 2022-06-11.

[19] de Boer, J., *Metrologia,* 32, 405, 1994/95.

[20] Maxwell, J. C., *Treatise on Electricity and Magnetism*, Oxford, Oxford University Press, 1873.

[21] Helmholtz, H., Zahlen und Messen, erkenntnistheoretisch betrachtet, Leipzig, Wiss Abh. III, 356, 1887.

[22] Mari L, Metrologia 54, 784, 2017

[23] Lodge A, Nature 30, 283, 1888

[24] Wallot, J., Dimensionen, Einheiten, Massysteme Handbuch der Physik II, Kap 1, Berlin Springer, 1926.

[25] https://www.ipq.pt/metrologia/, consultado a 2024-09-30.

[26] https://www.ipq.pt/metrologia/institutos-designados/, consultado a 2024-09-30.

[27] https://www.bipm.org/en/publications, consultado a 2022-06-11.

[28] https://storagewebsiteipq.blob.core.windows.net/website/VIM-Vocabula%CC%81rio--Internacional-de-Metrologia_IPQ_INMETRO_2012.pdf, consultado a 2024-09-30.

[29] https://storagewebsiteipq.blob.core.windows.net/website/Traducao_luso_brasileira_2021_SI.pdf, consultado a 2024-09-30.

[30] Decreto do Presidente da República n.o 43/91 de 23 de agosto.

[31] *Dicionário da Língua Portuguesa Contemporânea*, Academia das Ciências de Lisboa, Verbo, 2001.

[32] Pellegrino, O. & Gentil, S., Gazeta de Física, 42, fasc. 4/5, 33, 2020.

A Route to Absolute Salinity from SI Traceable Speed of Sound Measurement Results via Density and Refractive Index Measurements

João André
jf.andre@campus.unl.pt
NOVA School of Science and Technology, Universidade NOVA de Lisboa

Andreia Furtado
afurtado@ipq.pt
Instituto Português da Qualidade, Caparica, Portugal

Sara Moura
smoura@ipq.pt
Instituto Português da Qualidade, Caparica, Portugal

Raquel Quendera
rquendera@ipq.pt
Instituto Português da Qualidade, Caparica, Portugal

Olivier Pellegrino
opellegrino@ipq.pt
Instituto Português da Qualidade, Caparica, Portugal

Helena Navas
hvgn@fct.unl.pt ,
NOVA School of Science and Technology, Universidade NOVA de Lisboa

Abstract:
Speed of sound measurements have previously been used to derive seawater salinity and density over limited ranges where conductivity measurements have not been reliable. It has been conventional for several decades to derive the salinity of the seawater from measurements of conductivity. This study focuses on the validation of a new density and speed of sound measurement system, calibrated with various reference materials, exhibited negligible errors in the intervals [1255, 1484] m s^{-1} (maximum deviation of 0.2 %) and [1490, 1530] m s^{-1}, errors from 0.02 % to 0.42 % at 20 ºC. The study enabled to confirm the metrological compatibility of absolute salinity values obtained by refractometry and densimetry measurements in the [5, 40] g kg^{-1} absolute salinity interval, for seawater-like samples.

Keywords: Density, Refractive index, Salinity, Speed of sound

1. Introduction

The mass of dissolved salts found in seawater, brackish water, brine, or other saline solution, divided by the mass of the solution, defines salinity, S, usually expressed in SI units by grams per kilogram (symbol: g kg^{-1}), or expressed without any explicit measurement unit. Salinity values range from below a few g kg^{-1}, for rivers and lakes, to 35 g kg^{-1}, for seawater, 200 g kg^{-1} for the Dead Sea up to brine salinity values as high as around 260 g kg^{-1} (Furtado *et al.*, 2022).

It is important to note that there are two primary types of salinity that can be defined: absolute salinity (S_A) and practical salinity (S). The former represents the total amount of present dissolved salts in the solution, and the latter is calculated solely from conductive components. For oceanographic applications, S_A offers distinct advantages over S (Furtado *et al., 2022*).

1.1 Determination of salinity in aqueous solutions

Several studies have been performed by Furtado *et al.* (2010 and 2013) and Pellegrino *et al.* (2011a and 2011b) to investigate the metrological compatibility of the mass fraction results of some compounds, namely sodium chloride in aqueous solutions obtained by two different measuring techniques: refractometry and densimetry.

By definition, metrological compatibility is a property of a set of measurement results for a specified measurand, such that the absolute value of the difference of any pair of measured quantity values from two different measurement results is smaller than some chosen multiple of the standard measurement uncertainty of that difference. Indeed, the assignment of metrological compatibility to the measurement results, as defined in the International Vocabulary of Metrology, VIM (JCGM 200:2012), enables to decide whether the measurement results refer to the same measurand, when obtained by different measuring instruments, which would then be commutable.

In those studies, two measuring instruments were used: one digital refractometer and one oscillation-type density meter. In a more recent study, Furtado *et al.* (2022) evidenced a metrological compatibility for absolute salinity with a set of sodium chloride aqueous solutions in the [35; 215] g kg^{-1} interval. It was demonstrated that, for all those aqueous solutions or standard seawater sample (OSIL and ERM), the salinity uncertainties are very similar, even though, for low salinity values, measurement dispersion was greater. This metrological compatibility study was extended for the [5; 40] g kg^{-1} absolute salinity interval from density and refractive index measurement results.

In the present study, two density meters were used, where the sample is introduced into a borosilicate glass U-shaped tube, that is excited to oscillate at its characteristic frequency, which changes with temperature and density. The density, ρ, is calculated from the quotient of the U-tube oscillation period by a reference oscillation period according to:

$$\rho = A \cdot \tau^2 \cdot f_1 - B \cdot f_2 \tag{1}$$

where A and B are instrument specific coefficients, which are physically meaningful parameters of the oscillator determined by at least 2 calibration fluids, τ, the U-tube oscillation period divided by the oscillation period of the reference oscillator, and f_1, f_2 are the correction factors for temperature, viscosity, and nonlinearity.

The difference between the two density meter models is that the more recent provides deeper insights into the sample characteristics, a better viscosity correction, and better repeatability density measurement results, thanks to the "Pulsed Excitation Method".

1.2 Speed of sound in seawater

Speed of sound values in seawater samples were found to be deduced from salinity, temperature, and pressure values according to equations (Coppens, 1981; Chen & Millero, 1977) whose validity covers the salinity range of the samples under the present study. Therefore, from salinity reference materials, it is possible to validate speed of sound measurement results.

The set of Coppens' equations is given by the following (Coppens, 1981):

$$c(D, S, t) = c(0, S, t) + (16.23 + 0.253t)D + (0.213 - 0,1t)D^2 + (0.016 + 0.0002(S - 35))(S - 35)tD \tag{2}$$

$$c(0, S, t) = 1449,05 + 45,7t - 5,21t^2 + 0,23t^3 + (1,333 - 0,126t + 0,009t^2)(S - 35) \tag{3}$$

where: $t = \frac{T}{10}$, with T is temperature in ℃, S is the salinity in g kg⁻¹ and D is the depth in km.

The UNESCO equation is given as follows:

$$c(S, T, P) = Cw(T, P) + A(T, P)S + B(T, P)S^{\frac{3}{2}} + D(T, P)S^2 \tag{4}$$

$$Cw(T, P) = (C_{00} + C01T + C_{02}T^2 + C_{03}T^3 + C_{04}T^4 + C_{05}T^5) + (C_{10} + C_{11}T + C_{12}T^2 + C_{13}T^3 + C_{14}T^4)P +$$
$$(C_{20} + C_{21}T + C_{22}T^2 + C_{23}T^3 + C_{24}T4)P2 + (C_{30} + C_{31}T + C_{32}T^2)P3 \tag{5}$$

$$A(T, P) = (A_{00} + A_{01}T + A_{02}T^2 + A_{03}T^3 + A_{04}T^4) + (A_{10} + A_{11}T + A_{12}T^2 + A_{13}T^3 + A_{14}T4)P + (A_{20} +$$
$$A_{21}T + A_{22}T^2 + A_{23}T^3)P^2 + (A_{30} + A_{31}T + A_{32}T^2)P^3 \tag{6}$$

$$B(T, P) = B_{00} + B_{01}T + (B_{10} + B_{11}T)P \tag{7}$$

$$D(T, P) = D_{00} + D_{10}P \tag{8}$$

where: T is the temperature in ℃, S is the salinity in g kg⁻¹ and P is the pressure in bar.

One of the most used methods for measuring the speed of sound in liquid samples is the Acoustic Travel Time Method, which involves measuring the duration, known as time of flight, expressed in µs, for a sound wave to travel a known distance in the sample.

By dividing the distance, L_0 , between the transmitters by the time of flight, t_F, of the sound pulse, the speed of sound, c, in the sample can be calculated according to:

$$c = \frac{L_0 \cdot f_1}{t_F - f_2} \tag{9}$$

where f_1 is the correction factor associated to the change of path length due to densimeter temperature variation, e.g., for the used in this study DSA 5000M densimeter, this factor is given by $(1 + 1.6 \cdot 10^{-5} \cdot \Delta T)$, where ΔT is the temperature deviation from 20 °C, and f_2 is the correction term for electronic delay, temperature, and dispersion/diffraction effects.

Concerning the salinity interval values of the available reference materials used in this study, it is expected to reach the [1255.0, 1500.0] m s^{-1} speed of sound interval, at 20 ºC.

2. Material and Methods

2.1 Liquids under tests

As none certified reference material (CRM) was available in the [1001.8, 1026.8] kg m^{-3} density interval, a set of NaCl (NaCl for analysis, ACS, ISO, PanReac Applichem ITW Reagents) aqueous solutions was prepared gravimetrically, by using a mass comparator of Mettler Toledo, PR 2004. Ultrapure water (type I) (ISO 3696:1987) produced by the Milli Q Advantage water system (Merck Millipore) was used for the preparation of these solutions. To ensure acceptable homogeneity, all solutions were stirred for at least 60 min. The nominal values of mass fraction, X_m, density, ρ, dynamic viscosity, η, at 20 ºC, of the NaCl solutions under test are summarized in Table 1.

Table 1 – Nominal values of mass fraction, X_m, density, ρ, dynamic viscosity, η, at 20 °C, solutions under test.

Samples codification	$S_{A, nom.}$ /(g kg^{-1})	ρ_{nom} /(kg m^{-3})	η_{nom} /(mPa s)	$X_{m,NaCL}$ /(cg g^{-1})
NaCl_5	5	1001.8	1.011	0.50
NaCl_10	10	1005.3	1.020	1.01
NaCl_15	15	1008.9	1.031	1.50
NaCl_20	20	1012.5	1.036	2.00
NaCl_25	25	1016.1	1.057	2.49
NaCl_30	30	1019.6	1.052	2.99
NaCl_35	35	1023.2	1.084	3.50
NaCl_40	40	1026.8	1.068	4.00

(Source: Wolf, 1996; Söhnel and Novotny, 1985)

The study of the matrix effect on absolute salinity determination was also undergone with a set of standard seawater (SSW) samples of two different sources, both with a nominal S_A of 35 g kg^{-1}: an open-ocean Atlantic oceans water (OSIL) and an acidified coastal surface seawater (ERM).

2.2 Density

The density of the samples was measured with DMA 5000 and DSA 5000M (Anton Paar) density meters, with reference density values obtained by measuring the solutions on the former.

2.3 Refractive index

The refractive index, n, of a solution can vary with its composition, concentration, temperature, and the wavelength of the incident light. The refractive index of the solution is deduced from angle measurement thanks to the Snell-Descartes law, that expresses the refractive index in terms of the propagation angle.

The refractive indices of the samples were measured with a refractometer Abbemat 550 from Anton Paar, with a [1.300 000; 1.720 000] measuring interval, with SI traceability by calibration using certified reference materials for the refractive index from National Metrology Institutes (GUM - Poland; NIST - USA and PTB - Germany), ensuring a 0.000 010 refractive index standard uncertainty. Measurements of the Snell-Descartes law critical angle were performed by a charge coupled device (CCD) after refraction in the solution located in an approximately 0.4 mL cell, maintained at 20.00 °C and illuminated by a light emitting diode (LED) at a 589.3 nm wavelength.

2.4 Speed of sound

The speed of sound measurements of the samples were performed with the DSA 5000M (Anton Paar).

2.5 Salinity

The employed methodology to obtain the absolute salinity value of the test samples was like the one previously used (Furtado *et al.*, 2010, 2013; 2022 and Pellegrino *et al.*, 2011a, 2011b). Once the quantity of interest, the density, ρ, or the refractive index, n, was measured, internationally recognized reference tables were used to convert it into mass fraction, for the 20 ºC reference temperature, as the quantities are temperature dependent. Linear interpolation in the intervals of the two successive tabled data are performed to deduce mass fraction value, as it provides a smaller uncertainty deduced value (Pellegrino *et al.*, 2009).

NaCl mass fractions were determined from density measurements, using density reference values published in 1985 by Söhnel & Novotny, whereas for refractive index measurements, the reference values were published in 1966 by Wolf. For instance, to obtain NaCl mass fraction value, $X_m(\rho)_p$ from N (5 to 7), density measurement values, at 20 ºC, after correction based on certified reference materials (CRM), (by a density meter calibration function), with a C value according to:

$$\rho_p = \frac{\sum_{i=1}^{N} \rho_i}{N} + C \tag{10}$$

An interpolation was done by using a set of pairs of values ($\rho_{(p-1)}$, $X_m(\rho)_{(p-1)}$) and ($\rho_{(p+1)}$, $X_m(\rho)_{(p+1)}$) from the reference values published by Söhnel and Novotny (1985), following:

$$X_m(\rho)_p = \frac{\left[\rho_p - \rho_{(p-1)}\right]\left[X_m(\rho)_{(p-1)} - X_m(\rho)_{(p+1)}\right]}{\rho_{(p-1)} - \rho_{(p+1)}} + X_m(\rho)_{(p-1)} \tag{11}$$

From the interpolated value of the mass fraction in NaCl, $X_m(\rho)_p$, in cg g^{-1}, (Eq. 11), the value of absolute salinity was obtained by multiplication of a factor of 10, i.e. $S_A = 10\, X_m(\rho)_p$, in g kg^{-1}.

The same methodology was applied to refractive index values by using the refractometer calibration curve and the respective set of pairs of values from the reference values published by Wolf (1966).

2.6 Metrological traceability and uncertainty estimation

2.6.1 Density meter calibration

The validation of the density meter DSA 5000 M (Anton Paar) in density and speed of sound measurement results were performed on the density interval of interest [1001.8, 1026.8] kg m^{-3}, the one corresponding to the absolute salinity interval under study of [5, 40] g kg^{-1}.

The reference density values were obtained by measuring these solutions with a DMA 5000 (Anton Paar) density meter whose traceability of density measures to SI units is achieved by means of its calibration with CRM from National Metrology Institutes (GUM - Poland; NIST-USA and PTB - Germany) and by accredited laboratories (H&D Fitzgerald).

The SI traceability of temperature measurements performed by the DMA 5000 density meter is guaranteed by indirect thermometry using certified liquids for various temperatures and direct thermometry, by comparing the temperature indication of the density meter, with a 100 ohms platinum resistance thermometer (PRT) which was introduced into its measuring cell. This PRT was calibrated by the IPQ Temperature Laboratory,

For DSA 5000M the temperature calibration was performed only by indirect thermometry using n-Dodecane, in the temperature interval from [10, 40] ºC. The values from DMA 5000 were used as reference.

Table 2 – Reference density values, ρ and expanded uncertainties, U_ρ of the reference liquid used for temperature calibration, in the [10, 40] °C temperature interval.

Reference liquids	t / °C	ρ / (kg m^{-3})	U_ρ/ (kg m^{-3})	Source
n-dodecane	10	756.042	0.016	DMA 5000 values
	15	752.414	0.018	
	20	748.788	0.001	
	25	745.155	0.018	
	30	741.524	0.018	
	35	737.887	0.019	
	40	734.246	0.018	

2.6.2 Viscosity damping and calibration

The error due to viscosity damping and the calibration of viscosity indication of DSA 5000M was performed with 4 reference liquids, produced, and certified in density and viscosity by Cannon. The reference liquids used cover the dynamic viscosity interval of [0.66; 5] mPa s.

Table 3 – Reference values of density, ρ, dynamic viscosity, η, and respective uncertainties, of the reference liquids used for DSA 5000M viscosity calibration.

Samples codification	t / °C	ρ / (kg m^{-3})	U_ρ / (kg m^{-3})	η / (mPa.s)	U_η / (mPa.s)	Metrological Traceability
N .8	20.000	866.29		0.66	0.0011	
N 1.0	20.000	729.95	0.050	0.92	0.0015	Cannon
N 2.0	20.000	759.67		2.085	0.0033	
N 4.0	20.000	787.39		5.53	0.0088	

2.6.3 Speed of sound calibration

The speed of sound calibration of DSA 5000M (Anton Paar) was performed with 3 different liquids: degassed ultrapure water (ISO 3696:1987), n-dodecane, and n-decane, at 20 °C (Table 4). For ultrapure water the speed of sound indication values were compared with the ones given by Marczak (1997). For the remaining test liquids the speed of sound reference values were consulted at NIST Chemistry Book on the Web (https://webbook.nist.gov/).

Table 4 – Reference values of speed of sound, c_{ref}, and respective uncertainty values, $U_{c_{ref}}$ of the liquids used for DSA 5000M (Anton Paar) calibration.

Reference liquids	t / °C	c_{ref} / (m s⁻¹)	$U_{c_{ref}}$ / (m s⁻¹)	Source
n-Decane	20	1253.40	13	(Lemmon & Span, 2006)*
n-Dodecane	20	1301.20	6.5	(Lemmon & Huber, 2004)*
Ultrapure water	20	1482.38	0.0058*	Marczak, 1997)

Legend: *From NIST Chemistry Book on the Web (https://webbook.nist.gov/)

From the density measurement results of DSA 5000M of the set of NaCl aqueous solutions respective salinity values were determined as described earlier. With these salinity values the corresponding speed of sound values were determined by means of two reference equations: Coppens' equation (Eq. 2 and 3) and UNESCO equation (Eq. 4).

2.6.4 Uncertainty budget

The uncertainty budget associated with the measurements presented in this communication was calculated and expressed within the Guide to the Expression of Uncertainty in Measurement - GUM framework (JCGM 100:2008, BIPM.).

The uncertainty associated with each input quantity is a combination of the three main sources: measurements repeatability, i.e., dispersion; the correction of the input value due to the temperature of the sample; and the calibration of the measuring instruments. Concomitantly, the components of measurement uncertainty may be grouped into two categories, Type A and Type B, according to whether they were evaluated by statistical methods (Type A) or other methods (Type B).

The standard uncertainty, $u_c(y)$, of the measurand at the reference temperature is determined by taking the value of the square root of the quadratic sum of the uncertainties of the input quantities. This is obtained by using the law of propagation of uncertainties that consists on calculating the different uncertainty components, $u_i(y) = \left|\frac{\partial y}{\partial x_i}\right| u(x_i)$, where $u(x_i)$ represents the standard uncertainty of the input quantity x_i and $\frac{\partial y}{\partial x_i} = C_{x_i}$ is the called the

sensitivity coefficient. The number of effective degrees of freedom, ν_{ef}, was calculated according to the Welch-Satterthwaite formula, given by:

$$\nu_{ef} = \frac{u^4(y)}{\sum_{i=1}^{N} \frac{u_i^4(y)}{\nu_i}}, \text{ where } i = 1, 2, \ldots, N. \tag{12}$$

The expanded uncertainty, U, evaluates a confidence interval where the "true" value of the measurand is expected to lie. It is expressed by the combined standard uncertainty $u_c(y)$ multiplied by the expansion factor k, which, for a t-distribution with ν_{ef} effective degrees of freedom correspond to an expanded probability of 95 %.

$$U = k\, u_c(y) \tag{13}$$

a. Speed of sound measurement uncertainty

The mathematical model used in both cases for speed of sound determination was:

$$c(S, T, P) = c_{\text{Coppens or UNESCO}} + \delta S + \delta T + \delta P + \delta c_{\text{Coppens or UNESCO}} \tag{14}$$

Where:

δS is the error due to the salinity determination via density measurements. This error has zero average value but has a contribution value in uncertainty;

δT is the error due to the temperature measurements. It was assumed that this error has zero average value but has a contribution value in uncertainty;

δP is the error due to the pressure of the sample during measurements. It was assumed that this error has zero average value and a negligible contribution value in uncertainty as only low compressibility liquids were tested;

$\delta c_{\text{Coppens or UNESCO}}$ is the error due to the speed of sound obtained via Coppens (1981) or UNESCO (Allen, et al., 2017) equations. This error has zero average value and contribution value in uncertainty 0.1 m s^{-1} and 0.05 m s^{-1}, respectively.

Following the GUM uncertainty framework, it would be necessary to calculate sensitivity coefficients of the speed of sound equations. As a first approach, only the estimated uncertainties of the different components of Eq. (14) were used.

b. Salinity measurement uncertainty

The uncertainty budget of the absolute salinity, S_A, results obtained via density, $S_A(\rho)$, and refractive index, $S_A(n)$, measurements at 20 °C, is given on Table 5.

Table 5 - Uncertainty budget of the absolute salinity results, S_A, obtained via density, $S_A(\rho)$, and refractive index, $S_A(n)$, measurements at 20 ºC.

Contribution	Measurement	Standard uncertainty	Method of evaluation	Distribution	Degrees of freedom
Instrument resolution	Density Refractive index	$\frac{10^{-3}}{\sqrt{12}}$ kg m^{-3} $\frac{10^{-6}}{\sqrt{12}}$	Type B	Rectangular	50
Instrument calibration (including drift)	Density Refractive index	10^{-2} kg m^{-3} 10^{-5}	Type B	Normal	50
Measurement repeatability	Density Refractive index	$\frac{\sigma}{\sqrt{N}}$	Type A	Normal	N-1
Temperature[1]	Density Refractive index	-	Type A	Normal	50
Interpolation (from ref. values[2,3])	Density Refractive index	$6\ 10^{-3}$ kg m^{-3} $2\ 10^{-2}$	Type B	Rectangular	50

Legend: σ – standard deviation of the N measurement values; 1 – the temperature uncertainty component is already taken into account in the uncertainty of the calibration of the measuring instrument; 2 – according to (Söhnel & Novotny, 1985), with a $U_\rho = (1\ 10^{-1})/(3)^{1/2}$ kg m^{-3} and $U_{Xm\mathrm{NaCl}} = (1\ 10^{-1})/(3)^{1/2}$ cg g^{-1} uncertainties; 3 – according to (Wolf, 1966), with a $U_n = (1\ 10^{-4})/(3)^{1/2}$ and $U_{Xm\mathrm{NaCl}} = (1\ 10^{-1})/(3)^{1/2}$ cg g^{-1} uncertainties.

3. Results and Discussion

3.1 Validation of DSA 5000 M (Anton Paar) density and speed of sound meter

The validation of DSA 5000 M (Anton Paar) density and speed of sound measurement results are presented in the points below.

3.1.1   Density calibration

In Table 7, are resumed the results obtained in DSA 5000 M density calibration. The density interval of interest [1001.8, 1026.8] kg m^{-3} is the one corresponding to the [5, 40] g kg^{-1} absolute salinity interval. In Table 6, are presented the density reference values, ρ_ref and respective uncertainties, $U_{\rho_{ref}}$ obtained with DMA 5000 density meter, and the density indication results of DSA 5000 M, without viscosity correction, d_nc, and with viscosity correction, d, and respective expanded uncertainties, U_{d_nc} and U_d. The major contribution for the uncertainty of the reference value uncertainties, U_{ρ_ref} is arising from DMA 5000 calibration uncertainty, namely $U_{\rho_\mathrm{cal}} = 0.020$ kg m^{-3}, being the uncertainties contributions, the ones described in Table 7 with exception of the uncertainty due to the interpolation. The uncertainties values of DSA 5000 M only took into consideration the uncertainty due to density resolution and due to measurement repeatability.

Table 6 – DSA 5000 M density indications (d_{nc}, d) results, respective uncertainties ($U_{d_{nc}}$, U_d), and DMA 5000 density reference values (ρ_{ref}) and uncertainties ($U_{\rho_{ref}}$) obtained in density calibration results at 20 °C.

Samples codification	DMA5000		DSA 5000M			
	ρ_{ref}	$U_{\rho_{ref}}$	d_{nc}	$U_{d_{nc}}$	d	U_d
	/ (kg m^{-3})					
NaCl_5	1001.781	0.020	1001.775	0.001	1001.769	0.001
NaCl_10	1005.344	0.020	1005.340	0.001	1005.334	0.001
NaCl_15	1008.908	0.020	1008.902	0.001	1008.895	0.001
NaCl_20	1012.475	0.020	1012.478	0.001	1012.471	0.001
NaCl_25	1015.980	0.020	1015.973	0.001	1015.965	0.001
NaCl_30	1019.564	0.020	1019.564	0.002	1019.556	0.003
NaCl_35	1023.222	0.020	1023.229	0.001	1023.221	0.001
NaCl_40	1026.797	0.020	1026.791	0.001	1026.783	0.001

Table 7 summarizes DSA 5000 M density indication errors ($\delta d_{nc} = d_{nc} - \rho_{ref}$ and $\delta d = d - \rho_{ref}$) and respective expanded uncertainties ($U_{\delta d_{nc}} = \sqrt{U_{\rho_{ref}}{}^2 + U_{d_{nc}}{}^2}$ and $U_{\delta d} = \sqrt{U_{\rho_{ref}}{}^2 + U_d{}^2}$).

Table 7 – DSA 5000 M density indication errors (δd_{nc}, δd) and respective expanded uncertainties ($U_{\delta d_{nc}}$, $U_{\delta d}$) obtained in density calibration at 20 °C.

Samples codification	DSA 5000M			
	δd_{nc}	$U_{\delta d_{nc}}$	δd	$U_{\delta d}$
	/ (kg m^{-3})			
NaCl_5	-0.006	0.020	-0.012	0.020
NaCl_10	-0.004	0.020	-0.010	0.020
NaCl_15	-0.006	0.020	-0.013	0.020
NaCl_20	0.003	0.020	-0.005	0.020
NaCl_25	-0.007	0.020	-0.015	0.020
NaCl_30	0.001	0.020	-0.007	0.020
NaCl_35	0.008	0.020	-0.001	0.020
NaCl_40	-0.006	0.020	-0.014	0.020

From Figure 1, it is possible to observe that there is no relation between both density indication errors and density, and that the density indication errors are not meaningful as they are covered by the uncertainty, i.e., all the errors are lower than 0.020 kg m^{-3}. This means that there is no need to apply any correction to density indication values in this interval. Interestingly, it is to be noted that density indication errors without viscosity correction, δd_{nc}, were shown to be lower than the ones with viscosity correction, δd.
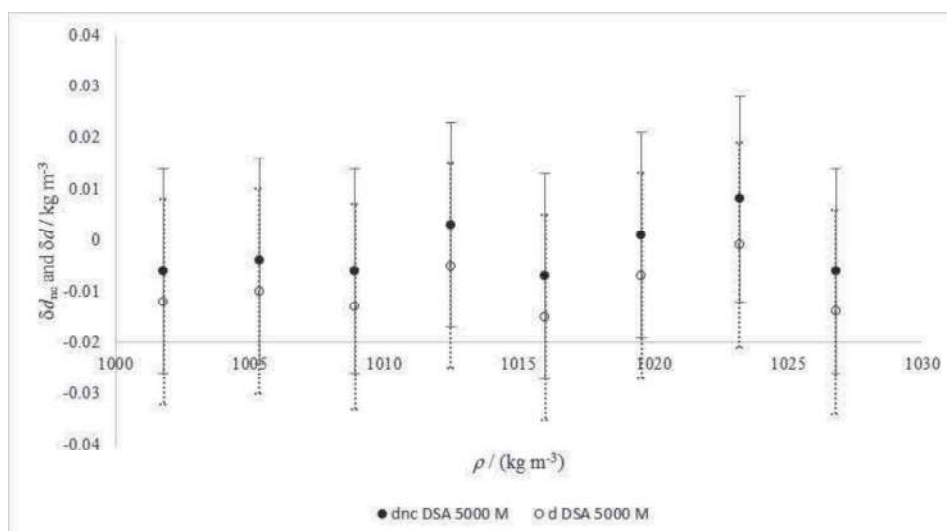
Figure 1 – Representation of DSA 5000 M density indication errors (δd_{nc}, δd) and respective expanded uncertainties ($U_{\delta d_{nc}}$, $U_{\delta d}$) obtained in density calibration at 20 °C.

3.1.2 Temperature calibration

DSA 5000M temperature calibration was performed by indirect thermometry by using n-dodecane, in the [10, 40] °C temperature interval as referred earlier. The results of this calibration are given in Table 8. From the reference density values given in Table 2 for n-dodecane, a relation of $t(\rho)$ was established to allow the calculation of temperatures values expected for the experimental density results. Using this approach, and from the results given in Table 10, a maximum temperature deviation was observed at 30 °C, and a minimum at 10 °C. From these results, a [-0.038 °C; 0.007 °C] tolerance interval was evidenced, which corresponds to an addition to a 0.045 °C tolerance value to the uncertainty budget of DSA 5000M.

Table 8 –DSA 5000 M density indication errors (δd_{nc}, δd) and respective expanded uncertainties ($U_{\delta d_{nc}}$, $U_{\delta d}$) obtained in temperature calibration.

Reference liquids	DSA 5000M				
	t	δd_{nc}	$U_{\delta d_{nc}}$	δd	$U_{\delta d}$
	/ °C	/ (kg m^{-3})			
n-dodecane	10	0.015	0.024	0.001	0.024
	15	0.021	0.025	0.006	0.025
	20	0.023	0.021	0.004	0.021
	25	0.029	0.025	0.013	0.025
	30	0.029	0.025	0.016	0.025
	35	0.031	0.025	0.018	0.025
	40	0.029	0.025	0.017	0.025

Table 9 –DSA 5000 M temperature indication errors ($\delta t(d_{nc}), \delta t(d)$) and obtained in temperature calibration.

t	DSA5000 M	
$/\,^\circ$C	$\delta t(d_{nc})$	$\delta t(d)$
	$/\,^\circ$C	
10	0.007	-0.003
15	-0.006	-0.016
20	-0.013	-0.025
25	-0.024	-0.035
30	-0.029	-0.038
35	-0.026	-0.034
40	-0.012	-0.021

3.1.3   Viscosity calibration

Due to the error induced by the viscosity damping, the calibration of viscosity indication of DSA 5000M was performed with 4 reference liquids from Cannon. The results are summarized in Table 10 and Table 11 and represented in Figure 2. It was expected that density indications errors have similar behavior with increasing viscosities. As can be seen in Figure 2, for d_{nc} indications, the errors are considered neglectable below viscosities of around 2 mPa s as the uncertainty is higher than the deviation. For 5.5 mPa s, it can also be observed a viscosity correction in d indication.

Table 10 –DSA 5000 M density indications (d_{nc}, d) results, respective uncertainties ($U_{d_{nc}}, U_d$) obtained in viscosity calibration results.

Samples codification	t $/\,^\circ$C	DSA5000			
		d_{nc}	$U_{d_{nc}}$	d	U_d
		$/$ (kg m^{-3})			
N .8	20	866.306	0.050	866.309	0.050
N 1.0	20	729.950	0.050	729.943	0.050
N 2.0	20	759.679	0.050	759.654	0.050
N 4.0	20	787.471	0.050	787.401	0.050

Table 11 –DSA 5000 M density indication errors ($\delta d_{nc}, \delta d$) and respective expanded uncertainties ($U_{\delta d_{nc}}, U_{\delta d}$) obtained in viscosity calibration.

Samples codification	t $/\,^\circ$C	DSA5000			
		δd_{nc}	$U_{\delta d_{nc}}$	δd	$U_{\delta d}$
		$/$ (kg m^{-3})			
N.8	20	0.016	0.071	0.019	0.071
N 1.0	20	0.000	0.071	-0.007	0.071
N 2.0	20	0.009	0.071	-0.016	0.071
N 4.0	20	0.081	0.071	0.011	0.071
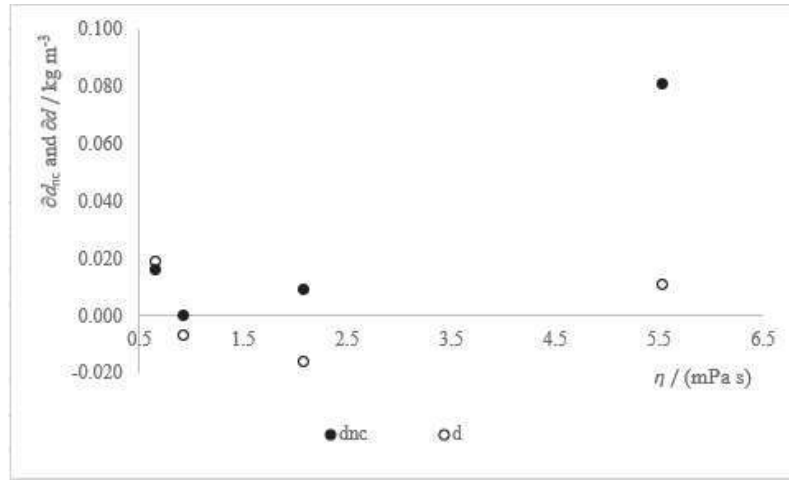
Figure 2 – Representation DSA 5000 M density indication errors (δd_{nc}, δd) versus dynamic viscosity, η obtained in viscosity calibration.

3.1.4 Speed of sound calibration

The speed of sound calibration of DSA 5000M (Anton Paar) was performed with 3 different liquids: degassed ultrapure water, n-dodecane and decane at 20 °C. The resume of DSA 5000 M speed of sound indications, c, respective uncertainties, U_c, error, δc, and uncertainty, $U\delta c$, obtained in the calibration are given in Table 12. The speed of sound indication errors, $\delta c'$, can be considered neglectable (with a maximum of 0.2 %) as they are comprised within the uncertainty, $U'\delta c$ (with a maximum of 2 %). This uncertainty value will be used as tolerance in future work.

Table 12 –DSA 5000 M speed of sound indications, c, respective uncertainties, U_c, error δc, and uncertainty, $U\delta c$ obtained in the calibration.

Reference liquids	t / °C	c / (m s^{-1})	U_c / (m s^{-1})	δc / (m s^{-1})	$\delta c'$ / %	$U\delta c$ / (m s^{-1})	$U'\delta c$ / %
n-decane	20	1255.0	25.2	2	0.2	25	2.0
n-dodecane	20	1298.9	13.1	-2	-0.2	13	1.0
Ultrapure water	20	1483.9	4.5	1.5	0.1	4.5	0.3

The primary objective of this study was to verify the accuracy of speed of sound measurements in seawater across the [5, 40] g kg^{-1} salinity intervalof, that corresponds to an approximately [1490, 1530] m s^{-1} speed of sound interval . For this purpose, the DSA 5000M was calibrated with 8 aqueous solutions of NaCl and 6 dilutions of seawater prepared from OSIL SSW. The reference values of speed of sound, c_{ref}, and respective uncertainty values, $U_{(c\_ref)}$ of NaCl aqueous solutions and OSIL aqueous solutions used for the calibration of DSA 5000M are presented, in Table 13 and Table 14, respectively, using Coppens and UNESCO equations.

Table 13: Reference values of speed of sound and respective uncertainty values for NaCl aqueous solutions.

Source		$S_A(\rho)$ /(g kg^{-1})	$U_{SA(\rho)}$ /(g kg^{-1})	Coppens equation		UNESCO equation	
Reference liquids	t / °C			$c_{SA\,C\,(\rho)}$ / (m s^{-1})	$U_{cSA\,C(\rho)}$ / (m s^{-1})	$c_{SA\,U\,(\rho)}$ / (m s^{-1})	$U_{cSA\,U(\rho)}$ / (m s^{-1})
NaCl_5	20	5.0	1.2	1487.94	0.10	1488.23	0.05
NaCl_10	20	10.1	1.2	1493.64	0.10	1493.94	0.05
NaCl_15	20	15.0	0.8	1499.11	0.10	1499.39	0.05
NaCl_20	20	20.0	1.2	1504.70	0.10	1504.94	0.05
NaCl_25	20	24.9	0.8	1510.16	0.10	1510.39	0.05
NaCl_30	20	30.0	1.2	1515.83	0.10	1515.95	0.05
NaCl_35	20	35.0	0.8	1521.49	0.10	1521.65	0.05
NaCl_40	20	40.0	1.2	1527.04	0.10	1527.25	0.05

Table 14: Reference values of speed of sound, and respective uncertainty values for OSIL aqueous solutions.

Source		$S_A(\rho)$ /(g kg^{-1})	$U_{SA(\rho)}$ /(g kg^{-1})	Coppens equation		UNESCO equation	
Reference liquids	t / °C			$c_{SA\,C\,(\rho)}$ / (m s^{-1})	$U_{cSA\,C(\rho)}$ / (m s^{-1})	$c_{SA\,U\,(\rho)}$ / (m s^{-1})	$U_{cSA\,U(\rho)}$ / (m s^{-1})
OSIL_5	20	5.1	1.1	1488.08	0.10	1488.34	0.05
OSIL_10	20	10.3	1.1	1493.82	0.10	1494.16	0.05
OSIL_15	20	15.3	0.8	1499.42	0.10	1499.72	0.05
OSIL_20	20	20.3	1.2	1504.98	0.10	1505.28	0.05
OSIL_25	20	25.2	0.8	1510.46	0.10	1510.72	0.05
OSIL_30	20	30.2	1.2	1516.08	0.10	1516.29	0.05

In Table 15 and Table 16, the results of the speed of sound of the same samples by DSA 5000M were assessed by means of the normalized error, E_n, with the reference values from Coppens and UNESCO equation. The results obtained were satisfactory, i.e., $E_n < 1$, in the entire salinity interval, meaning that the measurement of speed of sound in seawater, within the [5; 40] g kg^{-1} salinity interval is valid. It is important to state that $U\partial c_{DSA}$ magnitude is greater due to the uncertainty associated with the conversion of density to practical salinity arising from the reference values. So, it is of relevance to note that relative errors obtained for both type of solutions (NaCl and OSIL aqueous solutions), and from both reference equations (Coppens, UNESCO) are: 0.02 % $\leq \partial'c \leq$ 0.42 %. No trend seems to exist concerning relative errors $\partial'c$ and speed of sound results c_{DSA}. However, the relative error of the NaCl aqueous solutions is always higher than the OSIL aqueous solutions as is shown in Figure 3. We can observe that the errors magnitude are smaller than the uncertainty.

Table 15: DSA 5000 M Speed of sound results and respective uncertainty values for NaCl aqueous solutions.

Samples codification	c_{DSA}	Uc_{DSA}	Deviation from Coppens Eq.				E_n	Deviation from UNESCO Eq.				E_n
			δc	$U\delta c$	$\delta'c$	$U\delta'c$		δc	$U\delta c$	$\delta'c$	$U\delta'c$	
	/ (m s⁻¹)				/ %			/ (m s⁻¹)		/ %		
NaCl_5	1489.47	0.16	1.5	399	0.10	27	0.0	1.2	408	0.08	27	0.0
NaCl_10	1495.05	0.03	1.4	198	0.09	13	0.0	1.1	203	0.07	14	0.0
NaCl_15	1500.57	0.01	1.5	92	0.10	6.1	0.0	1.2	94	0.08	6.2	0.0
NaCl_20	1511.07	0.72	6.4	101	0.42	6.7	0.1	6.1	103	0.41	6.8	0.1
NaCl_25	1512.23	0.17	2.1	56	0.14	3.7	0.0	1.8	57	0.12	3.8	0.0
NaCl_30	1517.52	0.05	1.7	65	0.11	4.3	0.0	1.6	67	0.10	4.4	0.0
NaCl_35	1523.26	0.07	1.8	40	0.12	2.6	0.0	1.6	41	0.11	2.7	0.0
NaCl_40	1530.16	0.37	3.1	51	0.20	3.4	0.1	2.9	52	0.19	3.4	0.1

Table 16: DSA 5000 M Speed of sound results and respective uncertainty values for OSIL aqueous solutions.

| Samples codification	c_{DSA}	Uc_{DSA}	Deviation from Coppens Eq.				E_n	Deviation from UNESCO Eq.				E_n
			δc	$U\delta c$	$\delta'c$	$U\delta'c$		δc	$U\delta c$	$\delta'c$	$U\delta'c$	
	/ (m s⁻¹)				/ %			/ (m s⁻¹)		/ %		
OSIL_5	1489.35	0.13	1.3	367	0.09	25	0.0	1.0	376	0.07	25	0.0
OSIL_10	1494.54	0.01	0.7	183	0.05	12	0.0	0.4	188	0.03	13	0.0
OSIL_15	1500.05	0.18	0.6	90	0.04	6.0	0.0	0.3	92	0.02	6.2	0.0
OSIL_20	1507.41	0.80	2.4	99	0.16	6.5	0.0	2.1	101	0.14	6.7	0.0
OSIL_25	1510.34	0.01	-0.1	55	-0.01	3.6	0.0	-0.4	56	-0.03	3.7	0.0
OSIL_30	1515.84	0.10	-0.2	66	-0.02	4.4	0.0	-0.4	68	-0.03	4.5	0.0
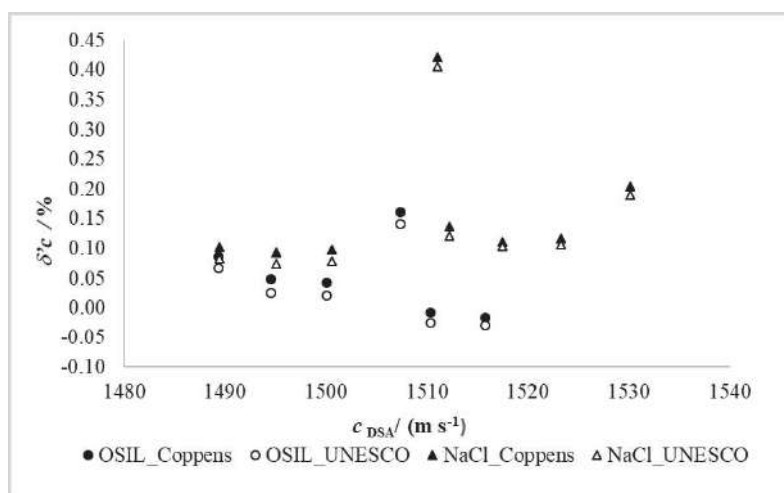
Figure 3: Speed of sound relative error versus speed of sound for NaCl and OSIL aqueous solutions.

3.2 Salinity determinations

The results of metrological compatibility of absolute salinity values, S_A obtained by refractometry and densimetry, investigated at 20 °C in the [5; 40] g kg^{-1} S_A interval, are given in Table 17. The obtained results were assessed by means of the normalized error, E_n, resulting from the quotient of the difference of salinities ($|S_A(n)- S_A(\rho)|$) by expanded uncertainty of this difference ($\sqrt{U_{S_A(n)}{}^2 + U_{S_A(\rho)}{}^2}$. The results were satisfactory, i.e., $E_n \leq 1$, in the entire salinity interval, meaning that these methodologies produce metrological compatible salinity results. Both methodologies generate similar uncertainty values.

Table 17 – Metrological compatibility of absolute salinity values, S_A obtained by refractometry and densimetry, investigated at 20 °C in the [5; 40] g kg^{-1} S_A interval.

Samples codification	$S_{A. nom.}$	$S_A(n)$	$U_{S_A(n)}$	$S_A(\rho)$	$U_{S_A(\rho)}$	δS_A	$U_{\delta S_A}$	E_n
				/(g kg^{-1})				
NaCl_5	5	4.8	1.3	5.0	1.2	0.2	1.7	0.10
NaCl_10	10	10.2	1.2	10.1	1.2	-0.2	1.7	0.12
NaCl_15	15	15.12	0.86	15.00	0.82	-0.1	1.2	0.10
NaCl_20	20	19.9	1.2	20.0	1.2	0.1	1.7	0.03
NaCl_25	25	24.71	0.86	24.89	0.82	0.2	1.2	0.15
NaCl_30	30	29.5	1.2	29.9	1.2	0.4	1.6	0.25
NaCl_35	35	34.76	0.86	35.04	0.82	0.3	1.2	0.24
NaCl_40	40	39.8	1.2	40.0	1.2	0.2	1.7	0.09

The results of the study of matrix effect on absolute salinity determination undergone with a set of standard seawater (SSW) samples of two different sources, both with a nominal S_A of 35 g kg^{-1}: OSIL and ERM, are given in Table 18. The salinity results obtained by both methodologies are shown to be metrological compatible as, the ones obtained for sodium chloride solutions, which renders the matrix effect despicable.

Table 18 – Metrological compatibility of absolute salinity values, S_A obtained by refractometry and densimetry, of the standard seawater samples.

Samples codification	$S_{A. nom.}$	$S_A(n)$	$U_{S_A(n)}$	$S_A(\rho)$	$U_{S_A(\rho)}$	δS_A	$U_{\delta S_A}$	E_n
	/(g kg^{-1})							
SSW_OSIL_35	35	36.80	0.91	37.21	0.90	-0.4	1.3	0.32
SSW_ERM_35	35	36.09	0.88	35.68	0.83	0.4	1.2	0.34

4. Conclusions

This work enabled not only to validate a DSA5000M (Anton Paar) density meter and speed of sound measurement system, but also to widen the salinity interval in which refractometry and densimetry could be used to determine salinity of seawater-like samples.

More specifically, it was possible to measure density of sodium chloride solutions with measurement errors below the corresponding measurement uncertainty, i.e. 0.020 kg m^{-3}. A 0.045 °C tolerance was deduced from the temperature calibration results and, regarding the viscosity calibration, as the study focused on small viscosity values, it was evidenced that the measurement density errors could be considered neglectable below viscosities of around 2 mPa s. Above this viscosity value, density measurement errors increased. In this work, viscosity of the study solutions are around 1 mPa s as shown in Table 1, where no corrections are necessary when considering viscosity. The speed of sound measurement errors, within the [1255, 1484] m s^{-1} interval at 20 °C, can be deemed negligible, with a maximum deviation of 0.2 %. These errors fall within the range of uncertainty, which has a maximum deviation of 2 %. From now on, these uncertainty values will serve as acceptable tolerance level.

Within the speed of sound [1490, 1530] m s^{-1} interval, the calibration of this measurement instrument with aqueous solutions of NaCl and various dilutions of seawater prepared from OSIL SSW, obtained relative errors derived from both reference equations (Coppens and UNESCO) range from 0.02 % to 0.42 %, with a relative expanded uncertainty of 2.6 % to 27 %. This higher uncertainty arose from the conversion of density to practical salinity associated with the reference.

Future work will aim to extensively explore the traceability of speed of sound measurement results across a wider interval while trying to reduce uncertainty through enhanced reference standards. Additionally, efforts will focus on establishing a reliable methodology for determining absolute salinity from speed of sound measurement results.

Conversely, it may also be tempting to straightforwardly deduce salinity from speed of sound measurements of seawater samples.

Acknowledgments

References

André, J. F. C. (2023). *Measuring absolute salinity through density, refractive index, and sound speed traceability* (Dissertação de Mestrado não publicada). Universidade Nova de Lisboa, Monte da Caparica.

Anton Paar GmbH. (2021) *Instruction Manual and Safety Information DSA 5000M Density and Sound Velocity Meter* instrument software version: from 2.98

Bilaniuk N. & Wong G.S.K.(1993). Speed of sound in pure water as a function of temperature. *J. Acoust. Soc. Am.* 93(3) pp 1609-1612. as amended by Bilaniuk N. and Wong G. S. K. (1996). Erratum: Speed of sound in pure water as a function of temperature [*J. Acoust. Soc. Am.* 93. 1609-1612 (1993)]. J. Acoust. Soc. Am. 99(5). p 3257.

Furtado A. (2019) *Metrological traceability of density and rheological measurements of liquids*. September 182 pp. Thesis (PhD in Science and Materials Engineering Specialty in Materials Science). Faculty of Science and Technology. New University of Lisbon. Portugal. https://run.unl.pt/bitstream/10362/92677/1/Furtado_2019.pdf

Furtado A., Napoleão A., Pereira J., Moura S., Quendera R. & O. Pellegrino O. (2022). Absolute salinity determination by oscillation-type densimetry and refractometry. *International Journal of Metrology and Quality Engineering.* 13, 10.

Furtado A., Oliveira C., Pellegrino O. *et al.* (2013) Metrological Compatibility of the Measurement Results of Aqueous Solutions Mass Fractions by densimetry and Refractometry. *IMEKO International TC8. TC23 and TC24* - 3rd Symposium on Traceability in Chemical. Food and Nutrition Measurements.

Furtado A., *Pellegrino* O., Alves S. *et al.* (2010) Determinação da fracção mássica de soluções aquosas de glucose por refractometria e densimetria de tubo vibrante. In *CONFMET2010*.

ISO 3696:1987 (1987) *Water for analytical laboratory use - Specification and test methods*

ISO/TR 3666:1998 - *Viscosity of water*

JCGM 100:2008 (2008) *Evaluation of measurement data − Guide to the expression of uncertainty in measurement*. BIPM.

JCGM 200:2012. *International Vocabulary of Metrology - Basic and General Concepts and Associated Terms.* VIM 3rd edition. BIPM.

Knapstad, B., Skjølsvlk, P.A. & Øye, H.A.(1989). Viscosity of Pure Hydrocarbons, *J. Chem. Eng. Data*, 34 (1), 37-43

Lemmon. E. W.. & Huber. M. L. (2004). Thermodynamic properties of n-dodecane. *Energy & fuels.* 18(4). 960-967.

Lemmon. E. W.. & Span. R. (2006). Short fundamental equations of state for 20 industrial fluids. *Journal of Chemical & Engineering Data*. 51(3). 785-850.

Lubbers. J. & Graaff. R. (1998). A simple and accurate formula for the sound velocity in water. *Ultrasound Med. Biol*. Vol 24. No 7. pp 1065-1068.

Marczak. W. (1997). Water as a standard in the measurements of speed of sound in liquids. *The Journal of the Acoustical Society of America*. 102(5). 2776-2779.

Pellegrino O. Furtado A & Filipe E (2009). Linear fitting procedures applied to refractometry of aqueous solutions. *In: 3rd Symposium on Traceability in Chemical*. Food and Nutrition Measurements. Lisbon. Portugal. 6-11 September 2009. Proc. XIX IMEKO World Congress Fundamental and Applied Metrology.

Pellegrino. O.. Furtado. A.. Alves. S.. Spohr. I. & Filipe. E. (2011a) *Compatibilidade metrológica de resultados de medição da fracção mássica de glucose em soluções aquosas por densimetria de tubo vibrante e refractometria*. In 4.º Encontro Nacional da Sociedade Portuguesa de Metrologia.

Pellegrino. O.. Furtado. A.. Alves. S.. Spohr. I. & Filipe. E. (2011b) *Refractometria e densimetria de tubo vibrante: técnicas complementares na determinação da fracção mássica de glucose em soluções aquosas*. In XXII Encontro Nacional da Sociedade Portuguesa de Química.

Söhnel. O.. & Novotný. P. (1985). *Densities of aqueous solutions of inorganic substances* (Vol. 22). Elsevier Publishing Company.

Spieweck. F.. & Bettin. H. (1992*)*. Solid and liquid density determination/Übersicht: Bestimmung der Dichte von Festkörpern und Flüssigkeiten. *Tm-Technisches Messen*. 59(7-8), 285-292.

Wolf. A.V. (1966). *Aqueous solutions and body fluids*. New York: Hoeber Medical Division.

Authors Profiles

João André is currently doing his thesis to obtain a master's degree in Mechanical Engineering from the NOVA School of Science and Technology-Nova University of Lisbon–Portugal

Andreia Furtado has received a PhD in Materials Science in 2012 from the Faculty of Sciences and Technology - Nova University of Lisbon – Portugal. She is the head of Properties of Liquids Laboratory of Portuguese Institute for Quality (IPQ). where she works as a senior metrology scientist since 2006.

Sara Moura has received a postgraduate degree in Management in Quality and Food Safety in 2004 from the Higher Institute of Health Sciences – South; Egas Moniz C.R.L. – Portugal. She is senior technician in Properties of Liquids Laboratory of Portuguese Institute for Quality (IPQ). where she works since 2021. Her research interests are in the areas of density. viscosity. surface tension and rheology.

Raquel Quendera is a chemist engineer and PhD student in Chemistry. She is the Head of the Electrochemistry Laboratory of IPQ. Her research interests are in the areas of electrochemistry (primary and secondary potentiometric methods for pH and pHT determination in seawater) and environmental analysis (such as metals determination by ICP-MS. ICP-OES. XRF and AAS).

Olivier Pellegrino has received a PhD in Physics in 1995 from the Pierre et Marie Curie University of Paris VI – France. He is the head of Photometry and Radiometry Laboratory of Portuguese Institute for Quality (IPQ). where he has worked as a senior metrology scientist since 2002.

Helena Navas has received a PhD from NOVA School of Science and Technology – Universidade NOVA de Lisboa – Portugal. She is currently Assistant Professor at the Department of Mechanical and Industrial Engineering of the NOVA School of Science and Technology – Portugal and researcher at UNIDEMI. Her research interests are in the areas of innovation, continuous improvement, quality, and process management.

Determining Liquid Properties for Application in Microfluidic Devices

João Lima
jmv.lima@campus.unl.pt
NOVA School of Science and Technology, Universidade NOVA de Lisboa

Andreia Furtado
afurtado@ipq.pt
Instituto Português da Qualidade, Caparica, Portugal

Elsa Batista
ebatista@ipq.pt
Instituto Português da Qualidade, Caparica, Portugal

Sara Moura
smoura@ipq.pt
Instituto Português da Qualidade, Caparica, Portugal

Helena Navas
hvgn@fct.unl.pt
UNIDEMI, NOVA School of Science and Technology, Universidade NOVA de Lisboa

Olivier Pellegrino
opellegrino@ipq.pt
Instituto Português da Qualidade, Caparica, Portugal

Abstract:
Liquids, between nano- to microlitres, have proprieties, such as surface tension, contact angle and refractive index, that play an important role in fluid dynamics and that are challenging to microfluidics engineers and scientists. This work displays a study of these proprieties for commonly used liquids in microfluidic devices, like ultrapure water, ethylene glycol and glycerol, in contact with plates of Topas and borosilicate glass, that are the materials of the microfluidics devices fabrication. For the study of these proprieties, the probes used were dimensional characterized by means of an interferometer and the determination of surface tension and contact angle (static and dynamic) by Wilhelmy plate method using a tensiometer. The refractive index of the tested liquids was also determined. This study also focuses on establishing metrological traceability and an uncertainty budget for each measurand as they are important tools for quality assessment of measurement results.
Indeed, these liquid proprieties are crucial for microfluidic flow properties such as resistivity and fouling, which are key performance parameters of microfluidic devices. A contribution with measurement results of challenging liquid properties for use in microfluidic devices is given in this work.

Keywords: Contact angle, microfluidics, surface tension, refractive index

1. Introduction

Microfluidics, which corresponds to the fluid-handling in the nano-to-microlitre scale, has major applications in the field of biomedical and chemical analysis [1]. At these small scales, surface tension forces play a key role in fluid dynamics and therefore must be estimated to be correctly used by microfluidics engineers and scientists. Surface tension is due to intermolecular forces, a characteristic of fluids interfaces and depend on surface properties like roughness, surface energy etc., which are due and lead to specific interactions between liquid and surfaces [2]. These interactions, fundamental for a knowledge of microfluidic flow properties such as resistivity and fouling, are key performance parameters of microfluidic devices, generally expressed by proprieties like hydrophobicity, hydrophilicity, and wettability [3].

As complementary available analyses of liquid/surface interactions, with SI traced measurement results, contact angle and refractive index measurements may be performed for the materials objects of this study. Furthermore, efficient, and correct measurement procedures of the liquid properties are needed to ensure traceable, accurate and precise measurement results of the most important parameters involved in microfluidic devices [4, 5].

Within the scope of the European Metrology Programme for Innovation and Research (EMPIR), the MFMET - Establishing Metrology Standards in Microfluidic Devices (20NRM02 MFMET) project has been focused on providing generic methodologies of accurate measurement of key quantities in microfluidic devices, such as surface tension, hydrophobicity, hydrophilicity, and wettability of the chip material, among others. Relationships of these proprieties with flow stability and flow control are then expected to be evidenced. This objective is proposed to be achieved by using and developing standardised methods and reference documents [6].

This work presents some results of the MFMET study about how contact angle, surface tension, and refractive index of three given liquids vary when put in contact with two different solids commonly used in microfluidic devices. One of the expected consequences of these results is a better knowledge of the influence of the interactions liquids/surfaces on flow and volume measurements at these scales and better definition for quality standards and procedures.

The surface property wettability is the degree by which a liquid is spread over a surface, i.e., the degree of wetting (adhesive contact between solid and liquid). This surface property is measured by the contact angle (or wetting angle), θ, which is the angle formed between the solid/liquid interface and the liquid/vapor interface [1]. The measured contact angle is independent of geometry and hence is a material property. However, several factors, such as surface energy, surface chemistry, surface roughness/texture, the surface preparation procedure,

surface cleanliness, and the properties of liquid and vapor phases influence the measured contact angle.

Surface tension, σ, is an important physical property of the fluid interfaces whatever they may be: between two fluids (gas-liquid or liquid-liquid) or between a fluid and a solid (solid-gas or solid-liquid). The SI-derived unit of surface tension is the newton per meter, with symbol N/m, although, in practice, its submultiple millinewton per meter, mN/m, is used. Surface tension is defined as the quotient of the force exerted perpendicularly on a linear element on a surface, and the length of that element. Surface tension is an interfacial tension of a liquid surface in equilibrium with its vapor phase, resulting from intermolecular forces at the interfaces [1].

In practice, microfluidic engineers and scientists test the wettability of a certain material using water, but other fluids can also be used [3]. Among the several ways of measuring the contact angle, the most common method used, involved looking at the profile of the droplet formed on the surface and measuring two-dimensionally the angle formed among the solid the vapour and the liquid (droplet profile) at the three-phase contact line.

To better take advantage of the surface tension measurements and perform accurate readings, measuring probes made of the same material and with the same constitution as microfluidics devices were chosen and submitted to an accurate dimensional characterization. Finally, the refractive index of the selected liquids was measured, due to its potential complementary information [7] applied to microfluidic devices.

After describing the materials, the experimental tools and methods used in this study, in part 2, the following part displays the most relevant measurement results. A discussion leads to some conclusions in the final part of this study.

2. Material and Methods

2.1. Liquids under tests

As previously mentioned, [3], other liquids than water are used in the study of wettability in microfluidics. In this study, ultrapure water (type I) [8] was produced by the Milli Q Advantage water system from Merck Millipore, ethylene glycol p.a. from Merk and glycerol 99.5 %, reagent grade from Scharlau. The nominal values of surface tension, σ, and density, ρ, of these liquids are summarized in Table 1.

Table 1 – Nominal values of surface tension, σ, and density, ρ, at 20 °C, of the liquids under tests.

Samples	σ /(mN m^{-1})	r_{nom} / (kg m^{-3})
Ultrapure water [8]	72.75	998.203
Ethylene glycol [9]	48.90	1113.50
Glycerol [9]	63.70	1258.50

2.2. Measuring probes

In addition to reference materials, the liquid surface properties measurements presented in this study were performed with liquids and materials commonly used in microfluidics devices. Indeed, in addition to a platinum plate, the reference material [10] for this experimental technique, the measuring instrument probes were made of D263® M Borosilicate glass [11] and a COC (Cyclo-olefin-copolymer, tradename "Topas") [12] and their features are described in Table 2.

Table 2 – Measuring probes features and photos.

Measuring probes	Manufacturer	Nominal dimensions / mm	Special features
Platinum plate	Krüss	10x20x0.2	Rough platinum, easily moistened, ensuring an approximately 0 º contact angle, θ [10]
COC (Cyclo-olefin-copolymer, tradename "Topas")	ChipShop	10x20x0.175	Thermoplastic polymer. Completely nonpolar and amorphous, very low permeability for water vapour and low capacity for water absorption[11].
Borosilicate Glass D 263® M	WillCo Wells	22x22x0.17	Chemically resistant borosilicate glass D 263® M of the first hydrolytic class. Thickness value, c = (0.170 mm ± 0.005 mm) [12]

However, the dimensions of the measuring probes were measured by means of a HEWLETT PACKARD 5528A interferometer. This measuring instrument was composed of a ZEISS KL 1500 LCD cold light source and a ZEISS Stemi 2000-C microscope linked to the interferometer. In order to access the reproducibility of the plates, the dimensions of each plate were measured 10 times and, for each measurement, a different plate was used, for surface tension or both methods of contact angle measurements.

2.3. Surface tension measurements

Measurements of surface tensions were performed by the Wilhelmy plate method [13] with a Krüss K100 MK2 tensiometer, using a thin, rectangular plate (by Krüss), made of metal platinum of known geometry [10]. The plate consists of rough platinum, easily moistened, ensuring a contact angle, θ, of approximately 0° ($\cos\theta = 1$). In this method, the plate is oriented perpendicular to the interface, at the surface of the liquid, and the force exerted on it was measured.

Before starting the measurements, the force sensor adjustment was realized with internal mass standard. The device was calibrated using different masses in the range of [50; 1000] mg and preceded by a measurement verification to determine the compliance with the quality criteria established.

The liquid was placed into a glass vessel in a thermoregulated platform and left for about one hour until thermal equilibrium was achieved. The temperature in the platform was controlled by means of water jacket connected to a thermoregulated recirculation water bath (ThermoScientific Haake AC 150) and sensors were placed in the liquid and inside the tensiometer for temperature measurement (Anton Paar MKT 50).

The plate was cleaned between each measurement, using appropriate solvent first followed by flame. After preparation, the measuring plate was hanged on the tensiometer force transducer, where the sample was brought up almost into contact, and enabled to equilibrate for approximately 3 minutes, before starting the surface tension measurements.

Then, the sample contained in the vessel was raised until the contact of the surface of the liquid with the plate was recorded. The platform rose a little higher, as defined in the software [14], by immersing the plate in the liquid and then moved down again until its sitting at the surface of the liquid under test. At this instant, the maximum force acted on the tensiometer. For each sample, surface tension was measured at least 5 times.

Through Eq. 1, the surface tension value can be deduced using the measured force magnitude, $F_{máx.}$, and the wetted length value of the plate, L used in the measurement [13].

$$\sigma = \frac{F_{máx.}}{L \cdot \cos\theta} \tag{1}$$

The wetted length of the plate, L, in m, was given by the perimeter of the section at the gas-liquid interface, i.e. equals to the sum of twice the length, l, plus twice the thickness of the plate, c, according to:

$$L = 2\,l + 2\,c \tag{2}$$

The surface tension value at the reference temperature, σ_{t_0}, was given by:

$$\sigma_{t_0} = \sigma_t + \alpha_\sigma \cdot (t_0 - t) \tag{3}$$

Where σ_t, was the surface tension at the test temperature t, calculated by Eq. 1 and α_σ, the temperature coefficient of the surface tension of the liquid, determined by an established relationship of, at least, three experimental surface tension/temperature pairs.

2.4. Contact Angle

A Krüss K100 MK2 tensiometer was used for contact angle measured according to the static and the dynamic Wilhelmy plate methods. However, whatever the method, prior to each measurement, the plates were carefully cleaned with ethanol. For platinum plate, the remaining solvent was burned with a lab burner until slightly glowing.

The static method corresponds to the deduction of the contact angle through Eq. 4 [13], after obtaining the fluid surface tension as described in the previous subsection. Indeed, with a 0º assumed contact angle, θ, for the platinum plate and its known geometry, the fluid surface tension is calculated, σ_{PT}. Repeating the experiment with borosilicate glass and Topas plates and considering the previous measured tension value, the solid-liquid-vapor contact angle is calculated using Eq. 4, corresponding to the ratio between the surface force, $F_{\text{máx.}}$, and the acted force upon the same wetted length, L, along which the force acts for a totally wetted solid, L σ_{PT}:.

$$\cos\theta = \frac{F_{\text{máx.}}}{L \cdot \sigma_{PT}} \tag{4}$$

In practice, the contact angle value is related to wetting, so low contact angle values, i.e. below 90°, are related to good wetting whereas high contact angle values, above 90°, indicate poor wetting. When the contact angle is 0°, as in the case of the platinum plate, the surface is said to completely wet.

2.5. Dynamic contact angle method

In the dynamic method, the plate already immersed into the liquid is moved up and down. The depth of the immersion (between 1mm and 5 mm) and the movement speed (0.05 mm/s) are accurately measured by the tensiometer elevator, while the full cycle was repeated three times.

By measuring the force when moving the plate up and down and considering the buoyancy effect, the advancing, $\theta_{\text{adv.}}$ and receding $\theta_{\text{rec.}}$ contact angles and the contact angle hysteresis, $\theta_{\text{hys.}}$, were determined according to Equations 5 and 6.

$$F(h) = P\sigma\cos\theta - \rho Ahg \tag{5}$$

Where, P is the length of the plate perimeter plate, in metres, symbol m; σ is the liquid surface tension, the symbol of unit is mN/m; θ is the contact angle between the plate and the measured liquid, in degrees, of symbol °; ρ the liquid density, the symbol of unit is kg/m^3; A the area of the plate surface, the symbolof unit is m^2; h the immersion depth, in metres, m; and g the gravitational constant, with unit symbol m/s^2. The advancing and the receding angles can be solved by linear regression of the advancing and receding experimental curves at zero depth ($h = 0$ m), respectively.

$$\theta_{\text{hys.}} = \theta_{\text{adv.}} - \theta_{\text{rec.}} \qquad (6)$$

The density of air was calculated by the CIPM-2007 formula [15] based on pressure, temperature, and humidity measurements results, obtained with a VAISALA PTU 301 multi-sensor.

2.6. Refractive Index

Like for any materials, the refractive index, n, of a liquid is influenced by its composition, concentration, temperature, and the wavelength of incident light. For some binary solutions, correspondences between concentration and refractive index values, at fixed pressure and temperature conditions, have been published [16]. Thus, by measuring the refractive index of these solutions, for given temperature and pressure conditions, the concentration of a compound can be deduced.

The measurements were conducted at a controlled temperature of 20 ºC, monitored using a VAISALA PTU 301 instrument, with an Anton Paar Abbemat 550 refractometer. Readings were acquired at regular intervals of, at least, 14 seconds to obtain the measurement value stability, the result being the mean of the 5 last readings. For each liquid refractive index, three measurement results were obtained, always cleaned with ultra-pure water in between. The accuracy of the readings is verified by determination of ultra-pure refractive index, with 1.33 reference value, before new sample reading.

For the present study, the refractive index of the liquids under test were determined, namely ultrapure water, ethylene glycol and glycerol. The nominal values of the refractive index of these liquids are summarized in Table 3 [9].

Table 3 –Nominal values of the refractive index, *n*, at 20 °C, of the liquids under test [9].

Samples	*n* /1
Ultrapure water	1.33
Ethylene glycol	1.43
Glycerol	1.47

Refractive index measurements in microfluidic devices may also quantify solutions at controlled temperature and eventually identify the presence of adsorb layers of solutions components on surfaces [16].

2.7. Metrological traceability and uncertainty estimation

Metrological traceability of the different methods is ensured when the used measuring instruments are calibrated with national and international standards, or certified reference materials for the specified parameters.

The uncertainty budget associated with the measurements presented in this work was calculated and expressed according to the Guide to the Expression of Uncertainty in Measurement - GUM framework [17].

The uncertainty associated with each input quantity is a combination of the three main sources: measurements repeatability, i.e., dispersion; the correction of the input value due to the temperature of the sample; and the calibration of the measuring instruments. Concomitantly, the components of measurement uncertainty may be grouped into two categories, Type A and Type B, according to whether they were evaluated by statistical methods (Type A) or other methods (Type B).

The standard uncertainty, $u_c(y)$, of the measurand at the reference temperature is determined by taking the value of the square root of the quadratic sum of the uncertainties of the input quantities. This is obtained by using the law of propagation of uncertainties that consists on calculating the different uncertainty components, $u_i(y) = \left|\frac{\partial y}{\partial x_i}\right| u(x_i)$, where $u(x_i)$ represents the standard uncertainty of the input quantity x_i and $\frac{\partial y}{\partial x_i} = C_{x_i}$ is the called the sensitivity coefficient. The number of effective degrees of freedom, ν_{ef}, was calculated according to the Welch-Satterthwaite formula, given by:

$$\nu_{\text{ef}} = \frac{u^4(y)}{\sum_{i=1}^{N} \frac{u_i^4(y)}{\nu_i}} \text{ for } i = 1, 2, ..., N. \tag{8}$$

The expanded uncertainty, U, evaluates a confidence interval where the "true" value of the measurand is expected to lie. It is expressed by the combined standard uncertainty $u_c(y)$ multiplied by the expansion factor k, which, for a t-distribution with ν_{ef} effective degrees of freedom correspond to an expanded probability of 95 %.

$$U = k\, u_c(y) \tag{9}$$

2.7.1. Dimensional characterization

The uncertainty budget for dimensional measurements included different contributions to the standard uncertainty of the determination of length (l) and thickness (c). They were the instrumental measurement uncertainty arising from the interferometer and input quantities, like the standard deviation of the dimension mean and resolution of the instrument, their values, and associated standard uncertainties, together with their degrees of freedom, leading to the combined standard uncertainty, as well as the effective degrees of freedom.

2.7.2. Surface properties

The uncertainty budget for surface tension measurements is displayed in the cause-effect diagram (Figure 1) which represents the different contributions to the standard uncertainty of the determination of surface tension, σ, from the different input quantities (force, F, wetted length, L, temperature, t and thermal coefficient, α_σ).

Figure 1 - Cause-and-effect diagram of the contributions to the standard uncertainty of the surface tension determinations, from the different input quantities: force, F, wetted length, L, temperature, t and thermal coefficient, α_σ.
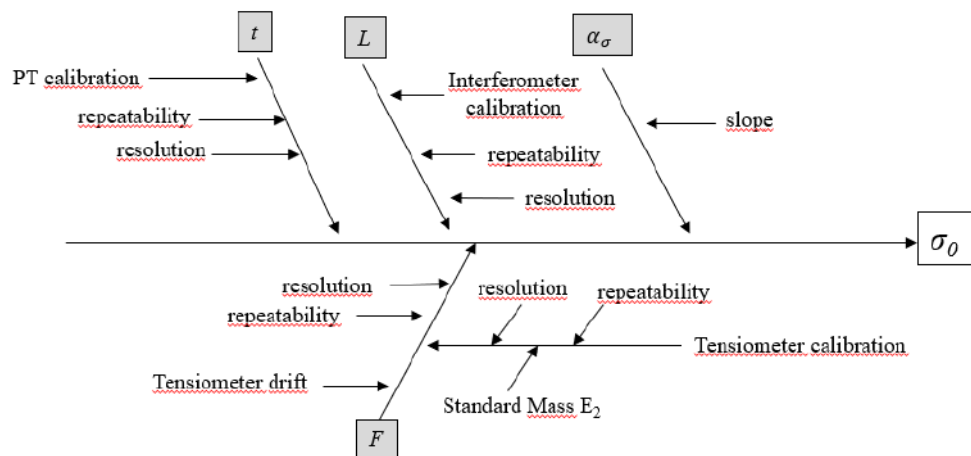
For the determination of surface tension, the value of σ obtained by Eq. 1 is a function of the following variables according to the relation: $\sigma = f(F_{\text{máx.}}, L)$. After correction for the reference temperature given by Eq. 3, it is obtained $\sigma_{t_0} = f(F_{\text{máx.}}, L, \alpha_\sigma, t)$.

The standard uncertainty, $u_c(\sigma_{t_0})$, of the measurand at the reference temperature is given by the following equation:

$$u_c(\sigma_{t_0}) = \sqrt{u_{F\text{máx.}}^2 \cdot C_{F\text{máx.}}^2 + u_L^2 \cdot C_L^2 + u_\alpha^2 \cdot C_\alpha^2 + u_t^2 \cdot C_t^2} \tag{10}$$

Table 4 – Uncertainty budget of surface tension values, σ, of the liquid under test

Contribution	Measurement	Standard uncertainty	Method of evaluation	Distribution	Degrees of freedom
Tensiometer	F (mN)	$\dfrac{s}{\sqrt{n}}$ $\dfrac{F_{\text{Res.}}}{\sqrt{12}}$ $\dfrac{U_{cal}}{k}$	Type A Type B Type B	Normal Normal Rectangular	$n-1$ 50 n
Wetted length	L (m)	$\dfrac{s}{\sqrt{n}}$ $\dfrac{L_{\text{Res.}}}{\sqrt{12}}$ $\dfrac{U_{cal}}{k}$	Type A Type B Type B	Normal Normal Rectangular	$n-1$ 50 n
Temperature coefficient	α_σ (mNm$^{-1\,\circ}$C^{-1})	S_b	Type B	Normal	50
Temperature	t (°C)	$\dfrac{s}{\sqrt{n}}$ $\dfrac{t_{\text{Res.}}}{\sqrt{12}}$ $\dfrac{U_{cal}}{k}$	Type A Type B Type B	Normal Normal Rectangular	$n-1$ 50 n

Legend: s – standard deviation of the n measurement values; $x_{\text{Res.}}$ – resolution of the measuring instrument for the quantity x; U_{cal} – expanded uncertainty of the calibration of measuring instrument; k – expansion factor; S_b – standard deviation of the slope

2.7.3. Contact angle

From the contact angle mathematical model, it was possible to determine the contribution of each uncertainty input by partial derivative of each input quantity, in order to obtain the corresponding sensitivity coefficients.

The standard uncertainty, $u_c(y)$, of the measurand, at the reference temperature, is determined by taking the value of the square root of the quadratic sum of the uncertainties of the input quantities considered significant using the law of propagation of uncertainties. The number of effective degrees of freedom, ν_{ef}, was calculated according to the Welch-Satterthwaite formula (Eq. 8).

2.7.4. Refractive Index

As referred for the others measurands, the uncertainty budget for refractive index measurements included different contributions to the standard uncertainty. They were the instrumental measurement uncertainty arising from the refractometer and input quantities, namely the standard deviation of the mean and resolution of the instrument, their values, and associated standard uncertainties, together with their degrees of freedom, leading to the combined standard uncertainty, as well as the effective degrees of freedom.

Table 5 - Uncertainty budget of the refractive index results

Contribution	Standard uncertainty	Method of evaluation	Distribution	Degrees of freedom
Instrument resolution	$\dfrac{10^{-6}}{\sqrt{12}}$	Type B	Rectangular	50
Instrument calibration (including drift)	10^{-5}	Type B	Normal	50
Measurement repeatability	$\dfrac{s}{\sqrt{n}}$	Type A	Normal	n-1
Temperature[1]	-	Type A	Normal	50

Legend: s – standard deviation of the n measurement values; [1] – the temperature uncertainty component is already considered in the uncertainty of the calibration of the measuring instrument.

3. Results and Discussion

3.1 Results of the dimensional characterization of the measuring probes

In Table 6, the results of the dimensional characterization of the measuring probes are summarized and they are used to obtain the surface properties values, as presented in section 2.

Table 6 – Results of the dimensional characterization of the measuring probes.

Measuring probes	Length, l / mm	U_l /mm	Thickness, c / mm	U_c /mm
Platinum plate	19.949	0.043	0.2066	0.0018
Topas	20.03	0.65	0.199	0.011
Borosilicate glass	21.990	0.042	0.1745	0.0043

3.2. Surface properties

The first surface tension measurements were performed with the ultrapure water as test liquid, at three different temperatures, by the Wilhelmy plate method using the platinum probe. The test liquid is filled into a glass vessel of approximately 70 mm diameter, placed in a thermoregulated vessel in the tensiometer and a sensor placed in the liquid for temperature measurement and left for about one hour until thermal equilibrium. Five measurements of surface tension were made with a sensor cleaning step between each measurement, first with appropriate solvent followed by flame. Before starting the measurements, the force sensor adjustment was realized with a mass standard.

For the other test liquids, surface tension was measured at one temperature, 20 ˚C. The results obtained are summarized in Table 7.

Table 7 – Test liquids results of surface tension, σ, at contact angle $\theta = 0°$ and different temperatures obtained by Wilhelmy plate method in platinum plate.

Samples	Temperature, t / ˚C	Surface tension, σ /(mN m⁻¹)	U_σ /(mN m⁻¹)
Ultrapure water	15.00	73.40	0.15
	20.00	72.67	0.15
	25.00	71.77	0.16
Ethylene glycol	20.04	48.74	0.22
Glycerol	19.99	64.37	0.22

After the platinum plate replacement by Topas or borosilicate glass plate, it was observed that in the time set for the measurement, equilibrium was not achieved, and an increment in force value over time was observed. In order to obtain equilibrium, the time set for experiments was increased to a maximum of five and a half hours, but still no equilibrium was achieved. Such a phenomenon may be associated with capillarity (intermolecular forces between the liquid and surrounding solid surface) or thermostabilization of the solid surface.

Preliminary results of static contact angles by Wilhelmy plate method are showed in Table 8, considering as reference for surface tension the value presented in Table 7 at 20 ˚C.

Table 8 – Results of static contact angles, θ at 20 ˚C, obtained by Wilhelmy plate method – using Topas and borosilicate glass plate.

Liquid	Ultra-pure Water		Ethylene glycol		Glycerol	
Probe	θ / °	U_θ / °	θ / °	U_θ / °	θ / °	U_θ / °
Borosilicate Glass	57.09	0.49	34.8	2.7	46.7	1.3
Topas	78.9	3.4	62.0	1.9	79.82	0.72

It is expected [2] that water evidences a smaller contact angle with glass due to its known adhesion forces. However, the experimental results evidenced a higher contact angle for water maybe due to the treatment of the borosilicate glass plate used (D263® M).

Also, as can be observed, all the liquids under test showed a higher contact angle in Topas than in borosilicate glass, meaning that Topas surface is less wettable than borosilicate glass.

In the dynamic method, the plate already immersed into the liquid was moved up and down. The depth of the immersion and the movement speed were accurately measured, while the full cycle was repeated three times. By measuring the force when moving the plate up and down and considering the buoyancy effect, the advancing and receding contact angles and, thus, the contact angle hysteresis was determined. The advancing contact angle can be described as a measure of the liquid-solid cohesion while the receding contact angle is a measure of liquid-solid adhesion.

The results of advancing and receding contact angles, and dynamic contact angle hysteresis together with their combined standard uncertainties are presented for a temperature of 20 °C in Table 9 for the borosilicate glass (BG) plates and in Table 10 for the Topas plates. Advancing and receding contact angles usually represent the maximum and minimum values that the static contact angle can have locally on the surface.

Table 9 – Results of static (θ_{BG}), advancing ($\theta_{BG,adv}$) and receding ($\theta_{BG,adv}$) contact angles, and dynamic contact angle hysteresis ($\Delta\theta_{BG,rec}$) together with their combined standard uncertainties, at 20 °C, obtained by dynamic contact angle method with borosilicate glass plates

Sample	$\theta_{BG} \pm U_\theta$ / °	$\theta_{BG,adv} \pm U_{\theta,adv}$ / °	$\theta_{BG,rec} \pm U_{\theta,rec}$ / °	$\Delta\theta_{BG,rec} \pm U_{\theta,rec}$ / °
Ultrapure water	57.09±0.49	54.4±2.5	36.1±4.5	18.3±5.1
Ethylene glycol	34.80±2.7	48.1±5.5	24.0±3.5	24.1±6.7
Glycerol	46.7±1.3	73.7±5.0	32.8±5.5	40.9±9.6

In Figure 1, a complete contact angle measurement cycle is presented for water with borosilicate glass.

Figure 1 – A complete contact angle measurement cycle for water with borosilicate glass at 20 ˚C, for the depth of the immersion (1 mm to 5 mm) and the movement speed (0.05 mm/s).
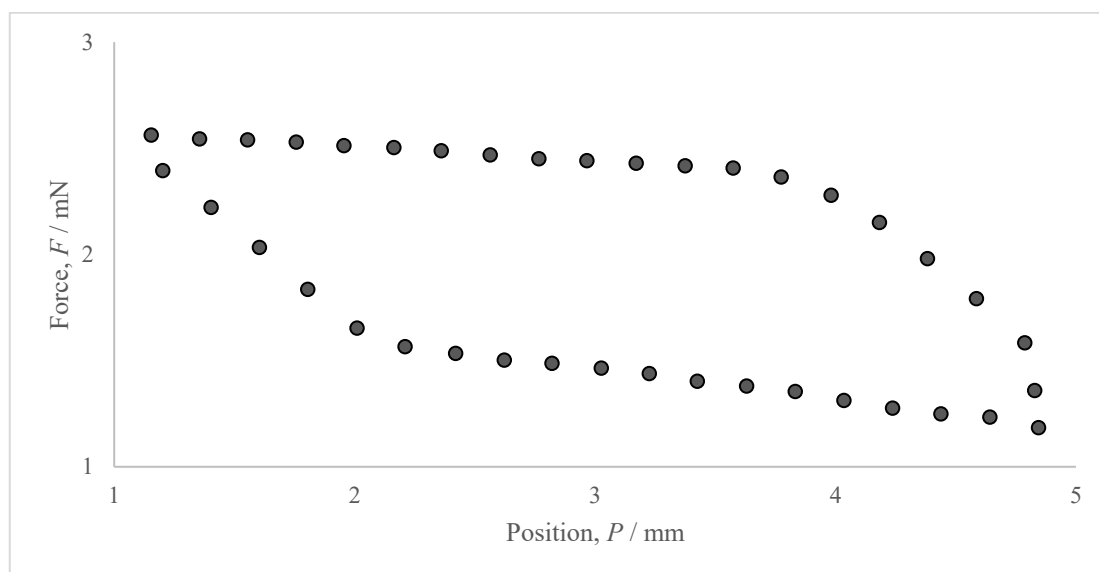

Table 10 – Results of static (θ_{Topas}), advancing ($\theta_{\text{Topas,adv}}$) and receding ($\theta_{\text{Topas,adv}}$) contact angles, and dynamic contact angle hysteresis ($\Delta\theta_{\text{Topas,rec}}$) together with their combined standard uncertainties, at 20 °C, obtained by dynamic contact angle method with Topas plates

Sample	$\theta_{\text{Topas}} \pm U_\theta$ / °	$\theta_{\text{Topas,adv}} \pm U_{\theta,\text{adv}}$ / °	$\theta_{\text{Topas,rec}} \pm U_{\theta,\text{rec}}$ / °	$\Delta\theta_{\text{Topas,rec}} \pm U_{\theta,\text{rec}}$ / °
Ultrapure water	78.9±3.4	90.7±2.4	77.5±5.3	13.2±5.8
Ethylene glycol	62.0±1.9	76.4±1.9	55.1±2.6	21.3±3.5
Glycerol	79.82±0.72	80.6±2.0	64.9±2.1	15.7±3.0

In Figure 2, a complete contact angle measurement cycle is presented for water with Topas.

Figure 2 – A complete contact angle measurement cycle for water with Topas at 20 ˚C, for the depth of the immersion (1 mm to 4 mm) and the movement speed (0.05 mm/s).
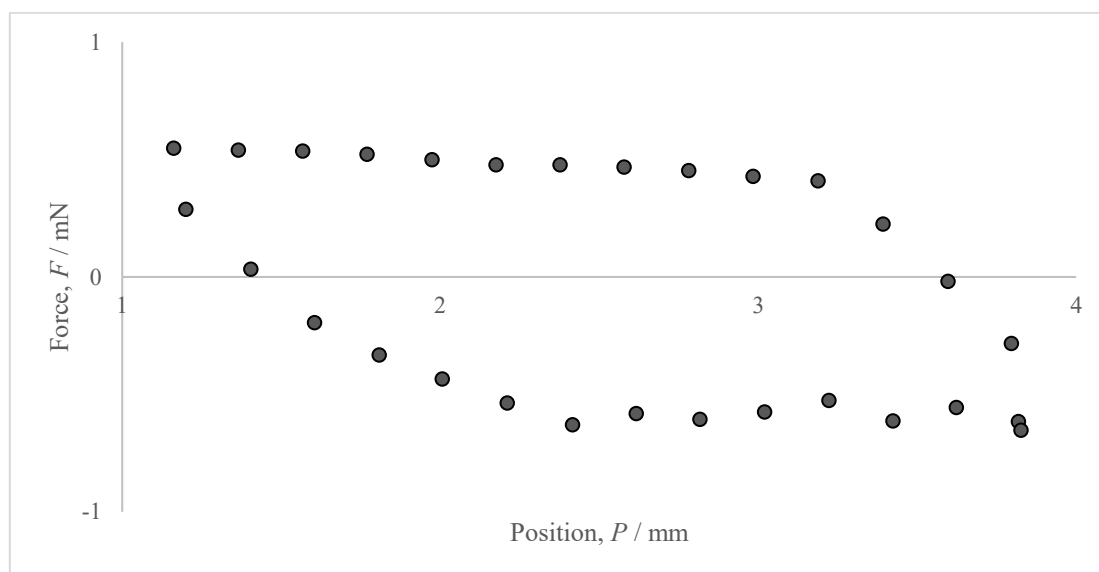
With Topas, as showed in Figure 2, the advancing part of the cycle presents negative forces. As set previously, for dynamic contact angle, Eq. 5 describes the force, *F*, for each position *h* of immersion. As the determination of the advancing/receding contact angle is made by linear regression of the experimental curve at zero depth, the buoyancy part of the Eq. 5 has no contribution, and it can be simplified according to:

$$F(h) = P\sigma \cos \theta \qquad (11)$$

The fact that the advancing part of the cycle presents negative forces for water must be further investigated. For instance, it is very likely that other contributions than hydrophobic interactions such as electrostatic forces can have a role in these results, as a contact angle greater than 90˚ was observed, see Tables 8 and 10.

Figure 3 – Pictures of the edges of the two measuring probes used in the dynamic contact angle method. A – Topas plate; B – Borosilicate glass plate
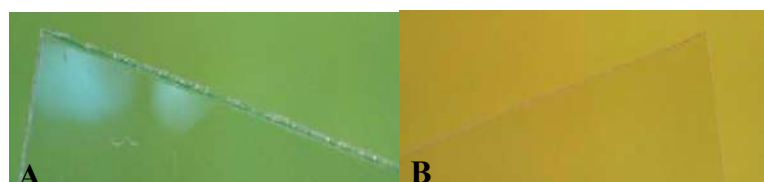

Figure 3 displays the pictures of the edges of the Topas and borosilicate glass, where irregularities on the edges of Topas probes are very noticeable, maybe due to the cutting

process. Therefore, a geometrical factor may also explain the low wettability of the Topas sample, in comparison with the borosilicate glass.

Figure 4 – Comparison between contact angles obtained in static and dynamic method for the test liquids in both surfaces. A – Borosilicate glass (BG); B – Topas
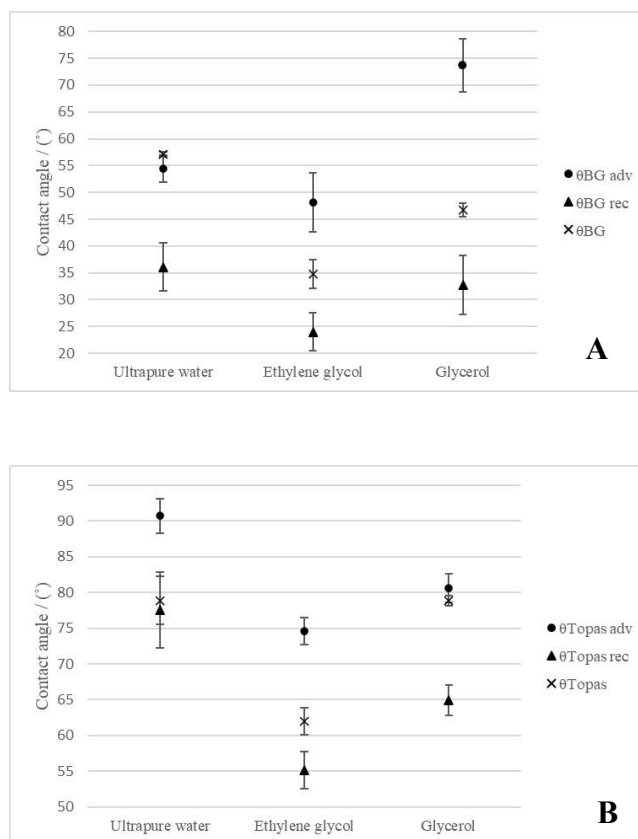
Legend: A - Results of static (θBG), advancing (θBG,adv) and receding (θBG,adv) contact angles with borosilicate glass. B - Results of static (θTOPAS), advancing (θTOPAS,adv) and receding (θTOPAS,adv) contact angles with Topas.

In Figure 8, it can be shown that the static angle value for water in borosilicate glass was out of the interval with a higher static contact angle. Additionally, the angles obtained are smaller for glass-water-air interface and higher for Topas-water-air interface, as it was previously observed that the latter had a low wettability behaviour.

For the contact angle hysteresis, both interfaces showed a small value, meaning a lower difference between advancing and receding contact angles, indicating that the ultrapure water wets and dries the surfaces more easily. This implies that these surfaces are homogeneous with a small roughness, which contradicts the discussion with the pictures of Figure 3.

3.3 Results of the refractive index

The measuring results of refractive index of both ultrapure water and ethylene glycol are presented in Table 11.

Table 11 - Results of the refractive index at 20 ˚C

Liquid	n / 1	U_n / 1
Ultrapure water	1.332 985	0.000 013
Ethylene glycol	1.431 224	0.000 013
Glycerol	1.458 932	0.000 013

As can be seen, the experimental outcome is similar to the nominal ones found in literature. Hence, this a motivating result in the sense of quantify the presence of compounds and chemical bounds, for a better knowledge of these small-scale systems [16].

4. Conclusions

This work aimed to study the interaction of test liquids and surfaces to contribute for the understanding of microfluidic liquid flow properties in microfluidic devices and the development of standardised methods and reference documents. For this purpose, the test liquids chosen were ultrapure water, ethylene glycol and glycerol and two solid materials commonly used in microfluidic devices manufacturer, borosilicate glass and Topas. In these preliminary results, some experimental challenges were met such as, for static contact angle measurements, a capillary phenomenon, for both probing materials and, for dynamic contact angle measurement, negative forces for Topas. Electrostatic interactions or geometrical irregularities may explain this behaviour.

It was also observed a higher static contact angle of any fluids with Topas than with borosilicate glass, meaning that the latter surface is more wettable than the former, which seems to be little wettable, in fact.

It is important to refer that it was difficult to find consistent reference values for contact angle as they are highly dependent of the solid-liquid-vapour interface, and coating treatment of the solid surface [18].

Further experiments could be conducted using different test liquids, and additional tests will be undertaken to enhance our comprehension of the interaction between the test liquids and Topas. This will contribute to a better understanding of the behaviour of test liquids in Topas when measuring microflow and microvolume.

The results of this study need to be further investigated as they involve the materials and the fluids of microfluidics. Refractive index results confirm the importance of this experimental technique for the characterization of such systems.

Acknowledgments

References

[1] Kirby BJ (2010). *Micro- and Nanoscale Fluid Mechanics: Transport in Microfluidic Devices*. NY, USA: Cambridge University Press.

[2] Morrison, S. Roy, (Ed.). (1990). *The chemical physics of surfaces* (2nd ed.). Springer

[3] Van Heeren, H. (2022, October 10). *Whitepaper on the measurement of hydrophobicity, hydrophilicity, and wettability*; Version: 1.0; Retrieved from; https://zenodo.org/record/7181091#.Y0b4WHbMJPY

[4] Batista, E., Sousa, J. A., Cardoso, S. & Silvério, V. (2020). Experimental testing for metrological traceability and accuracy of liquid microflows and microfluidics. *Flow Measurement and Instrumentation*, 71, 101691.

[4] Batista, E., Sousa, J. A., Alvares, M., Afonso, J. & Martins, R., (2021), Development of an experimental setup for micro flow measurement using the front tracking method. *Measurement: Sensors*, 18, 100152

www.mfmet.eu

[5] Singh, S. (2002), Refractive Index Measurement and its Applications. *Physica Scripta*, 65(2), 167-180. DOI: 10.1238/physica.regular.065a0

[6] ISO 3696:1987 (1987) *Water for analytical laboratory use - Specification and test methods*

[7] Taylor & Francis Group (2023) *Handbook of Chemistry and Physics* (104th Ed.), CRC Press,

Krüss Scientific. Retrieved from https://www.kruss-scientific.com/en/products-services/accessories/pl21

[8] Topas plates provided by Microfluidic ChipShop. Retrieved from Topas - COC - microfluidic ChipShop (microfluidic-chipshop.com)

[9] Glass plates commercially available from WillCo Wells. Retrieved from Specifications-glass-D-263-M.pdf (willcowells.com)

[10] ISO 304:1985 (reviewed in 2019); *Surface active agents – Determination of surface tension by drawing up liquid films and Technical Corrigendum* (1998)

[11] Krüss (s.d.). *User Manual* V3.2.2-11 Laboratory Desktop Software

[12] Picard, A., Davis, R. S., Gläser, M., & Fujii, K. (2008). Revised formula for the density of moist air (CIPM-2007). *Metrologia*, 45(2), 149.

[13] Purr, F., Bassu, M., Lowe, R. D., Thürmann, B., Dietzel, A., & Burg, T. P. (2017). Asymmetric nanofluidic grating detector for differential refractive index measurement and biosensing. *Lab on a Chip*, 17(24), 4265–4272. DOI:10.1039/c7lc00929a

[14] JCGM 100:2008 (2008) *Evaluation of measurement data – Guide to the expression of uncertainty in measurement*. BIPM.

[15] Lima, J. M. V. (2023). *Development and validation of methods for determination of liquid properties, volume and flow in microfluidic devices* (Dissertação de Mestrado não publicada). Universidade Nova de Lisboa, Monte da Caparica.

[16] ISO 19403-2 (2017) *Paints and varnishes — Wettability — Part 2: Determination of the surface free energy of solid surfaces by measuring the contact angle*

[17] JCGM 200 (2012), *International Vocabulary of Metrology - Basic and General Concepts and Associated Terms*. VIM 3rd edition. BIPM.

[18] Spieweck, F. & Bettin, H. (1992) Review: Solid and liquid density determination. *Technisches Messen* 59, pp. 285-292

Authors Profiles

João Lima is currently doing his thesis to obtain a master's degree in Mechanical Engineering from the NOVA School of Science and Technology – Nova University of Lisbon - Portugal

Andreia Furtado has received a PhD in Materials Science in 2012 from the Faculty of Sciences and Technology - Nova University of Lisbon – Portugal. She is the head of Properties of Liquids Laboratory of Portuguese Institute for Quality (IPQ), where she works as a senior metrology scientist since 2006.

Elsa Batista holds a PhD in Mechanical Engineering from NOVA School of Science and Technology in 2022, a master's degree in Analytical Chemistry from the University of Sciences in Lisbon in 2007 and has a degree in Applied Chemistry from the NOVA School of Science and Technology in 1999. Since 1999, she has worked at the Laboratório de Volume of Instituto Português da Qualidade as a superior technician and laboratory manager. She is the contact person and head of the volume subgroup of the EURAMET flow technical committee.

Sara Moura has received a postgraduate degree in Management in Quality and Food Safety in 2004 from the Higher Institute of Health Sciences – South; Egas Moniz C.R.L. – Portugal. She is senior technician in Properties of Liquids Laboratory of Portuguese Institute for Quality (IPQ), where she works since 2021. Her research interests are in the areas of density, viscosity, surface tension and reology.

Helena Navas has received a PhD from NOVA School of Science and Technology – Universidade NOVA de Lisboa – Portugal. She is currently Assistant Professor at the Department of Mechanical and Industrial Engineering of the NOVA School of Science and Technology – Portugal and researcher at UNIDEMI. Her research interests are in the areas of innovation, continuous improvement, quality, and process management.

Olivier Pellegrino has received a PhD in Physics in 1995 from the Pierre et Marie Curie University of Paris VI – France. He is the head of Photometry and Radiometry Laboratory of Portuguese Institute for Quality (IPQ) where he has worked as a senior metrology scientist since 2002.

ARTIGOS
EM CONFERÊNCIAS
CIENTÍFICAS

MEMQuD - Electrical characterization of memristive devices for metrological applications

Vitor Cabral [1], Xin Zheng [2,3], Fabio Michieletti [4], Ilia Valov [2,3], Gianluca Milano [5]

[1] IPQ - Instituto Português da Qualidade, Monte da Caparica, Portugal

[2] Research Centre Juelich, PGI-7, Wilhelm Johnen-Str, 52425 Juelich, Germany

[3] RWTH-Aachen university, IWE2, Sommerfeldstr. 24, 52074 Aachen, Germany

[4] POLITO - Politecnico di Torino, Corso Duca degli Abruzzi, 24 - 10129 Torino, Italy

[5] Istituto Nazionale di Ricerca Metrologica- Advanced Materials and Life Sciences Division, Strada delle Cacce 91, 10135 Torino, Turin, Italy

Memristive (or memristors) devices under specific conditions of operation can show low resistance states activated in the device corresponding to values multiple (or half-integer multiples) of the fundamental conductance value. This means that these devices offer a promising platform to observe and generate quantized resistance values in air, at room temperature, and without the need of any applied magnetic field as it is needed for the Quantum Hall Resistance Standard (QHRS) on which has been based for decades the practical realization of the electrical unit of resistance. These quantized values of resistance are in line with the spirit and fundamental characteristic of the last revision in 2019 of the International System of Units SI depending on the fixed values of the fundamental constants e, elementary charge and h, the Plank constant. The EMPIR project 20FUN06 MEMQuD - "Memristive devices as quantum standard for nanometrology" explores for the first time the potential of the quantum conductance effect in memrisitve devices to be applied in the metrology field as a quantum resistor standard.

In this work it is presented the relevant characteristics and working principles of memristive devices, the operation of these devices to produce quantized conductance states and their metrological electrical characterization.

Quantum Sensing and Metrology | Poster

(24797) - MEMRISTIVE DEVICES FOR QUANTUM METROLOGY

Vitor Cabral (Portugal)[1,2]; Luís Ribeiro (Portugal)[1,2]; Isabel Godinho (Portugal)[1]

1 - Instituto Português da Qualidade; 2 - European Metrology Network for Quantum Technologies

Memristive devices or memristors (from the contraction of memory + resistor) are a recent type of nanoscale devices where ionics is coupled with electronics and their functionalities rely on nanoionic effects. These are two-terminal devices where a switching film (usually a metal-oxide) is sandwiched in between two metal electrodes in a metal-insulator-metal structure. When operated under specific conditions, a conductive filament is formed between the metal electrodes and low resistance states can be activated in the device corresponding to values multiple (or half-integer multiples) of the fundamental conductance value, $G_0 = 2e^2/h$. These quantized values of conductance agree with the principle and fundamental characteristic of the last revision in 2019 of the International System of Units (SI) to the definition of the measurement units depending on only the fixed values of fundamental constants, e, the elementary charge and h, the Plank constant, in the case. The recent European EMPIR project 20FUN06 MEMQuD - "Memristive devices as quantum standard for nanometrology" explored for the first time the potential of the quantum conductance effect in memrisitve devices to be applied in the metrology field as a quantum resistor standard. In this work, it is presented the operation of memristive devices to produce quantized conductance states, a model for the related measurement uncertainty and their metrological characterization based on experimental measurements. ACKNOWLEDGEMENT: This work was supported by the European project MEMQuD, code 20FUN06, funded by the EMPIR programme co-financed by the Participating States and from European Union's Horizon 2020 research and innovation programme.

Keyword's : Memristive devices, quantum metrology

Quantum Communication | Poster

(24789) - PORTUGUESE QUANTUM COMMUNICATION INFRASTRUCTURE: SEED OF EUROQCI IN PORTUGAL

Margarida Vieira (Portugal)[1]; Catarina Bastos (Portugal)[1]; Andoni Santos (Portugal)[1]; Francisco Pinto (Portugal)[1]; Armando Pinto (Portugal)[2]; Nuno Silva (Portugal)[2]; Nelson Muga (Portugal)[2]; Diogo Matos (Portugal)[2]; Paulo André (Portugal)[2]; Emmanuel Cruzeiro (Portugal)[2]; Rui Rocha (Portugal)[2]; Francisco Fontes (Portugal)[3]; Rui Calé (Portugal)[3]; Miguel Freitas (Portugal)[3]; Carlos Marques (Portugal)[3]; Carlos Carvalho (Portugal)[4]; Luis Maia (Portugal)[4]; Luis Magalhães (Portugal)[4]; José Gonçalves (Portugal)[5]; António Gameiro Marques (Portugal)[6]; Manuel Honorato (Portugal)[6]; Paulo Santos (Portugal)[6]; Manfred Niehus (Portugal)[7]; António Serrador (Portugal)[7]; Mario Mendes (Portugal)[7]; Bruno Gonçalves (Portugal)[8]; Bruno Banha (Portugal)[8]; Rui Semide (Portugal)[9]; Isabel Godinho (Portugal)[10]; João Alves E Sousa (Portugal)[10]; Carlos Pires (Portugal)[10]; Ana Pinto (Portugal)[11]; João Nuno Ferreira (Portugal)[11]; Yasser Omar (Portugal)[12]; Preeti Yadav (Portugal)[12]; Pedro Mendes (Portugal)[12]; João Seixas (Portugal)[12]; João Monteiro (Portugal)[12]; Ricardo Chaves (Portugal)[13]; Tiago Dias (Portugal)[13]; Mário Caldeira (Portugal)[14]; João Nuno Sabino (Portugal)[14]

1 - Deimos Engenharia; 2 - Instituto de Telecomunicações; 3 - AlticeLabs; 4 - Adyta; 5 - IPTELECOM; 6 - Gabinete Nacional de Segurança; 7 - Instituto Superior de Engenharia de Lisboa; 8 - Warpcom; 9 - Omnidea; 10 - Instituto Português da Qualidade; 11 - FCCN; 12 - Instituto Superior Técnico; 13 - INESC-ID; 14 - PQI

Portuguese Quantum Communication Infrastructure (PTQCI) will be the first terrestrial segment of the European Quantum Communication Infrastructure (EQCI) in Portugal. PTQCI, making exclusive use of European technology, will be the first quantum enabled network testbed for which sovereign authorities can run use cases that demand high security levels in the Lisbon metropolitan area. Moreover, PTQCI will pave the way for next generation of highly secure networks in Portugal acting as testbed for other critical projects in Portugal. For instance, Égide which is the new secured network of National Security Agency to manage classified information up to Secret. PTQCI's use cases are based on: sharing quantum secure generated keys to enable applications like secure multiparty computation, secret sharing and other state-of-the-art cryptographic protocols; Connecting and extending secure networks using cipher machines feed by the quantum key to provide harden confidentiality and authentication; Connecting relevant data centres to share privately information. PTQCI will prepare the network expansion to farther locations in Portugal and to Spain, including the assessment of the ground locations to space segment infrastructures. Furthermore, it will be designed from the start with a strong engagement with Spanish EQCI counterparts, building on joint knowledge and fruitful collaboration to achieve full EQCI interoperability at Iberian scale.The testbed, that shall be developed in the metropolitan Lisbon area, involves both academic, public and private stakeholders, will be testing new or different technologies,

including free-space links and networking, as well as long-distance terrestrial and spatial solutions, including the connection to Space assets.

Keyword's : quantum communications, quantum network, euroQCI

OC1.14 Metrological study on a relationship between salinity and surface tension of buffered artificial seawaters

M. Serra, S. Moura, R. Quendera, O. Pellegrino

IPQ, Instituto Português da Qualidade, I.P., 2829-513 Caparica, Portugal
Email: smoura@ipq.pt

This work displays the preliminary results of a metrological study on a relationship between surface tension, γ, contact angle, θ, density, ρ, and absolute salinity, S_A, of buffered artificial seawater. Indeed, whereas natural seawater exhibits high variability in temperature, pressure and dissolved organic matter composition, playing a significant role in ocean water circulation,[1] its inorganic matter content remains relatively constant. Seawater samples density results measured with an oscillation-type densimeter, and refractive index results displayed a direct correlation to absolute salinity,[2] due to the total dissolved salt content. Concomitantly surface tension, linked to contact angle by the Young equation,[3] tends to depend on S_A and temperature, t, mainly due to intermolecular interactions within these systems. Tris(hydroxymethyl)aminomethane (TRIS) buffers and hydrochloric acid in artificial seawater matrix (ASW) within [35; 70] g/kg S_A interval and Standard Seawater were tested to assess the mathematical relationship between seawater γ and S_A and t relatively to that of ultrapure water, as evidenced by the International Association for the Properties of Water and Steam (IAPWS).[4] TRIS buffered ASWs are considered primary standards, traceable to the Harned cell, matching the composition of natural seawater, according to the International Association for the Physical Sciences of the Oceans (IAPSO) 2008 recommendations, and used to calibrate pH measurement instruments in oceanographic studies.[5-7] In this work, web-based software applications[8,9] were used to estimate measurement uncertainties, allowing the quantities of interest to characterize potential certified reference materials.

References

1. R. Pawlowicz; *Nature Education Knowledge* **2013**, *4*,13.
2. A. Furtado *et al; Int. J. Metrology Quality Eng.* **2022**, *13*, 10.
3. I. Gao *et al.; Langmuir* **2006**, *22*, 6234.
4. IAPWS, Revised release on surface tension of ordinary water substance, 2014. available from http://www.iapws.org.
5. T.A. DelValls, *et al.; Res. Papers* **1998**, *45*, 1541-1554.
6. G. M. Marion, *et al.; Marine Chem.* **2011**, *126*, 89-96.
7. A. G. Dickson *et al.; Metrologia* **2015**, *53*, R26.
8. National Institute of Standards and Technology (NIST), *NIST Uncertainty Machine*, available from https://uncertainty.nist.gov/.
9. Laboratoire National de Métrologie et d'Essais (LNE), *LNE Uncertainty software*, available from https://www.lne.fr/en/software/lne-uncertainty-evaluating-measurement-uncertainties-using-gum-and-monte-carlo.

AS "ARTES" DO MUSEU - DA PALEOGRAFIA E ARQUEOLOGIA... À INTELIGÊNCIA ARTIFICIAL

António Neves[1]
[1]Instituto Português da Qualidade, Rua António Gião, 2, 2829-513 Caparica
aneves@ipq.pt

RESUMO
O Museu de Metrologia do IPQ encontra-se num processo de transição digital, no que respeita às formas de divulgação da informação e apoio aos visitantes. Na Exposição Permanente "Pesos e Medidas em Portugal" é já possível aceder a informação sobre o contexto histórico da criação/utilização das peças expostas, utilizando um *smartphone*, através de códigos QRCode, que remetem para vídeos explicativos em português, construídos com tecnologias emergentes, incluindo inteligência artificial. Até final do ano, essa informação poderá também ser acedida em inglês e francês. Contudo, o conhecimento assim transmitido continua a depender de ferramentas de investigação tradicionais, nomeadamente, para os documentos escritos, a paleografia, e para os vestígios materiais não escritos, a arqueologia. Apresentam-se dois casos concretos da utilização destas "ciências", os quais contribuíram para produzir a narrativa histórica transmitida sobre a maior reforma metrológica anterior ao Sistema Métrico Decimal.

PALAVRAS-CHAVE: METROLOGIA, PALEOGRAFIA, ARQUEOLOGIA, HISTÓRIA, INTELIGÊNCIA ARTIFICIAL, TRANSIÇÃO DIGITAL

REFERÊNCIAS
[1] BARBOSA, Duarte (1812-1813) - "Livro de Duarte Barbosa"; in Colecção de notícias para a história e geografia das nações ultramarinas que vivem nos domínios portugueses ou que lhes são vizinhas. Lisboa: Academia Real das Ciências, tomo 2, n° 7, 231-396.
[2] COUVREUR, Raúl da Costa - O nome do marco abolido por D. João II por provisão de 14 de Outubro de 1488. In Anais das bibliotecas e arquivos de Portugal: Revista Trimestral de Bibliografia, Bibliografia, Biblioteconomia, Bibliotecografia, Arquivologia, etc. Vol. XVI, n.ºs 63 e 64 ([1942]). Lisboa: Tipografia da Emprêsa Nacional de Publicidade, 1944.
[3] Livro Em que dá relação do que viu e ouviu no Oriente Duarte Barbosa. Introdução e notas de Augusto Reis Machado. Lisboa: Divisão de Publicações e Biblioteca, Agência Geral das Colónias, 1946.
[4] LOPES, Luís Seabra - Os Marcos de Colonha e de Tria e a Reforma dos Pesos de Dom João II (1487-1488); in Revista Portuguesa de História. ISSN: 0870.4147, t. 51, (2020), p. 83-105.
[5] VIANA, Mário - O arrátel em Portugal nos séculos XIV e XV e o seu contexto económico; in Regulamentação dos Mesteres em Portugal nos Finais da Idade Média. Laboratório de Paisagens Património e Território, Vol. II, 2022. ISBN 978-989-8963-68-0. pp 13-25.

DA SUSTENTABILIDADE DO SI

Olivier Pellegrino[1]

[1]Instituto Português da Qualidade, Rua António Gião, 2, 2829-513 Caparica

opellegrino@ipq.pt

RESUMO

Esta comunicação pretende ilustrar a sustentabilidade do Sistema Internacional de unidades (SI) através das recentes alterações ocorridas. Em primeiro lugar, são apresentadas algumas consequências da revisão ocorrida em 2019. É assim abordada a utilidade da distinção entre as unidades de base e as unidades derivadas do SI [1].

Com efeito, essas unidades derivadas podem ser mais diretamente ligadas às constantes definidoras do que as unidades de base [2]. Num segundo lugar, o alargamento dos prefixos do SI, aprovado em 2022, é apresentado e é lembrado a evolução dos prefixos SI desde a criação do Bureau Internacional dos Pesos e Medidas (BIPM) [3]. Algumas sugestões de futuros desenvolvimentos são também apresentadas [4], [5].

PALAVRAS-CHAVE: METROLOGIA, CONSTANTES DEFINICIONAIS, UNIDADES SI, PREFIXOS SI

REFERÊNCIAS

[1] R. J. C. Brown "On the distinction between SI base units and SI derived units", Metrologia, 61, 013001, (2024).

[2] P. Blattner, R. J. C. Brown "Relating SI units to the 'defining constants'", Metrologia, 61, 043001, (2024).

[3] R. J. C. Brown "A further short history of the SI prefixes", Metrologia, 60, 013001, (2023).

[4] R. J. C. Brown "Considerations on compound SI prefixes", Measurement, 140, 237-9, (2019).

[5] R. J. C. Brown "Future requirements for non-decimal unit prefixes in chemical measurement", Accredit. Qual. Assur., 24, 245-7, (2019).

DESENVOLVIMENTO DE MÉTODOS PARA DETERMINAÇÃO DE CAUDAL E VOLUME EM SISTEMAS MICROFLUÍDICOS

Elsa Batista[1], João Alves e Sousa[1], Diogo Fortes[2]
[1]Instituto Português da Qualidade, Rua António Gião, 2, 2829-513 Caparica
[2]Universidade NOVA de Lisboa, 2829-516 Caparica
ebatista@ipq.pt

RESUMO

As aplicações da tecnologia microfluídica estão a crescer exponencialmente, especialmente na área da saúde, com destaque para órgãos em *chip* e a caracterização de novos fármacos em "Lab-on-a-chip" [1]. Esta tecnologia sustentável permite reduzir o tempo de ensaio e a quantidade de reagentes utilizados, graças às dimensões micrométricas dos dispositivos microfluídicos (área comum de canais microfluidícos na ordem de 50 mm por 100 mm). Portanto, é essencial garantir a exatidão das medições e a rastreabilidade destes dispositivos através de métodos de calibração e ensaio adequados para as diferentes grandezas medidas.

O Laboratório de Volume e Caudal do Instituto Português da Qualidade, no âmbito da sua participação no projeto MFMET - "Establishing Metrology Standards in Microfluidic Devices", financiado pelo "European Metrology Programme for Innovation and Research (EMPIR)", comparou diferentes métodos de medição de caudal e volume em sistemas microfluídicos, nomeadamente o método gravimétrico [2] e o método "front track" [3]. Foram utilizados vários *chips* microfluídicos de diferentes materiais, como vidro e PDMS (polidimetilsiloxano), e dois geradores de caudal distintos: uma seringa perfusora e uma bomba de pressão.

Os resultados obtidos pelos dois métodos foram consistentes, mas verificou-se que o método gravimétrico oferece melhor exatidão e menor incerteza nos resultados tanto em volume quanto em caudal. No entanto, o método "front track" tem a vantagem de permitir a medição do caudal diretamente no canal microfluídico.

PALAVRAS-CHAVE: VOLUME, CAUDAL, MICROCHIPS, INCERTEZA, GRAVIMETRIA, FRONT TRACK

REFERÊNCIAS

[1] Ayuso, J.M., et al., A role for microfluidic systems in precision medicine. Nature Communications, 2022. 13(1): p. 3086.

[2] Bissig, H., Petter, H. T., Lucas, P., Batista, E., Filipe, E., Almeida, N., ... & Sparreboom, W. (2015). Primary standards for measuring flow rates from 100 nl/min to 1 ml/min–gravimetric principle. Biomedical Engineering/Biomedizinische Technik, 60(4), 301-316.

[3] EURAMET Guide 27 - Guidelines for the Calibration of Drug Delivery Devices and Infusion Device Analysers | TC-F | Version 1.0, 02/2024.

ENSAIO DE APTIDÃO NACIONAL NO DOMÍNIO DE FORÇA

Isabel Spohr[1], Cláudia Silva[2]
[1]Instituto Português da Qualidade, Rua António Gião, 2, 2829-513 Caparica
[2]RELACRE, Campus do Lumiar – Edifício D, 1º Andar,1649-038 Lisboa
ispohr@ipq.pt

RESUMO

Os Ensaios de Aptidão nacionais têm como objetivo avaliar as capacidades de medição e de calibração dos laboratórios acreditados ou que pretendam vir a obter a acreditação, estruturando assim a cadeia nacional hierarquizada dos padrões.

As vantagens dos Ensaios de Aptidão são por exemplo: • A avaliação do desempenho dos Laboratórios; • A demonstração da competência técnica perante terceiros; • O reforço da autoconfiança no processo de aprendizagem; • O estabelecimento de confiança recíproca entre Laboratórios congéneres; • A exclusão de erros sistemáticos, não detetáveis por outros métodos; • A validação de métodos; • A implementação de ações corretivas e preventivas após análise dos resultados obtidos; • A obtenção de reconhecimento mútuo de resultados de ensaio, tanto a nível nacional como internacional.

O domínio de Força do Laboratório Nacional de Metrologia do Instituto Português da Qualidade, foi a entidade com a responsabilidade técnica pela realização da comparação nacional "Calibração de Transdutor de Força de 20 kN no modo de compressão", que decorreu entre outubro de 2023 e fevereiro de 2024 e em que participaram 3 laboratórios nacionais.

O IPQ possui os Padrões Nacionais de Força, constituídos por 3 Máquinas de Força Padrão (FSM):

• Sendo que as 2 primeiras FSM, Padrões de 5 kN e de 100 kN, são padrões primários, utilizando como princípio físico a 2.ª lei de Newton, e por isso designadas por padrões de massas suspensas;

• A terceira máquina é uma amplificação mecânica por intermédio de uma alavanca, tendo numa extremidade da alavanca a FSM de 100 kN e na outra extremidade conseguimos obter uma ampliação de 10 vezes o valor da força gerada, ou seja, o sistema de alavanca permite atingir o valor máximo de 1000 kN (1 MN).

As melhores capacidades de medição (CMC) do IPQ para valores de força de 50 N a 100 kN, estão publicadas no *Bureau International des Poids et Mesures* desde outubro de 2005.

Neste trabalho serão apresentados os resultados deste Ensaio de Aptidão, avaliando e demonstrando o desempenho da medição dos participantes, considerando o valor de referência determinado, bem como a estimativas dos valores de incerteza de cada laboratório participante

PALAVRAS-CHAVE: ENSAIO DE APTIDÃO, CALIBRAÇÃO, FORÇA, AVALIAÇÃO DE DESEMPENHO.

REFERÊNCIAS

[1] ISO/IEC 17043:2023 - Conformity assessment —General requirements for the competence of proficiency testing providers.
[2] NP EN ISO/IEC 17025:2018 - Requisitos Gerais de Competência para Laboratórios de Ensaio e Calibração.
[3] Evaluation of Measurement Data - Guide to the expression of uncertainty in measurement, JCGM 100:2008 (GUM 1995 with minor corrections).
[4] ISO 376:2011 - "Metallic materials -Calibration of force-proving instruments used for the verification of uniaxial testing machines".

ESTUDO METROLÓGICO SOBRE TENSÃO SUPERFICIAL E SALINIDADE ABSOLUTA

M. Serra[1], Sara Moura[1], Raquel Quendera[1], Olivier Pellegrino[1]
[1]Instituto Português da Qualidade, Rua António Gião, 2, 2829-513 Caparica
smoura@ipq.pt

RESUMO

A circulação de água nos oceanos deve-se às diferenças observadas na temperatura, pressão e teor de matéria orgânica dissolvida [1]. Sabe-se, no entanto, que a concentração de matéria inorgânica presente na água do mar permanece relativamente constante. Os resultados de massa volúmica do conteúdo total de sais presentes em amostras de água do mar, medidos com um densímetro de tubo vibrante, e os resultados de índice de refração mostraram uma correlação direta com a salinidade absoluta [2]. A água do mar artificial (*artificial seawater*, ASW) tamponada com TRIS (tris(hidroximetil)aminometano) é considerada um padrão primário, rastreável à célula de Harned, correspondendo à composição da água do mar natural, de acordo com as recomendações da Associação Internacional para as Ciências Físicas dos Oceanos (IAPSO) 2008. Em particular, a ASW é utilizada para calibrar instrumentos de medição de pH em estudos oceanográficos [3], [4], [5].

Este trabalho pretende apresentar os resultados preliminares de um estudo metrológico sobre a relação entre a tensão superficial, γ, e a salinidade absoluta, S_A, de amostras de água do mar tamponada artificial e soluções aquosas de NaCl (cloreto de sódio). Foram testadas matrizes de água do mar artificial com S_A= 35 g/kg (tampão TRIS e ácido clorídrico, em ASW e padrão de água do mar, OSIL) e soluções aquosas de NaCl no intervalo de S_A de [35; 100] g/kg para avaliar a relação matemática entre γ, S_A e t relativamente à da água ultrapura, como evidenciado pela Associação Internacional para as Propriedades da Água e do Vapor (IAPWS) [6], [7].

Observou-se que a tensão superficial apresenta uma relação com a salinidade absoluta e a temperatura, principalmente devido às interações intermoleculares nestes sistemas, permitindo relacionar matematicamente estas grandezas. Neste trabalho, o balanço das incertezas de medição foi realizado de acordo com o GUM (*Guide to the expression of uncertainty in measurement*) [8] e por meio de aplicações elaboradas por Laboratórios Nacionais de Metrologia disponíveis na *internet* [9], [10]. Obtiveram-se relações lineares entre tensão superficial e temperatura para cada valor de salinidade absoluta testada, assim como entre a tensão superficial e salinidade. Os valores obtidos foram comparados com os presentes na literatura [7]. Do mesmo modo, estudou-se a possibilidade da utilização de sistemas mais simples para mimetizar o comportamento da água do mar em tensão superficial, dando aso à sua futura utilização como material de referência certificado.

PALAVRAS-CHAVE: METROLOGIA, TENSÃO SUPERFICIAL, SALINIDADE ABSOLUTA, ÁGUA DO MAR ARTIFICIAL TAMPONADA

REFERÊNCIAS

[1] R. Pawlowicz "Key Physical Variables in the Ocean: Temperature, Salinity, and Density", Nature Education Knowledge, 4(4), 13, (2013).

[2] A. Furtado et al. "Absolute salinity determination by oscillation-type densimetry and refractometry", International Journal of Metrology and Quality Engineering, 13, 10, (2022).

[3] T. A. DelValls et al. "The pH of buffers based on 2-amino-2-hydroxymethyl-1, 3-propanediol ('tris') in synthetic sea water", Deep Sea Research Part I: Oceanographic Research Papers, 45(9), 1541-1554, (1998).

[4] G. M. Marion et al." pH of seawater ", Marine Chemistry, 126(1-4), 237-9, (2011).

[5] A. G. Dickson et al. "Metrological challenges for measurements of key climatological observables. Part 3: seawater pH", Metrologia, 53(1), R26, (2015).

[6] IAPWS (2014) Revised Release on Surface Tension of Ordinary Water Substance, disponível em: http://www.iapws.org.

[7] IAPWS (2019) Guideline on the Surface Tension of Seawater, disponível em: http://www.iapws.org.

[8] Evaluation of Measurement Data - Guide to the expression of uncertainty in measurement, JCGM 100:2008.

[9] National Institute of Standards and Technology (NIST), NIST Uncertainty Machine, disponível em: https://uncertainty.nist.gov/.

[10] Laboratoire National de Métrologie et d'Essais (LNE), LNE Uncertainty software, disponível em https://www.lne.fr/en/software/lne-uncertainty-evaluating-measurement-uncertainties-using-gum-and-monte-carlo.

PREPARAÇÃO DE PADRÕES GASOSOS DE ETANOL EM AR

Carlos J. Costa[1], Cristina Palma[1], Florbela A. Dias[1]
[1]Instituto Português da Qualidade, Rua António Gião, 2, 2829-513 Caparica
ccosta@ipq.pt

RESUMO

O Laboratório de Alcoolimetria do Instituto Português da Qualidade efetua a calibração de alcoolímetros de despiste e é responsável pelo controlo metrológico legal de alcoolímetros evidenciais, em Portugal.

Nos ensaios laboratoriais, são utilizadas misturas gasosas de etanol em nitrogénio para simular diferentes teores de álcool no ar expirado (T_{AE}), que, por sua vez, vão corresponder a diferentes teores de álcool no sangue (T_{AS}). Estes materiais de referência certificados (MRC) são preparados no Laboratório de Gases de Referência (LGR), do Instituto Português da Qualidade, de acordo com as normas ISO 6142-1:2015 [1], ISO 6143:2001 [2] e NP EN ISO 17034:2020 [3], e para o qual possui capacidade de medição e calibração (CMC), inscrita na base de dados do *Bureau Internacional des Poids et Mesures* (BIPM).

Com a recente republicação da portaria que regulamenta o controlo metrológico de alcoolímetros [4], passou-se a adotar as orientações da versão atual da Recomendação da Organização de Metrologia Legal (OIML), R 126 [5] [6]. Neste documento, é referido que, em caso de ser utilizado gás sob pressão para gerar os padrões gasosos de etanol, o principal componente deste deverá ser o ar seco. Assim, com vista à adoção desta medida nos ensaios realizados no Laboratório de Alcoolimetria, foi efetuado um estudo sobre a capacidade de produção deste tipo de misturas no LGR e estabelecida a correspondência com os padrões de etanol em nitrogénio, tradicionalmente utilizados.

Foram preparadas duas misturas com uma fração molar de aproximadamente 190 μmol/mol de etanol. Uma em matriz de nitrogénio e outra em matriz de ar seco. Ambas foram posteriormente calibradas por espectroscopia de infravermelho não dispersivo (NDIR) e por cromatografia gasosa com deteção por ionização de chama (GC-FID).

Neste trabalho, são apresentados os resultados obtidos, nomeadamente, o estudo de interferentes efetuado no analisador NDIR e a comparação dos resultados obtidos pelos dois métodos analíticos utilizados, NDIR e GC-FID. Futuramente, prevê-se enviar a mistura de etanol em ar seco para um laboratório congénere para um ensaio de comparação interlaboratorial, com vista à validação do método e suportar a inscrição de uma nova CMC.

PALAVRAS-CHAVE: ALCOOLIMETRIA, ALCOOLÍMETRO, ETANOL EM AR, MATERIAL DE REFERÊNCIA

REFERÊNCIAS

[1] ISO 6142-1:2015 – Gas analysis — Preparation of calibration gas mixtures — Part 1: Gravimetric method for Class I mixtures.

[2] ISO 6143:2001 – Gas analysis — Comparison methods for determining and checking the composition of calibration gas mixtures.

[3] NP EN ISO 17034:2020 – Requisitos gerais para a competência dos produtores de material de referência.

[4] Portaria n.º 366/2023, de 15 de novembro, Aprova o Regulamento do Controlo Metrológico Legal dos Alcoolímetros.

[5] OIML R 126-1:2021 (E), Evidential breath analysers, Part 1: Metrological and technical requirements.

[6] OIML R 126-2:2021 (E), Evidential breath analysers, Part 2: Metrological controls and performance tests.

RASTREABILIDADE AO SI EM MEDIÇÃO DE PARÂMETROS DE RUGOSIDADE

Fernanda Saraiva[1]

[1]Instituto Português da Qualidade, Rua António Gião, 2, 2829-513 Caparica
fsaraiva@ipq.pt

RESUMO

As atuais condições de produção e as exigências de qualidade dos produtos fabricados implicam investimentos. A metrologia, como garantia desta qualidade, deve fornecer alternativas sustentáveis e cientificamente válidas e adequadas às exigências desta fabricação. O IPQ, enquanto entidade nacional de metrologia, procura a atualização constante dos processos de medição implementados e dos serviços de calibração disponibilizados, sobretudo através da participação em projetos de investigação com os laboratórios congéneres. Ao participar no projeto EMPIR ProbeTrace com outros nove Institutos Nacionais de Metrologia, o IPQ entrou numa cadeia de transferência de conhecimentos na área da metrologia de equipamentos e padrões de medição de superfície [1]. Até à data, a rastreabilidade metrológica no IPQ, para medição e análise de parâmetros de rugosidade (ISO21920-2:2021), tem sido obtida através da calibração externa em laboratório congénere de um padrão de rugosidade tipo A (ISO 5436-1:2000).

O trabalho inicial do projeto ProbeTrace envolveu a caracterização metrológica de parâmetros de rugosidade de uma superfície, após a calibração do rugosímetro ter sido efetuada com diferentes tipos de padrões de rugosidade, artefactos rastreados ao SI [2]. Este método é o procedimento normativo atualmente utilizado.

Uma nova rota sustentável de rastreabilidade ao SI em medições da textura superficial será divulgada nesta comunicação, onde serão apresentados os estudos, os resultados e os desenvolvimentos implementados no IPQ, decorrentes do ProbeTrace, para a potencial utilização de transdutores de deslocamento linear portáteis como padrões de referência na calibração ou verificação de máquinas-ferramentas ou de equipamentos de medição, como o rugosímetro, quer na indústria querem laboratórios de calibração.

PALAVRAS-CHAVE: RASTREABILIDADE METROLÓGICA, RUGOSIDADE, SONDAS INDUTIVAS

REFERÊNCIAS

[1] 18RPT01 Probe Trace Traceability for contact probe and stylus instrument measurements, disponível em: www.probetrace.org.

[2] F. Saraiva, P. Neves, C. Pires, J. A. Sousa, "A Novel Traceability Route to the SI in Roughness Measurements at IPQ", Acta IMEKO, www.imeko.org,Vol. 12 No. 3 (2023) (https://doi.org/10.21014/actaimeko.v12i3.1456).

POSTERS

MEMRISTIVE DEVICES FOR QUANTUM METROLOGY

Vitor Cabral (Portugal)[1,2]; Luís Ribeiro (Portugal)[1,2]; Isabel Godinho[1] (Portugal)

1 - Instituto Português da Qualidade; 2 - European Metrology Network for Quantum Technologies

Background

Memristive devices or **memristors** (from the contraction of memory + resistor) are a recent type of nanoscale devices where ionics is coupled with electronics and their functionalities rely on nanoionic effects. These are two-terminal devices where a switching film (usually a metal-oxide) is sandwiched in between two metal electrodes in a metal-insulator-metal structure.
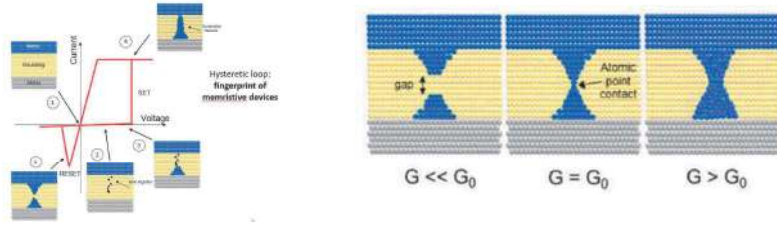
When operated under specific conditions (of the applied electric field), a conductive filament is formed between the metal electrodes and low resistance states can be activated in the device corresponding to values multiple (or half-integer multiples) of the **fundamental conductance** value, $G_0 = 2e^2/h$.

$$G(\mathrm{n}) = \mathrm{n} \times G_0 = \mathrm{n}\frac{2e^2}{h}$$

Metrological application as an intrinsic quantum standard for electrical resistance

Memristive quantized values of conductance (or resistance) agree with the principle and fundamental characteristic of the last revision in 2019 of the International System of Units (SI) to the definition of the measurement units depending on only the fixed values of fundamental constants, *e*, the elementary charge and *h*, the Plank constant.

The recent European EMPIR project **20FUN06 MEMQuD - "Memristive devices as quantum standard for nanometrology** explored for the first time the potential of the quantum conductance effect in memrisitve devices to be applied in the metrology field as an **intrinsic quantum resistor standard working at room temperature.**

The integration of memrisitve devices in CMOS circuits capability also opens the possibility of obtaining a **"zero chain traceability"** resistance standard available *in situ* and with the possibility to be integrated in any type of electronic measurement instrumentation to support **auto-adjustment** and **auto-calibration** process. The covered metrological range of applications will depend on the uncertainty that could be attributed to the generated reference quantity of resistance generated by these devices.

Electrical characterization of Ag/SiO$_2$/Pt based Memrisitve cell

A **program and verify approach** was applied to obtain and stabilize the desired quantized states, 1 G$_0$ and 2 G$_0$.

This approach consists firstly in cycling the device in a sequential set and reset process by applying a sweep voltage control signal.

The conductance of the formed filament in each set cycle is continuously measured and a condition was established to detect the values of 1 G$_0$ and 2 G$_0$ formed in the reset cycle: if the last 5 measured values remain in the interval 1 G$_0$ and 2 G$_0$ ± 0.5 G$_0$, the reset cycle is interrupted, and a constant voltage is applied to the device to sustain and read the conductance step.

Relevant Metrological characteristics
- *Parasitic resistance*
- Repeatability (variability of consecutive measurements in each step)
- Reproducibility (variability of the mean value for different steps obtained from different cycles)

**Conductance values for different cycles**
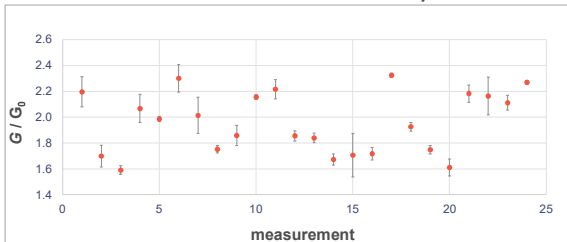
Dots - mean values of each step (limited to first 100 values)
Bars = standard deviation ((Repeatability)
Values scatter => reproducibility

Mean value (all points) = **1,96 G$_0$**;
Repeatability = **0,008 G$_0$**; Reproducibility = **0,048 G$_0$**
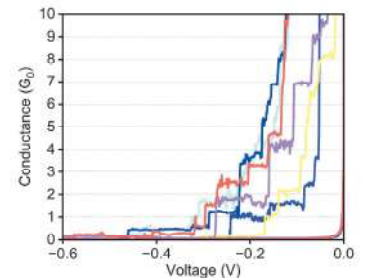
Set and reset cycle (electrical stimuli - sweep voltage signal)
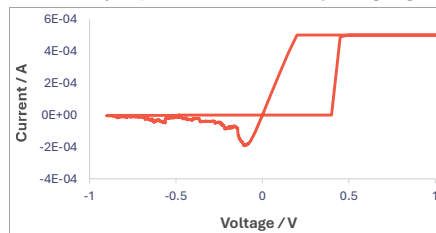
Conductance value along time for a stabilized state
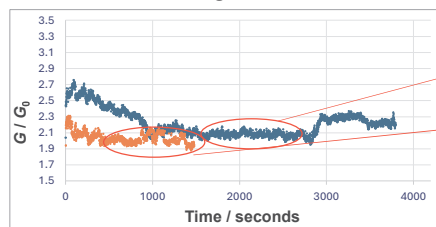
Measurements of different reset cycles

R = 6.19 kΩ (2.08 G$_0$) ± 0.04 %

R = 6.39 kΩ (2.02 G$_0$) ± 0.09 %

(*R* = mean value ± standard deviation of the mean)

Model Equation for the Resistance value , R

$$R = \frac{1}{nG_0} + \delta R_p + \delta R_{re} + \delta R_{rr}$$

δR_p is the correction of the equivalent parasitic resistance associated with the quantized resistance ($1/nG_0$); δR_{re} and δR_{rr} represent repeatability and reproducibility effects, respectively.

A combined uncertainty of R, could be expressed by the propagation of uncertainties to equation above, resulting in the following equation:

$$u_c^2(R) = u^2(\delta R_p) + u^2(\delta R_{re}) + u^2(\delta R_{rr})$$

$u(\delta R_p)$ is revealed by the difference between the mean value of R and the expected nominal value; $u(\delta R_p)$ and $u(\delta R_{rr})$ are estimated by the experimental standard deviation of the measurements.

Conclusions

- The potential of the quantum conductance effect in memrisitve devices was for the first time explored to be applied in the metrology field as an intrinsic quantum resistor standard.
- A metrological characterization of the conductance states 1 G$_0$ and 2 G$_0$ was conducted including an interlaboratory comparison.
- Improving the understanding of the relationship between this quantum phenomenon and the discrete atomic structures of the conductive filaments needs further investigation.

Future work: improve reproducibility and stability of quantized resistance states to minimize the related measurement uncertainty

References: G. Milano, F. Ferrarese Lupi, M. Fretto, C. Ricciardi, N. De Leo, L. Boarino, **Memristive Devices for Quantum Metrology**, Adv., Quantum Technol, 5, 2020, DOI: 10.1002/qute.202070051; V. Cabral, A.Cultrera, S. Chen, J. Pereira, L. Ribeiro, I. Godinho, L. Boarino, N. De Leo, L. Callegaro, S. Cardoso, I. Valov, G. Milano, **Memristive devices for metrological applications** - ACTA IMEKO ISSN: 2221-870X, September 2023, Volume 12, Number 3, 1 – 5; V. Cabral, X. Zheng, F. Michieletti, I. Valov, G. Milano, **MEMQuD - Electrical characterization of memristive devices for metrological applications**, European Materials Research Society - 2024 Spring Meeting - ALTECH 2024 - Analytical techniques for accurate nanoscale characterization of advanced materials

Instituto Português da Qualidade
Portuguese Institute for Quality (National Metrology Institute)

The influence of the acidity scale in seawater pH determination: application of the new unified pH scale

IPQ

Raquel Quendera[1,2,3], Maria João Nunes[2], Ana Luísa Fernando[2,3], Carla Palma[4], Olivier Pellegrino[1], João Alves e Sousa[1], Isabel Godinho[1]
[1]Instituto Português da Qualidade, [2]Nova School of Science and Technology-NOVA FCT, Universidade Nova de Lisboa,
[3]Mechanical Engineering and Resource Sustainability Center, [4]Instituto Hidrográfico, rquendera@ipq.pt

Introduction:

30% of anthropogenic CO_2 is absorbed by the oceans promoting the formation of carbonic acid, decreasing seawater pH and causing ocean acidification. Measuring pH in seawater is complicated due to its complex matrix and high ionic strength $(I \geq 0.7$ mol·kg-1), affecting the accuracy and the reliability of pH measuring systems. Accurate pH measurements require Certified Reference Materials (CRM) with an expanded uncertainty UpH ≤ 0.006, to accomplish with the Sustainable Development Goals (SDG) of the United Nations (UN) agenda for 2030.

A unified pH scale (pHabs) was developed during the EURAMET EMPIR Joint Research Project (2018-2021) to standardize pH measurements traceable to the International System of Units (SI). This work aims to validate the unified pH scale for saline matrices by comparing it with measurements from primary potentiometry and UV/VIS spectrophotometry, while also investigating the influence of salinity on pHabs measurements to reduce uncertainty for oceanographic applications.

Experimental:

➤ **Unified pH scale:**

Universal reference state $H^+_{(g)}$ at 1 bar and 25 °C: $\mu_{abs}(H^+, solv) = 0$ kJ mol^{-1} ➡➡ **Not experimentally realizable**
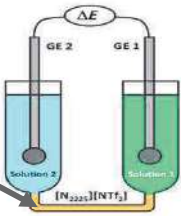
Differential potentiometry:

$$pH_{abs} = \frac{\mu_{abs}(H^+, solv)}{-RT\ln(10)}$$

Shifting to water

$$pH_{abs}^{H_2O} = pH_{abs} + \frac{\Delta G_{solv}(H^+, H_2O)}{RT\ln(10)}$$

❖ Two commercial pH glass electrodes immersed in a symmetric glass cell with different solutions and connected to an electrometer

❖ Salt bridge containing an ionic liquid (ILSB)

$[N_{2225}][NTf_2]$
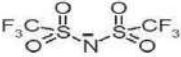
TriethylpentylammoniumBis(trifluoromethanesulfonyl)imide

Setup for pHabs measurements: electrometer, water bath, glass cell and pH glass electrodes

➤ Primary potentiometric pH$_T$ (Harned cell):

❖Three equimolal solutions of TRIS.TRIS-HCl buffers in artificial seawater:

❖ 0.02 mol·kg^{-1}, 0.05 mol·kg^{-1} and 0.08 mol·kg^{-1} gravimetrically prepared at salinities 35 and 50.

❖pH$_T$ was characterised by the primary potentiometric method (Harned cell) at the reference temperature of 25 ºC (Figure 1).

Figure 1 - Primary potentiometric system. A – Computer; B – Barometer, C – Multimeter and D – Harned Cell

➤ Spectrophotometric pH$_T$:

❖High resolution spectrophotometer

❖10 mm quartz cell cuvettes and m-cresol purple purified.

❖ The temperature was controlled with a Peltier system and monitored with a sensor with an accuracy better than 0.05 ºC (Figure 2):

Figure 2 - UV/VIS Lambda 950 dual beam spectrophotometer with the Peltier system and the chamber compartment for the quartz cells

Results:

The pH$_T$ results of the three equimolal TRIS buffers characterized by the Harned cell at T=25 ºC at $S=35$ and $S=50$ with the expanded uncertainties (U) are presented in the table below and show good agreement with reference literature [1], [2] and [3]:

S	T/K	TRIS/mol·kg^{-1}	pH$_T$	U
35	298.15	0.02	8.086	0.003
		0.05	8.088	0.003
		0.08	8.090	0.003
50	298.15	0.02	8.118	0.003
		0.05	8.120	0.003
		0.08	8.123	0.003

The graphs show the differences between Harned cell pH (pH$_{T,pot}$) spectrophotometric pH (pH$_{T,spec.}$) and pH$_{abs}$ in TRIS buffer solutions in synthetic seawater:
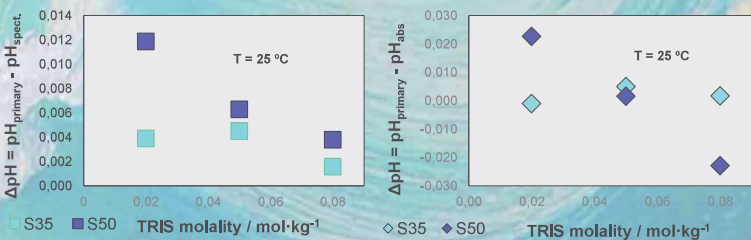
Conclusions and ongoing work:

✓The pH$_T$ results show good agreement with reference literature at 25 ºC .
✓This meticulous approach signifies a step towards unravelling the pH of saline solutions measurements with pH$_T$ standard uncertainties of 0.003 and pH$_{abs}$ with standard uncertainty of 0.12.
✓Despite the relatively good results obtained with the TRIS reference buffers which permitted to validate the pH$_{abs}$ scale, the uncertainty values are apparently overestimated. This is not sufficient for oceanographic purposes and climate goals.
✓On going work is to extend the pH$_T$ measurements at other temperatures and salinities (>50) and verify the influence of salinity in the pH$_{abs}$ values to reduce the uncertainty level.

References:
[1] DelValls, T. A., & Dickson, A. G. (1998). The pH of buffers based on 2-amino-2-hydroxymethyl-1, 3-propanediol ('tris') in synthetic sea water. Deep Sea Research Part I: Oceanographic Research Papers, 45(9), 1541-1554.
[2] Dickson, A. G. (1990). Thermodynamics of the dissociation of boric acid in synthetic seawater from 273.15 to 318.15 K. Deep Sea Research Part A. Oceanographic Research Papers, 37(5), 755-766.
[3] Papadimitriou, S., Loucaides, S., Rérolle, V., Achterberg, E. P., Dickson, A. G., Mowlem, M., & Kennedy, H. (2016). The measurement of pH in saline and hypersaline media at sub-zero temperatures: Characterization of Tris buffers. Marine Chemistry, 184, 11-20.
[4] Radtke, V., Stoica, D., Leito, I., Camões, F., Krossing, I., Anes, B., ... & Lawrence, N. (2021). A unified pH scale for all solvents: part I—intention and reasoning (IUPAC Technical Report). Pure and Applied Chemistry, 93(9), 1049-1060.
[5] Heering, A., Stoica, D., Camões, F., Anes, B., Nagy, D., Nagyné Szilágyi, Z., ... & Leito, I. (2020). Symmetric potentiometric cells for the measurement of unified pH values. Symmetry. 12(7), 1150.

Instituto Português da Qualidade

RUA ANTÓNIO GIÃO, N.º 2 | 2829-513 CAPARICA
T (+351) 212 948 100
WWW.IPQ.PT